



8-2001

# Surface Texture and Micromechanics of Ultra High Molecular Weight Polyethylene (UHMWPE) Orthopaedic Implant Bearings

Monica A. Schmidt

*University of Tennessee - Knoxville*

---

## Recommended Citation

Schmidt, Monica A., "Surface Texture and Micromechanics of Ultra High Molecular Weight Polyethylene (UHMWPE) Orthopaedic Implant Bearings." PhD diss., University of Tennessee, 2001.

[https://trace.tennessee.edu/utk\\_graddiss/3016](https://trace.tennessee.edu/utk_graddiss/3016)

This Dissertation is brought to you for free and open access by the Graduate School at Trace: Tennessee Research and Creative Exchange. It has been accepted for inclusion in Doctoral Dissertations by an authorized administrator of Trace: Tennessee Research and Creative Exchange. For more information, please contact [trace@utk.edu](mailto:trace@utk.edu).

To the Graduate Council:

I am submitting herewith a dissertation written by Monica A. Schmidt entitled "Surface Texture and Micromechanics of Ultra High Molecular Weight Polyethylene (UHMWPE) Orthopaedic Implant Bearings." I have examined the final electronic copy of this dissertation for form and content and recommend that it be accepted in partial fulfillment of the requirements for the degree of Doctor of Philosophy, with a major in Engineering Science.

David C. Joy, Major Professor

We have read this dissertation and recommend its acceptance:

Roberto S. Benson, Carl J. McHargue, Paul J. Phillips, Jack F. Wasserman

Accepted for the Council:

Dixie L. Thompson

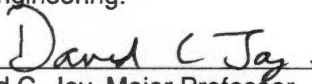
Vice Provost and Dean of the Graduate School

(Original signatures are on file with official student records.)

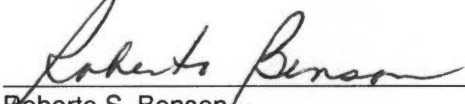
---

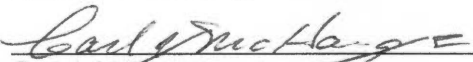
To the Graduate Council:

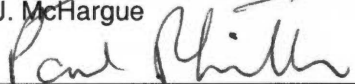
I am submitting herewith a dissertation written by Monica A. Schmidt entitled "Surface Texture and Micromechanics of Ultra High Molecular Weight Polyethylene (UHMWPE) Orthopaedic Implant Bearings." I have examined the final copy of this dissertation for form and content and recommend that it be accepted in partial fulfillment of the requirements for the degree of Doctor of Philosophy, with a major in Metallurgical Engineering.


  
\_\_\_\_\_  
David C. Joy, Major Professor

We have read this dissertation  
and recommend its acceptance:

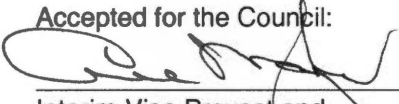
  
\_\_\_\_\_  
Roberto S. Benson

  
\_\_\_\_\_  
Carl J. McHargue

  
\_\_\_\_\_  
Paul J. Phillips

  
\_\_\_\_\_  
Jack F. Wasserman

Accepted for the Council:

  
\_\_\_\_\_  
Interim Vice Provost and  
Dean of the Graduate School

**SURFACE TEXTURE AND MICROMECHANICS OF  
ULTRA HIGH MOLECULAR WEIGHT POLYETHYLENE  
(UHMWPE) ORTHOPAEDIC IMPLANT BEARINGS**

**A Dissertation  
Presented for the  
Doctor of Philosophy  
Degree  
The University of Tennessee, Knoxville**

**Monica A. Schmidt  
August 2001**

**Copyright © 2001 by Monica A. Schmidt**

**All rights reserved**

## DEDICATION

This dissertation is dedicated to my husband, Russell W. Schmidt, and our two children,  
who have supported and encouraged me as I left full-time employment  
and pursued my goal of completing this degree  
and starting a new career,  
and  
to my parents, Betty and Dulany E. Brooks,  
who always encouraged me to pursue higher education  
and to use my talents and intelligence to the best of my ability.  
They were never disappointed to have an only daughter instead of an only son.

“A capable wife who can find? She is far more precious than jewels. The heart of her husband trusts in her, and he will have no lack of gain. She does him good, and not harm, all the days of her life. She seeks wool and flax, and works with willing hands.... She considers a field and buys it; with the fruit of her hands she plants a vineyard. She girds herself with strength, and makes her arms strong. She perceives that her merchandise is profitable.... Strength and dignity are her clothing, and she laughs at the time to come. She opens her mouth with wisdom, and the teaching of kindness is on her tongue. She looks well to the ways of her household, and does not eat the bread of idleness. Her children rise up and call her happy; her husband too, and he praises her: ‘Many women have done excellently, but you surpass them all.’ Charm is deceitful, and beauty is vain, but a woman who fears the Lord is to be praised. Give her a share in the fruit of her hands, and let her works praise her in the city gates.”

*Proverbs 31: 10 – 31*

## Acknowledgments

The author expresses her sincere appreciation to Dr. David Joy, her advisor and long-time professional colleague, for many years of support and encouragement, for sharing mutual interests in microscopy techniques and digital image analysis, and for giving her the opportunity to develop applications for confocal microscopy in materials science. He receives special thanks for allowing her to pursue and develop a research project based on her own technical interests, separate from his own research.

The author thanks Dr. Carl McHargue and the Center for Materials Processing at the University of Tennessee-Knoxville for providing a Research Assistantship and travel funds that allowed her to initiate a new research project in biomaterials. She also thanks Dr. McHargue for serving on her doctoral committee and suggesting nanoindentation.

The author thanks Joel Higgins and Biomet for providing partial funding and specimens suitable for this research. His support made it possible to study medical devices, rather than simulated specimens, and to implement a controlled study based on UHMWPE bearings that were fabricated from the same resin but by different fabrication methods.

The author graciously thanks her other committee members, who have provided technical expertise throughout her years as a student. Dr. Roberto Benson initially taught her about biomaterials, and later shared his expertise in polymers and in FTIR analysis. He also encouraged her to attend a NATO Advanced Training Institute on orthopaedic biomaterials in 1994. Dr. Paul Phillips developed her knowledge of polymer morphology and the applications of DSC and SAXS. Dr. Jack Wasserman taught her about biomechanics, encouraged her interests in orthopaedic implants, and most recently gave her an opportunity to develop her teaching skills within the Biomedical Engineering program at UTK.

The author appreciates encouragement and helpful discussions on biomaterials and biomedical engineering from Dr. Raymond Buchanan, Dr. David Gerard, Dr. Richard Jendrucko, and Dr. Judy Cezeaux (formerly at UTK). Other professors and staff who shared

their expertise include Dr. George Pharr and Dr. Greg Swadener (UT/ORNL, nanoindentation), Dr. John Dunlap and Mr. Dick Williams (cryomicrotoming), Dr. Joseph Spruiell (WAXD, teaching), Dr. William Becker (mechanical behavior, teaching), Dr. Charlie Brooks (microscopy, teaching), and Dr. Tom Shannon and Dr. Patrick Taylor (teaching).

The author greatly appreciates the expertise and helpful discussions shared by Dr. J. S. Lin at Oak Ridge National Laboratory. Without his help, the SAXS experiments and analyses would not have provided such a complete explanation of the morphology differences and changes within the UHMWPE bearings.

The author appreciates the insights on nanoindentation of polymers shared by Dr. Barry Lucas, a colleague and a friend. Dr. Lucas' previous research and dissertation gave her excellent insights into how to conduct nanoindentation experiments on polyethylene.

The author persisted in graduate school, in part, through the encouragement and insights of other students, including Dr. Zhou Zhang, Dr. A. Mohan, Dr. Justin Hwu, Dr. Rosanne Smith, Dr. John Wagner, Dr. Shima Clarke, Gary Holt, and Anita Dimeska. Their friendships made these long years of graduate school far more pleasant and enjoyable. Discussions with them also expanded what was learned in the classroom.

The author received wonderful support from secretaries including Jennifer Trollinger, Sandy Maples, Carla Lawrence, Jewell Johnson, and Angela McCarter.

The author thanks Dr. Jack Lemons (University of Alabama-Birmingham) for encouraging her interests in biomaterials and for introducing her to many other professionals world-wide in the field of Biomedical Engineering.

Most especially, the author thanks Dr. Hal Cates, M.D., for sharing his expertise in orthopaedic surgery (specifically total joint replacements), for providing his perspective on clinical problems with biomaterials, and for making key contacts with implant manufacturers.

The author appreciates encouragement and positive thinking from her husband and children, parents and extended family, and her friends at church and in Girl Scouting.



Acknowledgment for nanoindentation experiments performed at ORNL:

Research at the Oak Ridge National Laboratory ShaRE Collaborative Research Center was sponsored by the Division of Materials Sciences and Engineering, U.S. Department of Energy, under contract DE-AC05-00OR22725 with UT-Battelle, LLC, and through the ShaRE Program under contract DE-AC05-76OR00033 with Oak Ridge Associated Universities.

Acknowledgment for small-angle X-ray experiments performed at ORNL:

The research at Oak Ridge was sponsored in part by the U. S. Department of Energy under Contract No. DE-AC05-00OR22725 with the Oak Ridge National Laboratory, managed by the UT-Battelle, LLC.

## Abstract

Tibial bearings of ultra-high molecular weight polyethylene (UHMWPE) were characterized to identify differences in morphology, surface texture (roughness and skewness), and micro-scale mechanical behavior. These orthopaedic implant components were fabricated by direct molding or by machining after isostatic compression molding. Sterilization was by gamma irradiation (3.3 Mrad) in air, followed by shelf aging for 2 years. Comparisons were made between unsterile and sterile bearings to identify differences in structure and properties related to wear debris.

Characterization methods included confocal optical microscopy, nanoindentation, small angle X-ray scattering (SAXS), wide-angle X-ray diffraction (WAXD), Fourier transform infrared spectroscopy (FTIR), differential scanning calorimetry (DSC), and polarized light microscopy. Morphology was compared between bulk and surface (top and bottom) specimens of the bearings. Cryo-microtomy was used to prepare thin specimens transverse to the top surface for polarized microscopy. Nanoindentation was performed on the top bearing surfaces, near areas examined by confocal microscopy.

Processing methods affected both small- and large-scale morphology of UHMWPE. Direct molding produced thinner lamellae, thicker long periods, and slightly lower crystallinity than isostatic compression molding. Both bearing types contained a thick interface between the crystalline and amorphous phases. Interfacial free energy varied with interface thickness. Resin particles were consolidated better in direct molded bearings than in machined bearings. Segregated amorphous regions were observed in the machined bearings.

Sterilization and shelf aging affected nanometer-scale morphology. Chain scission significantly decreased the interface thickness, causing an increase in lamellar thickness and a small increase in crystallinity. Only a small decrease in the amorphous thickness resulted. Heterogeneous oxidation increased these changes in interface thickness and lamellar

thickness at the surfaces. Thin lamellae were created in the direct molded bearing, uniformly through its thickness, following chain scission and crystallization at low temperature.

Both surface roughness and morphology affected micromechanical behavior by nanoindentation. Indents must extend deeper than the peak-to-valley height (2 – 11  $\mu\text{m}$ ) of surface features, near the scale of wear debris. Hardness and elastic modulus correlated with lamellar thickness. Machined bearings were harder and stiffer than direct molded bearings. Sterilization increased lamellar thickness, so properties of the sterile, molded bearing approached those of the unsterile, machined bearing.

# TABLE OF CONTENTS

<u>SECTION</u>	<u>PAGE</u>
1. INTRODUCTION .....	1
2. SIGNIFICANCE OF THE RESEARCH TO ORTHOPAEDICS .....	5
2.1 Application of UHMWPE Bearings in Biomedical Implants .....	5
2.1.1 Importance to clinical medicine and surgery .....	5
2.1.2 Frequency of total joint replacements .....	5
2.1.3 Load bearing applications in orthopaedic devices .....	6
2.1.4 Wear of UHMWPE bearing surfaces .....	7
2.2 Significance of UHMWPE Wear Debris .....	8
2.2.1 Linkage between wear debris, osteolysis & loosening .....	8
2.2.2 Effect on performance lifetime of implants .....	9
2.3 Importance of UHMWPE Surface Properties .....	10
2.3.1 Importance of surface condition to wear performance .....	10
2.3.2 Clinical differences: machined vs. molded implants .....	11
2.3.3 Fabrication differences: machined vs. molded surfaces .....	13
2.3.4 Gamma sterilization as a significant factor in wear .....	14
3. REVIEW OF RELATED LITERATURE .....	16
3.1 Principles of Wear and Lubrication .....	16
3.2 Clinical Wear of UHMWPE .....	20
3.2.1 Increased wear in machined vs. molded acetabular cups .....	20
3.2.2 Wearing-in period and wear rates vs. time .....	25
3.2.3 Wear from non-articulating surfaces of bearing components .....	28
3.3 Engineering Studies of UHMWPE Loading and Wear .....	29
3.3.1 Biomechanics and stress distribution .....	29
3.3.2 Results of engineering wear studies .....	31
3.4 UHMWPE Structure and Processing .....	33
3.4.1 Crystallinity and molecular structure .....	33
3.4.2 Resin types .....	34
3.4.3 Ram extrusion vs. compression molding vs. isostatic molding .....	34
3.4.4 Direct compression molding of components to final shape .....	38
3.4.5 Machining vs. direct molding of implant components .....	38
3.4.6 Fusion defects and "grain" boundaries .....	40
3.5 Sterilization of UHMWPE Components .....	42
3.5.1 Sterilization methods .....	42
3.5.2 Primary electronic excitations from gamma irradiation .....	43
3.5.3 Secondary chemical reactions via free radicals .....	45
3.5.3.1 Heterogeneous vs. homogeneous oxidation .....	45
3.5.3.2 Radiation degradation in inert gas or vacuum .....	46
3.5.3.3 Radiation degradation in air .....	48
3.5.3.4 Post-irradiation effects .....	50
3.5.4 Longevity of free radicals in UHMWPE .....	51
3.5.5 Oxidation and post-irradiation aging .....	53
3.5.6 Subsurface "white band" from irradiation .....	58
3.5.7 Crosslinking from irradiation .....	63
3.5.8 Effect of irradiation on mechanical properties .....	65
4. PRINCIPLES OF EXPERIMENTAL TECHNIQUES .....	73
4.1 Confocal Microscopy .....	73
4.2 Nanoindentation .....	80
4.3 Polymer Morphology Measurements .....	84
4.4 Small Angle X-Ray Scattering .....	88

4.5	Wide Angle X-Ray Diffraction .....	93
4.6	FTIR Spectroscopy .....	94
4.7	Differential Scanning Calorimetry .....	95
4.8	Polarized Light Microscopy .....	96
5.	OBJECTIVES AND HYPOTHESES .....	97
5.1	Objectives .....	97
5.2	Hypotheses .....	98
6.	EXPERIMENTAL PROCEDURES .....	100
6.1	Tibial Components and Other Specimens .....	100
6.2	Confocal Microscopy .....	100
6.2.1	Specimen preparation .....	102
6.2.2	Measurement of surface texture .....	102
6.3	Nanoindentation .....	103
6.3.1	Specimen preparation .....	103
6.3.2	Calibration of contact area versus depth .....	104
6.3.3	Measurement of micromechanical properties .....	105
6.4	Small Angle X-Ray Scattering .....	106
6.4.1	Specimen preparation .....	107
6.4.2	Measurement of long period and lamellar thickness .....	107
6.5	Wide Angle X-Ray Diffraction .....	108
6.5.1	Specimen preparation .....	108
6.5.2	Measurement of crystallinity .....	108
6.6	FTIR Spectroscopy .....	109
6.6.1	Specimen preparation .....	109
6.6.2	Measurement of crystallinity .....	110
6.7	Differential Scanning Calorimetry .....	110
6.7.1	Specimen preparation .....	110
6.7.2	Measurement of thermal properties .....	111
6.8	Polarized Light Microscopy .....	111
6.8.1	Specimen preparation .....	111
6.8.2	Examination of morphology .....	112
7.	RESULTS .....	113
7.1	Confocal Microscopy .....	113
7.2	Nanoindentation .....	122
7.3	Small Angle X-Ray Scattering .....	133
7.4	Wide Angle X-Ray Diffraction .....	145
7.5	FTIR Spectroscopy .....	145
7.6	Differential Scanning Calorimetry .....	150
7.7	Polarized Light Microscopy .....	166
8.	DISCUSSION .....	170
8.1	Morphology of Unsterile UHMWPE .....	170
8.2	Morphology of Irradiated & Aged UHMWPE .....	179
8.3	Surface Texture .....	182
8.4	Micromechanics .....	186
9.	CONCLUSIONS .....	193
10.	PROPOSALS FOR FUTURE RESEARCH .....	200
	REFERENCES .....	202
	VITA .....	220

## LIST OF FIGURES

<b><u>Figure</u></b>	<b><u>Page</u></b>
Figure 1. The Stribeck Curve.....	18
Figure 2. Optics of a tandem scanning confocal microscope.....	74
Figure 3. Confocal image intensity versus height for the 10X objective lens (100X).....	76
Figure 4. Image intensity varies with distance from the focal plane for optical sections focused at different heights on the specimen surface.....	76
Figure 5. Confocal image intensity versus height for the 20X objective lens (200X).....	78
Figure 6. Determination of the minimum roughness average (Ra) for a flat, planar surface.....	81
Figure 7. Geometry of the Berkovich indenter.....	82
Figure 8. Schematic representation of polymer crystallite.....	85
Figure 9. Parameters for measurement of polymer morphology.....	87
Figure 10. Typical one-dimensional correlation function for a polymer with a crystallinity of 50 to 70% by volume.....	91
Figure 11. Confocal images of a machined tibial bearing surface. Optical sections were acquired in Z-increments of 4 $\mu\text{m}$ over a vertical range of 100 $\mu\text{m}$ .....	114
Figure 12. Confocal images of a direct molded tibial bearing surface. Optical sections were acquired in Z-increments of 4 $\mu\text{m}$ over a vertical range of 100 $\mu\text{m}$ .....	116
Figure 13. Confocal images of a machined tibial bearing surface. Optical sections were acquired in Z-increments of 1.5 $\mu\text{m}$ over a vertical range of 49.5 $\mu\text{m}$ .....	117
Figure 14. Confocal images of a direct molded tibial bearing surface. Optical sections were acquired in Z-increments of 1.5 $\mu\text{m}$ over a vertical range of 49.5 $\mu\text{m}$ .....	118
Figure 15. Load-displacement results (covering the entire load range) for nanoindentations.....	123
Figure 16. Load-displacements results at low loads (for displacements near the scale of wear debris formation) from nanoindentations on the top surfaces.....	126
Figure 17. Hardness vs. contact depth results from nanoindentations on the top surfaces.....	129
Figure 18. Elastic modulus vs. contact depth results from nanoindentations.....	131

Figure 19.	Lorentz plots compare intensity data from small angle X-ray scattering of bulk UHMWPE specimens. ....	136
Figure 20.	Lorentz plots compare $q^2 I(q)$ versus scattering angle. ....	137
Figure 21.	One-dimensional correlation functions from SAXS analyses of bulk specimens from UHMWPE tibial bearings. ....	139
Figure 22.	Measured average thicknesses of crystalline lamellar, interfacial, and amorphous phases from SAXS analyses. ....	140
Figure 23.	Morphology variations between the surfaces and the bulk, from SAXS analyses of UHMWPE tibial bearings. ....	144
Figure 24.	Crystallinity vs. depth results from FTIR spectroscopy for direct molded vs. machined tibial bearings (unsterile). ....	149
Figure 25.	Bar chart of crystallinities from DSC analyses of UHMWPE tibial bearings comparing the top surface, the bulk, and the bottom surface. ....	153
Figure 26.	Bar chart of peak melting temperatures from UHMWPE tibial bearings comparing the top surface, the bulk, and the bottom surface. ....	154
Figure 27.	Peak melting temperature (from DSC) vs. inverse of lamellar thickness (from SAXS) for UHMWPE specimens from tibial bearings. ....	155
Figure 28.	Interfacial free energy versus interface thickness. ....	158
Figure 29.	Melting cycles from DSC for top, bulk, & bottom specimens. ....	159
Figure 30.	Difference functions from DSC analysis for top & bottom specimens. ....	161
Figure 31.	Polarized light microscopy with a quarter wave plate (200X, color). ....	167
Figure 32.	Polarized light microscopy with crossed linear polarizers (400X, B&W). ....	168
Figure 33.	Polarized light microscopy with crossed linear polarizers (1000X, B&W). ....	169
Figure 34.	Comparison of crystallinity measurements by DSC, FTIR, WAXD, and SAXS. ....	173
Figure 35.	Comparison of melting cycles from DSC for types of tibial bearings. ....	177

## LIST OF TABLES

<b><u>Table</u></b>		<b><u>Page</u></b>
Table 1.	Comparison of clinical wear rates for machined vs. direct molded UHMWPE acetabular cups in Charnley total hip arthroplasties. ....	22
Table 2.	Comparison of wear rates for machined vs. direct molded UHMWPE acetabular cups in patient matched groups. ....	24
Table 3.	UHMWPE Manufacturers and Resin Types. ....	35
Table 4.	Consolidation Methods for UHMWPE Resins. ....	36
Table 5.	Particle size distribution for Himont 1900H UHMWPE resin. ....	101
Table 6.	Surface texture parameters from machined versus direct molded tibial bearings. ....	119
Table 7.	Summary of Hardness and Elastic Modulus Results from Nanoindentation. ....	134
Table 8.	Results from 2-phase analysis of SAXS 1-dimensional correlation functions. ...	141
Table 9.	Results from 3-phase analysis of SAXS 1-dimensional correlation functions. ...	142
Table 10.	Results from Wide Angle X-Ray Diffraction.....	146
Table 11.	Results from FTIR Spectroscopy and DSC determine the amount of interface. ....	148
Table 12.	Results from Differential Scanning Calorimetry.....	152



# 1. INTRODUCTION

Wear from ultra high molecular weight polyethylene (UHMWPE) bearing components is a significant technical issue for extending the long-term performance of orthopaedic total joint replacements (TJR's). The significance of UHMWPE wear is primarily due to the *release of microscopic wear debris particles* from the bearing surface into the surrounding biological tissue, and resulting biological reactions to these particles, rather than due to the bulk failure or wear-through of the UHMWPE component. Materials engineering can make a significant contribution by characterizing the structure and properties of the UHMWPE components at the scale on which this debris is formed. This will contribute to understanding how the UHMWPE wear debris is generated and released at the microscopic level. Many engineering studies have focused on wear as a macroscopic process, and have ignored the fact that wear debris is released on a microscopic scale (as particles are often submicron in size).

Polyethylene wear debris particles are closely associated with biological tissue changes (i.e. osteolysis, or bone resorption) that limit the performance lifetimes of medical implants. The size and shape of debris particles can affect how cells engulf these particles, contributing to changes in biological tissue. Osteolysis causes the surrounding bone to deteriorate, so that it no longer mechanically supports the implant. This leads to loosening of the implant, with associated pain and instability near the joint. Thus the total joint replacement no longer performs satisfactorily for the patient, and is considered to have "failed." This is a medical, or clinical, definition of failure, which is quite different from the typical engineering definition of failure. The components within the medical device may still be intact, not having either broken or worn through after years of use within the patient.

Wear of UHMWPE bearings has been the focus of much research in the field of orthopaedics, yet is still poorly understood. Clinical studies have characterized the wear debris released in-vivo (in the human body), and carefully measured its physical dimensions and shape using electron microscopy techniques. Engineering wear studies have focused on the

gross wear behavior of UHMWPE, measuring wear as either weight loss or volume change over millions of wear cycles. Wear has been measured both in-vitro (in laboratory tests) and in-vivo (in the human body), and results are now compared to show that in-vitro test results (wear rates, form of surface damage, and debris particles) are similar to clinical performance. As the understanding of wear mechanisms has improved, laboratory wear studies have had to demonstrate that the resulting surface damage and wear debris are similar to that observed in clinical studies (i.e. in-vivo). Thus research is moving toward an emphasis on how mechanical loading interacts with materials structure to generate wear, or the loss of material. Many previous wear studies did not provide information about the structure, chemistry, or processing of the UHMWPE materials that were tested, and this is now considered critical information to evaluate the wear test results.

Clinical wear studies have now found differences in wear rates that are linked to processing variables (i.e. resin, fabrication method, sterilization method) for the UHMWPE component. Earlier studies treated all UHMWPE components as identical, ignoring potential materials issues. Differences in wear behavior in-vivo have now been related to fabrication differences in the UHMWPE components. In particular, components direct molded from resin powder had less wear than components machined from extruded rod or compression molded sheet. This difference in wear performance has not been explained, but is of great technical interest. Understanding the differences between the direct molded and the machined components could contribute to significant improvements in UHMWPE component performance.

Wear is a phenomenon that occurs at surfaces. Wear is the progressive loss of material (debris) from load-bearing surfaces that slide or roll while in contact with other component surfaces. Debris from UHMWPE components is released as microscopic (often submicron) particles, particularly under abrasive or adhesive wear mechanisms, indicating that materials structures and properties need to be evaluated at the microscopic scale.

Surface texture can have a significant effect on wear. Most engineering analyses of loading assume an idealized contact zone in which both surfaces are perfectly smooth and thus touch at all points. However, the true contact areas between bearing surfaces occur at microscopic surface irregularities that are pressed together. Thus the true contact areas are smaller than the idealized contact areas, resulting in the true localized stresses being higher than those from engineering calculations. Variations in surface topography of the UHMWPE will affect the true contact areas and also the micromechanical surface interactions with the opposing bearing surface. Previous studies of implants have not attempted to quantify the 3-dimensional texture of UHMWPE bearing surfaces and to relate this to micromechanical behavior.

Machining and direct molding of UHMWPE implant components are quite different manufacturing processes, and will affect the structure and properties of the resulting components. The surface texture produced by machining can vary over a wide range, depending on a number of machining variables. In contrast, the surface texture produced by direct molding of resin should depend primarily on the surface texture of the mold, if the temperature and pressure cycle is well controlled to consolidate the resin. The thermal cycle for producing a direct molded component may be quite different from that for producing a commodity ram extruded rod or compression molded sheet. Uniform consolidation should be easier to achieve in a small part than in an extremely large rod or sheet. The difference in thermal history can produce significant differences in polymer morphology, and thus in mechanical properties of the polyethylene. These differences can be localized, as at the surfaces of UHMWPE components, or occur throughout the bulk. Machining will also induce heating, thus modifying the polymer morphology near the machined surface.

The proposed research focuses on identifying differences between the microscopic surface texture, large-scale polymer morphology, crystallinity, and micromechanical behavior of direct molded versus machined UHMWPE bearing components. Several clinical studies have quantified differences in wear between UHMWPE acetabular cups in total hip

replacements manufactured by these methods. (Wear is much easier to measure quantitatively in hip components than in knee components.) However, the components were not evaluated to determine what differences in materials variables were also present. The clinical studies involved components from different implant manufacturers, which thus may have been fabricated from different UHMWPE resins. This may be the first study to carefully evaluate differences in properties between carefully controlled implant components fabricated from the same UHMWPE resin.

Differences in surface texture, large-scale polymer morphology, and crystallinity are expected to relate to differences in micromechanical behavior. Surface texture will be measured quantitatively in three dimensions using confocal microscopy and image analysis techniques. Polymer morphology will be examined using polarized light microscopy and electron microscopy techniques. Crystallinity will be measured with differential scanning calorimetry. Micromechanical behavior will be studied using nanoindentation to record load-displacement curves, and then hardness and elastic modulus will be determined from the results.

## **2. SIGNIFICANCE OF THE RESEARCH TO ORTHOPAEDICS**

### **2.1 APPLICATION OF UHMWPE BEARINGS IN BIOMEDICAL IMPLANTS**

#### **2.1.1 Importance to clinical medicine and surgery**

Ultrahigh molecular weight polyethylene (UHMWPE) is a polymer that is used as a bearing component in many surgical implants, primarily artificial joints. The most common applications are in orthopaedic total joint replacement implants for hips and knees. Both the acetabular cup component in total hip implants and the tibial plateau component in total knee implants are commonly fabricated from UHMWPE, frequently with a metal backing which is attached to bone.

Total joint replacements are used to treat patients with severe pain or disability resulting from osteoarthritis, rheumatoid arthritis, fractures, or other bone disorders.<sup>1</sup> Before surgery, the patient either has severe pain and difficulty in walking, or may be bedridden. Surgical replacement of the joint with an implant relieves pain and suffering, provides increased mobility, and returns the patient to a more normal lifestyle in most cases. Thus significant benefits are obtained through the use of artificial joints fabricated from engineering materials.

#### **2.1.2 Frequency of total joint replacements**

Artificial joints are being used extensively both in the United States and internationally. Between 1985 and 1988, an average of 531,000 joint repair surgeries (arthroplasties) were performed annually in the United States in short-term general hospitals. Hip surgeries (38.4%) and knee surgeries (35.8%) were the most frequent arthroplasty procedures during this period. Total hip replacements averaged 123,000 per year (23.2%), total knee replacements averaged 95,000 per year (17.9%), and femoral head replacements (hip) averaged 58,000 per year (10.9%).<sup>1,2</sup> Thus surgeries to replace hip and knee joints through the use of artificial implant components made up 52.0% of all arthroplasty surgeries during this period.

The number of joint replacement surgeries increases each year as the success of these procedures continues to be demonstrated. This has a significant impact on national healthcare costs, as Medicare covers approximately 70% of patients having major joint replacement surgeries. The number of total hip replacements covered by Medicare increased from 50,799 in 1985 to 62,918 in 1989, increasing at a compounded annual rate of 5.5%. Even more significant, the number of total knee replacements increased from 45,368 in 1985 to 80,647 in 1989, increasing at a compounded annual rate of 15.5%.<sup>1,3</sup>

By 1988, 1,295,000 people in the United States reported having one or more artificial joint replacements. Of this number, 79,000 were over 85 years old, 725,000 were between 65 and 84 years old, and 491,000 were younger than 65 years.<sup>1,4</sup> The increasing numbers of younger patients receiving artificial joint replacements place higher technical demands on the engineered implant components and materials. Younger patients require a longer performance lifetime from an implant before revision surgery is necessary. This was not a significant issue when most patients were over 85 years of age, and was less of an issue when all patients were over 65 years of age. Younger patients also tend to be more mobile and physically active, placing higher and more frequent stresses on the implant components. This results in more rapid wear and/or mechanical deterioration of the load bearing materials.

### **2.1.3 Load bearing applications in orthopaedic devices**

The two major applications of UHMWPE in total joint replacements are the acetabular cup of the hip and the tibial plateau of the knee. Both components are major load bearing, articulating surfaces within the total joint replacement, and articulate against a metal counterface. The opposing, articulating metal bearing components are typically fabricated from titanium, titanium alloy, or cobalt-chromium alloy, although stainless steel was sometimes used in the past. The UHMWPE bearing component is frequently attached to a metal backing component, which is then attached to the bone by some combination of methylmethacrylate

bone cement, screw fixation, or bone ingrowth into a porous metal coating. Some UHMWPE acetabular cups are cemented directly to the bone of the acetabulum, without a metal backing.

The load distribution and range of motion of the hip and knee implants are quite different. Loading in the hip occurs between two conforming surfaces with spherical geometry, so that the compressive stress distribution remains fairly uniform during the walking cycle. Because of the spherical contact geometry, the articulation of the joint components primarily occurs as sliding. Loading in the knee occurs between the tibial plateau and the two condyles of the distal femur, where the surface contact areas are much smaller and the surface geometries are often nonconforming. Thus the resulting stresses are higher, and fatigue occurs as the contact area moves back and forth across the bearing components. The articulation of the joint occurs as a combination of rolling and sliding motion in flexion/extension, with rotation of the tibia relative to the femur as well.

Revision surgery to replace the primary (initial) total joint components can result from many factors, including both implant-related failures and biological causes. Failure of the orthopaedic implant usually occurs in the UHMWPE component first, before significant damage is observed on the metal components. Failure of UHMWPE is most often due to wear at the articulating surface, with an additional contribution from creep. These mechanisms lead to thinning of the UHMWPE bearing, release of wear debris from the articulating surface, and changes in contact geometry which affect the stress distribution within the UHMWPE. In extreme cases, localized wear-through of the UHMWPE bearing results in metal-on-metal contact between the metal bearing component and the metal backing for the UHMWPE.

#### **2.1.4 Wear of UHMWPE bearing surfaces**

Wear phenomena in UHMWPE articulating surfaces are significantly different between total hip and total knee implants, due to the differences in loading and motion described above. Both types of implants also experience less extensive wear on the UHMWPE non-articulating surfaces that contact the metal backings.

Wear inside the acetabular cup of the hip is primarily observed as scratching and burnishing of the articulating surface, with some localized pitting, combined with a directional reduction in the UHMWPE thickness along the loading direction. This results from abrasion and adhesion mechanisms between the articulating surfaces due to sliding wear, and from creep of the viscoelastic UHMWPE due to compression along the loading axis.

Wear in the tibial plateau of the knee includes scratching and burnishing, but more pitting and often delamination is observed as well. Delamination occurs when large sheets of material separate from the bearing surface (parallel to the surface) and results from fatigue-type loading. Subsurface cracks initiate and grow below the load-bearing surface, and the cracks propagate faster as the number of loading cycles increases. Finally the crack deviates toward the bearing surface, and the entire sheet of material splits away and is ground apart between the articulating bearings. This releases a large volume of wear debris.

## **2.2 SIGNIFICANCE OF UHMWPE WEAR DEBRIS**

### **2.2.1 Linkage between wear debris, osteolysis & loosening**

The release of wear debris can lead to revision surgery and replacement of the primary artificial joint even when major failure (wear-through or fracture) of its components has not occurred. Wear debris will eventually induce osteolysis (bone resorption) around the implant, which is one of the main biological processes leading to aseptic loosening. Loosening of the implant results in the patient experiencing pain and instability, which require that the artificial joint components be replaced.

Aseptic loosening (i.e. loosening in the absence of bacterial or other microbiological infections) is the primary cause of late revisions (after 9-15 years) in total hip replacements. Particulate wear debris is transported biologically from the articulating surfaces into the tissue of the joint capsule, where it is stored in mononuclear histiocytes or multinucleated giant cells until it can be transported away via the lymph system. When the rate of accumulation of debris exceeds the rate of transport and excretion, the tissue membranes have to store the debris,



and osteolysis results.<sup>5,6,7</sup> All implant materials, including UHMWPE, bulk metals, metal coatings, and bone cement, either experience wear or release particles by other mechanisms and contribute to the problem of osteolysis, but UHMWPE is considered to be the major contributor.

Studies are still underway to examine the effect of particulate wear debris characteristics on osteolysis, with emphasis on debris type (UHMWPE, bone cement, metal), morphology, size, surface area, shape, etc.<sup>8,9,10,11,12,13</sup> Polyethylene debris has been found in a wide range of sizes from 0.2 to 300  $\mu\text{m}$ , but the mean size is consistently in the range of 0.5 to 0.6  $\mu\text{m}$ .<sup>5</sup> The largest particles are ingested or surrounded by giant cells, while the smaller particles are ingested by histiocytes. The smaller, submicron particles are considered to have the worst effect in contributing to osteolysis, so UHMWPE wear debris is of great concern.

## **2.2.2 Effect on performance lifetime of implants**

Typical linear wear rates for UHMWPE acetabular cups have been measured clinically (using radiographic techniques) as 0.05-0.20 mm/year. A typical cup design has a thickness of 7-10 mm, so this seems to translate into a performance lifetime (limited by wear) of 35-200 years before wear-through. This estimated lifetime is much higher than the typical values of 10-15 years obtained from clinical practice. Aseptic loosening frequently occurs after 9-15 years,<sup>6</sup> leading to revision surgery and replacement of the primary implant components. Bone resorption makes fixation of the second implant more difficult, and its performance lifetime may be even shorter. Deterioration of the bone quality may limit a patient to three implants (two revision surgeries) within a single joint. This becomes a significant problem for the youngest patients, who may have a primary joint replacement performed when they are in their 20's or 30's.

The importance of UHMWPE wear to the lifetime of orthopaedic implants results not from the linear wear rate, but rather from the number of released particles contributing to osteolysis. As an example, consider the release of particulate debris from the acetabular

component of the hip under optimal conditions. Wear volume is calculated from the linear wear rate based on a cylindrical geometry oriented parallel to the loading axis. For a moderate-sized acetabular cup (28 mm diameter) with a very low wear rate (0.05 mm/year), the wear volume is calculated as 30.8 mm<sup>3</sup>/year. An average spherical wear particle with a diameter of 0.60 μm occupies a volume of 0.113 μm<sup>3</sup>. Thus the rate of wear debris generation equals 2.7 x 10<sup>11</sup> particles/year, or 7.5 x 10<sup>8</sup> particles/day. This is a huge particulate load for the body to transport and process. The absolute numbers of particles released will vary depending on individual implant parameters, but the magnitude of wear debris generated over the life of the implant remains large.

Thus implant performance and lifetime are critically dependent upon the wear characteristics of each device. Many factors affect wear, including component design, biomechanics of motion, lubrication mechanisms, and material properties. Each of these factors includes many variables that contribute to wear. This proposed research project will focus on specific materials variables (i.e. microstructure and micromechanical properties) which can affect the release of particulate debris from implant surfaces, both articulating and non-articulating load-bearing surfaces.

## **2.3 IMPORTANCE OF UHMWPE SURFACE PROPERTIES**

### **2.3.1 Importance of surface condition to wear performance**

Wear is a phenomenon of materials degradation that occurs at surfaces. It is affected by stress distributions and conditions below the surface, but the release of material (particulate debris) occurs from the surface. How the term “surface” is defined, in terms of physical dimensions, will vary depending on the many factors affecting wear. But it is obvious that the condition and properties of the material at the surface should have a significant effect on the wear behavior, i.e. the release rate of wear debris, the size and shape of wear debris, etc.

Consider the scenario described above for the wear of the UHMWPE acetabular component of the total hip implant. If the linear wear rate is 0.10 mm/year, this equals

0.27  $\mu\text{m}/\text{day}$ . Assuming an average spherical diameter of 0.60  $\mu\text{m}$ , a monolayer of particulate wear debris would be removed from the articulating surfaces about every two days. Reducing this linear wear rate by a factor of three might seem like a small change, but it would increase time for removal of a monolayer of wear debris to almost a week. This change might be very significant to biological mechanisms related to osteolysis. Allowing a longer time for encapsulation and transport of particulate wear debris within the body could significantly delay or reduce the development of osteolysis. This would lead to a distinct increase in the successful clinical performance and lifetime of the total joint replacement.

The microstructure and micromechanical properties of the material at the surface will have a significant impact on the release of wear debris. The tribology of the wear process must also be evaluated, involving the roughness of both articulating surfaces, the properties of the lubricant, the load transmitted between the surfaces, and the large-scale and small-scale contact geometries. The interactions between all these variables must be carefully considered to understand wear phenomena. The tribological conditions will determine the stresses applied to the articulating surface, but the surface's microstructure and micromechanical properties will control the mechanisms by which debris is released. Improvements in the surface properties of UHMWPE could significantly reduce the release rate for wear debris.

### **2.3.2 Clinical differences: machined vs. molded implants**

Clinical studies of UHMWPE wear rate take several different forms. Clinical examination of implanted orthopaedic devices uses radiography to examine the condition of the surrounding bone and to record the position of the implant within the joint. Detailed measurements on the resulting radiographic films have been used to quantify the wear rates of acetabular cups based on the time since initial surgery. After revision surgery, dimensional (linear or volume) measurements on the retrieved implants have also been used to determine wear rates. If many similar retrieved components are measured after different implantation times, variations in wear rates with service life can be obtained. However the wear rates can

vary significantly between patients with identical implants, so that a wide range of wear rates is frequently reported within each study.

Wear rates of UHMWPE acetabular cups, determined by these techniques, have been correlated to many different clinical factors. These include design of the implant system, patient variables, and materials variables. Two observations from these clinical studies are of particular significance to this proposed research project. First, machined UHMWPE components experience a “wearing-in” period immediately following surgery when the machining marks are removed from contacting surfaces<sup>14,15</sup> and the wear rate may be higher than the steady-state wear rate that follows (for components with good fixation).<sup>16,17</sup> Second, and perhaps of more importance, UHMWPE components fabricated by direct molding of the resin to the final shape (and surface finish) have lower wear rates than components fabricated by machining of bulk rod or sheet stock.<sup>18,19,20,21</sup>

Clinical studies also evaluate implant designs based on performance issues related to long-term survival rates as well as the patients’ pain and function during follow-up examinations. The use of a direct molded tibial component in one total knee implant design [Anatomic Graduated Component (AGC), Biomet, Inc.] has resulted in good patient function and an extremely high survival rate (98% for both tibial and femoral components) after 10 years follow-up, despite its flat-on-flat articulating surfaces.<sup>22</sup> Other designs with similar flat-on-flat geometry have shown high failure rates associated with polyethylene wear.<sup>23</sup> The excellent performance of the AGC knee implant was attributed to the quality achieved by direct molding of the UHMWPE tibial component.

In contrast, poor clinical performance has been documented for another total knee implant design [Porous Coated Anatomic (PCA-I), Howmedica] in which the surface of the UHMWPE tibial component was intentionally modified.<sup>24</sup> The failure rate after 4 to 7 years was 6% for revisions required due to severe wear of the surface-modified tibial and patellar components.<sup>25</sup> The PCA-I knee implant had a flat-on-flat articulating geometry, similar to that of the AGC implant. However the PCA-I tibial component was treated by heat pressing the

machined, articulating surface of the UHMWPE. This produced a modified microstructure down to a depth of about 1 mm, with a distinct boundary between the heat-treated zone and the bulk.<sup>26</sup> Failures were associated with severe wear of the UHMWPE, delamination of the articulating surface along the boundary of the heat-treated zone, and cracking and fragmentation of the bulk.<sup>25,27</sup> Delamination sometimes occurred from both the top and bottom surfaces of the component, releasing additional debris directly to the metal backing. Thus the surface properties and structure of this UHMWPE implant component had a significant effect on its clinical performance.

### **2.3.3 Fabrication differences: machined vs. molded surfaces**

Most UHMWPE components are fabricated by machining from commodity rod or sheet stock. Consolidation of UHMWPE resin to form a solid product form is difficult due to the high pressures required to sinter the resin, even above its melting temperature.<sup>28</sup> Molten UHMWPE has an extremely high viscosity<sup>29</sup> and does not flow except under high pressure. Only two commercial polymer converters process UHMWPE resin (using ram extrusion or unidirectional compression molding) within the United States to produce commodity rod or sheet stock for implants.<sup>30</sup> One implant manufacturer processes UHMWPE resin using isostatic compression molding to produce bar stock that is then machined.<sup>31</sup> Relatively few implant manufacturers have invested in the technology and equipment required to process UHMWPE resin into direct-molded components<sup>32</sup> since machining is much simpler and cheaper.

Machining is a fabrication process used to cut bulk material stock (rod, bar or sheet) into the final component shape, including both geometry and surface finish. The surface finish of machined components is known to contain machining marks or ridges, whereas surfaces on direct-molded components are smooth<sup>15</sup> and often glossy.<sup>32</sup> In addition to these topographical differences that may affect surface integrity, microstructural and chemical differences may result at the surfaces due to plastic deformation and heating that occurs during machining.<sup>33</sup>

In direct-molded components, the UHMWPE resin is melted and then molded to the final shape and surface finish. Solidification and crystallization of the polymer will be initiated at the mold surfaces, so that the morphology at the component surface may be different from that in the center. In particular, the crystallite size at the surface is expected to be smaller.

In machined components, the final surface of the component will be machined from the interior of the bulk stock. Uniformity of the morphology of bulk UHMWPE stock has not been reported. Machining will induce plastic deformation, frictional heating, and possibly chemical changes (mechanoradicals and oxidation) in the outer surface layer. The effects of machining on the morphology and chemical state of the outer surface layer have not been reported.

Differences in the surfaces of machined and molded UHMWPE components may be significant to the survival lifetime of total joint replacements. Changes in the surface layer relative to the bulk will affect the wear behavior of the UHMWPE implant component, particularly during the “wearing-in” period. This would affect the release of wear debris during the initial period following implantation of the artificial joint, and could contribute to the development of osteolysis.

#### **2.3.4 Gamma sterilization as a significant factor in wear**

Clinical and engineering studies have examined the wear performance of UHMWPE in orthopaedic implants. Recent studies have begun to focus on materials rather than design issues. Materials variables of concern include resin type, method of consolidation, and sterilization technique.

Sterilization has become a major concern since it was learned that gamma irradiation (the most frequently used sterilization method) forms free radicals within polyethylene, leading to crosslinking, chain scission, and subsurface oxidation. Subsurface oxidation is of significant concern to knee implants, since the region of damage correlates closely with clinically observed delamination and subsurface cracking. Oxidation is expected to significantly change

the mechanical properties in the damaged region, resulting in embrittlement. Chain scission can produce an increase in crystallinity. Crosslinking is considered to be generally beneficial, since it might decrease the rate of wear debris release. This is expected to have the most benefit to hip implants, due to the compressive load distribution within the acetabular cup. Crosslinking may also benefit knee implants, but local variations in mechanical properties could contribute further to fatigue problems.

Gamma irradiation has advantages over other sterilization methods, such as the ability to prepackage implants prior to sterilization. This is of significant value to the implant manufacturers, so this sterilization method is being carefully evaluated before a different method is implemented. Thus this method was selected for this proposed research project because of its extensive use in industry and its known effects on the subsurface morphology and chemistry of UHMWPE.

### **3. REVIEW OF RELATED LITERATURE**

#### **3.1 PRINCIPLES OF WEAR AND LUBRICATION**

Wear has been defined as “the progressive loss of substance from the operating surface of a body occurring as a result of relative motion at the surface.”<sup>34</sup> Wear between solid surfaces can result from four separate mechanisms, which often interact, including: (1) abrasion, (2) adhesion, (3) surface fatigue, and (4) tribo-chemical interactions. Relative motions between the solid bearing surfaces may occur as: (1) sliding, (2) rolling, (3) impact, and (4) oscillation. When a liquid lubricant is added to the bearing system, flow of the liquid and/or entrained particles also occurs.<sup>34</sup>

In UHMWPE implant components, the mechanisms of abrasion, adhesion, and surface fatigue predominate in the wear process. In the total hip replacement, relative motion occurs primarily as sliding and oscillation, which primarily results in abrasive and adhesive wear mechanisms acting through surface asperities at the microstructural level. In the total knee replacement, relative motion occurs with rolling in addition to sliding and oscillation. The decreased contact area (as compared to the total hip) between bearing surfaces results in significant surface fatigue affecting macro scale regions in addition to abrasive and adhesive wear mechanisms.

Each wear mechanism produces distinct wear patterns on the solid bearing surfaces, which have been observed on retrieved UHMWPE implant components. Abrasion results in scratches, grooves, and embedded debris (from 3rd-body particles) in the UHMWPE surface. Abrasion can result from the surface roughness of the metal bearing surface or from 3rd-body particles such as metal wear debris, PMMA bone cement debris, metal coating debris, calcium phosphate coating debris, or bone particles. Adhesion results in the transfer of material from the UHMWPE to the metal bearing surface (and possibly back again), leaving flakes, lumps, smears, and shallow pits in the UHMWPE surface. Surface fatigue results in subsurface cracking that leads to deep pitting or delamination of sheets from the UHMWPE surface.



Fatigue cracks can be identified from the concentric rings formed as the crack progressively grows from its initiation site. Most retrieved implants show a combination of these wear patterns after implantation for several years.

Human joints are lubricated by synovial fluid, and this lubrication is gradually reestablished in total joint replacements as well. Thus lubrication modes must be considered in evaluating the wear behavior of implants. The Stribeck curve is used to describe the frictional behavior of lubricated, moving surfaces as a function of the lubricant viscosity ( $\eta$ ), the velocity ( $v$ ), the applied normal load ( $F_N$ ), the combined surface roughness ( $R$ ), and the separation of the bearing surfaces ( $h$ ). The Stribeck curve is shown schematically in Figure 1. Three lubrication modes are identified as: (I) hydrodynamic lubrication (and elastohydrodynamic, EHD, lubrication), (II) partial EHD or mixed lubrication, and (III) boundary lubrication.

In hydrodynamic lubrication, a continuous lubricant film separates the two bearing surfaces so that no direct physical contact occurs. The separation of the surfaces,  $h$ , is much larger than their combined surface roughness,  $R$ . Friction results from the viscosity of the lubricant, and can be determined based on fluid mechanics. Friction increases linearly with viscosity and velocity, but decreases with increasing normal force. Wear can only occur by surface fatigue, cavitation, or fluid erosion. When the normal force (or pressure) becomes sufficiently high but the surfaces are nonconforming, elastic deformation of the surfaces and pressure dependence of the lubricant viscosity must be considered. This mode is referred to as elastohydrodynamic lubrication.<sup>34</sup> These modes are not expected in conventional metal-on-UHMWPE implant bearings, but would be beneficial due to the elimination of abrasive and adhesive wear.

In mixed lubrication, the lubricant film is thinner so that some limited physical contact occurs between micro asperities on the two bearing surfaces. Relative to hydrodynamic

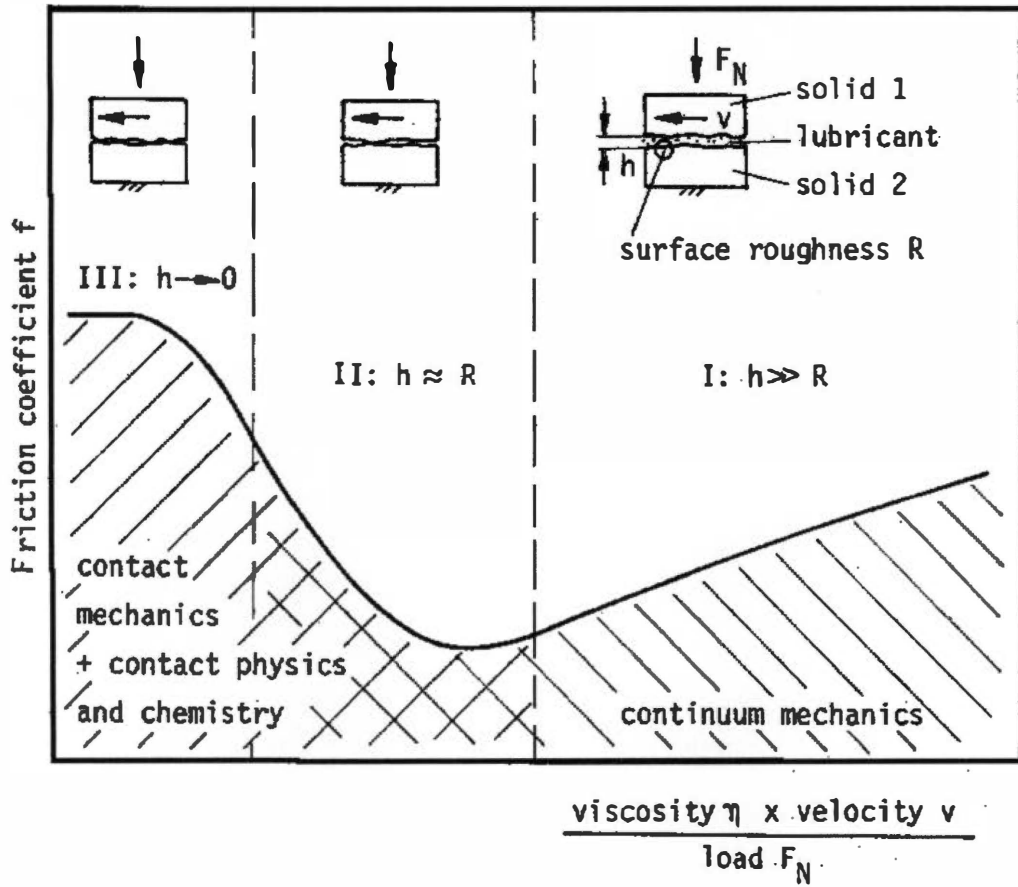


Figure 1. The Stribeck Curve.<sup>34</sup>

lubrication, the viscosity and/or the velocity decrease or the normal force increases to reduce the separation,  $h$ , of the surfaces until it is of the same magnitude as the combined roughness,  $R$ . Friction results from both the micro contacts between asperities on the bearing surfaces plus the viscosity of the lubricant. Thus wear can occur by all four of the mechanisms (between solid surfaces) described previously.<sup>34</sup> Conventional metal-on-UHMWPE implant bearings are expected to function in the mixed lubrication mode, with a thin layer of synovial fluid separating the bearing surfaces but allowing micro contacts to occur due to combined roughness of the two surfaces. This mode has the advantage of including the lowest friction level from the Stribeck curve, but the friction will increase rapidly if the lubricant thickness decreases further.

In boundary lubrication, the thickness of the lubricant film drops down to a few monolayers or less separating the bearing surfaces, so that the separation,  $h$ , is much less than the combined roughness,  $R$ , and approaches zero. Significant physical contact and deformation occur between micro asperities on these surfaces, carrying most of the normal load and raising the friction level to its maximum where it reaches a plateau. The lubricant has little effect on friction and wear. Wear occurs primarily by the mechanism of tribo-chemical interactions between the solid bearing surfaces.<sup>34</sup> This lubrication mode normally does not occur in conventional metal-on-UHMWPE implant bearings, but it is desirable to keep the surface roughness of each component low so that this mode will be avoided even when the volume of synovial fluid is small (such as immediately after surgery).

Thus the surface finish on implant bearing components becomes extremely important to wear performance because of its effect on lubrication. If the surface roughness is too high then the lubricant cannot separate the bearing surfaces, and boundary lubrication leads to high frictions levels and wear. At conventional surface roughness levels, the lubricant separates the bearing surfaces but allows contacts between micro asperities. Mixed lubrication leads to abrasion, adhesion, and surface fatigue. If the surface roughness can be reduced further, the lubricant may be able to completely separate the bearing surfaces so that hydrodynamic

lubrication occurs. This could potentially eliminate abrasive and adhesive wear mechanisms, although the friction level would increase slightly. Thus the smooth surface finishes found on directly molded implant components may contribute to their improved wear performance by affecting the lubrication mode *in-vivo*.

## **3.2 CLINICAL WEAR OF UHMWPE**

### **3.2.1 Increased wear in machined vs. molded acetabular cups**

Many clinical studies have measured the linear wear and wear rate of UHMWPE acetabular components *in-vivo* based on quantitative analysis of diagnostic radiographs obtained during patient follow-up examinations. Standard anteroposterior pelvic radiographs are used for the measurements, which are calibrated relative to the known diameter of the femoral head.<sup>35</sup> Measurements can be made on both all-polyethylene and metal-backed acetabular components. The technique reported by Livermore<sup>36</sup> is normally followed to measure the orientation and depth of linear wear into the cup, which is then converted into a linear wear rate based on the time since implantation.

Such clinical measurements of wear rate have been used to compare the performance of different total hip replacement designs and materials combinations. Studies have examined variables such as machining vs. direct molding of UHMWPE components,<sup>18,37,38,39</sup> all-polyethylene vs. metal-backed acetabular components,<sup>37,38,40,41</sup> different sizes of implants (i.e. diameter of the femoral head),<sup>36,37,39</sup> cemented vs. uncemented acetabular/femoral components,<sup>20,37,39,41</sup> one-piece vs. modular femoral components,<sup>39</sup> and alloy composition<sup>38,41,42</sup> of the femoral head. Other variables which may affect the results but are often not reported include sterilization method, UHMWPE resin type and processing methods, and surface roughness or dimensional specifications for the femoral<sup>43</sup> and acetabular bearing surfaces. Obviously many clinical variables could also affect the wear rate, including patient activity level, weight, sex, age, and other medical conditions.<sup>39,41,44</sup> Thus interpretation of these wear rate measurements must be carefully done, and the most defensible results are obtained

by matching large numbers of patients with similar clinical variables as well as similar implants.<sup>18,38</sup>

Typical linear wear rates for UHMWPE acetabular cups have been measured as 0.05-0.30 mm/year, covering a variety of design and materials combinations. Two major clinical studies have examined differences between machined and direct molded acetabular cups.

One study compared cemented Charnley total hip arthroplasties that had been implanted for at least 15 years, within a single surgeon's practice. This Charnley design used a one-piece femoral component (22.25 mm head) fabricated from stainless steel. The acetabular cups did not have a metal backing. Machined cups manufactured by Thackery were implanted from 1970 to 1972, and then direct molded cups manufactured by Zimmer were implanted from 1976 to 1978. Sterilization methods were not specified. No attempt was made to differentiate between patient-related clinical variables, i.e. no patient matching was performed. Linear wear rates were reported after 5, 10, 15, and 20 years, as listed in Table 1.<sup>39</sup> Note that the wear rate of direct molded cups decreased slightly between 5 and 10 years follow-up, and was slightly lower than that of machined cups. However the differences in wear rate were not statistically significant when the standard deviations were considered. The wear rate of machined cups remained nearly constant even after 15 years. All of these wear rates would be considered moderate.

The second study compared cemented total hip arthroplasties of two similar designs (Zimmer TR-28 and Johnson & Johnson Triad) that were implanted by two different surgeons. Both designs used a one-piece femoral component (28 mm head) with a cobalt-chromium head, although the Triad had a titanium stem that was permanently attached to the head. The acetabular cups did not have a metal backing. The TR-28 acetabular cup was direct molded (Himont resin) by Zimmer, and was implanted from 1978 to 1980. The Triad acetabular cup was machined from extruded bar stock (Hoechst Germany resin) from the Westlake Corporation, and was implanted from 1982 to 1984. Both component types were sterilized by

**Table 1. Comparison of clinical wear rates for machined vs. direct molded UHMWPE acetabular cups in Charnley total hip arthroplasties.<sup>39</sup>**

<b>FOLLOW-UP PERIOD</b>	<b>WEAR RATE OF MACHINED CUPS For 23 Devices (Mean +/- Std. Dev.)</b>	<b>WEAR RATE OF MOLDED CUPS For 61 Devices (Mean +/- Std. Dev.)</b>
5 Years	0.12 +/- 0.07 mm/year	0.11 +/- 0.12 mm/year
10 Years	0.12 +/- 0.06 mm/year	0.08 +/- 0.06 mm/year
15 Years	0.11 +/- 0.07 mm/year	0.09 +/- 0.06 mm/year
20-22 Years	0.10 +/- 0.07 mm/year	-----

gamma irradiation (2.5-3.2 Mrad). Results were reported for all prostheses (162 TR-28 and 74 Triad) as well as for a patient-matched group which compared 54 pairs of patients with consistent age, weight, follow-up time, and gender (26 female and 28 male pairs), as listed in Table 2.<sup>18</sup> Note that these wear rate measurements are averages covering a range of follow-up periods (up to a limit of 17 years) and other patient variables. Only in the patient-matched groups are these averages directly comparable. The patient-matched group (108 patients) had an average age of 66 years old, an average weight of 161 pounds, and an average follow-up period of 6.7 years. The wear rate of the molded TR-28 cups was significantly lower than that of the machined Triad cups, for both methods of grouping the prostheses, even when the standard deviations were considered. The wear rate of the molded cups would be considered low, while that of the machined cups would be considered moderate.

Comparison of results from these two studies shows consistency in the wear rates of the machined cups, but differences in the wear rates of the direct molded cups. Molded cups always had lower average wear rates than machined cups, but this difference was not always statistically significant. The standard deviations reported in the second study (0.06-0.07 mm/year) were consistent with those reported from the first study, showing similar variability between patients.

Machined cups had average wear rates of 0.10-0.12 mm/year, despite differences in implantation dates (1970-72 vs. 1982-84), follow-up periods, manufacturers, patient characteristics, and femoral ball material (stainless steel vs. cobalt-chromium). Direct molded cups implanted in 1976-1978 had average wear rates of 0.08-0.11 mm/year, while those implanted in 1978-80 had average wear rates of 0.05 mm/year. Zimmer manufactured all the direct molded cups, probably using similar fabrication techniques during these consecutive time periods (unless significant process improvements were implemented). None of the cup designs used a metal backing. The difference in femoral ball materials (stainless steel vs. cobalt-chromium) might affect molded components differently than machined components,

**Table 2. Comparison of wear rates for machined vs. direct molded UHMWPE acetabular cups in patient matched groups.<sup>18</sup>**

<b>PROTHESES GROUPING</b>	<b>WEAR RATE OF MACHINED TRIAD CUPS (Mean +/- Std. Dev.)</b>	<b>WEAR RATE OF MOLDED TR-28 CUPS (Mean +/- Std. Dev.)</b>
All Prostheses (74 + 162)	0.12 mm/year	0.05 mm/year
Patient Grouped (54 + 54)	0.11 +/- 0.07 mm/year	0.05 +/- 0.06 mm/year



due to differences in surface finish and micromechanical interactions. Differences in follow-up periods do not explain the difference in wear rates, as the relatively short average follow-up period (6.7 years) from the patient-matched group of the second study would be expected to lead to a higher wear rate instead of a lower one. Differences in sterilization methods and patient variables cannot be evaluated because they were not reported in the first study.

One study of retrieved components from revision surgeries has also been used to compare the wear rates of machined vs. direct molded acetabular cups. James et al.<sup>21</sup> noted that the incidence of osteolysis with uncemented femoral components ranged from 28% to 56% with machined, ram extruded UHMWPE acetabular cups down to only 7% with direct compression molded cups. In a retrieval study of 43 UHMWPE acetabular cups with Ti-6Al-4V metal shells, significantly lower wear rates (measured by oil displacement) were found in direct molded components than in machined components. Volumetric wear rates were measured as 0.062 cm.<sup>3</sup>/year from 16 cups molded directly into metal shells (no exterior plasma spray coating), as 0.098 cm.<sup>3</sup>/year from 12 machined, extruded cups with metal shells (partial exterior plasma spray coating), and 0.172 cm.<sup>3</sup>/year from 15 machined, extruded cups with metal shells (complete exterior plasma spray coating). Corresponding linear wear rates for these 28 mm ID cups would be approximately 0.10 mm/year, 0.16 mm/year, and 0.28 mm/year. The direct compression molded cups were observed to have better consolidation, i.e. fewer fusion defects, whereas the other cups seemed to have embrittled surfaces resulting from machining. All acetabular cups were paired with the same model of femoral stem (Taperloc by Biomet, cementless fixation with proximal porous coating). The average implantation time for all 43 acetabular cups was 8.0 ± 2.1 years, but no additional patient data was provided (no patient matching of results).

### **3.2.2 Wearing-in period and wear rates vs. time**

Visual examinations of retrieved UHMWPE components have shown that contact regions can be located on machined components by observing where the machining marks

have worn away.<sup>15,45,46</sup> A combination of wear and creep contribute to the eventual removal of machining marks from load-bearing surfaces on the UHMWPE. This phenomenon is referred to as the wearing-in period, when the initial machined UHMWPE surface undergoes changes leading to a smoother surface finish with a higher true contact area against the metal bearing. The linear wear rate during this period may be different from the steady-state rate that occurs after the machining marks have been removed. Only a few studies have tried to measure variations in wear rate as a function of implantation time; most studies assume that wear (depth or volume) increases linearly with time (constant wear rate) and measure only an average wear rate over the total implantation time. Radiographic measurements are more appropriate than studies of retrieved components, since variations in wear rates can be studied for each individual component (instead of averaging wear rates over different components and implantation times).

Walker examined retrieved hip and knee components fabricated of both machined and molded UHMWPE.<sup>15</sup> He observed that the articulating surfaces of machined components became worn and flattened over time, removing the initial machining marks. He did not comment on the initial machined condition of the components, except to note that the absence of machining marks was a visible indication of the wear contact area with the metal bearing. In contrast, the initial surfaces of direct-molded components were very smooth. Both machined and molded components had similar wear behavior after reaching steady-state conditions: visually, the surface appeared smooth and polished, but microscopically, grooves, cracks, and shredded filaments (fibrils) were present.

Charnley and Halley measured the variations in wear rates vs. implantation time in an early study of the wear of Charnley acetabular cups after 9 to 10 years follow-up. Serial radiographs for each of 72 total hip replacements were analyzed for total wear (at each follow-up), relative to the initial postoperative radiograph. Then both total wear and wear rate were plotted versus follow-up time. Results were averaged over all 72 hips, over 49 hips with below-average total wear (1.5 mm or less), and over 23 hips with above-average total wear (above

1.5 mm). For all three groups the highest wear rate occurred during the first year, then the wear rate gradually decreased or remained nearly constant through year 9. In the overall group and the above-average group, a distinct peak in wear rate was present during the first year. The overall group had a peak wear rate of about 0.35 mm/year, which then dropped below 0.25 mm/year in the following year and gradually decreased to about 0.15 mm/year. The below-average wear group had a peak wear rate of about 0.20 mm/year, which gradually decreased to about 0.10 mm/year. The above-average wear group had a peak wear rate of about 0.70 mm/year, which then dropped below 0.40 mm/year in the following year and gradually decreased to about 0.25 mm/year.<sup>16</sup>

Another radiographic study examined variations in wear rate for 10 Charnley acetabular cups selected (from retrieved components) due to severe long-term wear. Most of these cups experienced much higher wear rates than the average values reported for Charnley cups, which have been studied extensively. Typical average wear rates, measured radiographically, are from 0.07 to 0.15 mm/year,<sup>14,46</sup> but rates up to 0.6 mm/year have been recorded from individual cases.<sup>16</sup> Serial radiographs for each of the 10 retrieved components were analyzed for total wear (at each follow-up), covering implantation times of 7 to 13 years. Wear depth vs. follow-up time was examined for each component, and showed a linear relationship (without an initial peak) in all 10 cases. Wear rates varied from 0.12 to 0.52 mm/year.<sup>14</sup> A significant difference from the above study is that all of these components had been removed in revision surgeries, whereas Charnley and Halley were examining wear in components which were still performing successfully.

A third radiographic study examined variations in wear rate for Charnley acetabular cups at 5-year intervals, as described in the previous section. Comparisons in wear rate were made between machined and direct molded acetabular cups. Wear during the first year of follow-up was not measured, but slight decreases in wear rate over 5-year intervals were reported. The decrease in wear rate for molded components (from 0.11 to 0.08 mm/year) occurred faster than that for machined components (from 0.12 to 0.10 mm/year),<sup>39</sup> and

indicated that molded components also experience a wearing-in period. All the components in this study were still performing successfully after 15-22 years.

A fourth radiographic study examined variations in wear rate for Müller acetabular cups which were implanted with either cast CoCrMo (Protasul-2) or forged CoNiCrMo (Protasul-10, Cr plated) balls (Sulzer Brother, Switzerland). Serial radiographs were analyzed for total wear after 6 months, 1 year, and continuing 1-year intervals up to 108 months for 149 hips with Protasul-2 balls and for 105 hips with Protasul-10 balls. Results were averaged over all hips of each type, and then both total wear and wear rate were plotted versus follow-up time. Wear rates were consistently highest (0.5 mm/year) during the first 6-month interval, then decreased to about 0.3 mm/year after the first year. Wear rates decreased to a stable level of about 0.2 mm/year after 3 to 4 years, then remained fairly constant for both ball types. The Protasul-2 ball consistently had slightly higher wear than the Protasul-10 ball, after the initial 6-month interval.<sup>47</sup>

### **3.2.3 Wear from non-articulating surfaces of bearing components**

By the early 1990's a new source of wear debris from UHMWPE bearing components began to be studied: micromotion between the back surface of the bearing and either its metal backing<sup>48,49,50,51</sup> or bone.<sup>52</sup> Although the total volume of debris released from the back surface is typically small relative to that from the articulating surface, this debris has been linked to osteolysis behind the implant.<sup>53,54,55,56</sup> Wear debris released from the back side of components can be released through screw holes in the metal backing (if present) directly into subchondral bone. Damage has been observed on the back surfaces of both acetabular and tibial components,<sup>57,58</sup> in the form of burnishing/fretting, surface deformation, and embedded metal debris.<sup>53,54</sup> Creep of the polyethylene into screw holes is common,<sup>54,59,60</sup> as is fretting or abrasion against screw heads.<sup>61,62</sup>

### 3.3 ENGINEERING STUDIES OF UHMWPE LOADING AND WEAR

#### 3.3.1 Biomechanics and stress distribution

Many studies have analyzed human gait to determine the force distribution, flexion-extension angles, and rotation of the hip and knee joints during normal activities (walking,<sup>63,64,65,66,67,68</sup> carrying loads,<sup>69</sup> and climbing stairs<sup>70</sup>). Some surgeons have even used instrumented hip implants to measure the joint forces *in-vivo*.<sup>71,72,73,74</sup> Results of these studies have been used in elasticity calculations and finite element models to calculate the stress distributions in implant components.

Several studies have modeled the contact stress and stress distribution in the UHMWPE acetabular cup as a function of its thickness, size (inner diameter), design (unbacked, metal-backed, etc.), and radial clearance (i.e. tolerance) with the femoral head. Contact stress increases as the inner diameter of the cup decreases<sup>75,76</sup> and also as the wall thickness decreases.<sup>77,78,79</sup> Typical values of contact stress range from 8 to 25 MPa (compression). The maximum (tensile) and minimum (compressive) principal stresses are located at the inner bearing surface of the acetabular cup, with the minimum principal stress located at the center of the contact area with the femoral ball and the maximum principal stress located near the periphery of the contact area. The magnitude of the range of principal stresses (minimum to maximum) increases slightly as the inner diameter of the cup decreases, and occurs over a smaller radial distance on the cup surface as well.<sup>77</sup> The maximum shear stress increases significantly as the inner diameter of the cup decreases. The maximum shear stress is located at the inner surface of the acetabular cup when the radial clearance with the femoral head is small (0.01 to 0.1 mm), but moves below the surface for larger clearances. Increases in radial clearance cause significant increases in the contact stress,<sup>76,78</sup> the maximum principal stress, and the maximum shear stress due to decreased contact area. Radial clearances of the magnitude expected due to machining tolerances may result in compressive stresses that exceed the compressive yield strength of UHMWPE.<sup>75</sup>

Additional studies have modeled the contact stress, contact area, and stress distribution in the UHMWPE tibial plateau (metal-backed) as a function of its thickness, conformity with the femoral condyles, and orientation in the gait cycle (flexion vs. extension). Peak stress levels are consistently higher in the knee than in hip components, and are higher in flexion than in extension because of decreased conformity (contact area) in this position. Contact stress is affected primarily by the orientation of the joint, with significant increases (around 100%) occurring when moving from extension to full flexion.<sup>77</sup> Conformity has the next largest effect on contact stress,<sup>80</sup> with significant increases occurring as the medial-lateral radius of the condyle contact zone decreases.<sup>81</sup> Thickness of the UHMWPE component has little effect on contact stress for thicknesses above 6 to 8 mm, but increases the stress level in thinner components. Typical values of contact stress range from 12 to 30 MPa (compression) in extension<sup>81</sup> and from 22 to 60 MPa (compression) in flexion.<sup>77,82</sup> Other studies have made physical measurements of contact stress and area in total knee components to compare with results of analytical models. One such study found that contact stresses varied distinctively along the ridges and troughs corresponding to machining marks.<sup>83</sup> Another study found that contact areas increased non-linearly with increasing applied load and varied with flexion angle (affecting stress distributions) and that significant variations in contact area result from different implant designs.<sup>84</sup> Six different implant designs were tested, and all six generated peak contact stresses above 10 MPa suggesting that fatigue damage may occur at the UHMWPE surface.

The maximum (tensile) and minimum (compressive) principal stresses are located at the top tibial bearing surface, with the minimum principal stress located at the center of the contact area and the maximum principal stress located near the periphery of the contact area (within a distance of a few millimeters).<sup>77,82</sup> The contact area is elliptical and changes its dimensions during flexion, so that its major radius is oriented in the anterior-posterior direction at extension but in the medial-lateral direction at full flexion. The magnitude of the range of

principal stresses (minimum to maximum) increases significantly (100% or more) when moving from extension to full flexion,<sup>77</sup> but is affected less by changes in conformity.<sup>82</sup>

The maximum shear stress, maximum von Mises stress, and the maximum von Mises strain are located 1 to 2 mm below the center of contact on the tibial bearing surface.<sup>77,80,82</sup> The maximum shear stress increases significantly when moving from extension to flexion, with a slight further increase with higher loads. Incorporation of rolling and sliding actions in the finite element model (in addition to direct compressive loading) raised the shear stress levels at the bearing surface, and moved the position of the maximum shear stress closer to the surface.<sup>85</sup> The maximum von Mises stress and strain vary with conformity of the bearing surfaces, but the strain decreases much more with increasing conformity. These stress and strain levels determine plastic deformation of the component, and have been associated with subsurface delamination<sup>80</sup> and pitting.<sup>82</sup>

One study used finite element modeling to evaluate residual stresses generated by density changes in gamma-irradiated UHMWPE tibial components. Density changes were assumed to occur without a change in total mass, so that volume changes were incorporated into the model. Density changes were modeled near the surfaces, and generated residual von Mises stress levels up to nearly 3.0 Mpa.<sup>86</sup>

### **3.3.2 Results of engineering wear studies**

A number of engineering wear studies have examined the effects of various sterilization methods on the wear rates of UHMWPE. Both joint simulator and bench-scale tests<sup>87,88</sup> have been performed to compare wear rates between unsterilized, ethylene oxide (EtO) sterilized, and gamma irradiated specimens in different packaging atmospheres (air, nitrogen, argon, vacuum). Some wear tests have combined sterilization methods with other variables including resin type (i.e. molecular weight, calcium stearate) and processing methods (machining of ram extruded bar,<sup>89</sup> machining of compression molded sheet,<sup>114,168</sup> machining of isostatically molded bar,<sup>90</sup> direct molding<sup>89</sup>).

Hip simulators are commonly used to measure the wear rates of acetabular components in total joint replacements. Although the wear rates measured in various studies are not directly comparable due to differences in simulator design and operation, consistent trends have been observed from recent studies. Acetabular cups sterilized by EtO consistently have higher wear rates than those sterilized by gamma irradiation<sup>168,90,91</sup> (attributed to the beneficial effects of crosslinking). Packaging atmosphere affects the wear rate of cups sterilized by gamma irradiation, with air resulting in higher wear rates (attributed to oxidation degradation) than any of the oxygenless atmospheres.<sup>168,198,89,92</sup> Resin type and processing method affect wear rates also, as cups machined from GUR 1020 sheet have lower wear rates than cups machined from either GUR 1120 sheet<sup>114</sup> or GUR 4150 rod<sup>168</sup> after gamma irradiation under comparable conditions (vacuum or air, respectively). Resins GUR 1120 and GUR 4150 contain calcium stearate, whereas GUR 1020 does not, and GUR 4150 has a higher molecular weight than the other two resins.

One hip simulator study compared direct compression molding to machining of extruded bar stock (both from GUR 4150 resin), followed by oxygenless packaging and gamma irradiation. The wear rate of the direct compression molded cups was 12% lower than that for the machined cups after 5 million cycles.<sup>89</sup> The wear tests were performed at different laboratories, using similar procedures and equipment, and consistent wear rates were obtained for machined, extruded cups irradiated in air.

Another hip simulator study examined the effects of third body wear on the roughening of the femoral head surface and the wear of unirradiated vs. gamma irradiated acetabular cups. The bovine serum used as a lubricant in this study was unfiltered, contained high levels of inorganic calcium and phosphorus, and was considered mildly abrasive. Profilometry measurements on the femoral heads showed increasing surface roughness with number of cycles. The wear rate of the unirradiated cups increased gradually with number of cycles, whereas the wear rate of the irradiated cups was initially higher but decreased gradually with number of cycles. After 2.5 million cycles the two wear volume curves crossed, and at longer



cycle times the wear volume and wear rate of the irradiated cups were lower than that of the unirradiated cups.<sup>93</sup>

## 3.4 UHMWPE STRUCTURE AND PROCESSING

### 3.4.1 Crystallinity and molecular structure

Ultra-high molecular weight polyethylene (UHMWPE) is polymerized from ethylene using the Ziegler process<sup>28</sup> and has the chemical formula  $C_2H_4$ . It is a linear form of polyethylene, with very few, short branches attached to the main carbon chain. This linear molecular structure results in significant crystallization of the molecules, and UHMWPE is considered a high-density form of polyethylene. Its crystal structure is orthorhombic, with unit cell dimensions of  $a = 0.74$  nm,  $b = 0.493$  nm, and  $c = 0.254$  nm.<sup>94</sup>

Melt solidified UHMWPE crystallizes without the formation of spherulites. Transmission electron microscopy has been used to examine the lamellar structure of thin sections stained with chlorosulfonic acid.<sup>32</sup> The Kanig technique<sup>95</sup> was used to stain and crosslink amorphous regions with chlorosulfonic acid, to differentiate the phases and stabilize the specimen.<sup>96</sup> Examination of extruded UHMWPE (GUR 415 and GUR 412 resins) using field emission scanning electron microscopy (FESEM) and transmission electron microscopy has revealed lamellar long periods of approximately 50 nm.<sup>97</sup> Ruthenium oxide ( $RuO_4$ ) staining was used to highlight the crystalline lamellae.

The significant difference between UHMWPE and other grades called high-density polyethylene (HDPE) is molecular weight. UHMWPE resins typically have molecular weights of 3-6 million grams/mole,<sup>28</sup> while HDPE resins have molecular weights of 0.05-0.2 million grams/mole.<sup>32</sup> Thus the molecules of UHMWPE occur as much longer chains. This results in lower crystallinity and density but a great deal of toughness due to entanglement of the chains.

Thus UHMWPE generally has higher toughness but lower tensile modulus and tensile yield strength than HDPE.<sup>32</sup> It also has better abrasion resistance and is not susceptible to stress cracking. Both grades have the good lubrication properties and chemical resistance of

polyethylene.<sup>28</sup> The excellent toughness is what makes UHMWPE most appropriate as a bearing material in orthopaedic implants. Under high loads it is able to deform rather than fracture.

### **3.4.2 Resin types**

Two polymer manufacturers produce UHMWPE resins within the United States. Montell Polyolefins (formerly Himont U.S.A., Inc., Wilmington, Delaware) produces 4 resins, Hoechst Celanese (Houston, Texas) produces 5 resins, and Hoechst Germany produces 4 resins that are marketed overseas. Significant differences between the various grades include molecular weight and the presence of stearate additives (calcium stearate). Table 3 lists the characteristics of these resins. The American Society for Testing and Materials (ASTM) has approved a standard specification for the UHMWPE powder and fabricated form used for production of surgical implants.<sup>98</sup>

By 1996 Montell Polyolefins had stopped sale of resins to the medical device industry because of concerns over product liability.<sup>30</sup> The loss of Montell's resins impacted only two orthopaedic device manufacturers (Biomet and Zimmer) who were molding some of their own UHMWPE products directly from resin. Most orthopaedic device manufacturers purchase UHMWPE in the form of rod or sheet stock from the two converters in the United States (Poly Hi Solidur in Fort Wayne, Indiana, and Westlake Plastics in Lenni, Pennsylvania). Both converters have used resins from Hoechst Celanese since the late 1980's, when they switched from use of the Himont resins.

### **3.4.3 Ram extrusion vs. compression molding vs. isostatic molding**

The consolidation methods used for UHMWPE implant components are listed in Table 4, with some of the process differences. The conversion of UHMWPE resin into rod, bar or sheet stock is done by three processes: ram extrusion, unidirectional compression molding, and isostatic compression molding. The two commercial converters use the first two processes, and Biomet uses the third process to produce its ArCom® product.<sup>31</sup>

**Table 3. UHMWPE Manufacturers and Resin Types.**

<b>RESIN</b>	<b>MANUFACTURER</b>	<b>STEARATE ADDITIVE</b>	<b>MOLECULAR WEIGHT (Grams/Mole)</b>
4150 HP	Hoechst Celanese	Yes	5 Million
4150 (415)	Hoechst Celanese	Yes	5 Million
4050 (405)	Hoechst Celanese	No	5 Million
4120 (412)	Hoechst Celanese	Yes	3.3 Million
4020 (402)	Hoechst Celanese	No	3.3 Million
1150	Hoechst Germany	Yes	5 Million
1050	Hoechst Germany	No	5 Million
1120	Hoechst Germany	Yes	3.3 Million
1020	Hoechst Germany	No	3.3 Million
RCH 1000	Ruhrchemie		
Hifax 1900L	Montell	No	3.2 Million
Hifax 1900	Montell	No	4 Million
Hifax 1900H	Montell	No	5 Million
Hifax 1900CM	Montell	Yes	4 Million

**Table 4. Consolidation Methods for UHMWPE Resins.**

<b>FABRICATION METHOD</b>	<b>LOADING AXIS</b>	<b>PRODUCT FORM</b>	<b>PROCESS TYPE</b>
Ram Extrusion	Longitudinal	Rod Stock	Continuous
Uniaxial Compression Molding	Thickness	Sheet Stock	Batch
Isostatic Compression Molding	Isostatic, Primarily Radial	Rod or Bar Stock	Batch
Direct Compression Molding	Thickness	Final Component Geometry	Batch

Ram extrusion is a more efficient process than the others because it can be operated continuously. Resin powder is continuously fed into the extruder, which uses an oscillating ram to force the resin through a heated die, forming a rod or bar. The resin initially melts at the surface of the die, then heat is conducted into the interior of the rod or bar. If the centerline reaches a sufficiently high temperature during the high pressure cycle, then good quality is obtained in the final product. Otherwise consolidation defects can result along the centerline of the final product. These defects would then appear in the final machined components for implant devices.

Uniaxial compression molding is a batch process, but offers the advantage that pressure is applied along the shortest dimension of the resulting product. The pressure is applied continuously over the mold surface, and again the mold is heated externally. The pressure is held for sufficient time to allow the resin in the center of the mold to melt, and the pressure level can be varied during the melting and crystallization cycles of the resin. A temperature of 200°C must be maintained, with pressures of 6.9 Mpa or more, and these conditions may be maintained for several hours.<sup>28</sup> Careful control of the temperature and pressure during these cycles has been predicted to improve the quality of the resulting product. Higher temperatures will degrade the UHMWPE due to oxidation.<sup>99</sup> The uniformity of the resulting sheet can vary depending on the initial distribution of the resin powder loaded into the press.

Isostatic compression molding is also a batch process, but uses a pressurized fluid (gas or liquid) to uniformly compress the resin from all surfaces. The resin is initially compressed in a mold without heating to form the rod or bar shape. Then this form is “canned” by sealing it in a non-fluid-permeable container. The canned form is then placed in an isostatic pressure chamber to uniformly apply heat and pressure on all surfaces. Like uniaxial compression molding, the pressure level can be varied during the melting and crystallization cycles of the resin. Application of pressure in isostatic molding is more uniform

because it is not as dependent on uniform distribution of the resin within the mold. This is predicted to improve the uniformity of the resulting product.

#### **3.4.4 Direct compression molding of components to final shape**

Direct compression molding is a batch process that is quite similar to uniaxial compression molding, except on a much smaller scale. The molded product is the final medical device component, which requires only a minor amount of trimming prior to sterilization. The UHMWPE may be molded as a separate component, or may be molded directly onto the metal backing for the acetabular cup or the tibial bearing.<sup>31</sup>

In direct compression molding, the mold is in the geometry of the final component. Careful quality control over the resin is possible by the device manufacturer, rather than depending on resin selection by the converter. Resin powder is loaded into the mold, which is then heated and pressurized uniaxially onto the final bearing surface. Tighter control over the temperature/pressure cycle is possible than in other consolidation methods because of the smaller volume of the mold.

#### **3.4.5 Machining vs. direct molding of implant components**

Industry normally uses machining to produce UHMWPE components (including non-medical devices) with fine details. Machining of UHMWPE is easy provided that sharp tools and cooling are used.<sup>28</sup> Machining is performed by using a cutting tool to remove unwanted material, in the form of chips, from the bulk stock.<sup>100</sup> Machining operations include drilling, milling, turning, sawing, planing, and screw cutting.

Research on metals has contributed to understanding the microstructural mechanisms that affect machining. Cutting occurs through a mechanism of localized shear deformation in the material directly ahead of the cutting tool, which forms the chip. Radial compression from the cutting tool generates dislocations and shear bands in the outer layer of the material, which undergoes plastic deformation and splits apart to form the chip.<sup>100</sup> This is comparable to an extreme but controlled form of wear.

Machining is known to affect the integrity of surfaces. In addition to creating surface roughness, machining of metals is known to result in plastic deformation; tears, laps, and crevice-like defects; changes in hardness; macroscopic and/or microscopic cracks; residual stresses; processing inclusions; and voids, pits, burrs, debris, or contaminant inclusions in the surface region. The combined effects from plastic deformation, frictional heating, and lubricants (where used) can also result in microstructural changes (phase transformations, grain size, twinning, localized melting) or chemical changes (intergranular corrosion or oxidation, dissolution, pitting, or embrittlement).<sup>33</sup>

Thus it is not unexpected that significant differences have been observed between the surfaces of machined and direct molded UHMWPE components. Li and Burstein<sup>32</sup> described direct molded components as often having a highly glossy surface, and noted the absence of machining lines. Walker<sup>15</sup> noted the presence of machining marks on some retrieved hip and knee components, and contrasted these to the very smooth surfaces present on other similar components which had been fabricated by direct molding. Bhambri compared the microstructures of two resin powders with fracture surfaces from machined vs. molded components. He found that submicron particles in the resins were retained in the final components, but that machined components retained these submicron particles much more than molded components did.<sup>101</sup> Machined surfaces are expected to expose these submicron particles (for release during wear) more than molded surfaces, due to surface damage and larger surface area exposed by machining.

The American Society for Testing and Materials is preparing a specification for acetabular prostheses<sup>102</sup> that includes surface finish requirements for polymer or metal bearings. The draft specification requires a polymer surface finish obtaining a roughness average ( $R_a$ ) of 2  $\mu\text{m}$  or better in accordance with ISO<sup>103</sup> or ANSI/ASME<sup>104</sup> standards. This can be obtained directly from machining. In contrast, the metal surface finish must be 0.125  $\mu\text{m}$  or better. Grinding or honing<sup>33</sup> can produce this surface finish on metals,<sup>33</sup> but might result

in embedded abrasive debris on polymers. Surface finish requirements for ceramic bearings had not been added to this draft specification as of May, 1997.

### **3.4.6 Fusion defects and “grain” boundaries**

Internal fusion defects have been found in some, but not all, UHMWPE parts. Originally these defects were observed in retrieved tibial and acetabular components,<sup>105,106,107,108</sup> but later studies found them in rod and bar stock and never-implanted components as well.<sup>32,109,110,111,112,113,114,115,116,117</sup> The distribution of UHMWPE defects was generally uniform for both tibial and acetabular components. In tibial components, the defect density in loaded, condylar regions was similar to that in unloaded, bridge regions.<sup>110</sup> It was finally concluded that the defects were produced during the initial consolidation of the resin powder, rather than resulting from in-vivo deterioration due to stress distributions within the implant component.

Fusion defects were detected by slicing or microtoming thick sections (100-200  $\mu\text{m}$  thick) of UHMWPE, then examining the slices microscopically using transmitted light at low magnifications (10-60X). The defects appeared as dark particles, 25-200  $\mu\text{m}$  in diameter, which were not well consolidated into the surrounding matrix.<sup>32</sup> Analysis of the dark particles did not identify any impurities in the UHMWPE. Microscopic examination with a heating stage demonstrated that the particles melted at 140-145°C and then were consolidated into the matrix.<sup>32</sup> The particles were similar in size and shape to the initial resin powder, so it was concluded that they were poorly fused particles of UHMWPE resin.

Compression molded sheets fabricated from resins GUR 1120 (with calcium stearate) and GUR 1020 (without) were examined for fusion defects.<sup>114</sup> These resins have the same molecular weights, but differ based on the addition of calcium stearate. Fusion defects and grain boundaries were visible in the GUR 1120 sheet, with calcium stearate, but were negligible in the GUR 1020 sheet. Tensile properties and wear rates were also improved in the GUR 1020 relative to the GUR 1120 product.



Recent detailed analysis of fusion defects in retrieved acetabular components used infrared microscopy to identify calcium stearate in the boundary layer between fusion defects and the matrix.<sup>118</sup> The calcium stearate was detected at the boundary, but not within the non-consolidated particle nor within the matrix. The resins used in these components were unknown. Specimens of bar stock fabricated of GUR 4150 and 4050 resins and of sheet stock fabricated of Himont 1900 resin were analyzed for comparison. Fusion defects were observed in the GUR 4150 bar stock, and calcium stearate was detected in the boundary layer as it had been in retrieved components. Virtually no fusion defects were observed in the GUR 4050 bar stock and the Himont 1900 sheet stock, and calcium stearate was not detected since it is not added to these resins. This study may have confirmed an important link between calcium stearate and the formation of fusion defects.

In a separate study, fusion defects were observed in both ram extruded bar and uniaxially compression molded sheet stock fabricated of GUR 412 resin, and in ram extruded bars fabricated of Hifax 1900 resin, but were not observed in ram extruded bars fabricated of GUR 415 resin.<sup>110</sup> Calcium stearate is added to GUR 412 and 415 resins, but is only added to one grade of Hifax resins (Hifax 1900CM). No analysis was done to detect calcium stearate in this study. Fusion defects in bar and sheet stock were uniformly distributed, as they had been in implant components. A third study examined the variations in quality of GUR 4150HP extruded bar stock, and found that the density of fusion defects varied by a factor of 20 across eight lots of bar stock.<sup>116</sup> Thus it appears that the quality of UHMWPE bar and sheet stock is poorly controlled by the converters.

Fusion defects have been statistically linked to cracking, delamination, and wear of tibial components in total knee replacements.<sup>108,109,110,119</sup> Thus fusion defects are believed to contribute to fatigue failures of tibial components. It has been noted that retrieved tibial components without fusion defects had lower frequencies of fatigue damage. Fusion defects have not been statistically linked to damage modes in acetabular components of total hip

replacements, but the primary damage mechanisms there are abrasive and adhesive wear rather than fatigue.

Direct compression molded components (both tibial and acetabular) have been found to contain fewer fusion defects than machined components.<sup>108,110,117,120,121</sup> The components were obtained from revision surgeries or from never-implanted devices. For older retrieved components, the fabrication details (including resin type and consolidation method) often remain unknown. The resins used for direct compression molding were identified as Himont 1900 and 1900H (without calcium stearate) from two studies. Direct compression molding may offer significant improvements by reducing fusion defects and improving fatigue performance, particularly when resins without calcium stearate are used.

### **3.5 STERILIZATION OF UHMWPE COMPONENTS**

#### **3.5.1 Sterilization methods**

All surgical implant components must be sterilized and packaged after manufacturing. The two most common methods of sterilization for UHMWPE components are gamma irradiation and exposure to ethylene oxide (EtO) gas. Other methods include electron beam irradiation and gas plasma irradiation. Sterilization methods using dry heat or steam cannot be used on polyethylene because of its low melting temperature.<sup>122</sup>

Gamma irradiation is frequently used for sterilization because it offers the advantage that the implant components can be prepackaged and then sterilized while sealed within the final container. Thus the implant and its packaging materials are sterilized together, eliminating the risk of recontamination if the packaging was performed after sterilization. The packaged implant is exposed to radiation from a <sup>60</sup>Co source that produces two photons with energies of 1.17 and 1.33 MeV.<sup>123,124</sup> A dose of 2.5–4.5 Mrad is typically used,<sup>125,126</sup> although research is being conducted to evaluate the effectiveness of lower doses.<sup>127</sup>

High-energy irradiation (either by gamma rays or electrons) of polyethylene causes structural changes in the polymer molecules. Both free radicals and ionic species are formed,

which undergo reactions leading to both cross-linking and chain scission. In the presence of oxygen, oxidation also occurs and enhances chain scission.<sup>123</sup> Cross-linking may improve the mechanical properties and wear performance of UHMWPE, but chain scission and oxidation have the opposite effect. Deterioration of some mechanical and morphological properties has been associated with UHMWPE components that were gamma irradiated. Thus the effect of gamma irradiation is being carefully evaluated, and packaging in inert gas or vacuum is being implemented to eliminate oxygen during sterilization and storage.<sup>128</sup> Packaging in nitrogen has been shown to be effective above doses of 1.0 Mrad, but at lower doses the benefit is lost because of dissolved oxygen in the bulk polymer.<sup>129</sup>

Ethylene oxide gas is highly toxic and sterilizes medical devices through a chemical reaction affecting the DNA in bacteria, viruses, and spores. Components to be sterilized are sealed in the sterilization chamber, preconditioned at elevated temperature and humidity, exposed to EtO gas at elevated temperature for several hours, and then aerated for a much longer time.<sup>130</sup> Sterilization occurs over a long time period as EtO gas diffuses into the UHMWPE component, then an even longer aeration period is required to remove residual gas from the component. Chemical burns can result to human tissues if implant components retain too much EtO. Residual EtO contents in UHMWPE tibial components were found to range from 23 to 9 ppm at 3 to 9 days after sterilization.<sup>130</sup> The Food and Drug Administration has proposed a maximum safe level of 100 ppm residual ethylene oxide for implantable medical devices.<sup>131</sup> Ethylene oxide gas presents risks to the environment<sup>132</sup> and to employee safety<sup>133</sup> because of its toxicity, and its use for sterilization is highly regulated.<sup>134</sup>

### **3.5.2 Primary electronic excitations from gamma irradiation**

The initial interactions between gamma photons and polymers result from electronic excitations within single atoms, which later may lead to chemical changes. There are three physical mechanisms for the interaction of gamma photons with electrons: (1) the photoelectric effect, in which the photon's energy is completely absorbed by a single electron,

which is then ejected with an energy equal to the difference between the photon's energy and the electron's initial binding energy in the atom; (2) Compton scattering, in which part of the photon's energy is absorbed by an electron, which is then ejected (but with less energy than from the photoelectric effect), and a photon of reduced energy is scattered from this atom; and (3) pair production, in which a positron-electron pair is created and then creates an additional gamma photon of 0.511 MeV through the annihilation of the positron. Dominant mechanisms are determined by the energy of the gamma photons and the atomic composition of the polymer.<sup>135</sup>

Compton scattering is the dominant mechanism for organic polymers, including polyethylene. Thus the primary responses to irradiation are the ejection of a high-energy electron from a polymer molecule and the scattering of a lower energy photon:



The ejected electron and the scattered photon each have sufficient energy to interact with other molecules, resulting in the ejection of additional electrons.<sup>135</sup> These electrons have a range of energies, with an average energy of 580 keV from cobalt-60 gamma radiation.<sup>124</sup> This cascade of electrons initiates a series of chemical changes in the polymer molecules. Because of this cascade effect and the high penetration of gamma radiation, the population of ejected electrons increases to a maximum with depth (on the scale of millimeters) and then decreases (depending on the thickness of the polymer).<sup>136</sup>

These electrons recombine with the polymer ions rapidly due to Coulombic attraction, but the excess energy produces excited electronic states in the polymer molecules:



These excited states release energy via several mechanisms to return to their ground states, including radiationless decay to produce heat, radiative decay via the emission of light, and also homolytic bond cleavage to initiate primary free radicals:<sup>135</sup>



The population of resulting primary free radicals is proportional to the total radiation dose. Bond cleavage occurs non-selectively, unlike that from ultraviolet irradiation. Primary radicals may be formed by breaking bonds between the carbon chain and side groups or between neighboring carbon atoms along the main chain.

### 3.5.3 Secondary chemical reactions via free radicals

In polyethylene, there are two mechanisms for the initiation of primary free radicals via irradiation. The initial homolytic bond cleavage may occur from the loss of hydrogen side groups:



or from scission of the carbon-carbon bonds in the main chain:



All the resulting radicals are chemically active, and will undergo secondary reactions either in their germinate pair or with other molecular species.

The primary free radicals undergo chemical reactions that are determined by their environment (i.e. availability of gases, monomers, radicals, or other molecules for reaction), their rate of formation (i.e. dose rate), and their mobility (i.e. molecular size, liquid vs. solid, crystalline vs. amorphous phase, temperature). Alkyl radicals are extremely reactive with oxygen, so the environment in which irradiation occurs has a significant effect on these secondary reactions. Irradiation under vacuum or inert gas produces quite different reactions from irradiation in air.

#### 3.5.3.1 Heterogeneous vs. homogeneous oxidation

Gamma irradiation in air results in oxidation reactions via radical reactions in polyethylene. There is an important interaction between the radiation dose rate, as well as the total dose, and the extent of oxidation (heterogeneous vs. homogeneous) immediately following irradiation.<sup>135,137</sup> Oxidation reactions within the bulk polymer are limited by the diffusion of

oxygen into the solid during irradiation, relative to the rate of radical formation that is controlled by the dose rate.

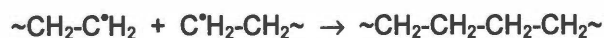
At high dose rates in air the outer surfaces of the polymer are oxidized, but the oxygen within the bulk of the solid is quickly consumed during irradiation. The oxygen diffusion rate is much lower than the rate of radical formation. Thus the reactions within the bulk resemble those resulting from irradiation under an oxygen-free environment, while the outer surfaces undergo oxidation to a finite depth. This is known as heterogeneous oxidation. This condition results from gamma sterilization of UHMWPE medical devices in air. Depending on the total radiation dose, the level of surface oxidation can be low immediately following irradiation.

At sufficiently low dose rates (which might have to be extremely low for dense UHMWPE), oxygen should diffuse throughout the bulk polyethylene fast enough for uniform oxidation to occur during irradiation. This condition is known as homogeneous oxidation. As dose rates decrease further, oxidation should remain uniform with depth and become independent of dose rate (i.e. dependent only on total dose).

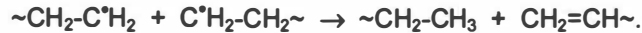
### **3.5.3.2 Radiation degradation in inert gas or vacuum**

When irradiation is performed at high dose rates in air, the interior of the bulk polyethylene reacts as if it were irradiated in an oxygen-free environment. Due to oxidation degradation reactions, many UHMWPE medical devices are now gamma sterilized in either inert gas or vacuum. Under either of these conditions, the main short-term secondary reactions produce either crosslinking or chain scission.

Homolytic bond cleavage of the polymer chain forms a geminate pair of primary alkyl radicals which are constrained by the surrounding matrix in the solid state.<sup>138</sup> This cage effect increases the probability of termination reactions between the geminate pair, as either recombination:



or as disproportionation, which is one mechanism for chain scission:



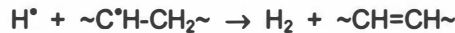
Recombination restores the polymer molecule to its original condition, whereas disproportionation causes a reduction in molecular weight and an increase in unsaturation.<sup>135</sup>

These termination reactions are most likely to occur in the crystalline phase, due to the constraints on molecular conformations and mobility.

Cleavage of a side group bond in polyethylene forms a primary alkyl radical and an atomic hydrogen radical, which is quite mobile because of its small size. The hydrogen radical can travel far from its source molecule before reacting with another species. Some of these radical pairs will undergo termination reactions via recombination:



or via disproportionation:



with their geminate partner.<sup>135,138</sup> However many more hydrogen radicals will diffuse away and propagate more radicals via hydrogen abstraction, in which they remove a second hydrogen atom from its position as a side group (on either the same or a different polymer molecule). This results in the formation of a stable hydrogen molecule and a new alkyl radical in the chain backbone:<sup>135,138</sup>



Double bonds in the backbone chain are particularly susceptible to hydrogen abstraction, in which case allyl radicals rather than alkyl radicals are formed:



Primary alkyl radicals within the polymer chain also undergo further reactions with their geminate partner, other radicals, or other hydrogen atoms attached to a polymer chain. These alkyl radicals can be located at chain ends or along the chain backbone, as described above. Reactions between two alkyl and/or allyl radicals result in chain extension, branching or

crosslinking, depending on the locations of these radicals.<sup>138</sup> Combination reactions result in termination, and molecular weight is increased. Alkyl and allyl radicals can also propagate via hydrogen abstraction, similar to the reaction described above for hydrogen radicals. The radical will remove a hydrogen side group from an adjacent polymer molecule, saturating the first radical and propagating a new alkyl (or allyl, as described above) radical.<sup>135</sup>



In polyethylene, the yields are typically  $G(X)=3.0$  crosslinks per 100 eV of energy absorbed and  $G(S)=0.88$  scissions per 100 eV of energy absorbed from gamma irradiation under vacuum or inert gas, performed at room temperature.<sup>123</sup> Crosslinks are formed within the amorphous phase of the polymer, while scissions can occur within either the amorphous or the crystalline phase. Gaseous decomposition products from polyethylene include  $\text{H}_2$  and volatile hydrocarbons such as  $\text{CH}_4$  and  $\text{C}_2\text{H}_6$ , formed from decomposed side branches.<sup>139</sup>

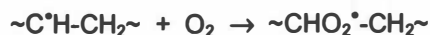
### 3.5.3.3 Radiation degradation in air

When gamma irradiation is performed in air, oxidation usually dominates the degradation mechanisms for polyethylene. Oxygen must be available to react with the free radicals, so oxidation predominates at surfaces and shallow subsurface depths. Unfortunately the radiation-oxidation mechanisms are not as well characterized or as predictable as those reactions that occur in an inert environment. Oxidation reactions will begin as free radicals are initiated during irradiation. However, autoxidation can continue to propagate for months or years after irradiation has ended due to the long lifetimes of chemical species involved. Basic radical reaction mechanisms and short-term results of irradiation are discussed in this section, and long-term post-irradiation effects are covered in the following section.

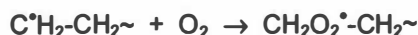
Initiation of primary free radicals occurs by the same mechanisms described in the previous section, i.e. bond cleavage within the polyethylene molecules. However oxygen reacts quickly with primary alkyl radicals to limit crosslinking and to increase chain scission.<sup>137</sup> Thus termination reactions between the geminate pairs of primary radicals are reduced, often



significantly. Propagation of oxidation begins as radicals (along the chain backbone or at chain ends) react with oxygen molecules forming peroxy radicals:<sup>135</sup>



or



Propagation continues through a series of reactions that create new free radicals, increase the population of these radicals, and result in a combination of chain branching, scission, and crosslinking. The first reaction is hydrogen abstraction by the peroxy radical:<sup>135</sup>



which creates a metastable hydroperoxide group plus a new alkyl radical. The alkyl radical can undergo further oxidation, crosslinking, or branching reactions as described previously.

The hydroperoxide group has a moderately low activation energy for decomposition, and will break down over time to form two new radicals:<sup>135</sup>



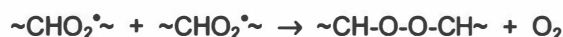
The effects of this hydroperoxide group are significant, because (1) it adds a time-temperature dependence to the degradation mechanisms, resulting in long-term postirradiation effects (due to autoxidation)<sup>137,138</sup>, and (2) its decomposition creates two new radicals from a neutral species, significantly increasing the population of radicals formed after irradiation. The alkoxy radical remains in this polymer chain, but the hydroxyl radical is mobile and can diffuse away. These two radical types can undergo further hydrogen abstractions, forming new alkyl or allyl radicals along polymer chains. These alkyl and allyl radicals are then available for chain branching, crosslinking, or further oxidation reactions.

The alkoxy radical (formed from decomposition of the hydroperoxide group) can cause chain scission (known as  $\beta$ -scission) and unsaturation as it also decomposes:<sup>137</sup>



to create an aldehyde and an alkyl radical. This reaction competes with hydrogen abstraction for propagation from alkoxy radicals.

Terminations result from oxidation when two radicals combine as a result of crosslinking, branching, or chain extension. Oxygen molecules can be incorporated into the chain or branch backbone when peroxy or alkoxy radicals are involved in termination reactions. When two peroxy radicals combine in a termination reaction, an oxygen molecule is released:<sup>135</sup>



that will further contribute to autoxidation. Other gaseous products from irradiation in air include CO<sub>2</sub>, CO, H<sub>2</sub>O, H<sub>2</sub>, and hydrocarbons.

#### 3.5.3.4 Post-irradiation effects

Chemical changes, particularly oxidation, have been observed during long-term storage of UHMWPE after irradiation.<sup>126,140,141,142,143,144</sup> These post-irradiation effects result from (1) long-term stability and/or propagation of radicals produced during irradiation, and (2) decomposition of hydroperoxides produced during previous radical reactions.

Radicals initiated within crystalline regions of polyethylene are unable to crosslink or react with oxygen due to the tight packing within the lamellae.<sup>125,123</sup> However these radicals are able to migrate (via hydrogen abstraction) over long time periods to reach boundaries with the amorphous phase, where radical propagation reactions can proceed.<sup>135</sup>

The propagation of radical reactions within the amorphous phase can continue long after irradiation, as described in previous sections. These reactions will continue until all radicals have been terminated. This is particularly true when the polymer is exposed to oxygen or air and autoxidation can occur.<sup>135</sup> Oxidation contributes to most of the deterioration in properties that continues after irradiation has ended. Hydroperoxide decomposition makes the post-irradiation degradation sensitive to temperature changes for long time periods.

### 3.5.4 Longevity of free radicals in UHMWPE

Gamma irradiation of polyethylene produces free radicals and ionic species that react with each other and the environment to produce both cross-linking and chain scission. Cross-linking of the polymer chains releases hydrogen molecules, and reactions with oxygen enhance the scission of polymer chains.<sup>123</sup>

Free radicals have been detected in UHMWPE sterilized by gamma or electron beam irradiation.<sup>125,145,146,147,148,149,150</sup> Electron spin resonance (ESR) spectrometry was used to analyze for these free radicals. The primary free radicals formed are the alkyl (-CH<sub>2</sub>- $\dot{C}$ H-CH<sub>2</sub>-) and allyl (-CH=CH- $\dot{C}$ H-CH<sub>2</sub>-) types, which then react with oxygen from the environment to form secondary peroxy radicals<sup>148</sup> and carbonyl groups.<sup>125</sup> Similar UHMWPE specimens sterilized with EtO gas were analyzed by ESR spectrometry and found to contain minimal or no free radicals, of both primary and secondary types.

The distribution of free radical types within irradiated UHMWPE varies with form of the UHMWPE (resin vs. consolidated bulk), position within the bulk, radiation dose, environment (atmosphere and temperature), and time since irradiation. Resin powders and extruded rods (GUR 4150HP) irradiated under vacuum at 77 K, then stored under liquid nitrogen through ESR analysis, contained alkyl radicals, while similar specimens irradiated under vacuum or in air at 25°C contained allyl radicals. Both specimens irradiated at 25°C (in vacuum or air) were resistant to rapid oxidation, as peroxy radicals were not detected after exposure to oxygen for 24 hours.<sup>146</sup> Resin powders (GUR 415) or fibers stored in air for 3 years following irradiation contained peroxy radicals, but no primary radicals, which is consistent with their long exposure to oxygen and their high surface areas.<sup>148,149</sup> The surfaces of bulk specimens (GUR 415), irradiated in air then aged from 18 to 104 months, contained peroxy radicals but little or no primary radicals.<sup>147,148,149</sup> However, the cores of these same specimens contained primary radicals but only small concentrations of peroxy radicals. A similar bulk specimen, irradiated and stored in nitrogen gas for 18 months, contained a mixture of primary and peroxy radicals

in the surface.<sup>147</sup> Another specimen, irradiated then stored under vacuum for 8 years, also contained primary radicals.<sup>148</sup> Primary alkyl/allyl radicals can remain stable within UHMWPE for years, provided that the environment does not contain oxygen or that oxygen is unable to diffuse through the bulk of the component. When primary radicals are exposed to oxygen, they react over time to form secondary peroxy radicals that may also remain stable for long periods.

The consolidation methods applied to UHMWPE resins do not significantly affect the density of free radicals formed after gamma irradiation. One study compared the densities of free radicals in UHMWPE based on 4 different fabrication methods: ram extrusion of bar stock, uniaxial compression molding of sheet stock, isostatic molding of bar stock, and direct compression molding of components. Specimens of each form were sealed into packaging under vacuum, gamma irradiated to a dose of 3.55 Mrad, and stored in their packaging prior to the first ESR analyses (which were repeated 40 hours later). The densities of primary alkyl/allyl radicals were initially  $37.0\text{--}47.0 \times 10^{16}/\text{cm}^3$ , and decreased to  $19.0\text{--}24.0 \times 10^{16}/\text{cm}^3$  after 40 more hours. The densities of the secondary peroxy radicals were  $2.80\text{--}3.60 \times 10^{16}/\text{cm}^3$ , and decreased to  $1.50\text{--}1.90 \times 10^{16}/\text{cm}^3$  after 40 more hours.<sup>145</sup> Another study also observed that the density of primary alkyl/allyl radicals decreased with time after irradiation, particularly at the outer surface of bulk specimens.<sup>150</sup>

In the above study, 2 treatment options to reduce the free radical densities were tested on all 4 UHMWPE product forms. One treatment consisted of exposing the specimens to 15 psi of hydrogen for 2 hours, and the other treatment consisted of holding the specimens at 50°C for 182 hours. Then all specimens were submitted for ESR analyses, and the results were compared to the control specimens described above. After hydrogen treatment, the densities of primary alkyl/allyl radicals dropped to  $5.3\text{--}10.0 \times 10^{16}/\text{cm}^3$ , and the densities of secondary peroxy radicals dropped to  $0.06\text{--}0.20 \times 10^{16}/\text{cm}^3$ . After the 50°C thermal treatment, the densities of primary alkyl/allyl radicals dropped to  $8.4\text{--}9.5 \times 10^{16}/\text{cm}^3$ , and the densities of secondary peroxy radicals dropped to  $0.54\text{--}0.80 \times 10^{16}/\text{cm}^3$ .<sup>145</sup> Both treatments reduced the

free radical densities, but the hydrogen treatment was more effective at reducing the density of peroxy radicals.

Chain scission or cross-linking reactions by free radicals are expected to primarily occur in amorphous regions of the polymer, since bonding within crystalline regions is constrained by the lattice.<sup>125</sup> Free radicals formed within crystalline regions may remain trapped there for long time periods.<sup>123</sup> Thermoluminescence measurements have been used to differentiate between free radicals located in amorphous vs. crystalline regions of UHMWPE.<sup>151</sup> Specimens of extruded rod (GUR 412) were gamma irradiated to doses of 2.5-4.0 Mrad, then stored in liquid nitrogen or dry air. The specimen stored in liquid nitrogen (to minimize oxidation and chain scission) for 6 weeks emitted a strong peak from free radicals in the amorphous region, with a secondary peak from free radicals in the crystalline region. The specimen stored in dry air (to allow oxidation to proceed) for 6 weeks emitted much smaller peaks, indicating a lower density of free radicals, with the main peak from free radicals in the crystalline region and a much smaller peak from free radicals in the amorphous region. The specimen stored in dry air for 6 months emitted a very weak peak due to free radicals in the crystalline region, with no contribution from free radicals in the amorphous region. This data supports the expectations that the density of free radicals decreases with time and that free radicals in amorphous regions are able to undergo faster chain scission or cross-linking reactions while those in crystalline regions may remain stable for longer time periods.

### **3.5.5 Oxidation and post-irradiation aging**

Free radicals formed in polyethylene during irradiation are known to undergo reactions leading to either cross-linking or chain scission and oxidation.<sup>123</sup> Oxidation of surface and subsurface regions of UHMWPE components has been studied extensively, particularly for tibial components, due to its negative impact on mechanical properties.

Oxidation and chain scission reactions produce carbonyl groups and lower molecular weight chains in localized regions near the UHMWPE surfaces. The formation of carbonyl

groups changes the polyethylene from hydrophobic to hydrophilic, allowing a small amount of fluid absorption.<sup>106,125</sup> The formation of lower molecular weight chain fragments leads to increases in crystallinity and density, which then affect mechanical properties as well.<sup>32</sup>

The extent of oxidation, as a function of depth from the surface, is studied by measuring variations in density (by density gradient column), infrared spectra (based on carbonyl peaks near  $1720\text{ cm}^{-1}$ ), and percent crystallinity (by differential scanning calorimetry,<sup>152,153</sup> DSC). Specimens are typically cut through the thickness of the bulk, then microtomed parallel to the original surface prior to analyses. Some infrared spectra are obtained from sections microtomed transverse to the original surface by analysis through an optical microscope with calibrated stage motion.

The infrared spectra are collected in transmission mode to examine the carbonyl absorption peaks, including the ester band ( $1738\text{ cm}^{-1}$ ), the ketone band ( $1720\text{ cm}^{-1}$ ), and the acid band ( $1697\text{ cm}^{-1}$ ). The largest peak is typically at the ketone band, which does not always indicate chain scission, with a secondary peak at the carbonyl acid band, which does result in chain scission. Never-implanted components usually have little or no peak at the ester band,<sup>154</sup> but retrieved components often produce an ester peak near the bearing surface.<sup>155,156,157</sup> Infrared spectra collected in diffuse reflectance mode are not always sufficiently sensitive to these peaks because of the shallow depth analyzed from the specimen.

A number of studies on UHMWPE (generally extruded GUR 415), irradiated to 2.5-4.5 Mrad and stored in air (never implanted), have shown that the initial oxidation depth (from infrared spectra) is less than 0.5 mm,<sup>158</sup> but that oxidation continues with time<sup>154,159,160</sup> so that the depth may extend to 3.0 mm or more after a year,<sup>161</sup> or up to 6.0 mm after 5-7 years.<sup>126</sup> The densities and infrared oxidation spectra from within the bulk of the sterilized materials were higher than those from unsterilized specimens, and reached peak values at or just below the surface.<sup>161</sup> Measurements of carbonyl peaks (infrared spectra), density (DGC), and crystallinity (DSC) have been found to correlate closely for never-implanted, gamma irradiated components aged for 2-14 years.<sup>156</sup>

Similar data has been obtained from a series combined from retrieved and never-implanted tibial components, all machined in-house from controlled batches of uniaxial compression-molded sheet (GUR 412 and GUR 415). Previous characterization of the sheet stock (from both resins) included density as a function of position through its thickness, both before and after gamma irradiation. Tibial components had been irradiated to 2.66-3.44 Mrad prior to implantation or storage in air. Detailed records of the retrieved components allowed determination of their total age since irradiation, including both storage time and implantation time. These retrieved and never-implanted components had aged much longer than in the above study, from 14 to 47 months.<sup>162</sup>

Densities were measured vs. depth from both the superior and inferior surfaces of each component, with specimens taken from the load-bearing medial condyle and some also taken from the non-load-bearing intercondylar region. Densities in load-bearing regions were not significantly different from those in non-load-bearing regions. Within the bulk of each component, density values remained relatively constant or followed a linear trend consistent with the density gradient in the initial molded sheet. Densities of both retrieved and never-implanted components increased near the superior and inferior surfaces, peaking at or below the outer surfaces. For components with total ages since irradiation of approximately 2 years or less, the density curves peaked at or very near to the outer surfaces. For components with total ages longer than 2 years, the density curves peaked farther away from each surface, and as age increased the magnitude of the subsurface density peak tended to increase and extend deeper into the bulk.<sup>162</sup> Thus oxidation reactions continued for several years after irradiation, for both shelf-aged and retrieved UHMWPE components.

Some Fourier transform infrared (FTIR) spectra were analyzed from selected specimens used for density measurements to confirm the presence of the oxidation peak in retrieved as well as never-implanted components. The oxidation peak at  $1720\text{ cm}^{-1}$  was observed in both retrieved and never-implanted components, but specimens taken near the outer surfaces (superior and inferior) of retrieved components also had a peak at  $1740\text{ cm}^{-1}$ .

This peak was absent from spectra taken from all never-implanted components, as well as from specimens of retrieved components taken deeper within the bulk.<sup>162</sup>

One recent study examined the effect of different resins and fabrication methods on the level of oxidation in shelf-aged implant components. Direct molded components (Himont 1900) were compared to machined components (GUR 415, RCH 1000, and Hylamer). Oxidation level vs. depth was evaluated using measurements of density and percent crystallinity (from DSC). The maximum crystallinity values were compared for unirradiated specimens and irradiated components that had been shelf-aged for 1 to 13 years. Packaging methods were not reported. All irradiated components had higher density and/or percent crystallinity values than unirradiated specimens. Direct molded components (Himont 1900) experienced smaller property changes than all of the other machined components, and seemed to be more resistant to long-term oxidation.<sup>163</sup>

Density increases with aging after irradiation, but density has also been linked to changes in mechanical properties. Thus mathematical models of kinetic density changes may be valuable in estimating long-term bulk properties. One study has quantified the density changes with post-irradiation aging times up to 50 months, based on measurements from retrieved tibial components plus one shelf-aged component (all with known fabrication and clinical histories). Density values (averaged over the entire component thickness) were found to increase linearly at a rate of  $1.86 \times 10^{-4}$  g/cm<sup>3</sup>/month. Surface density values (averaged over a depth of 2 mm from the bearing surface) increased linearly at a slightly higher rate of  $1.96 \times 10^{-4}$  g/cm<sup>3</sup>/month.<sup>164,165</sup>

Methods for simulating the long-term oxidation behavior of UHMWPE have been developed<sup>166</sup> to evaluate the effectiveness of new irradiation procedures (i.e. packaging in nitrogen, argon, or vacuum) and fabrication variables (i.e. resin type, consolidation method) in preventing oxidation. Accelerated aging tests have demonstrated that packaging in non-oxygen environments can delay the oxidation process,<sup>129,159,167,168,169,170</sup> but that oxidation will



proceed when the UHMWPE is removed from its protective packaging and exposed to oxygen or air.<sup>158,171, 172,173,174</sup>

Additional accelerated aging tests have suggested that the presence of calcium stearate in resins slightly lowers their oxidation resistance, and that compression molded components have better oxidation resistance than ram extruded components.<sup>175,176</sup> One study compared direct molded specimens without calcium stearate (Himont 1900) to extruded and machined specimens with (GUR 4150) or without (Himont 1900) calcium stearate. The direct molded specimens were found to have very consistent densities, with much less variability than the extruded specimens (from the same resin) in the unsterilized, unaged condition. After irradiation and accelerated aging, the direct molded specimens contained few or no fusion defects whereas the extruded and machined specimens (from both resins) had fusion defects.<sup>177</sup>

Mechanisms have been examined which lead to the development of the initial oxidation profile, with the maximum oxidation level occurring at the surface, and to time-dependent changes which increase the maximum oxidation level and move it into the subsurface region. The oxidation rate,  $r$ , was related to the oxygen,  $[O_2]$ , and free radical,  $[R\dot{ }]$ , concentrations by:<sup>178</sup>

$$r = k [O_2] [R\dot{ }] = A \exp(-\Delta H/T) [O_2] [R\dot{ }]$$

where  $k$  is the reaction rate constant,  $A$  is a proportionality constant,  $\Delta H$  is the activation energy for oxidation, and  $T$  is the absolute temperature.

The free radical concentration is directly related to the absorbed radiation dose. Dosimeters mounted in wedge-shaped blocks of UHMWPE were used to measure the absorbed dose profile of gamma radiation as a function of depth. The absorbed dose at the surface increased with depth, stabilizing at the maximum level 5 mm below the surface. The absorbed dose remained nearly constant until a depth of 11 mm was reached, and then decreased continually until the initial surface dose level was reached at 16 mm (thicker than

most implant components).<sup>178</sup> In contrast, the initial oxygen concentration is diffusion controlled with the maximum occurring at the outer surface.

Heating induced during irradiation increases the reaction rate, but the oxygen level dissolved in the subsurface region and in the bulk is low and limited by diffusion. Thus initially the oxidation level reaches a maximum at the surface and decreases with depth, even though the maximum free radical concentration is subsurface. This oxidation profile occurs even with oxygenless packaging, due to dissolved oxygen in the amorphous phase from prior exposure to air. During shelf aging the free radicals at the surface have been largely consumed by the oxidation reaction, but their concentration increases rapidly with depth where the dissolved oxygen has been consumed. As oxygen diffuses into the subsurface region, the number of free radicals available increases so that the oxidation level can increase above that developed at the surface. At sufficient depths the oxidation level again falls off, limited by the slow diffusion of oxygen to maintain the reaction. Thus the oxidation profile continues to increase with time, and the initial surface peak progressively moves deeper into the subsurface region while increasing in magnitude.

### **3.5.6 Subsurface “white band” from irradiation**

An opaque “white band,” associated with subsurface oxidation, has been observed in many irradiated UHMWPE implant components. It is observed visually, or at low magnifications, below component surfaces when thin cross-sections are examined. The band appears white in reflected light, or dark in transmitted light, and typically begins 0.5-1.0 mm below the outer surfaces of the component. Some bands are discontinuous, and do not outline all the surface regions. Sometimes the white band may have been misinterpreted as a non-uniform distribution of fusion defects.<sup>32</sup>

Staining techniques have recently been evaluated to emphasize subsurface oxidation. A technique using Oil Red O staining has been shown to highlight the white band, where the oxidized layer absorbs the red stain poorly. This staining technique can identify subsurface

oxidized regions before the white band becomes visible, so it may be very useful in examining short-term aging effects.<sup>179</sup> A similar technique uses chlorosulfonic acid to stain the oxidized regions brown, while the unoxidized bulk remains white or light colored.<sup>180</sup> A third technique uses SO<sub>2</sub> gas to stain oxidized regions so that they become fluorescent.<sup>181</sup> This technique has been used with laser scanning confocal microscopy to reveal the 3-dimensional distribution of oxidation in the microstructure.<sup>182</sup>

The white band was first reported and described as “thin-section flaking” in a study of fusion defects in retrieved tibial components (40) and acetabular cups (10). Each component was rated on a scale from 0 (not present) to 5 (present) for the extent of the white band, and statistical methods were used to compare the results for different specimen types and locations. Post-irradiation shelf age was not considered. Machined components were found to have much higher ratings than direct molded components. Among tibial components, no significant differences were found between loaded and unloaded regions of the bearing surface. High ratings were correlated to cracking, delamination, total wear rating, and implantation time.<sup>110</sup>

The properties of the white band were characterized in a detailed study of 150 retrieved and 36 never-implanted acetabular cups. Components were examined from 18 different manufacturers, with estimated ages from 2 to 22 years. Comparisons were made between unsterilized components and components sterilized by gamma irradiation or ethylene oxide, and the effects of post-sterilization aging were considered. Retrieved components were rated for clinical wear damage, and the results were statistically evaluated for correlations to the sterilization technique and the presence of the white band. The white band was characterized based on its physical dimensions, chemistry, and mechanical properties.<sup>111,183</sup>

The presence of the white band was linked to the clinical wear modes of cracking and delamination in retrieved acetabular components. Scratching and burnishing were the primary modes of wear observed overall, but cracking or delamination occurred in 19% and 14%, respectively, of the 150 components examined. Only components which had been gamma

irradiated in air were found to have cracking or delamination, and the white band was observed in 100% of those with cracking and in 95% of those with delamination.<sup>111</sup>

The white band was linked to gamma irradiation and a minimum period of post-irradiation aging. No unsterilized components or retrieved components sterilized with ethylene oxide contained the white band, but 68% of those sterilized with gamma irradiation did. The white band only appeared in irradiated components after 3 or more years of aging, but it was present in 71% of the retrievals and 59% of the never-implanted components which met this criterion.<sup>111</sup> Other processing or fabrication variables (i.e. resin type, calcium stearate additives, consolidation method) may affect the development of the white band after irradiation, but these details were not available from this study.

The white band was located just below the surface of each component, at an average depth of 0.7-0.8 mm and with an average thickness of 1.1 mm. It appeared uniformly around the contour of never-implanted components, but its presence was variable in retrievals, located mainly around the flange and along the articulating surface but rarely along the interface with the metal backing.<sup>111</sup>

Analysis of oxidation by FTIR spectroscopy in non-sterilized, ethylene oxide sterilized, and gamma irradiated components confirmed the linkage between near-surface oxidation, gamma irradiation, and the white band. Non-sterilized or ethylene oxide sterilized components (never-implanted) had extremely low levels of oxidation and no white band. Retrieved components which had not been gamma irradiated sometimes had slight oxidation levels at the surface, attributed to in-vivo service, but no white band. Gamma irradiated components with white bands (both never-implanted and retrieved) had elevated oxidation levels near the surface, peaking at 0.2 to 0.8 mm subsurface which corresponded to the locations of the white bands. The magnitudes and depths of oxidation increased with time after irradiation.<sup>111</sup>

Tensile tests were performed on non-standard C-shaped specimens obtained from thin cross-sections of these acetabular cups. Components which had not been gamma irradiated, and did not have a white band, had the highest ultimate tensile strength and

elongation, followed by components which had been gamma irradiated but did not have a white band, which had a lower ultimate tensile strength but the same elongation. Gamma irradiated components with a white band had a still lower ultimate tensile strength and an extremely low elongation.<sup>111</sup> Brittle fracture consistently occurred within the white band region before ductile deformation proceeded within the central bulk region and the outer edges. Similar results were obtained from tensile tests on microtensile specimens cut from different regions of thin cross-sections containing the white band. Specimens from within the white band consistently had lower ultimate tensile strengths and elongations than specimens from either the outer surface or the central region. Oxidation thus contributes to embrittlement of the UHMWPE within the subsurface damaged region.

The above study was followed up by examining 239 retrieved and 95 never-implanted tibial plateaus for the presence of the white band. Results to date have been similar to those from acetabular cups: the subsurface white band was associated with elevated oxidation levels, and its appearance intensified with post-irradiation aging time in air. Differences between never-implanted and retrieved components were observed based on uniformity and physical dimensions (depth, thickness) of the white band.<sup>184</sup>

Another study of 8 never-implanted tibial components (aged 7-83 months post-irradiation) examined the white band by polishing cross-sections for examination with reflected light microscopy. These components were machined from GUR 415 rod stock and gamma irradiated to doses of 2.5 to 4.5 Mrad. The white band appeared to extend from the outer surfaces uniformly down to a distinct boundary line, which separated the white band from the core. Its thickness increased rapidly with time over the first 2 years post-irradiation, and then leveled off at 5-6 mm. after 5 years. Characterization of the white band demonstrated that it correlated to an oxidized surface layer (infrared spectra) with increased crystallinity (DSC), density (density gradient column), and hardness (Shore D durometer hardness) relative to the core.<sup>126,185</sup>

A separate study examined the formation of the white band in 40 retrieved and 7 never-implanted Charnley acetabular cups, but described the phenomenon as a banded, or non-uniform, distribution of nonconsolidated particles. The never-implanted components were gamma irradiated, but sterilization methods were not reported for the retrieved components. Only 5 retrieved components and 4 never-implanted components contained this banded structure of defects, in contrast to a random distribution of nonconsolidated particles that occurred in most of the components. All 5 retrieved components with the white band also had radial cracking along the rim of the cup. Density vs. depth profiles from 4 retrieved cups suggested that the presence of the white band might correlate with overall higher densities in the surface and bulk regions, but relatively few components were tested. Density vs. depth profiles from 7 never-implanted cups demonstrated that subsurface density peaks increased in magnitude with time since irradiation (1-9 years), and in 4 out of 5 cups a high maximum value of density was linked with the presence of the white band (after 6-9 years).<sup>112</sup>

Embrittlement from the white band was linked to increased clinical wear rates in a study of 107 retrieved acetabular cups. These components had been implanted for 5-20 years, and represented a variety of manufacturers. Clinical records were available for all patients. Wear volume was measured directly based on fluid displacement. The white band was observed in thin sections cut from each component, and rated as none, mild, moderate, or severe based on its dimensions. The white band was observed in 50.5% of the 107 acetabular cups, but was more common in cups implanted after 1982 (74%) than those implanted between 1970 and 1982 (29%). Gamma radiation was used to sterilize components throughout this earlier period. The wear rate was found to increase with the white band (embrittlement) rating, although wide standard deviations were observed for wear rate values because of the multifactorial effects involved.<sup>186</sup>

Structural characteristics of the white band have been evaluated using X-ray techniques, both wide angle X-ray diffraction (WAXD) and small angle X-ray scattering (SAXS). Crystallinities of unsterilized vs. post-irradiation aged specimens were compared

using both density and SAXS measurements. Crystallinity values from both techniques were fairly consistent, but distinct differences were observed between specimens. Unirradiated specimens had the lowest values (50-53%), followed by specimens from above the white band (61-64%) and then specimens from within the white band (83-86%) of post-irradiation aged specimens.<sup>187</sup>

Measurements of the long period, or inter-lamellar spacing, from SAXS also showed distinct structural differences. Unirradiated specimens had a long period of 67 nm, which decreased to 49 nm in post-irradiation aged specimens. Near the surfaces of these aged specimens, long periods of both 49 nm and 19 nm were observed, and within the white band a third long period of 8 nm was added.<sup>187</sup> In another presentation of SAXS results from Hifax 1900 components, a long period of 94 nm was measured in unsterile specimens, and long periods of both 94 nm and 48 nm were measured in aged, irradiated specimens.<sup>188</sup> These changes in the long period indicate that the molecular weight of polymer chains decreased in the oxidized surfaces, due to chain scission. The addition of distinct long period values to that from the bulk suggests that in the subsurface region, new lamellae may form within the initially amorphous phase (between the original lamellae from solidification). In a separate study, electron microscopic examination of unsterile and gamma irradiated (in N<sub>2</sub>) components revealed a shortening of molecular chains after irradiation, although the white band was not present.<sup>189</sup>

### **3.5.7 Crosslinking from irradiation**

Crosslinking that results from gamma irradiation has the potential to improve mechanical properties and wear behavior, particularly for acetabular cups, and has been evaluated in some research studies. The extent of crosslinking is analyzed by determining the gel content of polyethylene,<sup>190,191</sup> based on extraction of the soluble phases with solvents such as decahydronaphthalene or xylene. The gel content is the weight percent of insoluble phase, or gel, present in the specimen. Gel contents in unsterilized and EtO sterilized specimens

have been measured as 0-10%, while values of 45-60% were obtained for identical specimens irradiated in air.<sup>192</sup>

Crosslinking varies with depth in gamma-irradiated components, but varies inversely to oxidation so that crosslinking decreases near surfaces but increases to a maximum within the bulk. This trend was confirmed by characterization of acetabular cups that had previously been tested in joint simulators. Gel contents of 20-44% were measured on the outer bearing surfaces of two components, while the values increased to 60-78% at the peaks within the bulk.<sup>193</sup> Unfortunately many studies do not report details of specimen locations and sampling methods, and few studies have examined the variation of crosslinking with depth.

The effects of radiation dose, atmosphere (i.e. packaging), and heat treatment on crosslinking have been examined. Crosslinking increased with radiation dose when specimens were packaged in nitrogen (from 0.4 to 10 Mrad)<sup>129,167</sup> or air (from 2.5 to 5.0 Mrad).<sup>194</sup> Packaging in nitrogen (47%) or under vacuum (42%) increased crosslinking levels above those from packaging in air (30%), after irradiation to 2.5 Mrad.<sup>194</sup> Another study measured the crosslinking in extruded rods of UHMWPE (GUR 415: unsterile, irradiated in air, and irradiated in nitrogen and stabilized by heat treatment) as a function of radial depth in the rod. The gel content of unsterile rods varied from 5-8% at the surface to 42-61% at the center. After irradiation in air, the gel content was unchanged at the surface but increased to 94-99% at the center. After irradiation in nitrogen and stabilization treatment, the gel content at the surface increased significantly to 79-83% and increased to 98-100% at the center.<sup>191</sup> The heat treatment (at 50°C for 144 hours) had been advocated as a method to stabilize UHMWPE<sup>195,196,197</sup> (irradiated in nitrogen) by removing free radicals and thereby preventing oxidation. A different study found that this heat treatment (after irradiation in nitrogen) did not change the gel content from identical specimens (direct molded tibial components) without the stabilization treatment.<sup>174</sup> This study showed that the stabilization treatment had little effect on most properties (gel content, tensile properties, density, percent crystallinity, and oxidation by FTIR) as compared to specimens irradiated in nitrogen without heat treatment.



Other studies have also evaluated the effect of irradiation atmosphere on crosslinking. Irradiation under vacuum (i.e. vacuum-sealed foil pouches) has been found to increase crosslinking over irradiation in air.<sup>198</sup> Crosslinking vs. depth was measured for acetabular cups irradiated in air vs. vacuum, and the results were correlated to hip simulator wear test results. After post-irradiation aging for 3.5 months, crosslinking was a minimum at the outer surface and reached a maximum level at a depth of about 200  $\mu\text{m}$  for both packaging atmospheres. Acetabular cups irradiated under vacuum had higher levels of crosslinking in the surface layer than cups irradiated in air, and this was linked to a lower wear rate as well. Wear rates for irradiated cups showed initially high wear rates, near the rate measured for EtO sterilized cups, but the wear rates decreased with increasing wear cycles as the bearing surface wore down into the crosslinked subsurface region.<sup>168</sup>

### **3.5.8 Effect of irradiation on mechanical properties**

The oxidation and crosslinking that result from gamma irradiation affect the mechanical properties of UHMWPE components, and the properties continue to change with time (after irradiation) as oxidation proceeds. Property changes have been measured both in bulk specimens and in localized, subsurface regions. Mechanical properties significantly contribute to the performance of implant components, due to the high stress levels that must be supported in vivo by the bearing surfaces. In addition to basic tensile or compressive properties (yield strength, ultimate strength, ductility, and elastic modulus), creep and fatigue also contribute to the long-term performance in terms of both wear and failure behavior.

Mechanical properties of the unsterilized polymer control the properties obtained after irradiation. These initial properties depend on several variables: resin type, consolidation method, and processing variables (cooling rates, pressure, time) that affect recrystallization. Thus large variations in mechanical properties have been reported. One study found that processing variables used in direct compression molding of GUR 4150 resin resulted in variations of 5 to 30% in tensile strength and elastic modulus, which did not always correlate

with variations in crystallinity.<sup>199</sup> Even larger variations would be expected between different resins and consolidation methods. Within the United States, ASTM Standard F648 specifies that the unsterilized, bulk UHMWPE from which components are fabricated must meet minimum mechanical properties values of:<sup>98</sup>

Yield Tensile Strength:	21 MPa (Type 1) or 19 MPa (Types 2 or 3)
Ultimate Tensile Strength:	35 MPa (Type 1) or 27 MPa (Types 2 or 3)
Elongation:	300% (Types 1 or 2) or 250% (Type 3)

No maximum property values are specified, and no specifications are applied to the final, sterilized implant component.

A draft data requirements document for UHMWPE is being developed for implementation by the Food and Drug Administration.<sup>200</sup> This document specifies that a conventional UHMWPE (both unsterile and sterile) should have mechanical properties (based on ASTM Standard D 638)<sup>201</sup> within the following ranges:

Yield Strength:	19 - 26 MPa
Ultimate Tensile Strength:	27 - 60 MPa
% Elongation:	200 - 450%
Tensile Elastic Modulus:	0.6 - 1.6 GPa

An early study that examined the effects of irradiation on UHMWPE found that the tensile yield point was increased slightly after irradiation in air. These tensile tests were run at extremely low strain rates (crosshead speed of 0.0508 cm/min). The unsterile specimens experienced macroscopically affine deformations, whereas the irradiated specimens underwent necking with strain localization, and a greater degree of stress whitening. Additional specimens were tested for fatigue by cycling in tension (up to  $1.72 \times 10^4$  KPa) for a fixed number of cycles ( $2.5 \times 10^6$  to  $10^7$ ), then performing a tensile test. Again the irradiated specimens had higher yield points, but decreased values of lower yield stress. Several specimens loaded for  $10^7$  cycles experienced necking during cyclic loading, which was more pronounced in irradiated specimens. After  $10^7$  cycles, the upper yield point phenomenon of

the polymer was not observed, and the irradiated specimens had lower yield strengths than the unsterile specimens.<sup>125</sup>

Fatigue tests have shown that irradiation in air degrades the fatigue performance of UHMWPE relative to unsterile or EtO sterilized specimens. Specimens were tested to failure (or runout at  $10^7$  cycles) using a cantilever rotating beam methodology (at 3 Hz) with progressive variations in maximum stress. The fatigue strengths (at  $10^7$  cycles) measured were 31 MPa for unsterile, 28-31 MPa for EtO sterilized, and 17.5 MPa for UHMWPE gamma irradiated in air.<sup>202,203</sup>

Tensile tests have been performed on specimens machined from 14 retrieved tibial components to examine differences between sterilization methods (7 gamma irradiation vs. 7 EtO). Components sterilized by gamma irradiation had significantly lower ultimate tensile strength, elongation, and toughness than those chemically sterilized with EtO. This trend was obvious even when the effect of implantation time was considered as well. Significant differences were not observed for yield stress and Young's modulus.<sup>204</sup> Only one specimen was obtained from each retrieved component, so statistical evaluation of the results is somewhat limited.

A mathematical model has been developed which relates uniaxial tensile properties (for true stress-true strain) to density changes resulting from post-irradiation oxidation. This model was based on data from GUR 415 UHMWPE tensile specimens that were gamma irradiated in air (to 2.8-3.7 Mrad) and then artificially aged by heating in air at 127°C for times up to 14 hours. According to this model:

True Stress (MPa) =  $29.350 - 26.333 \exp \{[-63.361 - 2026.17 \times (\rho - 0.95)] \times \text{True Strain}\}$

where  $\rho$  is density (range of 0.935 to 0.954 g/cm<sup>3</sup>), and True Strain is below 0.12.<sup>205</sup>

Other studies examined the effects of irradiation in inert gas (nitrogen or argon) or under vacuum. Packaging in nitrogen (in one study) was found to increase the ultimate tensile

strength and the elongation at break (over unsterile specimens), whereas packaging in air increased the ultimate tensile strength but slightly lowered the elongation.<sup>129</sup>

Another study examined the interactions between consolidation methods (using a different resin for each method) and irradiation in either air or nitrogen, using unsterile specimens as controls. Isostatic molding (Himont 1900H) resulted in the highest yield strength (24 MPa) and ultimate tensile strength but the lowest elongation, before sterilization. Ram extrusion (GUR 4150HP) gave an intermediate yield strength (23 MPa), and uniaxial compression molding (GUR 1050) gave the lowest yield strength (21 MPa). After sterilization, specimens from all consolidation methods had increased yield strengths and ultimate tensile strengths but decreased elongations, which resulted from irradiation-induced crosslinking. Larger property changes resulted from irradiation in air than from irradiation in nitrogen.<sup>206</sup>

A third study compared tensile properties from isostatic molded (Himont 1900H) vs. ram extruded (GUR 4150HP) specimens, with sterilization using either EtO or gamma irradiation in argon. Unsterilized specimens were tested as controls. Specimens were tensile tested periodically over 6 months, but this short aging period did not result in significant property changes. Isostatic molding produced higher yield strength (25 MPa) and ultimate tensile strength (61 Mpa) than ram extrusion (24 Mpa, 55 MPa), but similar elongation (350-360%), in the unsterilized controls. This trend continued after irradiation in argon, but after EtO sterilization all three tensile properties were higher for isostatic molded than for ram extruded specimens. Irradiation (in argon) of both specimen types increased their yield strengths but decreased their ultimate tensile strengths and elongations, although the decrease in ultimate tensile strength was not statistically significant for isostatic molded specimens. Sterilization using EtO did not significantly change the tensile properties of isostatic molded specimens, but decreased the ultimate tensile strength and elongation of ram extruded specimens while their yield strength remained the same. Isostatic molding produced the highest yield strengths and ultimate tensile strengths for all unsterile and sterile conditions,

and higher elongations for specimens sterilized with EtO. Elongations for both consolidation methods were similar for unsterile and irradiated specimens.<sup>207</sup>

A related study compared the fatigue crack propagation rates of isostatic molded (Himont 1900H) vs. ram extruded (GUR 4150HP) specimens, following irradiation (2.8 Mrad) in either air or argon. Specimens were apparently tested shortly after irradiation, without extended shelf aging. Similar crack propagation rate curves ( $da/dN$  vs.  $\Delta K$ ) were obtained at an R ratio of -2 for all 4 specimen conditions. Although the test method used disregards the crack initiation phase of fatigue damage, the number of cycles to reach mature crack length in isostatic molded specimens ( $7.30 \times 10^5$  cycles) was much longer than that in ram extruded specimens ( $2.27 \times 10^5$  cycles).<sup>208</sup>

Mechanical properties versus depth have been measured in irradiated, aged (i.e. oxidized) or retrieved specimens by testing small, thin sections microtomed or cut parallel to the outer surface. Tensile tests performed on thin sections cut from retrieved acetabular cups showed significant variations in mechanical properties through the depth. Results were correlated to the presence and location of the subsurface white band. The average ultimate tensile strengths varied from 20 Mpa at the outer surfaces (both articulating & non-articulating) to 15 Mpa within the white band to 25 Mpa in the central bulk region. The average ultimate elongations varied from 170% at the outer surfaces to 10% within the white band to 60% in the central bulk region.<sup>111</sup>

Related results were obtained in the same study by microtoming cross-sections (through the thickness) from 23 acetabular cups, and performing tensile tests on these C-shaped specimens. Unsterilized control specimens were compared to retrieved cups that had been sterilized with gamma radiation (with or without a white band observed). The average ultimate tensile strengths varied from 45 MPa for unsterilized controls to 35 MPa for retrieved cups (without a white band) to 20 MPa for retrieved cups (with a white band). The average elongations varied from 630% both for unsterilized controls and retrieved cups (without a white band) to only 70% for retrieved cups (with a white band).<sup>111</sup> When a white

band was present in the thin section, brittle fracture initiated within the white band and then was followed by ductile deformation and failure of the central bulk and the outer surface regions.

A follow-on study was performed on shelf-aged tibial components which had been gamma irradiated either in air or vacuum. Tensile tests were performed on small, thin sections (200  $\mu\text{m}$ ) microtomed parallel to either the bearing or back surface. Immediately after irradiation (in either air or vacuum), the ultimate tensile strengths and the elongations decreased relative to values obtained from unsterilized bar stock. After shelf aging for 16-20 months, the ultimate tensile strength decreased about 20% for the specimen packaged in air but increased slightly for the specimen packaged under vacuum. Properties for components packaged in air were evaluated for shelf aging periods up to 84 months. Ultimate tensile strength decreased steadily with time, from about 45 MPa down to 25 MPa. In contrast, elongation remained fairly constant around 400% for at least 70 months, then dropped rapidly to about 220% at longer times. The elongation results correlated closely with FTIR measurements of oxidation, which showed that oxidation also increased rapidly after 60 months. When ultimate tensile strengths and elongations were plotted versus oxidation index values, both mechanical properties were found to decrease linearly with increasing oxidation.<sup>209</sup>

Tensile tests on microtomed thin films (125  $\mu\text{m}$  thick, 1.25 cm wide) have been used to examine the effect of radiation dose and dose rate (in nitrogen) on mechanical properties. Properties measured included ultimate tensile strength, ultimate elongation, and strain energy at break. At low doses of 0.4 to 2.5 Mrad (normal dose rate of 0.35 Mrad/hr), ultimate tensile strengths remained fairly constant (62-65 MPa) while distinct increases in elongation (762-812%) and strain energy (7.0-7.5 joule) were observed relative to the unsterile control (66 MPa, 631%, 6.3 joule). At higher radiation doses up to 10 Mrad, all mechanical properties decreased with increasing dose so that properties were lower than that of the unsterile control. At a higher dose rate (1.20 Mrad/hr), the increases in elongation and strain energy relative to

the unsterile control were extended to doses of at least 3.7 Mrad. These property changes were correlated to significant increases in density and crosslinking (gel content) with increasing radiation dose.<sup>167</sup>

Tensile tests on microtomed thin cross-sectional films (100  $\mu\text{m}$ ) have been used to evaluate variables including resin type, consolidation method, and aging environment. Specimens were microtomed from ram extruded, machined components from resins GUR 4150 (with calcium stearate), GUR 4050 and Himont 1900H (both without calcium stearate) that had been irradiated and artificially aged, and from control specimens that remained unsterile. After sterilization and aging, the tensile strength (at break) of the GUR 4150 specimen decreased 76% (to 10 MPa) relative to the control, that of the GUR 4050 specimen decreased 35% (to 33 MPa), and that of the Himont 1900H specimen decreased 41% (to 32 MPa). The corresponding elongations were 80% for GUR 4150, 420% for GUR 4050, and 360% for Himont 1900H. Compression molded specimens retained higher mechanical properties (after irradiation and artificial aging) than ram extruded specimens did. Molded specimens with varying concentrations of calcium stearate had significantly different tensile strengths (at break). Similar specimens were irradiated and then artificially aged in different environments, including oxygen, nitrogen, and argon. The specimen aged in oxygen had a tensile strength (at break) of 29 MPa and an elongation of 500%, the one aged in nitrogen had a strength of 43 MPa and an elongation of 800%, and the one aged in argon had a strength of 46 MPa and an elongation of 700%.<sup>175</sup>

In a related study, the same tensile test methods were used to obtain results from ram extruded specimens of GUR 4150 and Himont 1900 resins and from direct compression molded specimens of Himont 1900 resin. Specimens were gamma irradiated in air (3.7 Mrad) and artificially aged. Thin films from ram extruded specimens contained fusion defects that were visible before tensile testing, whereas films from compression molded films did not. Compression molding (Himont 1900) produced the highest tensile strength (43 MPa) and elongation (430%), followed by ram extrusion of Himont 1900 (32 Mpa, 380%) and then ram

extrusion of GUR 4150 (23 Mpa, 280%). The compression molded specimen from Himont 1900 resin had much higher mechanical properties than the ram extruded specimen from the same resin, although the compression molded specimen had much lower crystallinity and density (0.933 vs. 0.938 g/cm<sup>3</sup>).<sup>177</sup>



## 4. PRINCIPLES OF EXPERIMENTAL TECHNIQUES

### 4.1 CONFOCAL MICROSCOPY

Confocal microscopy is an optical microscopy technique that provides improved resolution in the lateral image plane and also allows measurement of dimensions in the vertical direction. Thus it can be used both to examine specimen features visually and to make measurements in three dimensions. Combined with digital image processing and analysis, confocal microscopy can be a powerful tool for characterizing surfaces at the scale of optical microscopy. Thus, the research uses this technique to examine the surfaces of implant bearings and to measure their surface topography.

Confocal means “single focus,” and refers to the pinhole optics providing its unique imaging characteristics.<sup>210</sup> Two pinholes are added to the conventional optical system in reflected light. The first pinhole is located in the path of the incoming light, to provide pinpoint illumination on the specimen surface. This reduces scattered light that might degrade image quality. The second pinhole is located in the path of the reflected light, after it passes through the objective lens. This pinhole blocks out light that has been reflected from points at heights away from the focal plane of the lens. Scattered or defocused light rays do not contribute to the image, so those areas appear dark.

Figure 2 shows a simplified diagram of the optics of a tandem scanning confocal microscope. This is the first type of confocal microscope to provide real-time imaging, and was invented in the late 1960's by Petran and Hadravsky.<sup>211</sup> A spinning Nipkow disk is used to provide the pinholes for the optical system, and each disk contains thousands of holes arranged in Archimedean spirals. Duplicate sets of holes are precisely aligned on opposite sides of the disk axis so that holes on one side function as the source aperture and corresponding holes on the other side function as the viewing aperture. The Nipkow disk spins rapidly during operation of the microscope, so that a real-time optical image is

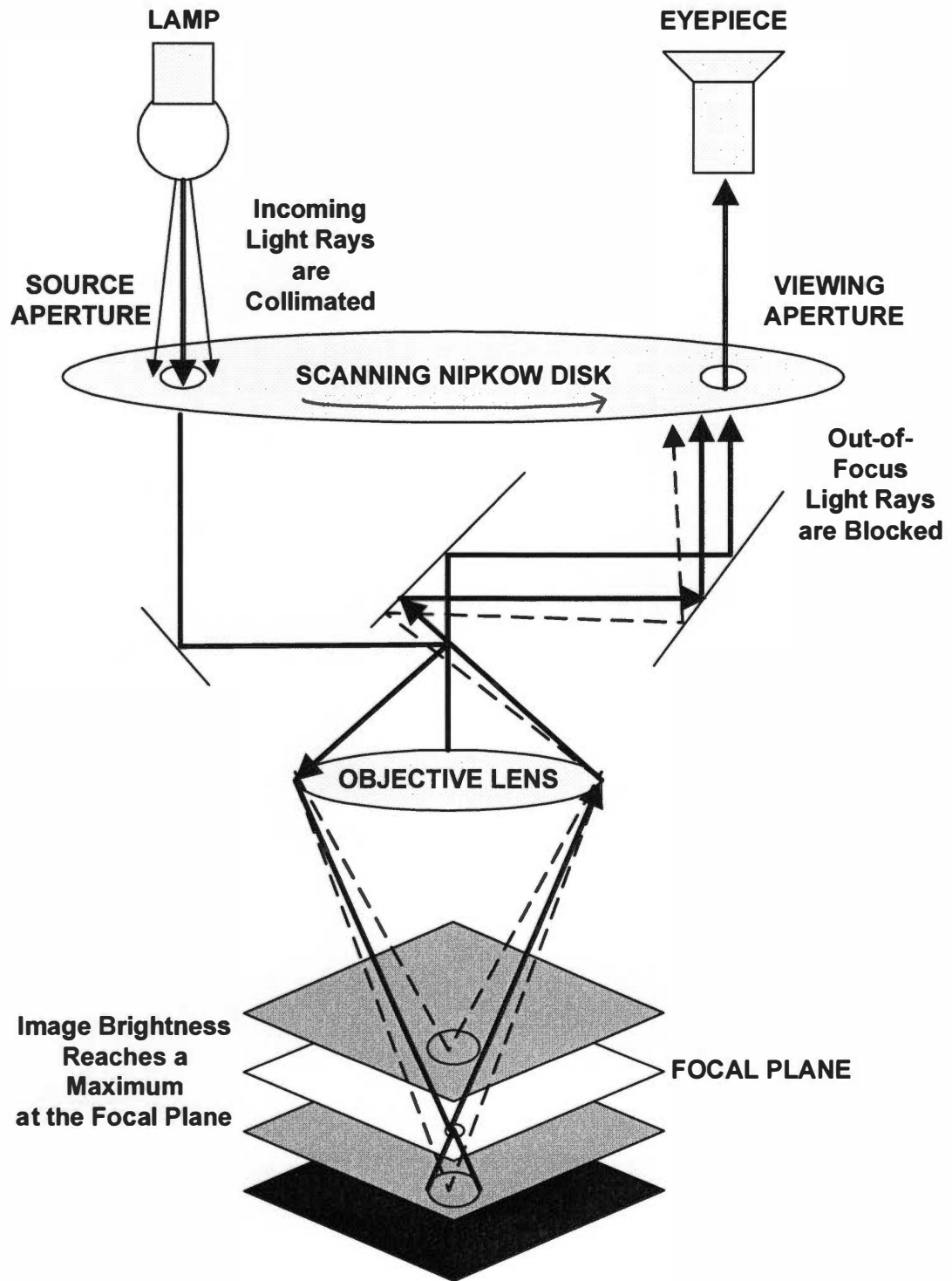


**Figure 2. Optics of a tandem scanning confocal microscope.**

produced as the pinpoints of light scan across the specimen. Thus the resulting confocal image can be observed visually through the eyepieces.

The images created in a confocal microscope, called optical sections, have unique characteristics that make this a powerful light microscopy tool. First, the images are very clearly focused with no blurriness from features that are located above or below the focal plane (i.e. out-of-focus). Second, each image only contains illumination from specimen features that intersect the focal plane of the objective lens. Light is blocked by the viewing aperture from features above or below the focal plane, so that these areas appear dark in the image. Thus the microscope “optically sections” a sample, similar to the way that a microtome physically sections or slices a specimen so that it’s interior can be examined. The technique has been developed primarily for biologists, for examining internal structures of tissue specimens, so some of terminology has been adapted from biology.

The intensity of reflected light from a plane varies with vertical distance (z) from the focal plane as:<sup>212</sup>

$$I(u) = [\sin(u/2) / (u/2)]^2$$

where  $u = (8\pi/\lambda) z \sin^2(\alpha/2)$

Intensity, or  $I(u)$ , varies with the normalized coordinate,  $u$ , which is related to the real vertical distance from the focal plane,  $z$ , the numerical aperture of the objective lens,  $\sin \alpha$ , and the wavelength of light,  $\lambda$ . Figure 3 shows digital image data taken with a 10X objective lens focusing on a flat reflective surface, with intensity plotted versus relative height,  $Z$ , recorded for a series of optical sections. The light intensity is very sensitive to vertical distance, reaching a maximum,  $I_{\max}(Z_f)$ , at the focal plane and dropping off rapidly as  $z = Z - Z_f$  varies from zero.

Figure 4 illustrates how light intensity varies for a series of optical sections focused at different heights on a specimen. The gray area represents the specimen with a ridge pointed upward. The dashed lines represent the focal planes for the series of three optical sections. The curve above each focal plane represents the image intensity versus lateral position within the optical section. At each height, the intensity reaches a maximum,  $I_{\max}(Z_f)$ , at the point

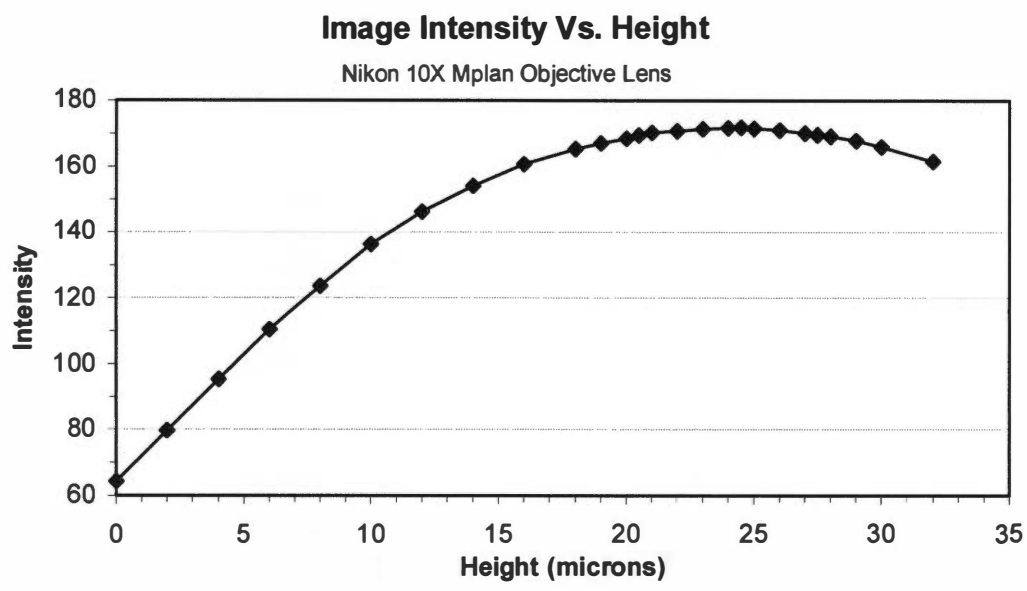


**Figure 3.** Confocal image intensity versus height for the 10X objective lens (100X).

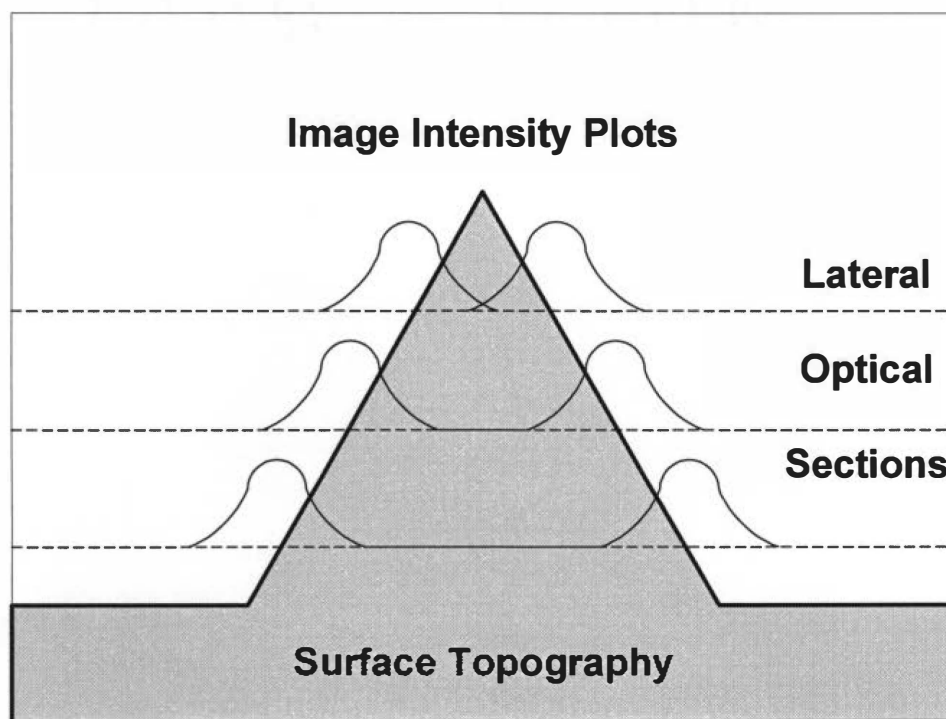


**Figure 4.** Image intensity varies with distance from the focal plane for optical sections focused at different heights on the specimen surface.

where the specimen surface intersects the focal plane, and drops off rapidly at adjacent points where the surface height is slightly higher or lower. Thus each optical section contains bands of brightness surrounded by dark areas representing out-of-focus specimen features. The images appear quite different from those normally observed from optical microscopy.

Confocal microscopes are interfaced to digital imaging systems for acquisition and processing of the optical sections. Each digital image records an intensity value (from 0 to 255) for each pixel in the image, as well as the lateral position (as X, horizontal, and Y, vertical) of the pixel. The size of the pixels depends on the image input device – a video camera is used on the Tracor Northern TSM-1 Tandem Scanning Confocal Microscope used in this research. The pixel resolution should be similar in scale to the optical resolution of the objective lens, and the pixel resolution is measured using a standard calibration slide.

Digital image processing and analysis make it possible to use the variation of light intensity with height to make quantitative measurements of specimen features in three dimensions. First a series of optical sections are acquired digitally, in equally spaced Z-increments across the range of heights covered by the specimen surface. Either the objective lens or the specimen is moved to control the spacing of the Z-increments. The specimen is kept in a fixed position laterally while this series of optical sections is acquired, so that the pixels remain aligned from one image to the next. For each pixel position in the resulting stack of optical sections, the image intensity will go through a maximum value corresponding to the relative height of that feature on the specimen surface.

The Z-increments should be scaled so that they are appropriate for the vertical sensitivity of the objective lens, which is largely controlled by its numerical aperture value. Figure 5 shows the image intensity versus height for the 20X objective lens, showing the detailed variation near the maximum intensity at the focal plane. Digital imaging allows distinction of intensity differences as small as one or two units, so the width of the curve at an intensity level of one to two units below the maximum is determined. Half of this width will be

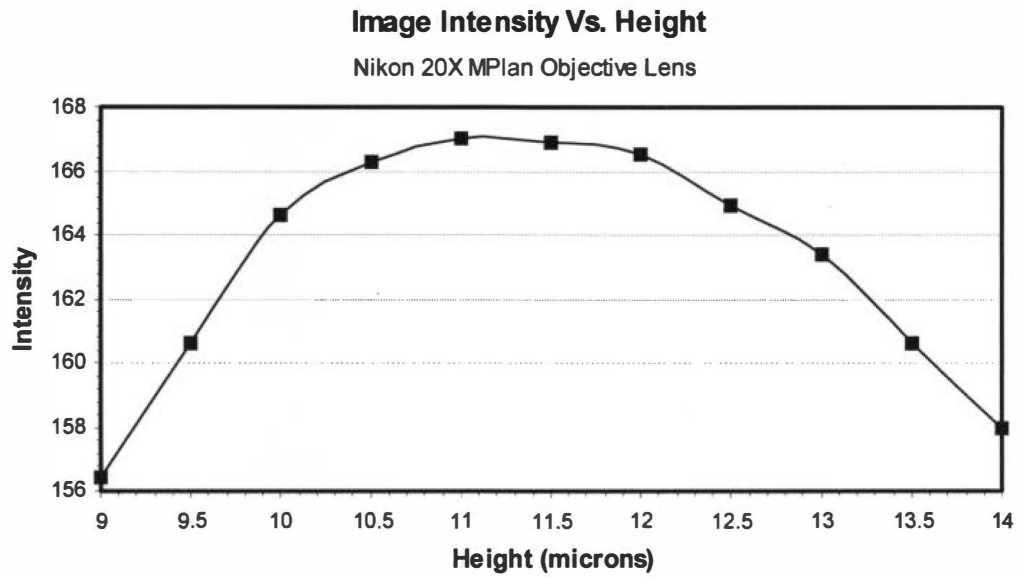


**Figure 5. Confocal image intensity versus height for the 20X objective lens (200X).**

used to define the Z-increment based on the operational limits of data acquisition on the TSM-1 tandem scanning confocal microscope. The Z-increment used at 200X will be 1.5  $\mu\text{m}$ .

Image processing of the stack of optical sections is performed next to generate images that are more useful to interpret. First a Maximum Intensity Image is processed by selecting the maximum intensity value,  $I_{\text{max}}(Z)$ , obtained at each pixel position. These intensities are combined into a single image that shows a perfectly focused image of the specimen surface. Next a Depth Map Image is processed by determining the  $Z_{\text{max}}$  values where the maximum intensity was recorded for each pixel position. Image intensities (ranging from 0 to 255) are set proportional to the range of  $Z_{\text{max}}$  values for pixels in the Depth Map Image. Thus this image displays topographic data about the three-dimensional shape of the specimen surface.

Surface texture parameters can be calculated from the topographic data in the Depth Map Image. First the image intensity data must be converted into a data file that contains values of relative heights ( $Z$ ). Then the data from each column is fit to a line using linear extrapolation. Residuals ( $R$ ) are calculated for each column by subtracting the fitted line from the actual measured heights. These residuals are then stored in a residual data file that is used to calculate the surface texture parameters. Then this entire process is repeated using a linear fit along rows instead of columns.

Surface texture parameters to be calculated include:<sup>213</sup>

- Roughness Average ( $R_a$ ) =  $(1/N) \sum IRI$
- Root Mean Square (RMS) Roughness ( $R_q$ ) =  $\{(1/N) \sum (R)^2\}^{1/2}$
- Skewness ( $R_{sk}$ ) =  $(1/NR_q^3) \sum (R)^3$

Roughness average and RMS roughness are parameters that relate to the height variations on the surface, whereas skewness relates to the shape of the surface profile. The height parameters always have positive values, but skewness can be either positive or negative. The minimum value of roughness average for a flat, planar surface is one-fourth of the maximum Z-increment, as shown in Figure 6. The maximum residual is one-half of the Z-increment, so

the average of the absolute values of the residuals will be one-four of the Z-increment. Note that none of these parameters relate to the lateral distance scale over which they are measured – only the residual (R) of the height is included in the calculations.

## 4.2 NANOINDENTATION

The nanoindenter is an indentation testing system that uses high-resolution instrumentation to control and measure the loads (P) and displacements (h) versus time as a small indenter is driven into and released from a specimen.<sup>214</sup> The loads and displacements are of small magnitudes, as low as 1 nN in load and 0.1 nm in displacement. Indentation is typically performed with a Berkovich indenter – a three-sided pyramidal diamond (see Figure 7) with the same contact depth to area relation as the Vickers pyramidal used in microhardness. Because the indents are microscopic, load-displacement results can be evaluated on a very small dimensional scale similar to the size of wear debris. Mechanical properties, such as hardness (H) and elastic modulus (E), can be calculated as a function of depth from the data that is collected during instrumented indentation.

Dynamic stiffness measurement techniques (also known as continuous stiffness) have been developed to allow continuous measurement of elastic contact stiffness (S) during indentation. Stiffness is a key parameter that is used to calculate the elastic modulus. In conventional nanoindentations, a single value of stiffness is determined from the unloading cycle of the load-displacement data. This value is sensitive to pile-up around the indent and to any time-dependent responses of the specimen. Thus the conventional analysis is not useful for polymers, which experience time-dependent mechanical behavior. The dynamic stiffness acquisition mode superimposes a small oscillating force on the primary load cycle and then measures the time-variant displacement response with a frequency-specific amplifier.<sup>214,215</sup> This provides a continuous measurement of stiffness as well as load and displacement versus time. This technique has previously been used to measure mechanical properties of polymers.<sup>216,217</sup>



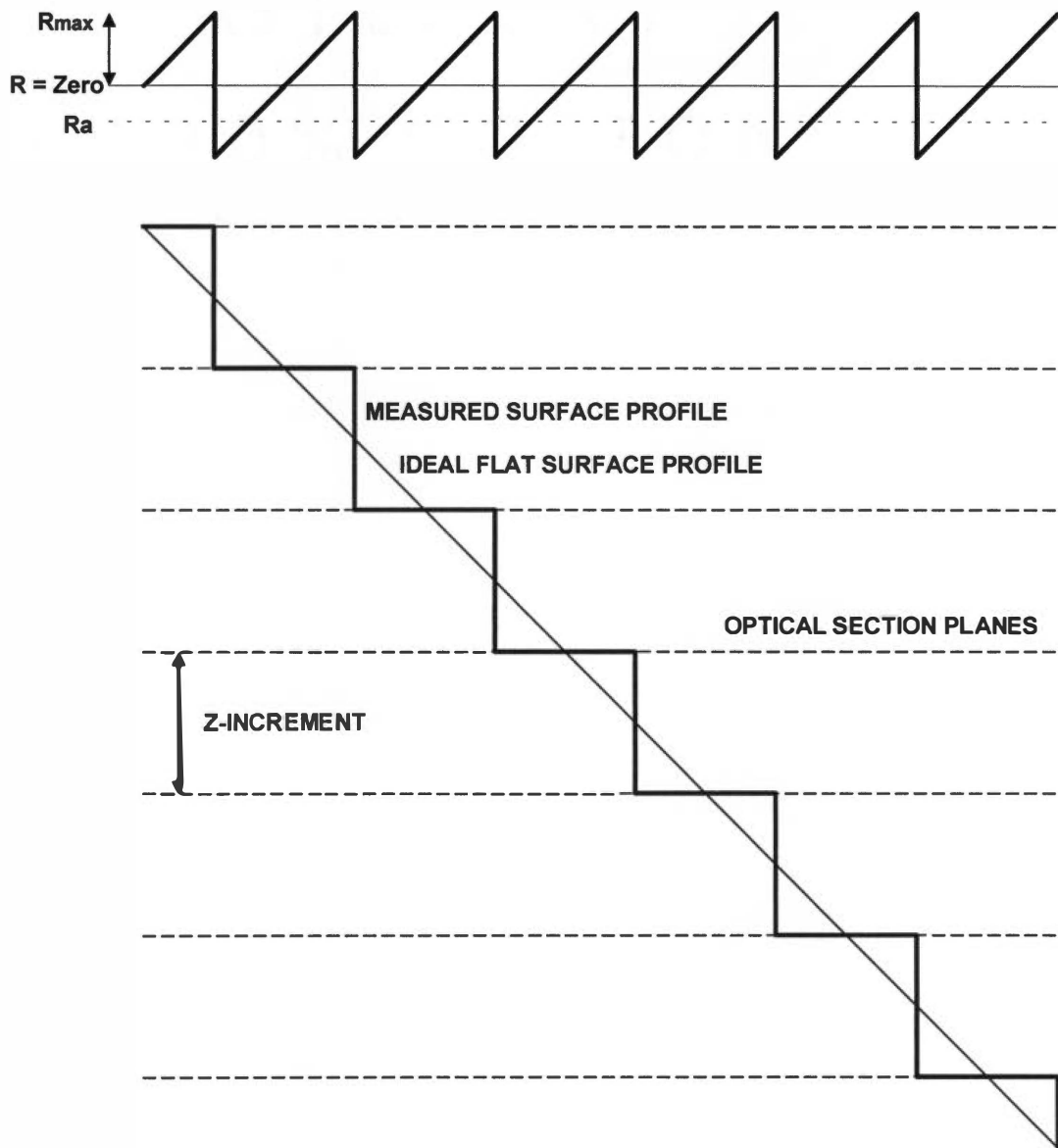
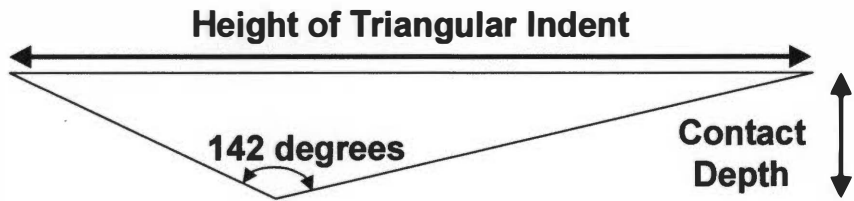
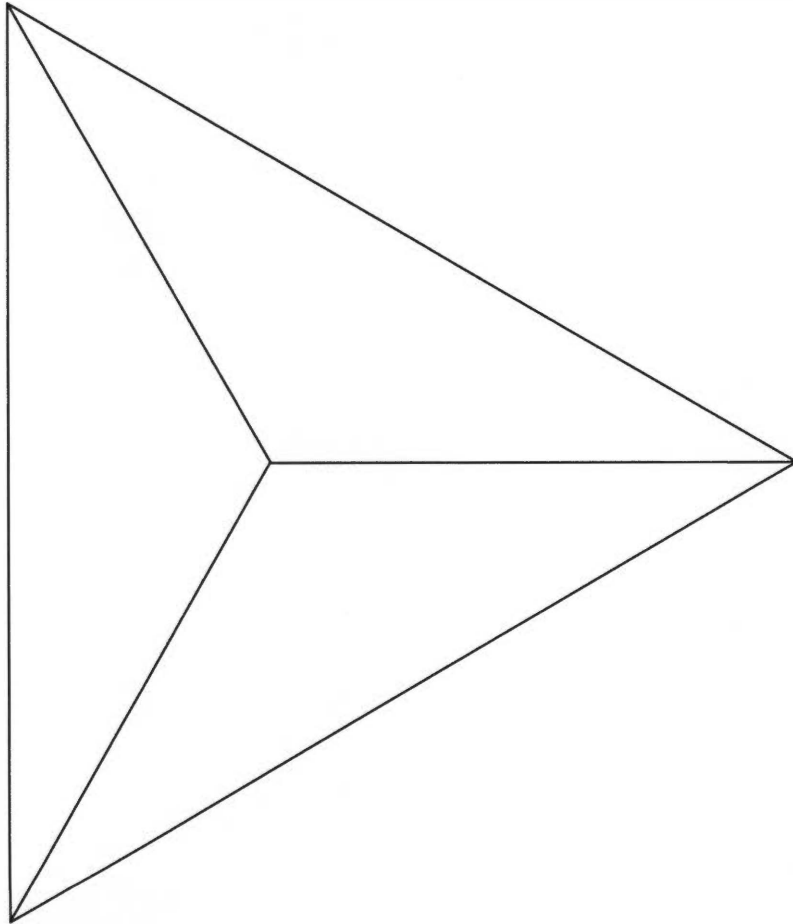


**Figure 6. Determination of the minimum roughness average ( $R_a$ ) for a flat, planar surface.**



A. Side view of Berkovich indenter.



B. Top view of Berkovich indenter.

**Figure 7. Geometry of the Berkovich indenter.**

Contact depth ( $h_c$ ) is a parameter that is required to determine hardness and modulus. Contact depth is the depth of contact between the indenter tip and the specimen (as a function of time), and is less than the measured displacement due to elastic deformation. Contact depth is primarily determined by the geometry of the indenter tip, and is calculated from the measured displacements as:

$$h_c = h - (\epsilon P / S)$$

where  $h$  is the measured displacement,  $P$  is the measured load,  $S$  is the measured stiffness, and  $\epsilon$  is an indenter geometry constant (0.75 for the Berkovich indenter).

Another critical parameter that is required for calculation of hardness and modulus is the projected contact area ( $A$ ). Nanoindentation differs from traditional microhardness tests in that contact area is calculated from the displacement data (using the geometry of the indenter tip) under load rather than being measured with a microscope after the load has been released. For a Berkovich indenter, the general formula for contact area is:

$$A = 24.56 h_c^2$$

Contact area is calibrated using fused quartz specimens for indents up to about 2  $\mu\text{m}$  in contact depth. The resulting calibration data is fit to a more complex formula for contact area, having the form:<sup>215</sup>

$$A = C_1 h_c^2 + C_2 h_c^1 + C_3 h_c^{1/2} + C_4 h_c^{1/4} + C_5 h_c^{1/8} + \dots$$

When contact depths significantly larger than 2  $\mu\text{m}$  are performed, an alternate calibration method has been developed whereby the three-dimensional geometry of the indenter tip can be measured using confocal microscopy. This allows measurement of the contact area to contact depths greater than 25  $\mu\text{m}$ , which may exceed the indent depth achievable because of load limits on the nanoindenter.

Hardness can then be calculated throughout the indentation cycle as:

$$H = P / A$$

Elastic modulus is determined from the formula:

$$E_r = S (\pi)^{1/2} / [2 \beta (A)^{0.5}]$$

where  $E_r$  is the reduced elastic modulus,  $S$  is the stiffness,  $\beta$  is a geometrical constant for the indenter (1.034 for the Berkovich indenter), and  $A$  is the projected contact area. Calculation of  $E_r$  results from elastic displacements in both the indenter and the specimen, as:

$$(1 / E_r) = [(1 - \nu^2) / E] + [(1 - \nu_1^2) / E_i]$$

where  $\nu$  is the Poisson's ratio of the specimen (0.46 for UHMWPE),  $E$  is the elastic modulus of the specimen,  $\nu_1$  is the Poisson's ratio of the indenter tip, and  $E_i$  is the elastic modulus of the indenter tip. For the Berkovich indents made of diamond,  $\nu_1 = 0.07$  and  $E_i = 1141$  GPa.

From the above equations, the modulus and hardness can be calculated as functions of contact depth to study variations in mechanical properties at the shallow depths achievable through nanoindentation. This allows measurement of mechanical properties and correlation to morphology variations on a scale that cannot be achieved through traditional mechanical testing in either tension or compression. In addition, nano-scale indents can be spaced across the surface of transverse specimens to examine variations in mechanical properties at larger depths below the surface.

### 4.3 POLYMER MORPHOLOGY MEASUREMENTS

The morphology of semicrystalline polymers is made up of crystalline lamellae surrounded by an amorphous phase of molecules in liquid-like conformations. Connecting these two phases is an interfacial zone of polymer chains in an intermediate structure, as shown in Figure 8.<sup>219</sup> Some of the chains in the interfacial zone bend around to reenter the adjacent lamella, but other chains cross this zone to enter the amorphous phase, perhaps later extending into another crystalline lamella.<sup>218</sup>

The interfacial zone has properties that are intermediate between those of the crystalline and amorphous phases, so it affects measurements of crystallinity that are based on a simpler two-phase model (which ignores the interfacial zone). Several different

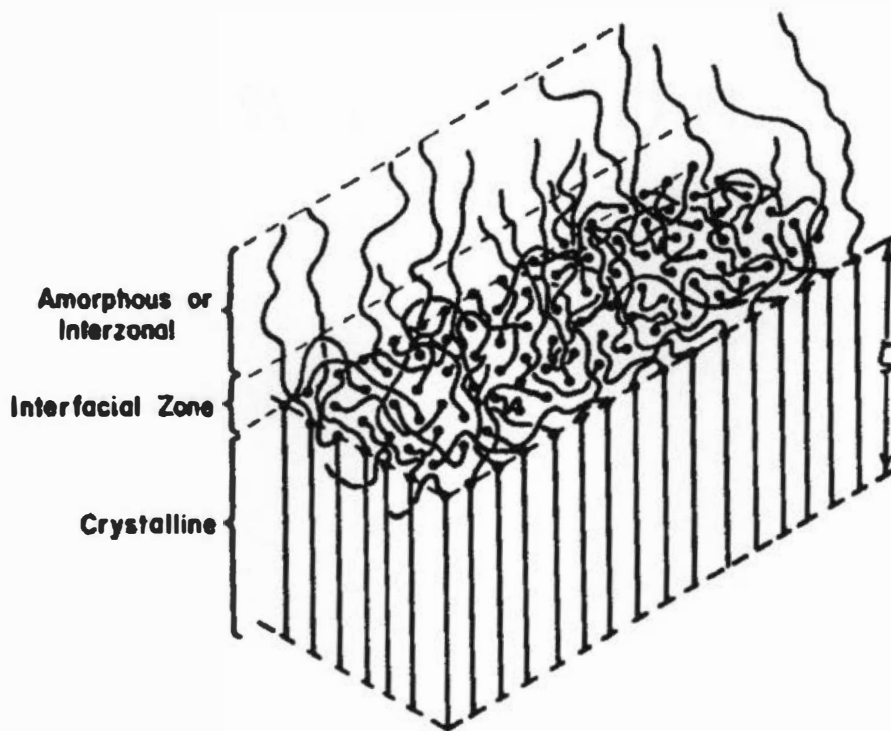


Figure 8. Schematic representation of polymer crystallite.<sup>219</sup>

experimental techniques are used to measure crystallinity, based on this two-phase model, and the effect of the interfacial zone on the measured properties is not the same between these techniques. Correct interpretation of the resulting data on crystallinity requires an understanding of these differences.

Parameters to measure the dimensions of polymer morphology are defined in Figure 9. These include the lamellar thickness,  $L_c$ , the amorphous thickness,  $L_a$ , the interface thickness,  $L_i$ , and the long period,  $L$ . The long period defines the repeat distance along the one-dimensional axis defined by the normal to the plane of the lamellae, and thus equals:

$$L = L_c + L_a + 2L_i$$

The long period ( $L$ ) can be measured from small angle X-ray scattering, and the lamellar thickness ( $L_c$ ) can be related to the peak melting temperature ( $T_m$ ) from differential scanning calorimetry through use of the Gibbs-Thomson equation:

$$T_m = T_m^\circ \left( 1 - \frac{2\sigma_e}{\Delta H_f L_c} \right)$$

where  $T_m^\circ$  is the theoretical melting temperature for an ideal crystal with infinite molecular weight,  $\sigma_e$  is the interfacial free energy,  $\Delta H_f$  is the heat of fusion of an ideal crystal, and  $L_c$  is the lamellar thickness. The lamellar thickness can also be estimated based on the crystallinity (by volume) ( $\omega_c$ ) and the long period:

$$L_c = \omega_c L$$

Crystallinity can be measured by small angle X-ray scattering, wide angle X-ray diffraction, infrared spectroscopy, differential scanning calorimetry, or density measurements. However, these methods do not all measure the same crystallinities when the effect of the interfacial zone on the two-phase crystallinity model is considered.

Small angle X-ray scattering assumes that the two-phase crystalline/amorphous layers fill the entire volume of the polymer, i.e. that there are no segregated regions of purely amorphous material separate from the stacks of lamellae. The long period is measured

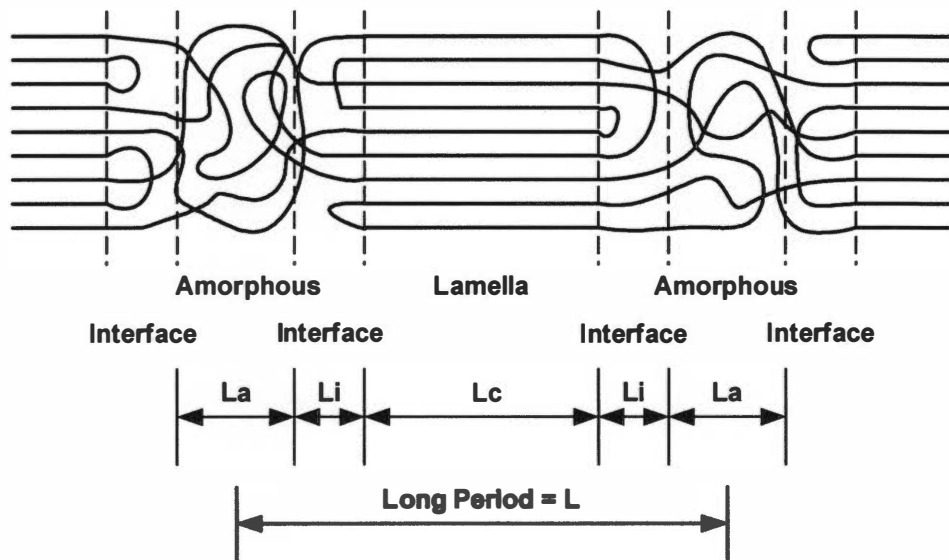


**Figure 9. Parameters for measurement of polymer morphology.**

directly as shown in Figure 9, but the lamellar thickness ( $l$ ) determined from the one-dimensional correlation function includes half of the thickness of the adjacent interfacial zones.<sup>220</sup>

$$l = L_c + \frac{2L_i}{2}$$

Thus the measured values of crystallinity (by volume) include the lamellar thickness plus half the interfacial zone:

$$\omega_c = \frac{L_c + L_i}{L}$$

Wide angle X-ray diffraction and infrared spectroscopy measurements have been normalized to match density measurements (with crystallinity,  $X_c$ , based on weight rather than volume), and these methods consider the crystallinity within the entire volume of the polymer. The interfacial zone is accounted for in the two-phase model (measuring volume crystallinity) by including it completely in the crystalline phase.<sup>219</sup>

$$\omega_c = \frac{L_c + 2L_i}{L}$$

Differential scanning calorimetry measurements of crystallinity are based on the relative heat of fusion of the crystalline lamellae, therefore the interfacial zone does not contribute to the measured crystallinity. Thus the volume crystallinity excludes the interface:

$$\omega_c = \frac{L_c}{L}$$

and the measured values of crystallinity can be significantly lower than those measured by other techniques.<sup>221</sup>

#### 4.4 SMALL ANGLE X-RAY SCATTERING

The small angle X-ray scattering (SAXS) camera records the intensity of X-rays scattered at very small angles, due to differences in electron densities within the specimen



being analyzed.<sup>222,223</sup> The scattering angle,  $\theta$ , is converted into the scattering vector,  $q$ , by the relationship:

$$q = \frac{4\pi}{\lambda} \sin\left(\frac{2\theta}{2}\right)$$

Variations in X-ray intensity as a function of scattering angle,  $I(q)$ , can be used to determine the spatial distribution of crystalline and amorphous phases in polymers such as polyethylene, due to their resulting electron density fluctuations between these phases. The long period,  $L$ , is defined as the sum of the crystalline lamellar thickness and the amorphous phase thickness, based on the 2-phase model.

Two different methods can be used to analyze SAXS intensity data to determine the average long period and the average lamellar thickness.<sup>224</sup> The simplest method applies the Lorentz correction to the corrected intensity data, and then uses the position of the peak in the curve to determine the long (or identity) period. The second method applies a Fourier transform to the intensity data,  $I(q)$ , producing its one-dimensional correlation function,  $K(R)$ . The shape of the correlation function can be used to determine the long period and the thickness of crystalline and amorphous phases, as well as to determine the presence of transition layers between these two phases.

The Lorentz correction used in the first method results from multiplying the scattered X-ray intensity,  $I(q)$ , by the square of the scattering vector,  $q^2$ . Thus a Lorentz plot results from plotting  $Iq^2$  versus  $q$ . For semicrystalline polymers, this plot will contain at least one peak, corresponding to the long period. The center of the first maximum ( $q_{\max}$ ) in the curve, measured along the  $q$  axis, corresponds to the long period,  $L$ . Using Bragg's Law, with  $n=1$ ,

$$n\lambda = 2d \sin \theta = 2L \sin \theta = \frac{Lq_{\max}\lambda}{2\pi}$$

the long period can be determined as:

$$L = \frac{2\pi}{q_{\max}}$$

This method assumes that lamellae are oriented parallel to each other, so that an independent measure of volume crystallinity can be multiplied by the long period to obtain the lamellar thickness. This assumption is approximately correct for most polymers of medium or high crystallinity, but may fail at lower crystallinity or with the presence of many chain defects.<sup>224</sup> The resulting long period is a weight average value, but the lamellar thickness is determined from a combination of weight average values for the long period and unspecified average values for the volume crystallinity.

The one-dimensional correlation function results from the Fourier transform of the Lorentz corrected scattering curve as:<sup>225</sup>

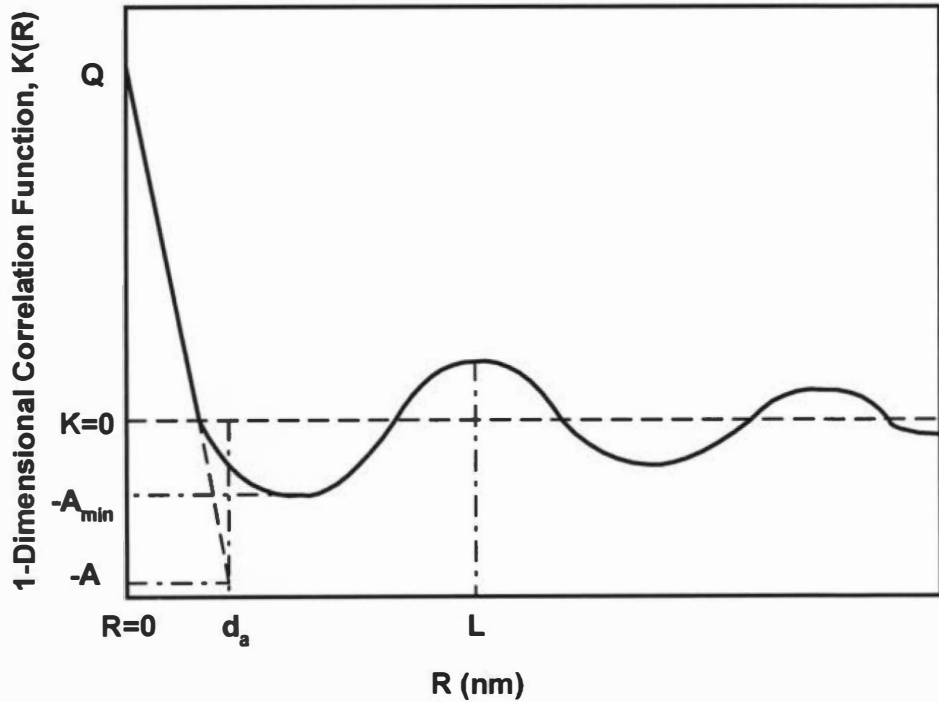
$$K(R) = \frac{1}{2\pi^2} \int_{q=0}^{\infty} I(q) \cdot q^2 \cos(qR) dq$$

A typical one-dimensional correlation function for a polymer with volume crystallinity between 50% and 70% is plotted in Figure 10A, with a diagram of the related electron density distribution shown in Figure 10B. The electron density for the crystalline phase is  $\eta_c$ , that for the amorphous phase is  $\eta_a$ , and the average is  $\langle \eta \rangle$ .

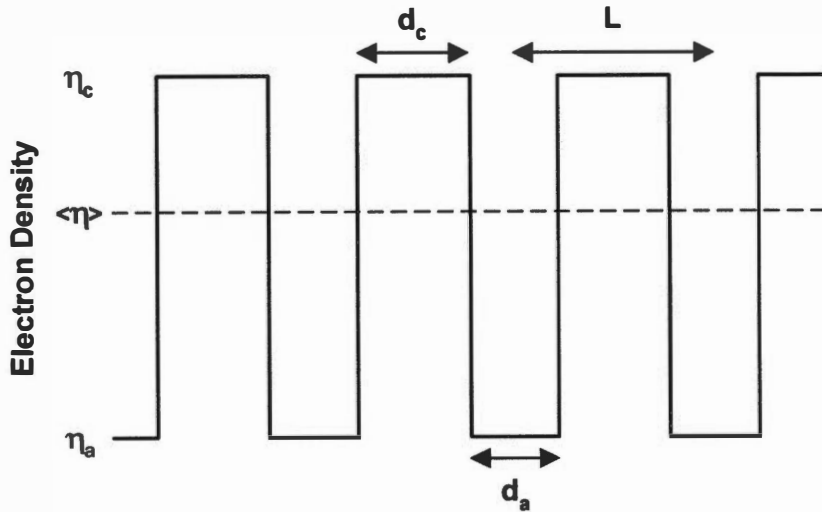
Analysis of the one-dimensional correlation function proceeds as follows. The intercept along the K axis, at  $R = 0$ , is shown as Q, which is known as the invariant. The value of Q can be used to determine the electron density difference,  $\eta_c - \eta_a$ , if the volume crystallinity,  $\omega_c$ , has been determined by another method (such as wide angle X-ray diffraction):

$$K(0) = Q = \omega_c (1 - \omega_c) (\eta_c - \eta_a)^2$$

The value of  $K(R)$  at the first minimum is related to the volume percent amorphous phase,  $\omega_a = 1 - \omega_c$ , when  $\omega_c$  is greater than 50% (or is related directly to the crystallinity if  $\omega_c$  is below 50%). When  $\omega_c$  is greater than about 70% the curve forms a flat segment at the first minimum, where  $K(R) = -A$ , and  $-A$  is related to the percent amorphous phase through the equation:



A.



B.

**Figure 10.** Typical one-dimensional correlation function for a polymer with a crystallinity of 50 to 70% by volume.

The correlation function,  $K(R)$ , is shown in (A), with the corresponding electron density distribution shown in (B).

$$K = -A = -(1 - \omega_c)^2 (\eta_c - \eta_a)^2$$

If  $\omega_c$  is above 50% but below about 70% then the first minimum does not form a flat segment in the curve and does not occur at the true value of  $-A$ . Instead  $K(R) = -A_{\min}$  provides a minimum limit to the volume percent amorphous phase (corresponding to a maximum limit to the crystallinity,  $\omega_{c,\max}$ ). In this case, the minimum volume percent amorphous phase,  $\omega_{a,\min}$ , can be determined as:

$$\omega_{a,\min} = \frac{\left( \frac{A_{\min}}{Q} \right)}{\left( 1 + \frac{A_{\min}}{Q} \right)}$$

and  $\omega_{c,\max}$  can be determined as  $1 - \omega_{a,\min}$ . The true baseline value,  $-A$ , must be determined from an independent measurement of the crystallinity and from the electron density difference determined from  $Q$ , the invariant. At low  $R$  values,  $K(R)$  follows a linear relationship with a negative slope. By extending this line to the intersection with the baseline at  $K(R) = -A$ , the average value of the amorphous phase thickness,  $R = d_a$ , can be determined. The value of  $R$  at the first maximum corresponds to the long period,  $L$ . The lamellar thickness,  $d_c$ , is determined as the difference between  $L$  and  $d_a$ , and the volume crystallinity is determined as the ratio of  $d_c$  to  $L$ . All above equations for analyzing the one-dimensional correlation function have assumed that the crystallinity is above 50%. If the crystallinity is below 50%, then the terms representing  $\omega_c$  and  $(1 - \omega_c)$  must be exchanged in these equations.

The volume crystallinity from SAXS is often higher than that from other methods, as it ignores amorphous material segregated outside the lamellar stacks and the values of  $d_c$  include half the thickness of any transition layers formed between the crystalline lamellae and the amorphous regions.<sup>224</sup> If such transition layers are present in the polymer, they will affect the one-dimensional correlation function in the low  $R$  region, as  $R$  decreases to zero. The linear section of  $K(R)$  will bend over as  $R$  approaches zero, so that the measured  $Q$  value will

be less than that obtained from linear extrapolation to  $R = 0$ . The  $R$ -range over which  $K(R)$  is non-linear (near  $R = 0$ ) is related to the thickness of the transition layer.

In planning a SAXS experiment, it is important to note the inverse relationship between the scattering vector,  $q$ , and values of  $R$  in the one-dimensional correlation function. Low values of  $R$  correspond to high  $q$  values, and high values of  $R$  relate to low  $q$  values. Thus accurate measurements of the long period,  $L$ , require SAXS measurements at low scattering vectors (which are ultimately limited by the beam stop), while accurate measurements of the linear region of  $K(R)$  near  $R = 0$  require measurements at high scattering vectors.

## 4.5 WIDE ANGLE X-RAY DIFFRACTION

The wide angle X-ray diffractometer measures the intensity of diffracted X-rays as a function of the angle  $2\theta$  between the directions of the transmitted X-ray beam and the diffracted beam. Diffraction results from the reinforcement of X-rays scattered by atoms positioned on a periodic structure in three-dimensional space, i.e. the crystalline lattice.<sup>226</sup>

In the case of highly crystalline polymers such as UHMWPE, most of the diffraction (occurring as distinct, but somewhat broad, peaks) results from the atoms within the crystalline lamellae. This diffraction obeys the Bragg Law:

$$n\lambda = 2d \cdot \sin \theta$$

where  $n$  is an integer called the order of reflection,  $\lambda$  is the wavelength of the X-rays,  $d$  is the interplanar spacing of the diffracting planes of atoms, and  $\theta$  is half of the angle  $2\theta$  described above. In polyethylene, most of the diffraction results from atoms in the 110 and 200 planes at  $2\theta$  values of  $21^\circ$  and  $24^\circ$  respectively. A second source of diffracted intensity results from atoms within the amorphous phase, creating a single, extremely broad peak superimposed on the background. The crystallinity can be determined from the ratio of the areas of these peaks, as:<sup>227,228</sup>

$$X_c = \left( \frac{I_{110} + I_{200}}{I_{110} + I_{200} + I_a} \right)$$

where  $I_{110}$  and  $I_{200}$  are the areas under the two crystalline peaks,  $I_a$  is the area under the broad amorphous peak, and  $X_c$  is the fraction crystallinity.

## 4.6 FTIR SPECTROSCOPY

The Fourier transform infrared spectrometer measures the intensity of transmitted infrared radiation ( $I$ ) as a function of wave number ( $\nu$ , inverse of wavelength). The ratio of the intensity of the incident radiation ( $I_0$ ) to that of the transmitted radiation is used to calculate the absorbance ( $A_\nu$ ) as a function of wave number:

$$A_\nu = \log\left(\frac{I_0}{I}\right)$$

Infrared radiation is absorbed by polymers when the molecular vibrations of the atoms produce a change in the electric dipole moment resulting from changes in the charge distribution. Thus, an oscillating dipole within the molecular structure is necessary for a vibration mode to be active by infrared spectroscopy.

Crystallinity is calculated from infrared absorbances using bands related to crystalline and amorphous phases in polymers. In polyethylene, the band at  $1894\text{ cm}^{-1}$  results from the crystalline phase, and the band at  $1303\text{ cm}^{-1}$  results from the amorphous phase.<sup>229, 230</sup> Using the Beer-Lambert law, the absorbance as a function of wave number can be calculated as:

$$A_\nu = \log\left(\frac{I_0}{I}\right) = \epsilon_i X_i \rho t$$

where  $I_0$  is the intensity of incident radiation,  $I$  is the intensity of transmitted radiation,  $\epsilon_i$  is the absorptivity (extinction coefficient) of the selected phase,  $X_i$  is the weight percent of the selected phase,  $\rho$  is the specimen density, and  $t$  is the specimen thickness. Thus, the weight percent crystallinity ( $X_c$ ) can be calculated as:

$$X_c = \frac{100\%}{\left[1 + \frac{(A_a / \epsilon_a)}{(A_c / \epsilon_c)}\right]}$$

where  $A_a$  is the measured absorbance of the amorphous phase at  $1303\text{ cm}^{-1}$ ,  $\epsilon_a$  equals  $26.535\text{ cm}^2/\text{g}$  for the amorphous phase,  $A_c$  is the measured absorbance of the crystalline phase at  $1894\text{ cm}^{-1}$ , and  $\epsilon_c$  equals  $6.2\text{ cm}^2/\text{g}$  for the crystalline phase.<sup>229</sup>

## 4.7 DIFFERENTIAL SCANNING CALORIMETRY

The differential scanning calorimeter measures the specific heat (input or released) required to vary the temperature of a specimen over a controlled range. It records heat flow as a function of temperature while the specimen is heated or cooled at a precisely controlled rate.<sup>230</sup> Specimen mass is precisely determined before the analysis, so that the heat of fusion or heat of crystallization can be calculated. Melting and crystallization temperatures are also determined.

Differential scanning calorimetry is an important technique for characterizing semicrystalline polymers such as polyethylene. Heats of fusion of polymers can be used to determine percent crystallinity (measuring the crystalline phase only, not including the interfacial region). The melting temperature varies with the thickness of lamellae, controlled for each polymer by the crystallization temperature at which the lamellae were formed. These parameters are affected by the thermal and/or mechanical history of a polymer.

Heat of fusion is determined by plotting the heat flow versus temperature, defining endpoints and a baseline for the melting peak, and integrating the area under the melting peak but above the baseline.<sup>231</sup> The baseline is defined by extrapolating the low-temperature heat flow data to form one background line, and by extrapolating the high-temperature heat flow data (for the polymer melt) to form a second background line. The points where the experimental heat flow curve deviates from these two background lines are used to define the endpoints of a linear baseline for the melting peak. The measured heat of fusion is then compared to an ideal value for a 100% crystalline polymer ( $289\text{ J/g}$  for polyethylene) to determine the weight percent crystallinity.

## 4.8 POLARIZED LIGHT MICROSCOPY

The polarized light microscope consists of two polarization filters (the polarizer and the analyzer) added to a conventional transmitted light microscope. The polarizer is placed between the light source and the condenser lens below the specimen, and the analyzer is placed between the objective lens and the eyepieces above the specimen. The polarizer and analyzer are oriented in the crossed position, so that no light passes through to the eyepieces when no specimen (or a non-birefringent specimen) is present. Sometimes a quarter wave plate is added between the analyzer and the eyepieces, so that the birefringence resulting from the specimen is shifted and displayed as vibrant colors.

Semicrystalline polymers that have a spherulitic morphology show a distinctive Maltese cross pattern under polarized light.<sup>230</sup> Other morphologies can be observed clearly in polarized light, but do not show this type of pattern. Orientations or internal tensions can also be observed in polymers, such as plastic deformation from machining.



## 5. OBJECTIVES AND HYPOTHESES

### 5.1 OBJECTIVES

The objective of this research was to identify differences between the bearing surfaces of UHMWPE tibial components fabricated by machining and those fabricated by direct molding, in both the unsterilized and sterilized (by gamma irradiation) conditions. Specific surface properties compared include surface texture, micromechanical behavior, crystallinity, and morphology. Tibial components (from Total Knee Replacements) were selected instead of acetabular components (from Total Hip Replacements) because commercial products were available that were fabricated from the same resin (Himont 1900H) using both direct molding and machining fabrication methods. Tibial components also have a relatively flat bearing surface geometry that is better suited to measurement of surface texture and micromechanical behavior. Specific objectives for comparison included:

1. To quantify the surface texture (at the micron scale) of the top bearing surface of unsterilized tibial bearings in three dimensions using confocal microscopy and image analysis techniques to measure tribological parameters including roughness average ( $R_a$ ), RMS roughness ( $R_q$ ), and skewness ( $R_{sk}$ ).
2. To examine the load-displacement behavior at the top bearing surface and to measure variations in hardness and elastic modulus with depth from the top bearing surface using nanoindentation. Both types of tibial bearings were examined in both the unsterilized condition and in the sterilized and shelf aged (in air) condition.
3. To measure long period, lamellar thickness, and amorphous phase thickness using small angle X-ray scattering, and to calculate crystallinity from these values. Both types of tibial bearings were examined in both the unsterilized condition and in the sterilized and shelf aged condition. Each bearing type was analyzed on the top bearing surface, in the bulk, and on the bottom bearing surface.

4. To measure crystallinity variations with wide angle X-ray diffraction in the specimens previously analyzed using small angle X-ray scattering.
5. To measure crystallinity variations with depth from the top and bottom bearing surfaces of unsterilized tibial bearings using Fourier transform infrared spectroscopy and differential scanning calorimetry.
6. To measure variations in melting temperature between the bulk and the top and bottom bearing surfaces of tibial bearings using differential scanning calorimetry, and to relate this to lamellar thicknesses.

## 5.2 HYPOTHESES

Based on review of the literature related to medical implants, polymer technology, machining, and tribology and wear, and on initial experimental results, the following hypotheses were made:

1. Surface texture parameters measured on bearing surfaces that are machined versus those that are direct molded would be significantly different, on a statistical basis. These parameters will include roughness average ( $R_a$ ), RMS roughness ( $R_q$ ), and skewness ( $R_{sk}$ ). Direct molded components would have lower values of  $R_a$  and  $R_q$  than machined components.
2. Polymer morphology in the near-surface regions would be different between machined and direct molded UHMWPE components. Machined components would have an outer layer of plastic deformation resulting from the machining process. This layer would not be present on direct molded components. However, molded components might experience a faster cooling rate at the surface during processing, which would affect its surface morphology relative to that in the bulk.
3. Polymer morphology in the bulk could be different between machined and direct molded UHMWPE components, as they were consolidated from resin using different processing methods. Thus, their thermal histories could be different, producing

different lamellar thicknesses or crystallinities that would result in different micromechanical properties.

4. Load-displacement behavior from nanoindentation would be different between machined and direct molded surfaces. The roughness of the surfaces (based on measurements of  $R_a$  and  $R_q$ ) would affect the consistency of the load-displacement curves for each group of nanoindents. Because direct molded surfaces were expected to have lower roughness values (from #1 above), they would also be expected to have more consistent load-displacement curves.
5. Nanoindentation measurements of elastic modulus and hardness would show small differences between machined and direct molded surfaces. The plastically deformed surface layer on machined surfaces would be expected to increase the elastic modulus and hardness relative to that within the bulk. Differences in thermal histories between these two types of implants (from #3 above) would create differences in lamellar thicknesses and/or crystallinities. Higher values of elastic modulus and hardness would result from either higher lamellar thicknesses or higher crystallinities or increases in orientation within the amorphous phase.
6. Nanoindentation measurements of elastic modulus and hardness would vary slightly with depth in both machined and direct molded surfaces, and this variation should be related to observed differences in morphology with depth from the surface.

## **6. EXPERIMENTAL PROCEDURES**

### **6.1 TIBIAL COMPONENTS AND OTHER SPECIMENS**

A controlled set of UHMWPE tibial bearing components was used for this study. The first group of bearings was fabricated by machining from isostatic compression molded rods of ArCom® UHMWPE (proprietary product of Biomet), and the second group of bearings was fabricated by direct molding of UHMWPE resin. The same resin powder (Himont 1900H, without calcium stearate) was used as the raw material for both groups of bearings. This allowed direct comparison of the morphology of the two different fabrication methods, independent of differences in starting resin. The particle size distribution for this resin is shown in Table 5. Within each group of bearings, some components were left unsterilized and others were gamma irradiated in air to a total dose of 3.3 Mrad (rate of 1.32 Mrad/hour for 2.5 hours), then shelf aged for approximately 2 years. Additional specimens of UHMWPE included Himont 1900H resin powder, a rod of ArCom® UHMWPE, and a direct molded blank with two machined grooves across the top surface. All UHMWPE materials were generously provided by Joel Higgins at Biomet, Inc. Irradiation was performed at Southwest Research Institute on May 27, 1998 (project number #06-8276-005).

### **6.2 CONFOCAL MICROSCOPY**

The confocal tandem-scanning optical microscope was used to visualize and quantify the 3-dimensional surface textures of the top bearing surfaces of machined versus direct molded UHMWPE tibial bearings (unsterile). All confocal experiments were conducted on the Tracor Northern TSM-1 confocal tandem-scanning microscope at the University of Tennessee, using reflected light with a 200 watt mercury vapor arc lamp.

**Table 5. Particle size distribution for Himont 1900H UHMWPE resin.<sup>232</sup>**

<b>Particle Size Range</b>	<b>Percentage of Particles</b>
20 mesh (> 841 microns)	< 0.5 %
40 mesh (420 – 841 microns)	< 3.0 %
60 mesh (250 – 420 microns)	< 15.0 %
80 mesh (177 – 250 microns)	60.0 % ± 30.0 %
100 mesh (149 – 177 microns)	15.0 % ± 19 %
200 mesh (74 – 149 microns)	13.0 % ± 9 %
Fines (< 74 microns)	< 0.4 %

### **6.2.1 Specimen preparation**

The UHMWPE tibial bearings were in the as-received condition – no special specimen preparation techniques (coatings, etc.) were required. After confocal analysis, some of these bearings were later cut into specimens for other experiments.

### **6.2.2 Measurement of surface texture**

Surface texture was characterized at two different magnifications: 100X (N.A. = 0.25) and 200X (N.A. = 0.4). At each magnification, a series of digital images (optical sections) were collected while moving the specimen stage (at 100X) or the objective lens (at 200X) vertically in specific Z-increments through the range of focus (from focused below the surface to focused above the surface). Each optical section was stored as a digital image of 640 x 480 pixels. At 100X the Z-increments were 4.0  $\mu\text{m}$ , and at 200X the Z-increments were 1.5  $\mu\text{m}$ , due to the focal depths of the objective lenses along the vertical axis. The total range of focus (along the Z axis) was about 100  $\mu\text{m}$  at 100X and about 50  $\mu\text{m}$  at 200X. The lateral pixel resolutions of the resulting digital images were 2.6  $\mu\text{m}/\text{pixel}$  at 100X and 1.3  $\mu\text{m}/\text{pixel}$  at 200X.

Each stack of optical sections was then processed using image analysis techniques to create the Maximum Intensity image and the Depth Map image. The Maximum Intensity image is a perfectly focused picture of the specimen surface. The Depth Map image is a topographic map of the specimen surface, where pixel intensity values are proportional to height. The Depth Map image file was then converted into a text file containing actual height values, rather than image intensities. This text file was used to calculate the surface texture parameters.

Roughness average ( $R_a$ ), RMS roughness ( $R_q$ ), and skewness ( $R_{sk}$ ) were calculated along both horizontal (X) and vertical (Y) directions in each Depth Map text file. A surface area with approximately planar topography was selected for these calculations, so that linear extrapolation along the X and Y axes could be used to determine the baseline for calculating the residuals. Each parameter was calculated for each row or column of height values, and

then statistical values of mean and standard deviation were calculated over all the rows or columns. These calculations provided statistical results for comparison of surface texture between machined and molded implant surfaces.

A text file of residual values was calculated from applying linear extrapolation to a planar region from each Depth Map text file. This data was analyzed to examine the variation of true contact area with contact depth, assuming a planar contact surface.

## **6.3 NANOINDENTATION**

Nanoindentation was used to compare the micromechanical behavior of machined versus direct molded surfaces of tibial bearings, and also to compare differences between unsterile and gamma irradiated and aged components fabricated by the same methods. The tests were conducted directly on the as-fabricated top surfaces of the tibial bearings. Nanoindents were made directly on these bearing surfaces, to evaluate the load-displacement behavior of micro contacts and also to measure the hardness and elastic modulus variations at shallow contact depths. All nanoindentation experiments were run on the Nanoindenter XP at the Oak Ridge National Laboratory (supported by the ShARE Program).

### **6.3.1 Specimen preparation**

Specimens were prepared by cutting small blocks from each tibial bearing, with the original bearing surface on the top. These blocks were cut from one of the regions where confocal measurements had previously been made. The original surface was preserved and protected, and nanoindents were made directly on this surface. The bottom of each block was cut so that the original top surface lay as flat as possible (since the bearing surface was slightly curved) and parallel to the bottom. The block thickness was 3 mm or more. Each block was secured with epoxy to a metal stub for mounting in the nanoindenter.

### 6.3.2 Calibration of contact area versus depth

The primary calibration of the contact area function for the Berkovich indenter tip in the Nanoindenter XP was based on indentation data from a fused quartz specimen. Two different types of indents were made, both operating under load control, in continuous stiffness mode. The small indents were loaded under a  $(1/P)(dP/dt)$  rate of  $0.025 \text{ sec}^{-1}$  to a maximum load of 350 mN, and the large indents were loaded under a  $(1/P)(dP/dt)$  rate of  $0.050 \text{ sec}^{-1}$  to a maximum load of 625 mN. Data was collected for load (P), displacement (d), and stiffness (S) versus time (t) during loading. The small indents reached contact depths of 1200-1300 nm, and the large indents reached contact depths of 1800-1900 nm.

Calibration of the contact area function coefficients, the DC load frame stiffness, and the AC load frame stiffness was based on values of 0.17 for the Poisson's ratio and 72.00 GPa for the elastic modulus of fused quartz. The following values were obtained from this calibration:

$$\text{DC Load Frame Stiffness} = 8.88146 \times 10^6 \text{ N/m}$$

$$\text{AC Load Frame Stiffness} = 8.88146 \times 10^6 \text{ N/m}$$

Area Function Coefficients:

$$C_1 = 25.1552 \text{ nm}^{-2}, C_2 = 2085.81 \text{ nm}^{-1}, C_3 = -17868.5 \text{ nm}^{-0.5},$$

$$C_4 = 61739.4 \text{ nm}^{-0.25}, C_5 = -43401.1 \text{ nm}^{-0.125}$$

This calibration covered the contact depth range from 300 nm to 1900 nm, but was not sufficient for the deeper indents that would result from similar maximum loads on UHMWPE (because of its much lower elastic modulus).

The secondary calibration of the contact area function for this Berkovich indenter tip was performed using confocal microscopy, using similar techniques to those described in Section 6.2. Optical sections were collected at magnifications of 600X (N.A.=0.70) and 1000X (N.A.=0.80) using objective lenses with long working distances (to avoid damaging the lenses with the diamond tip). At 600X the optical sections were collected in Z-increments of 1.0  $\mu\text{m}$  over a vertical range of 40.0  $\mu\text{m}$ , and at 1000X the optical sections were collected in



Z-increments of 0.5  $\mu\text{m}$  over vertical ranges up to 26.0  $\mu\text{m}$ . (Multiple datasets were analyzed at 1000X.) The lateral pixel resolutions of the resulting digital images were 0.46  $\mu\text{m}$  at 600X and 0.28  $\mu\text{m}$  at 1000X.

Depth Maps were processed from each stack of optical sections. Digital image analysis was used to measure the contact area at each Z-increment that intersected the surface of the Berkovich indenter tip. The measured areas of the optical sections within 2.0  $\mu\text{m}$  of the end of the tip were compared to values calculated using the area function coefficients ( $C_1$  to  $C_5$ , listed above), to determine more precisely the absolute position of the end (i.e. the true  $Z=0$  reference) of the indenter tip. The relative Z positions of the optical sections were corrected to the true  $Z=0$  reference, then the area function was used to calculate their ideal contact areas from the corrected Z values.

The measured contact areas were compared to the ideal contact areas, and were found to differ by 6% or less for contact depths up to a maximum of 35  $\mu\text{m}$ . This allowed use of the area function coefficients to calculate projected contact areas (A) from contact depths ( $h_c$ ) up to 35  $\mu\text{m}$ .

### **6.3.3 Measurement of micromechanical properties**

Multiple nanoindentations were made in the original top surface of each tibial bearing. The Nanoindenter XP was operated under load (P) control, in continuous stiffness mode (45 Hz, 2 nm amplitude), while controlling the  $(1/P)(dP/dt)$  rate at  $0.003 \text{ sec}^{-1}$  up to a maximum load of 625 mN. The maximum load was held for 5 minutes, then unloaded at 300  $\mu\text{N}/\text{sec}$  down to 10% of the maximum load, held for 5 minutes, and unloaded completely.

The Nanoindenter XP was set up to space the indents at least 500  $\mu\text{m}$  apart on each bearing, with positions selected on flat areas of surface topography. The indents were later examined with optical microscopy to confirm the minimum spacing between indents. Only one pair of successful indents fell below this minimum spacing (455  $\mu\text{m}$ ), and most indents were spaced at least 600  $\mu\text{m}$  apart. For an indent reaching a contact depth of 22  $\mu\text{m}$ , the side

length of the triangular indent area would be 165  $\mu\text{m}$ . Spacing the indents apart by three times this side length would require distances of 495  $\mu\text{m}$ .

Data was collected for load ( $P$ ), displacement ( $h$ ), and stiffness ( $S$ ) versus time ( $t$ ). Values calculated from this data included contact depth ( $h_c$ ), contact area ( $A$ ), hardness ( $H$ ), and elastic modulus ( $E$ ). Load was plotted versus time to confirm that all indents followed the programmed loading cycle. Indents that did not follow this loading cycle were removed from further analysis. After indents were made, each indent was examined with an optical microscope (attached to the Nanoindenter XP) to evaluate its condition. This identified some indents that were incomplete (i.e. shallow) or contained surface debris or other defects, so that these indents were removed from further analysis.

Results were plotted as load versus displacement, to compare micromechanical interactions at micro scale contacts on each bearing surface. These plots showed whether micro scale contacts were uniform or variable across the surface of a single bearing type. Differences in surface texture were expected to affect these micromechanical interactions. Results were related to surface texture parameters measured by confocal microscopy.

Results were also plotted as hardness and elastic modulus versus contact depth. These plots showed whether mechanical properties were constant or variable with depth at the top surface of each bearing. Variations in properties were expected to relate to variations in polymer morphology. These nanoindents were made directly into the bearing surface, so the contact depth range was limited by the geometry of the Berkovich indenter and the maximum load applied.

## **6.4 SMALL ANGLE X-RAY SCATTERING**

Small angle X-ray scattering was used to measure the long period, or combined thickness of crystalline lamellae and amorphous regions, based on the ideal two-phase model for semi-crystalline polymers. Analysis was performed on all four types of tibial bearings: machined, unsterilized; machined, sterilized; direct molded, unsterilized; and direct molded,

unsterilized. For each bearing type, three samples were analyzed to compare the top bearing surface, the bulk, and the bottom bearing surface. All SAXS experiments were conducted using the 10-m SAXS camera within the Solid State Division at the Oak Ridge National Laboratory under the guidance of Dr. J.-S. Lin.

#### **6.4.1 Specimen preparation**

Specimens were prepared by cutting square blocks (about 1 cm x 1 cm) from each tibial bearing, adjacent to the blocks cut for nanoindentation and within the area of the loading zone. Then slices (about 1 mm thick) were removed from the top bearing surface, the bottom bearing surface, and the bulk (using a razor blade and a hammer). These slices were not prepared by machining, to avoid thermal effects from machining that might affect the long period measurement.

#### **6.4.2 Measurement of long period and lamellar thickness**

The 10-m SAXS instrument<sup>233,234</sup> consisted of an X-ray source, a monochromator, a collimator, a specimen chamber, a two-dimensional position-sensitive detector, and a digital computer. The Rigaku-Denki X-ray generator used a rotating anode to produce monochromatic Cu K $\alpha$  radiation (using a pyrolytic graphite monochromator for  $\lambda = 1.54 \text{ \AA}$ ). It was operated at an accelerating voltage of 40 kV and a current of 60 – 100 mA. Specimens were mounted on a rotating stage for automated data acquisition. All specimens were analyzed at room temperature. Data was collected for 5400 seconds (1.5 hr) per sample.

The sample to detector distance (SDD) was 5.119 m for the low scattering vector range ( $q = 0.0479 - 0.9812 \text{ nm}^{-1}$ ) and was 1.119 m for the high scattering vector range ( $q = 0.2077 - 4.6305 \text{ nm}^{-1}$ ). Scattered X-rays were detected on a 20x20 cm<sup>2</sup> two-dimensional position-sensitive area detector with a virtual cell (element) spacing of about 3 mm. Corrections were made for instrumental backgrounds, dark current due to cosmic radiation and electronic noises in the detector circuitry, and the detector non-uniformity and efficiency (via an Fe<sup>55</sup> radioactive isotope standard which emitted x-rays isotropically by electron

capture) on a cell-by-cell basis. The data were radially averaged and converted to an absolute differential scattering cross section by means of pre-calibrated secondary standards.<sup>235</sup> The absolute scattering intensity is in  $\text{cm}^{-1}$  units.

Each specimen was analyzed over both scattering vector ranges, measuring intensity ( $I$ ) as a function of scattering vector ( $q$ ), and then a factor was applied to all the high range intensity data to match it to the low range data trend for  $I$  vs.  $q$ . The final dataset was created by combining the low angle intensity data for  $q = 0.0479 - 0.7586 \text{ nm}^{-1}$  with the adjusted high angle intensity data for  $q = 0.7589 - 4.018 \text{ nm}^{-1}$ . This dataset was then evaluated using Lorenz plots and the one-dimensional correlation function to determine the long period and the lamellar thickness.

## **6.5 WIDE ANGLE X-RAY DIFFRACTION**

Wide angle X-ray diffraction was used to measure the crystallinity of all four types of tibial bearings, using the 12 specimens analyzed with small angle X-ray scattering. Analysis was performed on all four types of tibial bearings: machined, unsterilized; machined, sterilized; direct molded, unsterilized; and direct molded, unsterilized. For each bearing type, three samples were analyzed to compare the top bearing surface, the bulk, and the bottom bearing surface. All experiments were conducted using the Rigaku WAXD diffractometer at the University of Tennessee.

### **6.5.1 Specimen preparation**

The same specimens were used as for small angle X-ray scattering. Refer to section 6.4.1 for specimen preparation procedures. Wide angle X-ray diffraction was performed on these specimens following the initial small angle X-ray scattering measurements.

### **6.5.2 Measurement of crystallinity**

The Rigaku diffractometer was operated with a copper  $K\alpha$  X-ray source at 37 kV, 30 mA. The diffraction spectra were collected continuously in reflected mode over the 2 $\theta$

range from 10.0° to 40.0° with a step size of 0.02° and a dwell time of 0.5 sec. The collected spectra were processed to remove the background, then to separate the amorphous halo from the remaining crystalline peaks. Crystallinity was determined from the ratio of the crystalline peak areas to the crystalline plus amorphous peak areas.

## **6.6 FTIR SPECTROSCOPY**

Fourier transform infrared (FTIR) spectroscopy was used to measure the crystallinity of three types of tibial bearings: machined, unsterilized; direct molded, unsterilized; and direct molded, sterilized. For each bearing type, two series of samples were analyzed versus depth from the top and the bottom bearing surfaces, respectively. All experiments were conducted using the Biorad FTS-6000e FTIR spectrometer at the University of Tennessee.

### **6.6.1 Specimen preparation**

Specimen blocks were cut from the load-bearing regions of the UHMWPE implants, 1.5-2.0 cm from the specimen blocks for confocal and nanoindentation analysis, and adjacent to the specimens for small angle X-ray scattering. The differential scanning calorimetry (DSC) measurements were made on a subset of the specimens analyzed with FTIR spectroscopy, following the FTIR measurements. All thin sections prepared from unsterilized tibial bearings were initially analyzed using FTIR, and then 3 specimens (from the top bearing surface, the bottom bearing surface, and the bulk) were analyzed with DSC.

Specimens were prepared as thin sections, so that each specimen represented a small depth range from the original bearing surface. A microtome with a steel knife was used to cut these thin sections from a small UHMWPE block removed from each tibial bearing. Each block was oriented so that the initial block face was located at the original tibial bearing surface (top or bottom). Thus the first slice from the block was the layer at the bearing surface. A series of specimens was first cut from the bottom bearing surface, then the block was reversed to cut a second series of specimens from the top bearing surface.

Serial slices were cut and collected, so that crystallinity versus depth from the surface could be measured using both FTIR and differential scanning calorimetry. Thin sections were cut as thin as possible, nominally 100-200  $\mu\text{m}$  thick. Circular specimens were removed from each thin section using a leather punch. The thickness of each serial section was measured with a micrometer prior to FTIR and DSC analyses.

### **6.6.2 Measurement of crystallinity**

The BioRad FTS-6000e spectrometer was operated in transmission mode to measure intensities over the wave number range from 400 to 4000  $\text{cm}^{-1}$  at a resolution of 4  $\text{cm}^{-1}$ , collecting 32 scans per spectrum. The spectra were processed to calculate absorbances from the transmitted intensities, then the absorbances for the crystalline peak (1894  $\text{cm}^{-1}$ ) and the amorphous peak (1303  $\text{cm}^{-1}$ ) were used to calculate the crystallinity for each specimen.

## **6.7 DIFFERENTIAL SCANNING CALORIMETRY**

Differential scanning calorimetry (DSC) was used to measure crystallinity (based on heat of fusion) and melting temperature variations between the top and bottom surfaces and the bulk of tibial bearings. Results were compared for a machined, unsterilized bearing (018A), a direct molded, unsterilized bearing (016A), and a direct molded, sterilized bearing (020A). It was not possible to analyze the machined, sterilized specimen (019A) due to the malfunction of the calorimeter.

### **6.7.1 Specimen preparation**

A subset of the specimens prepared for FTIR spectroscopy was analyzed with DSC. Refer to section 6.6.1 for specimen preparation procedures. FTIR spectrometry was performed on these specimens prior to differential scanning calorimetry. Sections selected for DSC analysis were carefully weighed and then individually sealed in aluminum specimen pans.

## **6.7.2 Measurement of thermal properties**

Calorimetry measurements were performed on a Perkin-Elmer DSC7 Differential Scanning Calorimeter attached to a cooling accessory. All measurements were made under a nitrogen purge for an inert atmosphere. Temperature was recorded with a resolution of 0.1°C, and heat flow was recorded with a resolution of 0.001 mW. Calibration was performed using an indium standard with an onset melting temperature of 156.6°C and a heat of fusion of 28.45 J/g. Calibration was verified by heating at 10°C/min to prove that the melting temperature was within ±0.1°C and the heat of fusion was within ±0.05 J/g for indium.

The crystallinity of interest was that present in the initial UHMWPE specimen, resulting from its processing and fabrication. Thus the DSC data was examined from the initial heating curve. Each specimen was initially cooled to -20°C and then heated at 10°C/min up to 180°C to record the thermal cycle for melting. Melting temperature and heat of fusion were determined. The percent crystallinity ( $X_c$ ) was calculated from the measured heat of fusion, based on the assumption that the heat of fusion is 289 J/g for a 100% crystalline specimen of polyethylene.

## **6.8 POLARIZED LIGHT MICROSCOPY**

Polarized light microscopy was used to examine variations in polymer morphology versus depth in thin section specimens from both machined and direct molded tibial bearings. Thin section specimens were oriented transverse to the top surface of tibial bearings, with the original surface along one edge. Thin sections were prepared from tibial components fabricated by either machining or direct molding, in the unsterilized condition. Differences in morphology with depth from the top surface were examined for each of the two specimen types.

### **6.8.1 Specimen preparation**

Thin sections for polarized light microscopy were prepared by cryomicrotoming small blocks cut from each tibial component. Blocks of suitable size and shape were cut using a

band saw. These blocks were oriented so that one edge (3-4 mm wide) contained the top surface of the tibial bearing, and the microtomed slices produced a transverse section (3-4 mm wide by 4-5 mm tall) through the partial thickness of the bearing. Each block was mounted in an ultramicrotome, positioned so that the original top surface of the bearing was the first edge to be contacted by the glass knife. The ultramicrotome chamber was cooled with liquid nitrogen to drop the temperature of the UHMWPE below its glass transition temperature. The block temperature was controlled at  $-120$  to  $-130^{\circ}\text{C}$ , and the glass knife temperature was controlled at  $-135$  to  $-140^{\circ}\text{C}$ . Due to plastic deformation on the block face (from the band saw), a minimum thickness of 0.5 mm was removed (as thick sections) from the face before any thin sections were kept for polarized light microscopy. Then sections were cut as thin as possible, nominally 10-30  $\mu\text{m}$  in thickness.

### **6.8.2 Examination of morphology**

Polarized light microscopy was used to examine the morphology of each thin section specimen, and how the morphology varied with depth from the original bearing surface. Features of specific interest were examined at the scale typical of wear debris, which extends into the submicron range, although light microscopy is limited to a lateral resolution of about 0.4  $\mu\text{m}$ . Thin sections were examined in transmitted light on a microscope with crossed polarizers. Photomicrographs were recorded either on film or digitally. A low magnification (200X) was used to examine large-scale variations in morphology with depth from the bearing surface, which related to processing and fabrication differences. Then higher magnifications (400X and 1000X) were used to examine small-scale birefringent structures in more detail. Calibration of the photomicrograph scale was performed by recording an image of a calibration slide, so that quantitative measurements were possible.



## 7. RESULTS

### 7.1 CONFOCAL MICROSCOPY

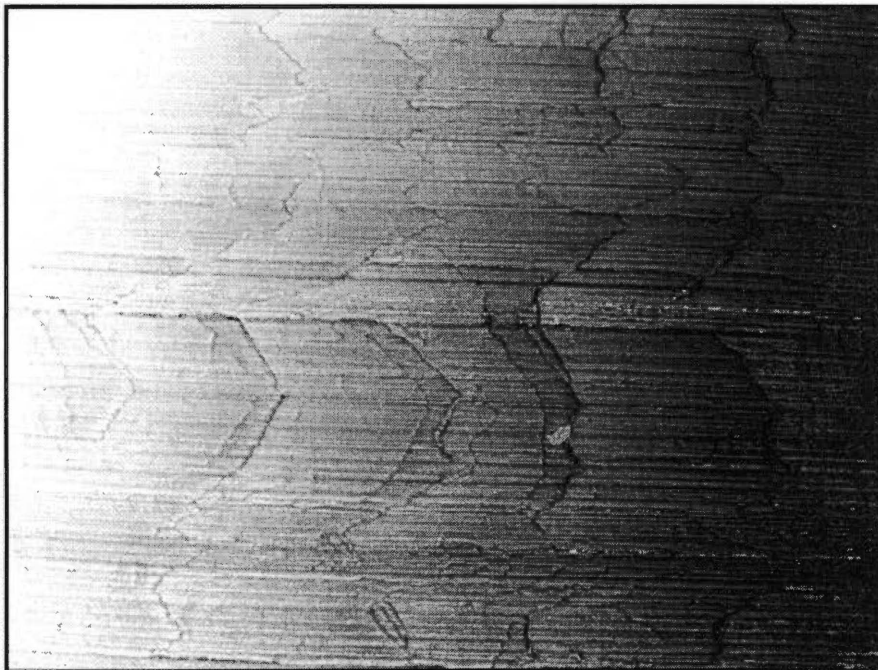
Surface texture was analyzed using confocal microscopy on four machined right tibial bearings (specimens 018A, 018B, 018C, and 018D) and on four direct molded right tibial bearings (specimens 016A, 016B, 016C, and 016D). All bearings were examined on the top surfaces, in approximately planar regions near the center of the loading zone for the implants. Surface texture was initially examined at 100X (specimens 018A and 016A). This analysis was repeated at 200X (to obtain better resolution in the Z-direction) on both sides (medial and lateral) of these first tibial bearings. Then the analysis at 200X was repeated on three additional bearings of each type (018B, 018C, 018D, 016B, 016C, and 016D) on one side (lateral).

Magnifications of 100X and 200X were selected because of the coarse surface texture of the machined tibial bearings, which extended over large lateral distances (150 - 350  $\mu\text{m}$ ). This texture was in contrast to the smooth surfaces of the direct molded tibial bearings. Sampling of representative surface areas on the machined bearings required using low magnifications and thus limiting sensitivity of vertical or Z measurements (due to low values of numerical aperture of the objective lenses). Image acquisition, processing, and analysis parameters were carefully controlled so that quantitative results could be compared directly between machined and direct molded tibial bearings.

Confocal images showing typical surface texture are shown in the following figures. In each figure, the Maximum Intensity Image shows a clearly focused photomicrograph of the surface, and the Depth Map shows a topographic map (displayed in grayscale) representing the elevation of surface features. Dark pixels represent low points and bright pixels represent high points on the surface, covering the range of heights recorded as optical sections. Figure 11 shows the top surface of a machined tibial bearing at 100X.



A. Maximum Intensity Image (100X, scale bar = 200  $\mu\text{m}$ ).



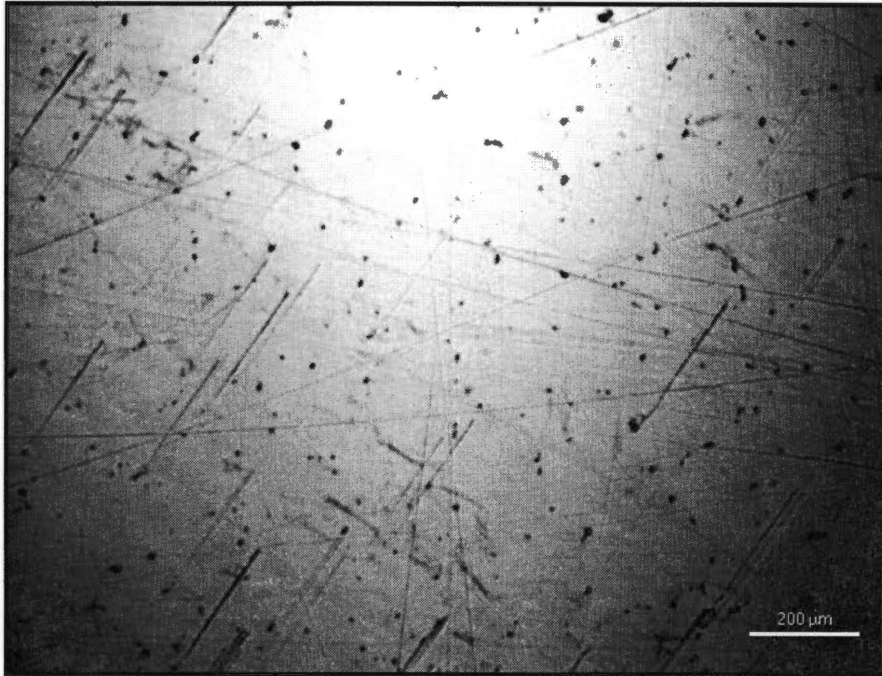
B. Depth Map Image (100X).

**Figure 11. Confocal images of a machined tibial bearing surface. Optical sections were acquired in Z-increments of 4  $\mu\text{m}$  over a vertical range of 100  $\mu\text{m}$ .**

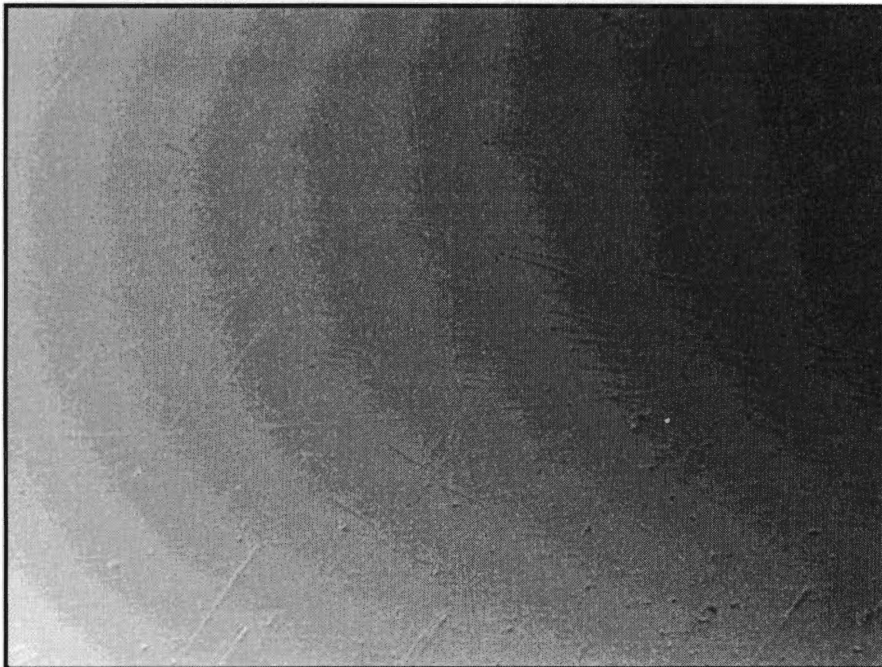
Figure 12 shows the top surface of a direct molded tibial bearing at 100X. Figure 13 shows the top surface of the machined tibial bearing at 200X. Figure 14 shows the top surface of the direct molded tibial bearing at 200X.

Quantitative surface texture parameters were determined from analysis of the data recorded in the Depth Maps, and are listed in Table 6. Surface texture parameters included the Roughness Average ( $R_a$ ), the Root Mean Square Roughness ( $R_q$ ), and the Skewness ( $R_{sk}$ ). Parameters were calculated based on linear extrapolation of the topographic data along both the X-direction (horizontal) and the Y-direction (vertical) in the Depth Maps. Parameters were calculated for each row or column of data in the Depth Map, and then averaged over all rows or columns so that both a mean and a standard deviation were reported for each data file. (The number of rows or columns analyzed is reported as N in the table.) Then results were averaged over all specimen areas (5) measured at 200X so that statistical comparisons could be made between machined versus direct molded tibial bearings.

Depth Maps in Figure 11B and Figure 13B showed that the machined surface was rough and irregular. Machining left an oriented topography on the surface along the machining direction, with fine machining lines (from defects in the cutting tool) oriented parallel to the X-direction (horizontal) of the micrographs. There were also features on the surface that were oriented generally normal to the machining lines (i.e. along the Y-direction). These features had an irregular, scalloped boundary, with the scallops extending over large lateral distances, and they were spaced 200-350  $\mu\text{m}$  apart (along the Y-direction) with a relatively smooth region in between. The scalloped edges indicated plastic deformation of the polymer as it was machined. These features were associated with localized plastic deformation of the polyethylene as it was cut (or torn) by the cutting tool. The lateral spacing of these features indicated that they were associated with the initial resin particles from which the machined bearing was fabricated, as the lateral dimensions were comparable to the particle size distribution with the resin (see Table 5, p. 101).

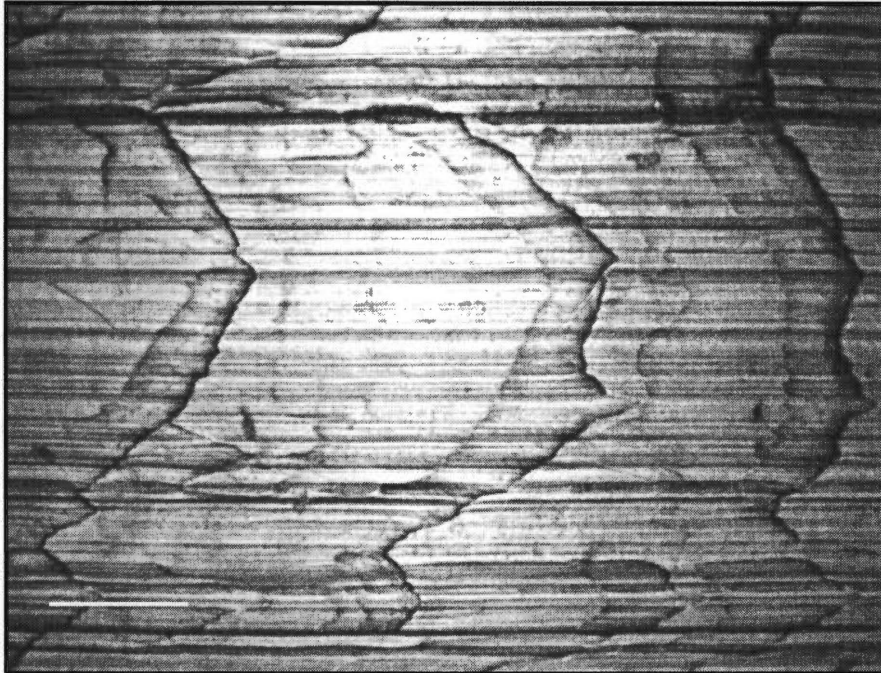


A. Maximum Intensity Image (100X, scale bar = 200 μm).

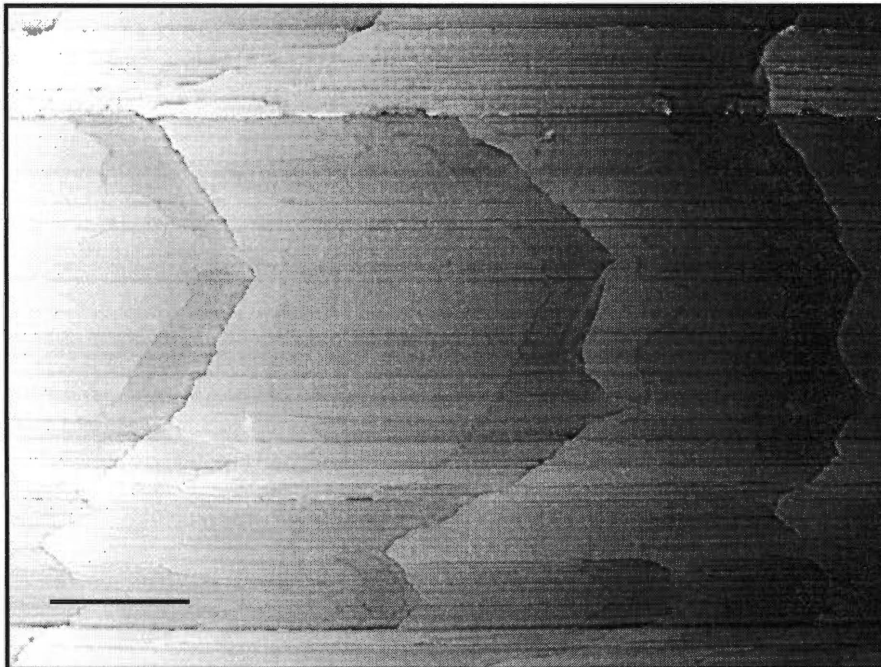


B. Depth Map Image (100X).

**Figure 12. Confocal images of a direct molded tibial bearing surface. Optical sections were acquired in Z-increments of 4 μm over a vertical range of 100 μm.**

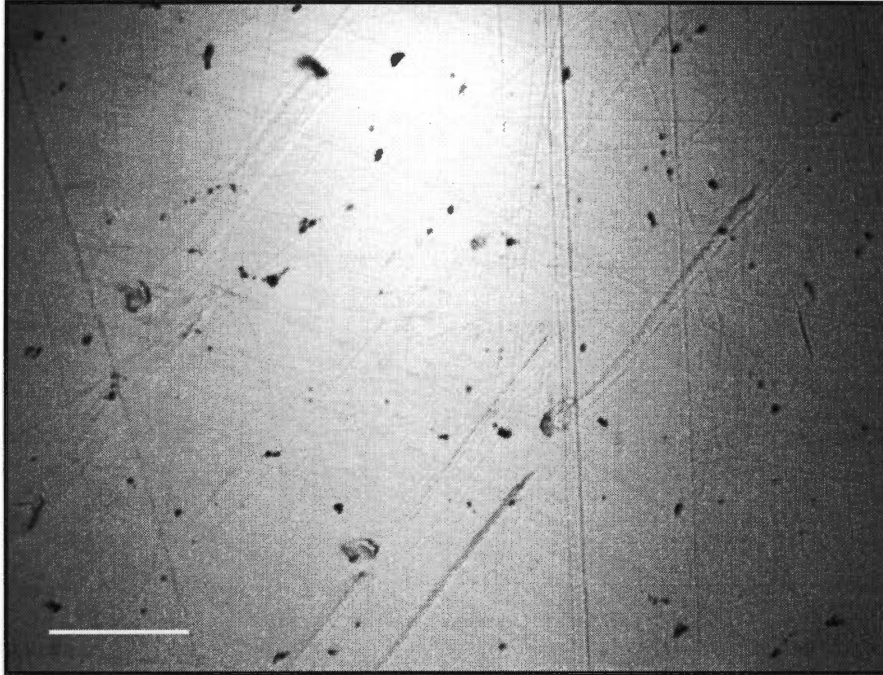


A. Maximum Intensity Image (200X, scale bar = 125  $\mu\text{m}$ ).

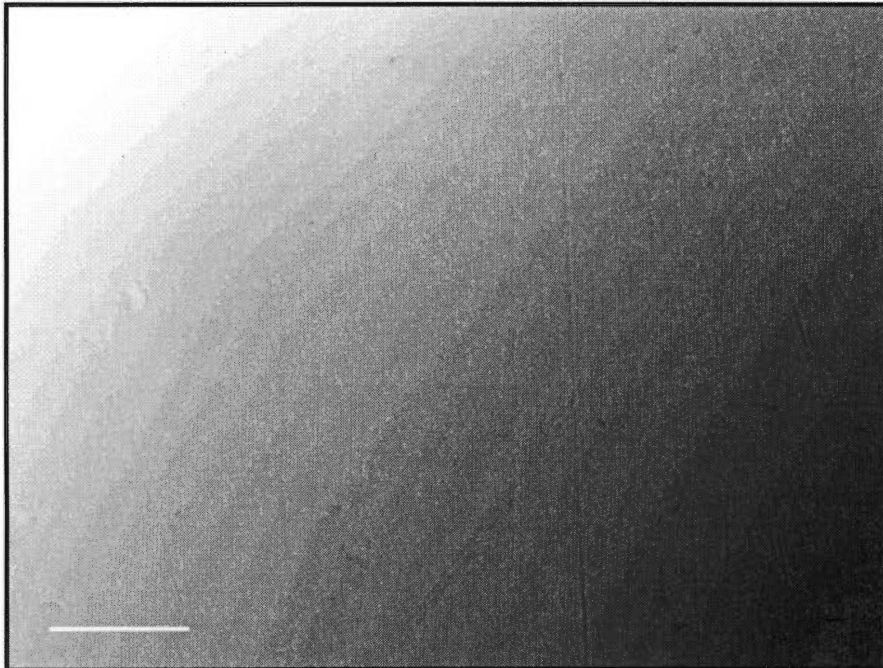


B. Depth Map Image (200X, scale bar = 125  $\mu\text{m}$ ).

**Figure 13. Confocal images of a machined tibial bearing surface. Optical sections were acquired in Z-increments of 1.5  $\mu\text{m}$  over a vertical range of 49.5  $\mu\text{m}$ .**



A. Maximum Intensity Image (200X, scale bar = 125  $\mu\text{m}$ ).



B. Depth Map Image (200X, scale bar = 125  $\mu\text{m}$ ).

**Figure 14. Confocal images of a direct molded tibial bearing surface. Optical sections were acquired in Z-increments of 1.5  $\mu\text{m}$  over a vertical range of 49.5  $\mu\text{m}$ .**

**Table 6. Surface texture parameters from machined versus direct molded tibial bearings.**

Bearing Type (ID #)	Magn	Z Increment	Linear Profiles Along X-Direction (Mean ± Standard Deviation)				Linear Profiles Along Y-Direction (Mean ± Standard Deviation)			
			Ra (µm)	Rq (µm)	Rsk	N	Ra (µm)	Rq (µm)	Rsk	N
Machined (018A)	100X	4 µm	3.7 ± 0.04	4.7 ± 0.05	-0.18 ± 0.02	480	4.0 ± 0.03	5.2 ± 0.03	-0.09 ± 0.02	640
Molded (016A)	100X	4 µm	1.2 ± 0.005	1.5 ± 0.007	+0.02 ± 0.01	480	1.3 ± 0.004	1.7 ± 0.006	+0.12 ± 0.01	640
Machined (018A)	200XA	1.5 µm	1.3 ± 0.02	1.6 ± 0.02	-0.53 ± 0.05	191	1.6 ± 0.01	2.1 ± 0.02	-0.15 ± 0.03	253
Machined (018A)	200XB	1.5 µm	1.8 ± 0.03	2.3 ± 0.03	+0.01 ± 0.03	480	2.2 ± 0.02	2.8 ± 0.02	-0.01 ± 0.03	640
Machined (018B)	200X	1.5 µm	1.3 ± 0.02	1.6 ± 0.03	-0.63 ± 0.05	162	1.9 ± 0.006	2.5 ± 0.01	-0.46 ± 0.02	510
Machined (018C)	200X	1.5 µm	1.2 ± 0.02	1.6 ± 0.02	-0.56 ± 0.04	399	1.6 ± 0.007	2.1 ± 0.01	-0.27 ± 0.02	481
Machined (018D)	200X	1.5 µm	1.3 ± 0.02	1.6 ± 0.03	-0.43 ± 0.03	466	1.9 ± 0.01	2.6 ± 0.01	-0.42 ± 0.01	521
Average of Machined	200X	1.5 µm	1.38 ± 0.24	1.74 ± 0.31	-0.428 ± 0.255	5	1.84 ± 0.25	2.42 ± 0.31	-0.262 ± 0.187	5
Molded (016A)	200XA	1.5 µm	0.5 ± 0.001	0.6 ± 0.002	+0.09 ± 0.01	480	0.5 ± 0.01	0.7 ± 0.01	+0.12 ± 0.03	220
Molded (016A)	200XB	1.5 µm	0.5 ± 0.001	0.6 ± 0.002	-0.03 ± 0.01	451	0.5 ± 0.004	0.7 ± 0.01	+0.01 ± 0.02	256
Molded (016B)	200X	1.5 µm	0.5 ± 0.001	0.6 ± 0.002	+0.06 ± 0.01	480	0.7 ± 0.007	0.9 ± 0.008	+0.22 ± 0.01	640
Molded (016C)	200X	1.5 µm	0.5 ± 0.001	0.6 ± 0.002	-0.20 ± 0.02	480	0.5 ± 0.004	0.7 ± 0.005	+0.11 ± 0.02	311
Molded (016D)	200X	1.5 µm	0.5 ± 0.003	0.6 ± 0.004	-0.10 ± 0.01	414	0.6 ± 0.002	0.8 ± 0.003	-0.30 ± 0.02	313
Average of Molded	200X	1.5 µm	0.50 ± 0.00	0.60 ± 0.00	-0.036 ± 0.118	5	0.56 ± 0.09	0.76 ± 0.09	+0.032 ± 0.200	5

Depth Maps in Figure 12B and Figure 14B showed that the direct molded surface was very smooth. The banded appearances of these images resulted from regions of constant height -- the surface was smoother than the Z-increment of the topographic measurements. This type of banded appearance appears as an artifact in any digital image where adjacent regions have constant intensity (gray-scale) values that vary by small increments. The slight curvature of these bands was representative of the true 3-dimensional topography of the bearing surface. Very fine scratches and surface defects were visible in the Maximum Intensity Images. Some of these were also visible in the corresponding Depth Maps, but others were too shallow to be resolved in the Z-direction.

Surface texture parameters in Table 6 also showed that the machined bearing surface was much rougher than the direct molded surface. At both 100X and 200X, the  $R_a$  and  $R_q$  values for the machined bearing were two to three times the values for the direct molded bearing, and the  $R_a$  values for the machined bearing were similar to or larger than the Z-increment of the data. The  $R_q$  values for the machined bearing were larger than the Z-increments at both magnifications. The theoretical  $R_a$  value for an ideally flat surface is one-fourth of the Z-increment. Thus the surfaces of the direct molded bearings were extremely smooth, approaching this ideal. The roughness values measured at 100X were two to three times the values measured at 200X for the same bearing specimens (machined 018A, direct molded 016A). This occurred because a smaller area (approximately one-fourth in size) of the specimen was measured at 200X, and fewer of the surface features contributing to roughness were included in this area. It was important to scale the measurements to the lateral dimensions of surface features, to sample a representative area or length. Otherwise, the roughness values would not accurately reflect the surface topography. The area sampled (controlled by magnification) had to be optimized against the resulting limitations in Z-increment (controlled by numerical aperture of the objective lens) to select the best measurement conditions.



Skewness is an indication of the shape of the surface profile, rather than a measurement of height variation or roughness. Positive values of  $R_{sk}$  indicate surfaces with peaks pointing upward, which are poor for load bearing. Negative values of  $R_{sk}$  indicate surfaces with rounded humps pointing upward and narrow valleys pointed downward, which are better for load bearing. Values of  $R_{sk}$  near zero indicate surfaces that are either flat or symmetric about the midline of the surface profile.

Skewness values were more negative for the machined bearings than comparable values for the direct molded bearings, which were near zero. These  $R_{sk}$  values also changed in magnitude at different magnifications, with higher (more positive) values measured at 100X than at 200X for both types of bearings. Again, it was important to select a representative surface area for the measurement. The theoretical skewness for a perfectly flat surface is zero. If the Z-increment is larger than the scale of surface roughness, so that  $R_a$  decreases to one-fourth of the Z-increment, then the skewness value decreases toward zero. This must be considered in interpreting results from the direct molded bearings.

Statistical tests using the t distribution (95<sup>th</sup> percentile level) were used to evaluate the significance of the surface texture parameters measured at 200X (after averaging 5 datasets):

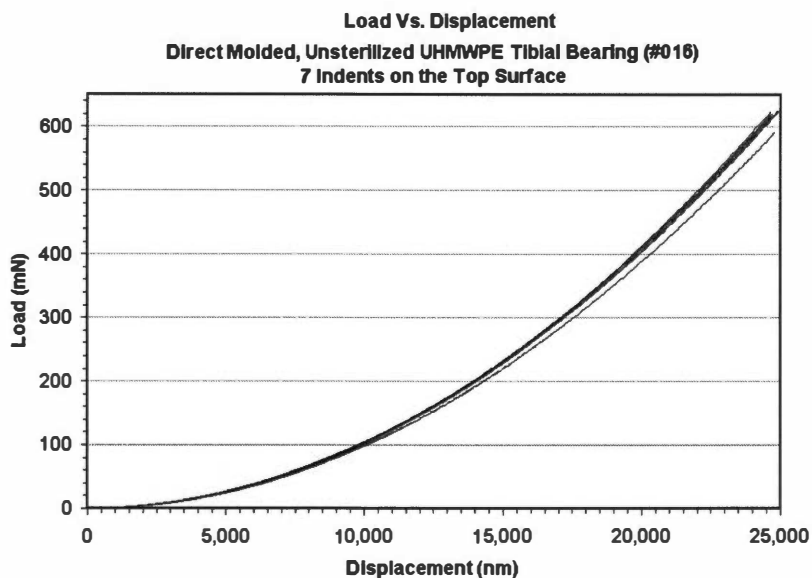
- The  $R_a$  values and the  $R_q$  values for the direct molded bearing were significantly lower at the 95<sup>th</sup> percentile level than the corresponding values for the machined bearing along both the X and Y directions.
- The  $R_{sk}$  values for the direct molded bearing were significantly higher (more positive) at the 95<sup>th</sup> percentile level than the corresponding values for the machined bearing along both the X and Y directions.
- The  $R_a$  and  $R_q$  values for the machined bearings along the Y-direction were significantly larger at the 95<sup>th</sup> percentile level than the corresponding values along the X-direction (parallel to machining lines).

- The  $R_a$  value for the direct molded bearings along the X-direction was not significantly different at the 95<sup>th</sup> percentile level from the value along the Y-direction.
- The  $R_q$  value for the direct molded bearings along the X-directions was significantly lower at the 95<sup>th</sup> percentile level than the corresponding value along the Y-direction.
- The  $R_{sk}$  value for the machined bearings along the Y-direction was not significantly different at the 95<sup>th</sup> percentile level from the value along the X-direction.
- The  $R_{sk}$  value for the direct molded bearings along the Y-direction was not significantly different at the 95<sup>th</sup> percentile level from the value along the X-direction.

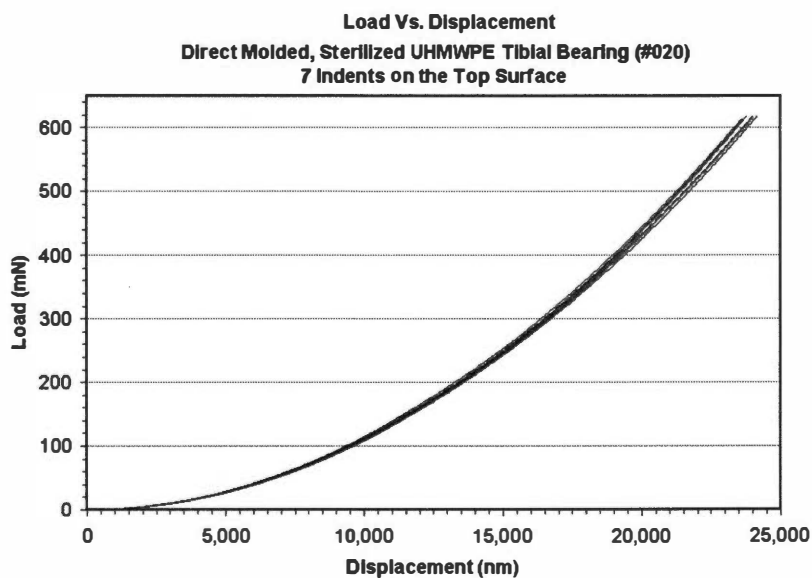
## 7.2 NANOINDENTATION

Nanoindentation experiments were run on one tibial bearing of each type: direct molded, unsterilized (specimen 016A); direct molded, sterilized (specimen 020A); machined, unsterilized (specimen 018A); and machined, sterilized (specimen 019A). All bearings were examined on the top surfaces, in approximately planar regions near the center of the loading zone for the implants, near one region where surface texture measurements were made with confocal microscopy. Multiple nanoindents were run on each specimen's top surface, to evaluate the reproducibility of the micromechanical behavior.

Figure 15 compares overall load – displacement behavior for these four types of tibial bearings, up to the maximum load of 625 mN. Load – displacement behavior was very consistent over multiple nanoindents on the direct molded bearing surfaces (both unsterilized and sterilized). Using identical loading cycles, the displacement behavior was not repeatable over multiple indents on the machined bearing surfaces (both unsterilized and sterilized). This related, at least in part, to the larger surface roughness present on machined relative to direct



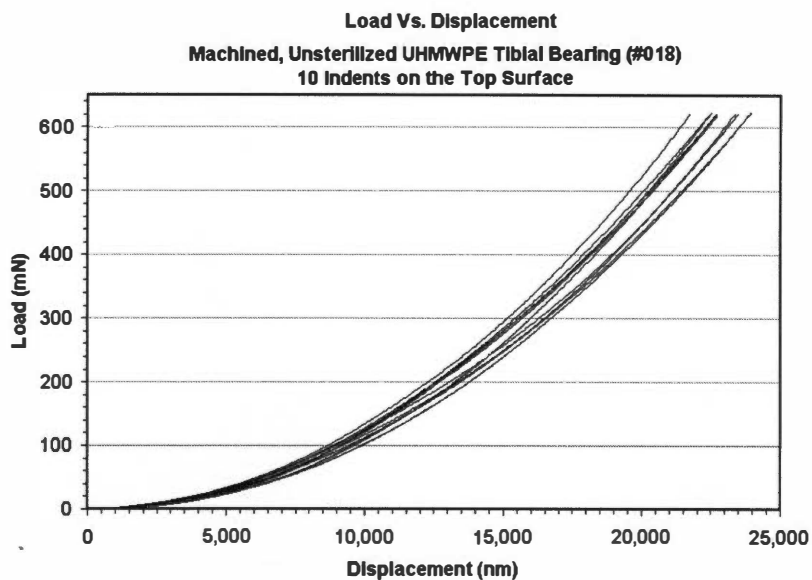
A.



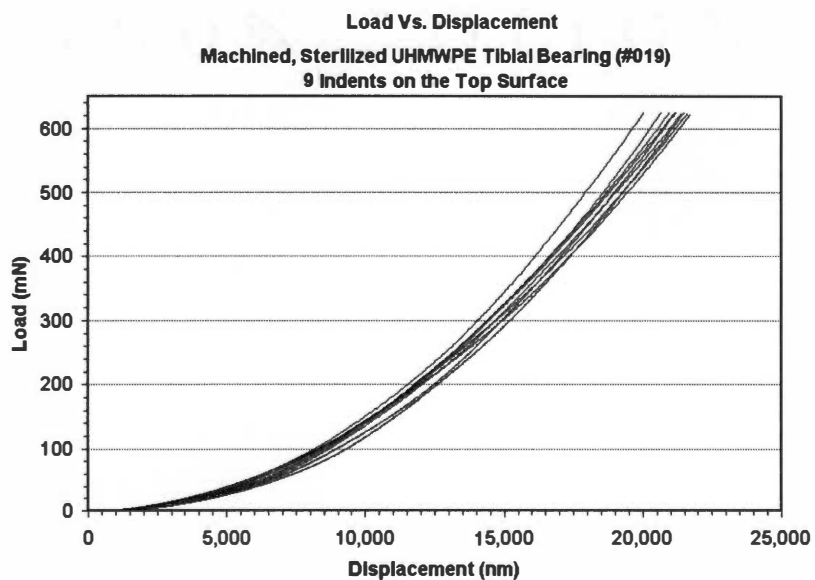
B.

**Figure 15. Load-displacement results (covering the entire load range) for nanoindents.**

**Nanoindents on the top surfaces of direct molded tibial bearings that are (A) unsterilized and (B) sterilized by gamma irradiation (continued on next page).**



C.



D.

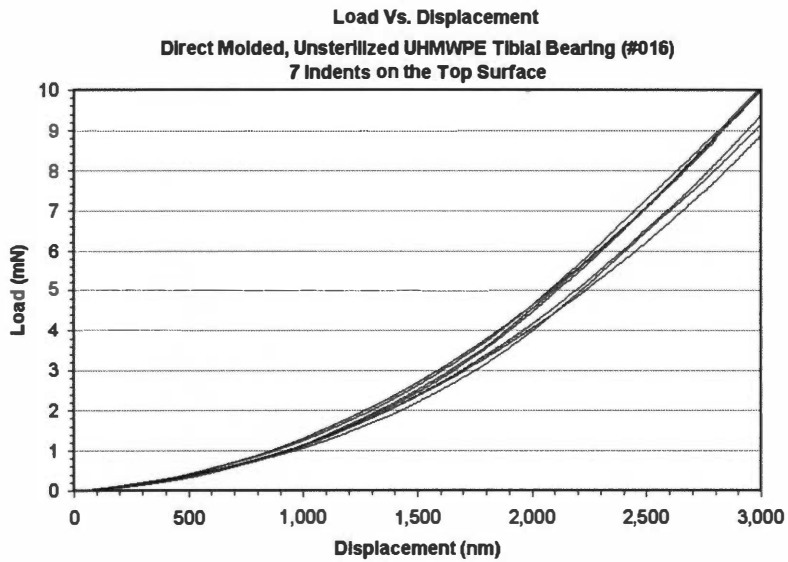
**Figure 15 (continued). Load-displacement results (covering the entire load range) from nanoindents on the top surfaces of machined tibial bearings that are (C) unsterilized and (D) sterilized by gamma irradiation.**

molded bearings. However, this variability in displacement response could also contribute to generation of wear debris due to non-uniform localized strains in the polyethylene.

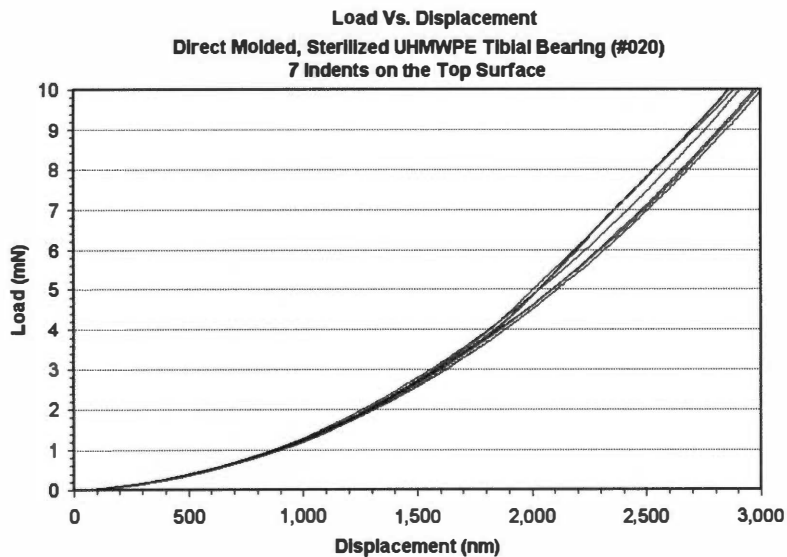
The four bearing types also showed differences in maximum displacement values. Ranking them in order from largest to smallest overall displacement gave: direct molded, unsterilized (specimen 016A); direct molded, sterilized (specimen 020A); machined, unsterilized (specimen 018A); and machined, sterilized (specimen 019A). These differences in maximum displacement related to mechanical property differences, as shown later by calculated values of hardness and elastic modulus. The two fabrication methods (direct molding vs. machining) resulted in different mechanical properties of the unsterilized bearings. Sterilization by gamma irradiation then increased the values of hardness and elastic modulus for each bearing type.

Figure 16 compares load – displacement behavior at very low loads, from 0 to 10 mN. The resulting displacements are comparable to the size of small wear debris particles, i.e. from 0.2 to 3.0  $\mu\text{m}$ . Recall that the mean size of wear debris is 0.5 – 0.6  $\mu\text{m}$ . Even at these low loads, the differences in reproducibility of displacement response between direct molded and machined implants were obvious. At displacements below 0.5  $\mu\text{m}$  the machined bearings showed variations in their displacement responses, whereas the direct molded bearings had very consistent, repeatable displacement responses. This observation was made for both unsterilized and sterilized tibial bearings.

At low loads up to 10 mN, differences in the absolute magnitudes of displacement were not distinct between the four types of tibial bearings. The direct molded bearings had a narrower range of displacements at each load than the machined bearings did, but values for the direct molded bearings fell within the range for the machined bearings. Sterilization had a small effect on the displacements for the direct molded bearings, but did not affect the machined bearings.

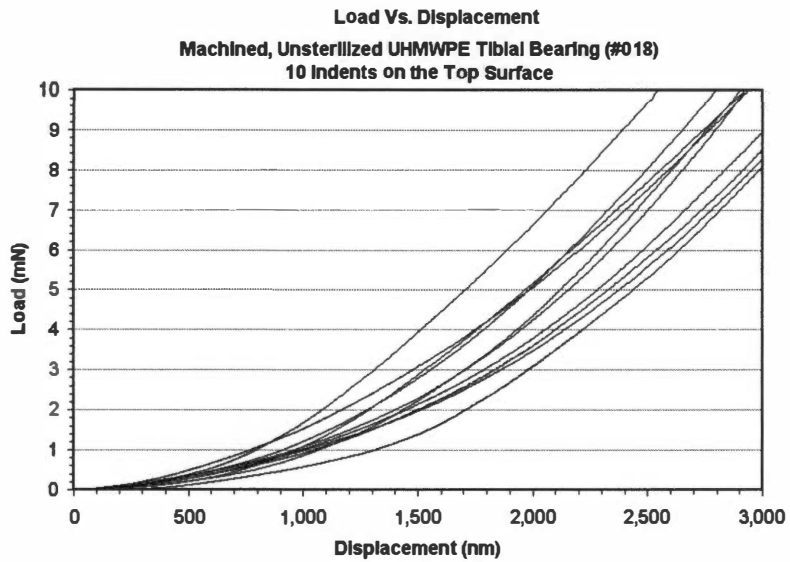


A.

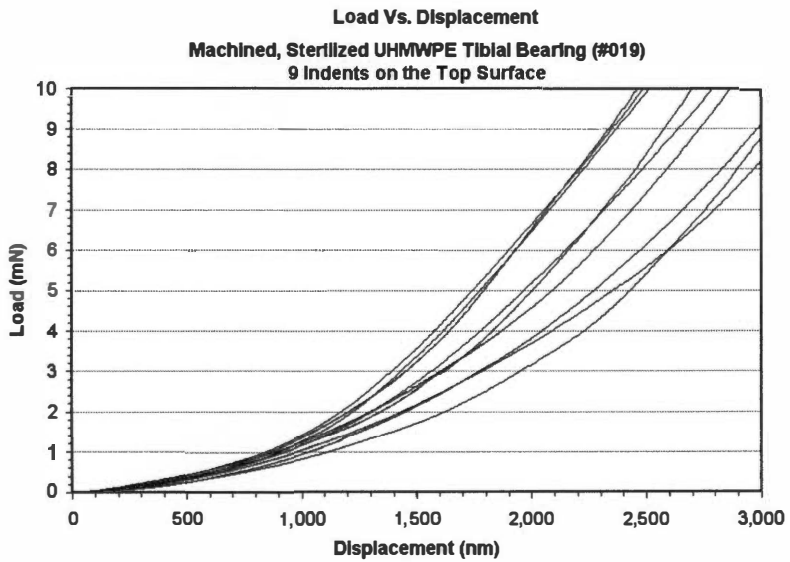


B.

**Figure 16. Load–displacements results at low loads (for displacements near the scale of wear debris formation) from nanoindents on the top surfaces. Nanoindents on direct molded tibial bearings that are (A) unsterilized and (B) sterilized by gamma irradiation (continued on next page).**



C.



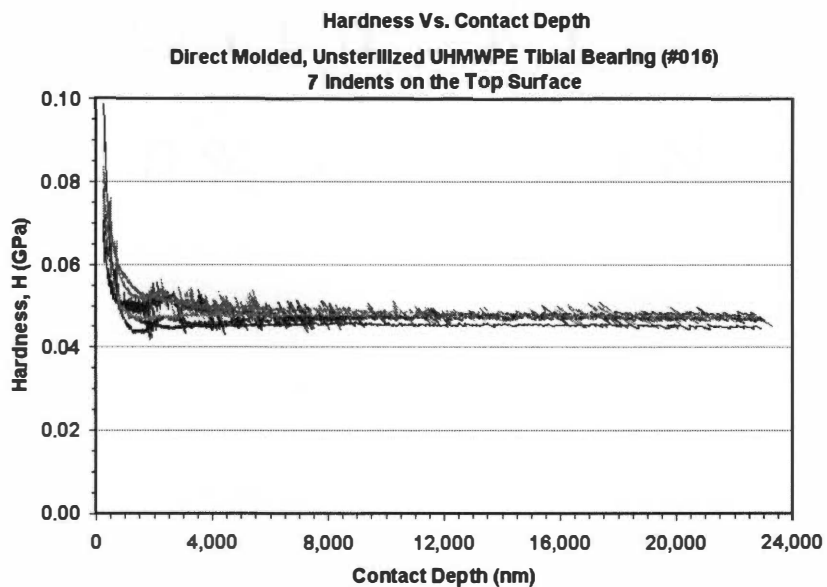
D.

**Figure 16 (continued). Load–displacements results at low loads (for displacements near the scale of wear debris formation) from nanoindents on the top surfaces of machined tibial bearings that are (A) unsterilized and (B) sterilized by gamma irradiation.**

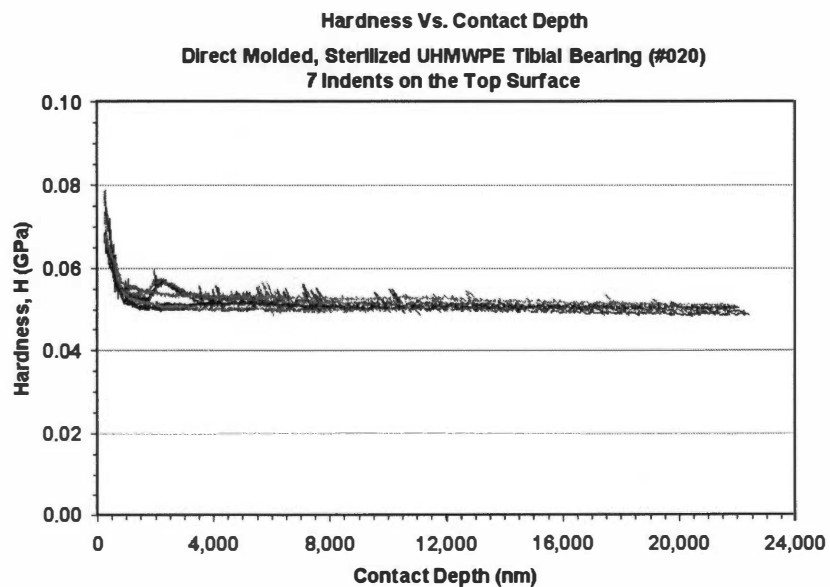
Figure 17 shows calculated results for hardness vs. contact depth throughout each loading cycle. Results for the direct molded bearings (both unsterilized and sterilized) were more consistent and repeatable than for the machined bearings (both unsterilized and sterilized). For each type of tibial bearing, all the indents reached a stable hardness value within the bulk material below the surface. However, this bulk hardness value varied between multiple indents on each specimen, and this variation was sizeable on the machined tibial bearings (both unsterilized and sterilized). Bulk hardness values were reached at different contact depths for direct molded vs. machined tibial bearings, and variations in surface layer thickness were observed between multiple indents on each specimen. Bulk properties were reached at contact depths of 2 – 4  $\mu\text{m}$  in direct molded tibial bearings and 5 – 10  $\mu\text{m}$  in machined tibial bearings. Surface variations in hardness were observed. Variations of hardness in the surface layer were different between direct molded and machined tibial bearings. For indents on direct molded bearings (both unsterilized and sterilized), the surface hardness usually increased from the bulk toward the shallowest contact depths. Variations in hardness values (within the surface layer) were relatively small between multiple indents on the direct molded tibial bearings. Some indents had a localized peak in hardness at contact depths of 2 – 3  $\mu\text{m}$ , but this did not always result. For indents on machined bearings (both unsterilized and sterilized), the variation in hardness near the surface was not consistent between multiple indents. Sometimes the hardness increased from the bulk toward the surface, and sometimes it decreased. Hardness values near the surface were even more variable than the bulk hardness values, for machined tibial bearings.

Figure 18 shows calculated results for elastic modulus vs. contact depth throughout each loading cycle. Results are similar in form to the results from hardness (see Figure 17), although the modulus curves are noisier than the hardness curves. Modulus curves from indents on the direct molded bearings are more consistent and repeatable than from indents on the machined bearings. Each bearing type showed modified properties in a surface layer, but the thickness of this layer was the same as that shown by hardness data (2 – 4  $\mu\text{m}$  for



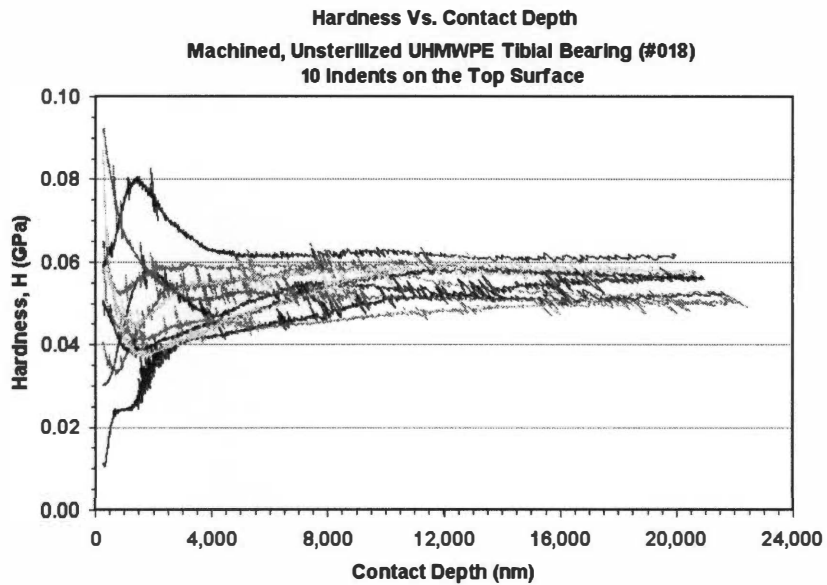


A.

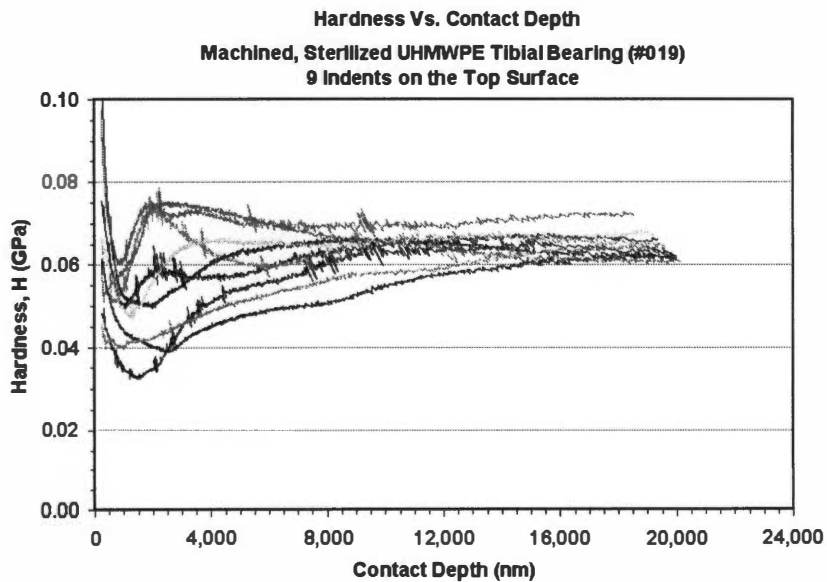


B.

**Figure 17. Hardness vs. contact depth results from nanoindents on the top surfaces. Nanoindents on direct molded tibial bearings that are (A) unsterilized and (B) sterilized by gamma irradiation (continued on next page).**

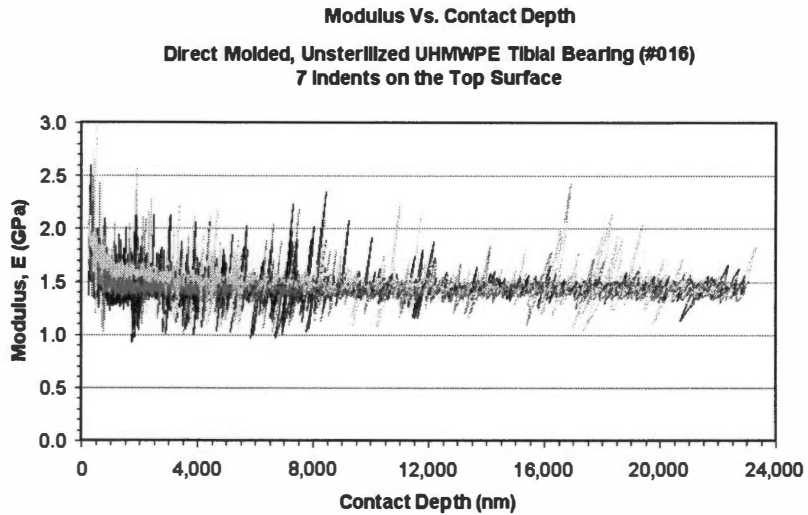


C.

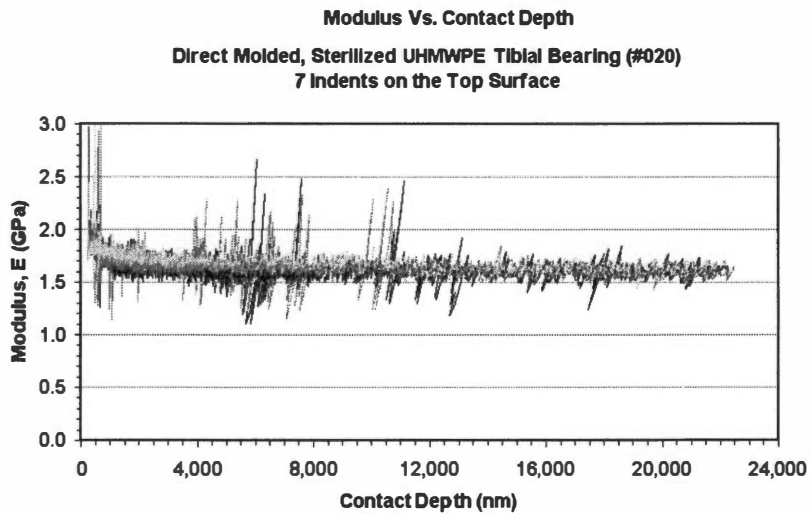


D.

**Figure 17 (continued). Hardness vs. contact depth results from nanoindents on the top surfaces of machined tibial bearings that are (C) unsterilized and (D) sterilized by gamma irradiation.**



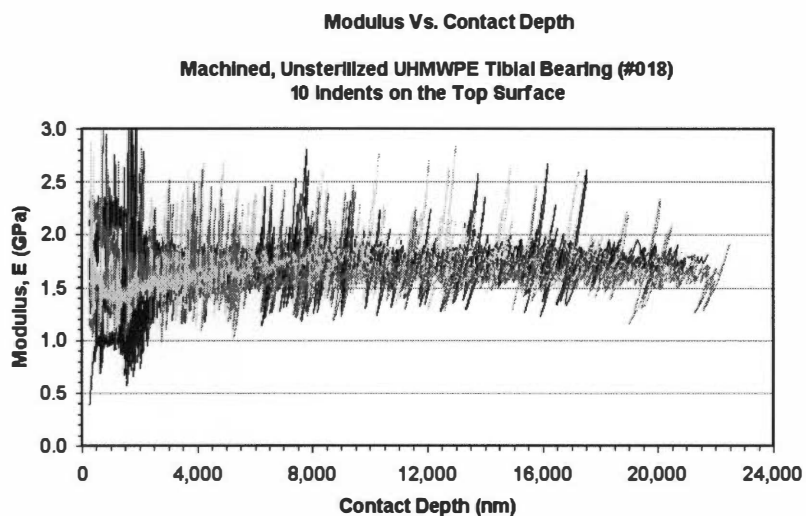
A.



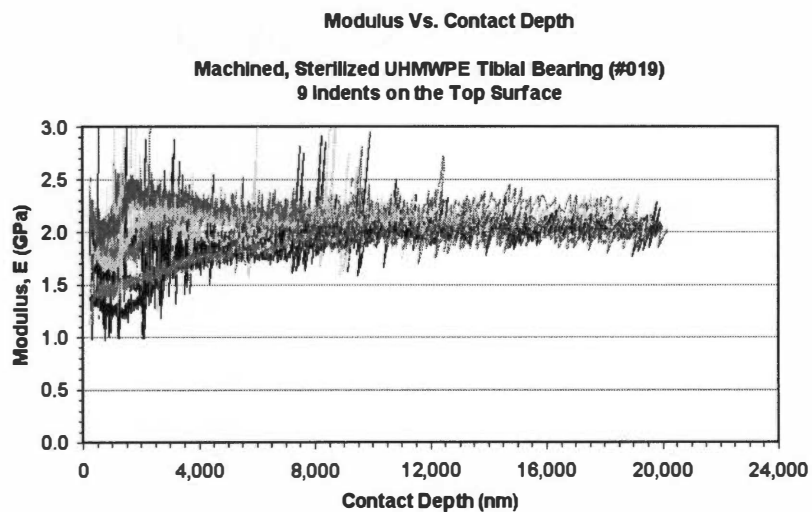
B.

**Figure 18. Elastic modulus vs. contact depth results from nanoindents.**

Nanoindents on the top surfaces of direct molded tibial bearings that are (A) unsterilized and (B) sterilized by gamma irradiation (continued on next page).



C.



D.

**Figure 18 (continued). Elastic modulus vs. contact depth results from nanoindents on the top surfaces of machined tibial bearings that are (C) unsterilized and (D) sterilized by gamma irradiation.**

direct molded bearings, and 5 – 10  $\mu\text{m}$  for machined bearings). Modulus variations in the surface layer followed the same trends as for hardness: in direct molded bearings, the modulus usually increased as the contact depth decreased; in machined bearings, the modulus was highly variable – sometimes it increased, and sometimes it decreased as the contact depth decreased. Indents on all bearing types reached a constant modulus level below the surface layer, in the bulk material.

Bulk hardness and elastic modulus values from nanoindentation are summarized in Table 7. Bulk properties were averaged for each indent, over all contact depths above 10.0  $\mu\text{m}$ . Then bulk properties for each bearing type were analyzed statistically, using the t test, as shown in this table. Results show that there are statistically significant differences in micromechanical properties between direct molded and machined bearings, in both the unsterilized and sterilized conditions. Direct molded bearings consistently have lower hardness and elastic modulus values than machined bearings. Sterilization by gamma irradiation increases hardness and elastic modulus values for both bearing types, but this effect is greater for machined bearings than for direct molded bearings. Variability in micromechanical properties has also been examined using the standard deviations for hardness and elastic modulus. Sterilization does not affect this variability within each bearing type. Comparison of standard deviations using the F Test has shown that the variability of both hardness and elastic modulus is statistically different between direct molded and machined bearings.

### **7.3 SMALL ANGLE X-RAY SCATTERING**

Small angle X-ray scattering experiments were run on one tibial bearing of each type: direct molded, unsterilized (specimen 016A); direct molded, sterilized (specimen 020A); machined, unsterilized (specimen 018A); and machined, sterilized (specimen 019A). Three specimens (each approximately 1 mm thick) were analyzed from each bearing, to compare the top bearing surface, the bulk, and the bottom bearing surface.

**Table 7. Summary of Hardness and Elastic Modulus Results from Nanoindentation.**

Results From Nanoindentation	Type of Tibial Bearing			
	Direct Molded, Unsterilized	Direct Molded, Sterilized	Machined, Unsterilized	Machined, Sterilized
Number of Indents	7	7	10	9
Bulk Hardness (MPa), Mean	47.2	50.6	55.1	64.5
Bulk Hardness (MPa), Standard Deviation	0.89	0.84	3.91	3.35
Bulk Hardness (MPa), 95% Confidence Interval on Means (t Test)	46.4 – 48.0	49.8 – 51.4	52.3 – 57.9	61.9 – 67.1
Bulk Modulus (GPa), Mean	1.44	1.61	1.71	2.08
Bulk Modulus (GPa), Standard Deviation	0.027	0.019	0.080	0.081
Bulk Modulus (GPa), 95% Confidence Interval on Means (t Test)	1.42 – 1.47	1.60 – 1.63	1.65 – 1.77	2.02 – 2.14

Figure 19 compares the scattering data, in the form of a Lorentz plot, for bulk specimens from the four different types of tibial bearings. Scattering occurs at very low scattering vectors ( $q \sim 0.1 \text{ nm}^{-1}$ ) for all specimens, with slight differences between direct molded and machined UHMWPE specimens. The center of the scattering peak occurs at higher  $q$  values for direct molded specimens than for machined specimens, indicating that direct molded specimens have a smaller long period than machined specimens. Figure 20 (A – D) compares the Lorentz plots for each of the specimens analyzed for each tibial bearing type. Specimens from the top bearing surface, the bulk, and the bottom bearing surface are similar within each tibial bearing type. Sterilization with gamma irradiation had little effect on the Lorentz scattering curves, except to decrease the scattering intensity.

One-dimensional correlation functions,  $K(R)$ , were calculated from the raw scattering data for each specimen, with typical functions shown in Figure 21 for bulk specimens from UHMWPE tibial bearings. These functions were analyzed assuming the ideal 2-phase model to determine the long period (from  $R$  at the first maximum), the maximum volume crystallinity [based on the ratio of  $K(R)$  at the first minimum to the intercept at the origin,  $K(0)$ ], and the amorphous region thickness (because the first minimum relates to the thickness of the amorphous phase when the volume crystallinity is greater than 50%). From these values, the lamellar thickness (as long period minus amorphous thickness) and the volume crystallinity (as lamellar thickness / long period) were calculated for each specimen, while ensuring that the net volume crystallinity did not exceed the maximum value determined above. Results of these calculations are summarized in Figure 22A, with details listed in Table 8.

Next the SAXS results were corrected to account for the interface zone, by using the difference in crystallinities measured by FTIR and DSC. A summary of the results were plotted in Figure 22B and listed in Table 9. Both FTIR and DSC analyses were performed on the same specimens (3 each from each type except for the machined sterilized bearing), so the difference between the measured crystallinities for each specimen equaled the percentage of the interface zone. Although the SAXS specimens were thicker than the FTIR and DSC

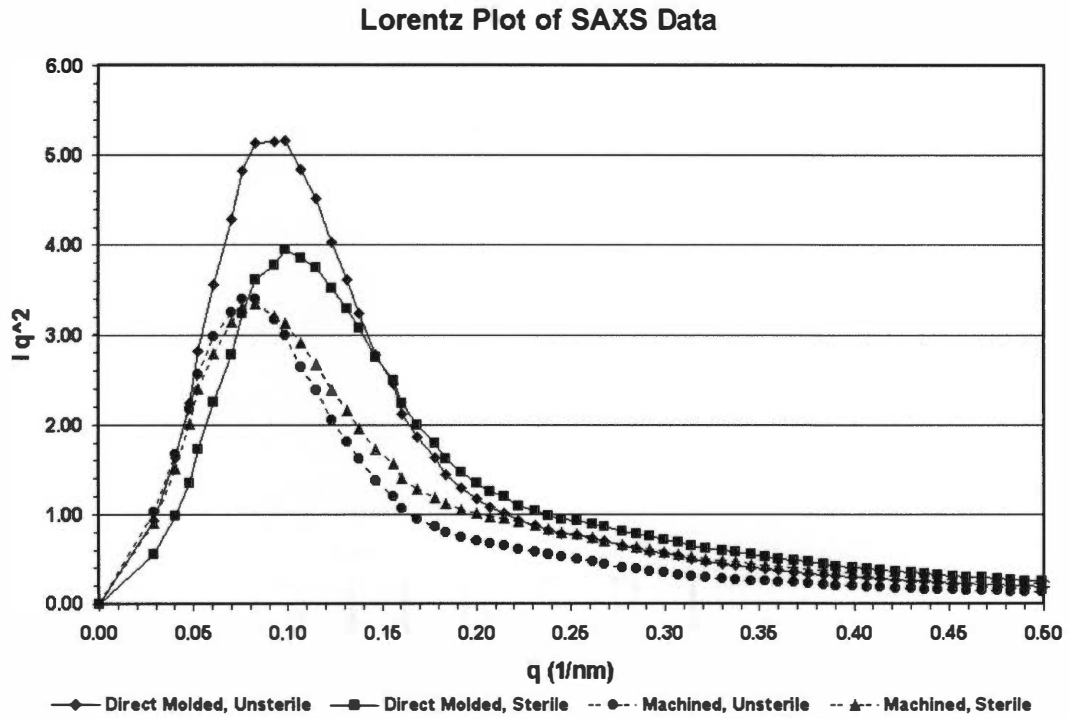
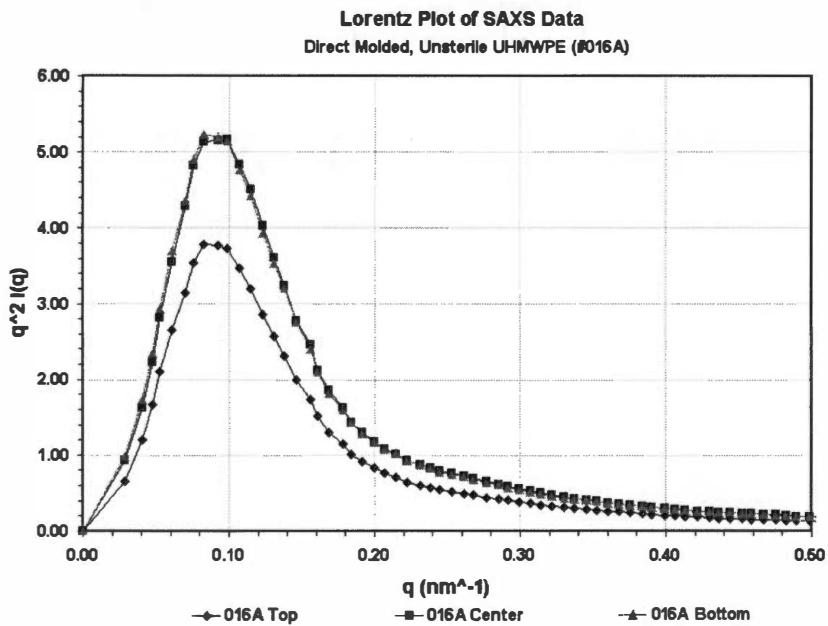
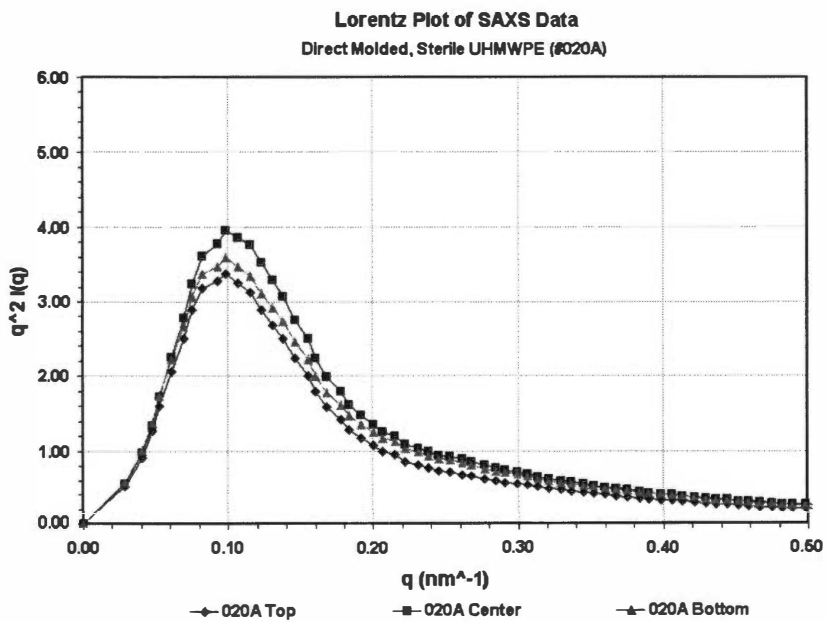


**Figure 19. Lorentz plots compare intensity data from small angle X-ray scattering of bulk UHMWPE specimens.**





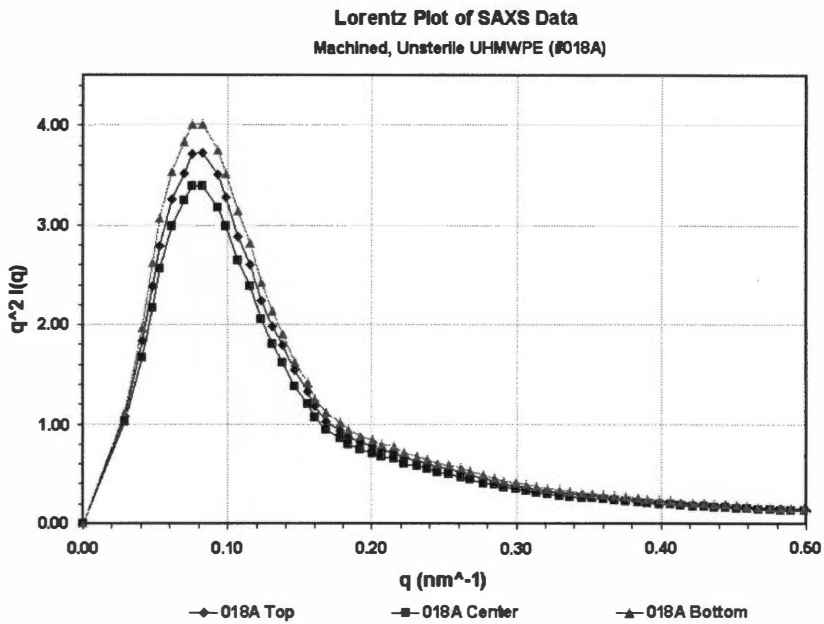
A.



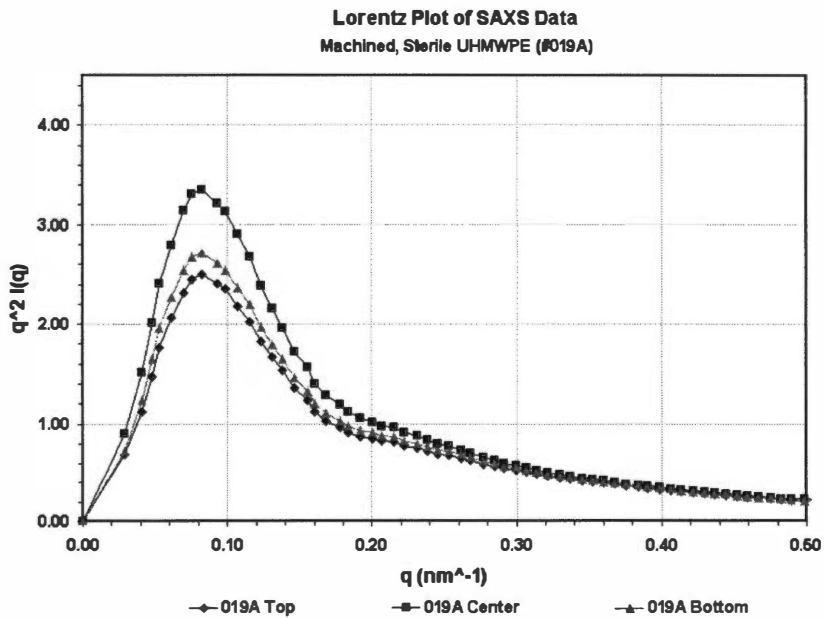
B.

**Figure 20. Lorentz plots compare  $q^2 I(q)$  versus scattering angle.**

**For UHMWPE tibial bearings that are direct molded and (A) unsterilized and (B) sterilized by gamma irradiation (continued on next page).**



C.



D.

Figure 20 (continued). Lorentz plots compare  $q^2 I(q)$  versus scattering angle for UHMWPE tibial bearings that are machined and (C) unsterilized and (D) sterilized by gamma irradiation.

### 1-Dimensional Correlation Function

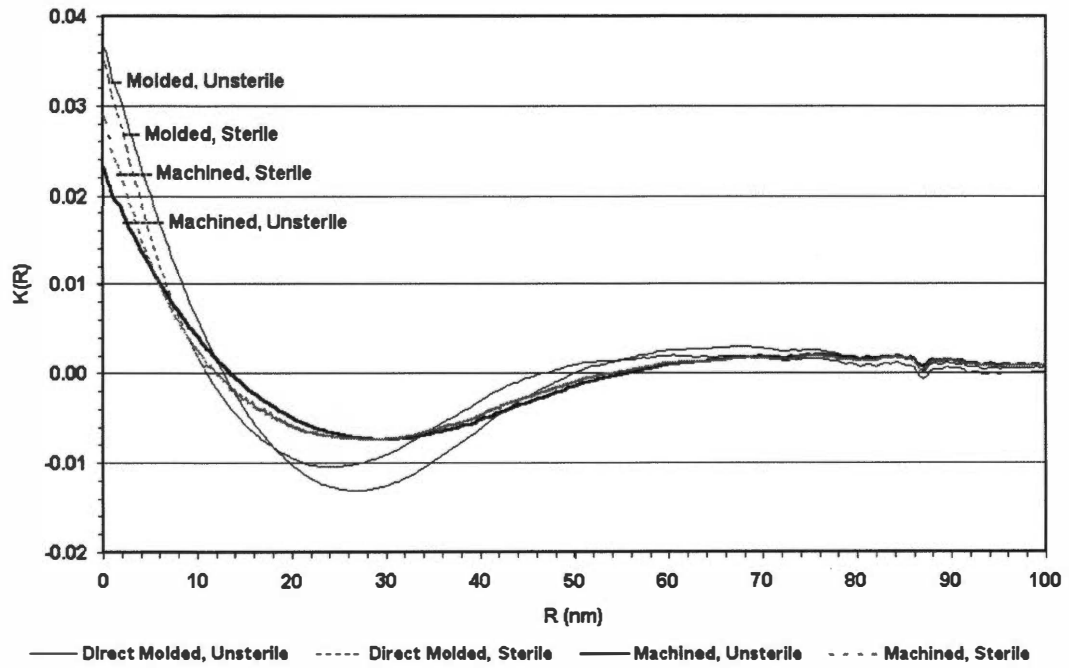
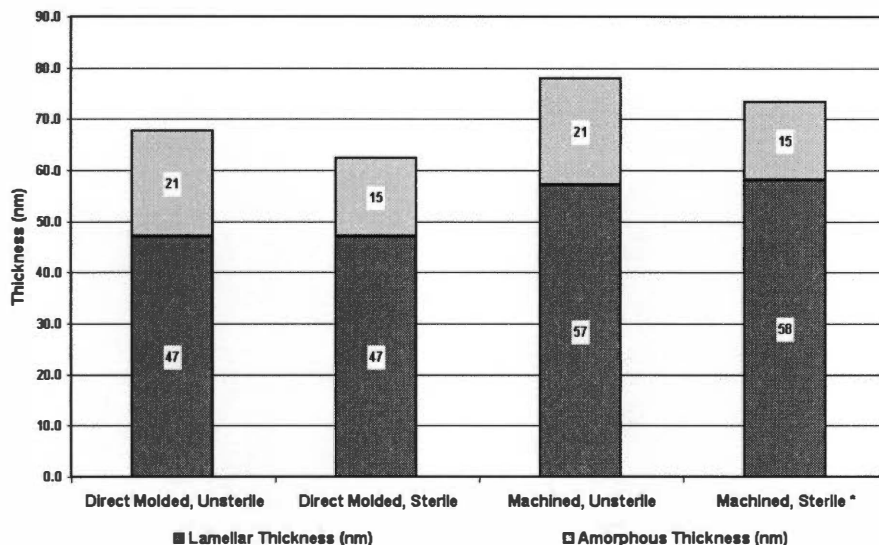


**Figure 21. One-dimensional correlation functions from SAXS analyses of bulk specimens from UHMWPE tibial bearings.**

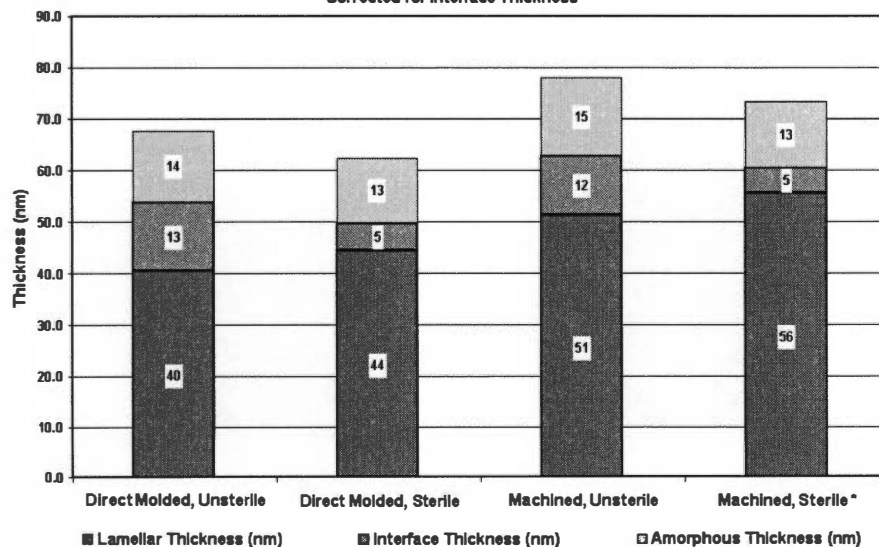
**SUMMARY OF SAXS RESULTS**



A. Based on 2-phase model.

**SUMMARY OF SAXS RESULTS**

Corrected for Interface Thickness



B. Based on 3-phase model with interface data from FTIR and DSC.  
 \* Values of the interface fraction were estimated for machined, sterile specimens.

**Figure 22. Measured average thicknesses of crystalline lamellar, interfacial, and amorphous phases from SAXS analyses.**

**Table 8. Results from 2-phase analysis of SAXS 1-dimensional correlation functions.**

<b>Specimen Type</b>	<b>Location</b>	<b>Long Period (nm)</b>	<b>Amorphous Thickness (nm)</b>	<b>Lamellar Thickness (nm)</b>	<b>Volume % Crystallinity (Maximum)</b>
Machined, Unsterile UHMWPE (018A)	Top Surface	68 - 84	20	48 - 64	70 - 76 % (76 %)
	Bulk	74 - 84	21	53 - 63	71 - 75 % (76 %)
	Bottom Surface	74 - 84	22	52 - 62	71 - 74 % (76 %)
	Mean ± Std. Dev.	78.0 ± 1.73	21.0 ± 1.00	57.0 ± 1.00	72.8 ± 0.29 %
Machined, Sterile UHMWPE (019A)	Top Surface	68 - 79	15	53 - 64	78 - 81 % (81 %)
	Bulk	68 - 79	16	52 - 63	76 - 80 % (80 %)
	Bottom Surface	68 - 78	15	53 - 63	78 - 81 % (81 %)
	Mean ± Std. Dev.	73.3 ± 0.29	15.3 ± 0.58	58.0 ± 0.50	79.0 ± 0.87 %
Direct Molded, Unsterile UHMWPE (016A)	Top Surface	64 - 71	21	43 - 50	67 - 70 % (74 %)
	Bulk	65 - 70	21	44 - 49	68 - 70 % (74 %)
	Bottom Surface	66 - 70	20	46 - 50	69 - 71 % (74 %)
	Mean ± Std. Dev.	67.7 ± 0.29	20.7 ± 0.58	47.0 ± 0.87	69.2 ± 0.76 %
Direct Molded, Sterile UHMWPE (020A)	Top Surface	59 - 68	16	43 - 52	73 - 77 % (77 %)
	Bulk	58 - 60	14	44 - 46	76 - 77 % (77 %)
	Bottom Surface	59 - 70	16	43 - 54	74 - 78 % (78 %)
	Mean ± Std. Dev.	62.3 ± 2.93	15.3 ± 1.15	47.0 ± 1.80	75.8 ± 0.76 %

**Table 9. Results from 3-phase analysis of SAXS 1-dimensional correlation functions.**

Specimen Type	Location	Long Period (nm)	Amorphous Thickness (nm)	Interface Thickness (nm)	Lamellar Thickness (nm)	Volume % Crystallinity (Lamellae Only)
Machined, Unsterile UHMWPE (018A)	Top Surface	76	13	14	49	65 %
	Bulk	79	16	9	54	68 %
	Bottom Surface	79	16	12	51	65 %
	Mean $\pm$ Std. Dev.	78.0 $\pm$ 1.73	15.0 $\pm$ 1.73	11.7 $\pm$ 2.52	51.3 $\pm$ 2.52	66.0 $\pm$ 1.73 %
Machined, Sterile UHMWPE (019A)	Top Surface	74	12	6	56	76 %
	Bulk	74	14	4	56	76 %
	Bottom Surface	73	13	5	55	75 %
	Mean $\pm$ Std. Dev.	73.3 $\pm$ 0.29	13.0 $\pm$ 1.00	5.0 $\pm$ 1.00	55.7 $\pm$ 0.58	75.7 $\pm$ 0.58 %
Direct Molded, Unsterile UHMWPE (016A)	Top Surface	68	13	16	39	57 %
	Bulk	68	15	12	41	60 %
	Bottom Surface	68	14	12	42	62 %
	Mean $\pm$ Std. Dev.	67.7 $\pm$ 0.29	14.0 $\pm$ 1.00	13.3 $\pm$ 2.31	40.7 $\pm$ 1.53	59.7 $\pm$ 2.52 %
Direct Molded, Sterile UHMWPE (020A)	Top Surface	64	13	6	45	70 %
	Bulk	59	13	2	44	75 %
	Bottom Surface	65	12	8	45	69 %
	Mean $\pm$ Std. Dev.	62.3 $\pm$ 2.93	12.7 $\pm$ 0.58	5.3 $\pm$ 3.06	44.7 $\pm$ 0.58	71.3 $\pm$ 3.21 %

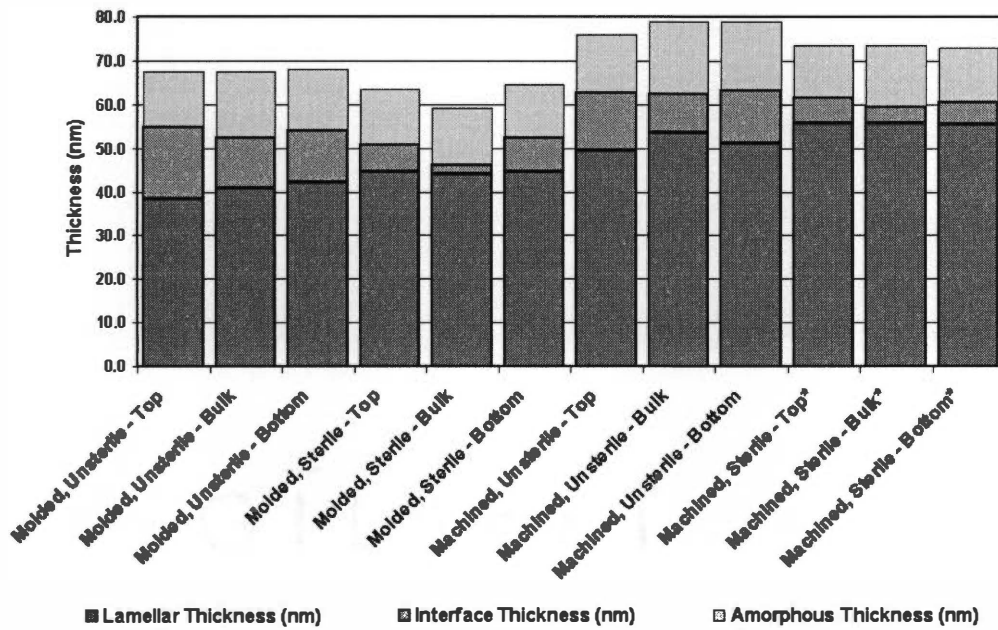
specimens, it was assumed that the relative percentage of the interface zone would be the same. For the SAXS data on machined, sterilized specimens, there was not corresponding FTIR and DSC data. For each of these machined specimens, the interface thickness (as a fraction of the long period) was assumed to decrease by 55% following irradiation, which was comparable to the decrease that occurred for direct molded specimens.

Results show that the average lamellar thickness was significantly different between direct molded and machined UHMWPE tibial bearings, based on the 2-phase model, as shown in the stacked bar chart in Figure 22A. Direct molded bearings had a lower lamellar thickness than machined bearings. The thickness of the amorphous phase was similar in both bearing types. Sterilization by gamma irradiation appeared to have little effect on lamellar thickness for both bearing types, but significantly decreased the mean thickness of the amorphous phase. When the 3-phase model was used to correct for the presence of the interface zone, the effects of gamma irradiation on the polymer morphology became more distinct. In addition to the decrease in amorphous phase thickness (by 10-15%), effects on the interface and lamellar thicknesses were observed. The interface significantly decreased in thickness (by about 60%), and the lamellae increased in thickness (by about 10%). Thus despite an overall decrease in long period after sterilization, the lamellar thickness was shown to increase. The sizeable decrease in the interface thickness was larger than the decrease in the long period, but was partially offset by the increase in lamellar thickness. These observations from the 3-phase model were based on measurements from the direct molded bearing type, but were estimated for the machined bearing type because DSC data could not be obtained.

The variation of morphology with specimen position (top, bulk, bottom) in each type of tibial bearing is plotted in Figure 23. The lamellar thicknesses varied slightly with position in the unsterile bearings, for both direct molded and machined, but after sterilization the lamellar thicknesses were extremely uniform between the surfaces and the bulk. The interface thickness was higher in the top surface of the direct molded, unsterile, bearings; but after gamma irradiation the bulk had a much lower interface thickness than either surface. The

## SUMMARY OF SAXS RESULTS

Corrected for Interface Thickness



\* Values of the interface fraction were estimated for machined, sterile specimens.

**Figure 23. Morphology variations between the surfaces and the bulk, from SAXS analyses of UHMWPE tibial bearings.**



interface thickness was lower in the bulk than in either surface of the machined, unsterile bearing. The amorphous thickness was lower in the top surfaces of both the direct molded and the machined bearings that were unsterilized. After sterilization, the amorphous thickness was uniform at all three positions in the direct molded bearing. Results plotted for the machined, sterilized bearing were estimated rather than measured, as described previously.

## **7.4 WIDE ANGLE X-RAY DIFFRACTION**

Wide angle X-ray diffraction experiments were run on one tibial bearing of each type: direct molded, unsterilized (specimen 016A); direct molded, sterilized (specimen 020A); machined, unsterilized (specimen 018A); and machined, sterilized (specimen 019A). Three specimens (each approximately 1 mm thick, from SAXS analyses) were analyzed for each bearing, to compare the top bearing surface, the bulk, and the bottom bearing surface.

Results from wide angle X-ray diffraction experiments are listed in Table 10. All the crystallinity measurements fell within a similar range, from 63% to 77% by weight or from 59% to 74% by volume. The trend in terms of average crystallinity between the four UHMWPE bearing types was:

Machined, Unsterile < Machined, Sterile ≈ Direct Molded, Unsterile < Direct Molded, Sterile

The differences in crystallinity between the top and bottom surfaces and the bulk were small for all four bearing types. Generally the bulk had a slightly lower crystallinity than either surface, except for the direct molded, sterilized, tibial bearing which had its highest crystallinity in the bulk.

## **7.5 FTIR SPECTROSCOPY**

FTIR spectroscopy experiments were run on unsterilized specimens of direct molded (016A) and machined (018A) tibial bearings. For each bearing, two series of thin sections were analyzed: one series beginning at the top bearing surface, and the other series beginning at the bottom bearing surface. A few selected sections from the top surface, the

**Table 10. Results from Wide Angle X-Ray Diffraction.**

<b>Specimen Type</b>	<b>Location</b>	<b>Weight % Crystallinity</b>	<b>Equivalent Volume % Crystallinity</b>
<b>Machined, Unsterile (018A)</b>	Top Surface	72.9 %	69.7 %
	Bulk	62.7 %	59.0 %
	Bottom Surface	64.0 %	60.3 %
	Mean ± Std. Dev.	66.5 ± 5.55 %	63.0 ± 5.84 %
<b>Machined, Sterile (019A)</b>	Top Surface	68.8 %	65.3 %
	Bulk	66.2 %	62.6 %
	Bottom Surface	69.2 %	65.7 %
	Mean ± Std. Dev.	68.1 ± 1.63 %	64.5 ± 1.69 %
<b>Direct Molded, Unsterile (016A)</b>	Top Surface	70.2 %	66.8 %
	Bulk	66.0 %	62.4 %
	Bottom Surface	68.1 %	64.6 %
	Mean ± Std. Dev.	68.1 ± 2.10 %	64.6 ± 2.20 %
<b>Direct Molded, Sterile (020A)</b>	Top Surface	70.2 %	66.8 %
	Bulk	77.1 %	74.1 %
	Bottom Surface	70.5 %	67.1 %
	Mean ± Std. Dev.	72.6 ± 3.90 %	69.3 ± 4.13 %

bulk, and the bottom surface of the direct molded, sterile (020A) bearing were also analyzed. Each thin section was 100-200  $\mu\text{m}$  thick, so that a more precise determination of crystallinity variation with depth could be determined than from X-ray techniques where the specimens were about 1 mm thick.

Table 11 summarizes FTIR results from the top surface, the bulk, and the bottom surface of each type of bearing. Crystallinity from FTIR is compared to that from differential scanning calorimetry, and the percentage of the interface zone is calculated as the difference between these two measures of crystallinity. The crystallinity from FTIR is higher in the machined specimens than in the direct molded ones, in the unsterile condition. Sterilization of the direct molded bearing had little effect on its average crystallinity. The percent interface zone is higher in the direct molded bearing than in the machined bearing, in the unsterile condition. Sterilization of the direct molded bearing resulted in a sizeable decrease in the percent interface zone.

Figure 24 shows the crystallinity results from FTIR spectroscopy plotted as depth profiles, for the unsterile specimens. The top bearing surface is plotted as zero depth at the left, and the bottom bearing surface is plotted at the right (although the bearings were actually much thicker than 4 mm – about 8 mm thick). Due to physical constraints in microtoming the thin sections from the specimen block, depths could only be analyzed to about 1 mm from the bottom and about 2.5 mm from the top.

The range of crystallinities for all UHMWPE specimens was 57 – 74% by FTIR spectroscopy, which is similar to that from wide angle X-ray diffraction. The FTIR data shows that the direct molded tibial bearing had a more uniform distribution of crystallinity vs. depth than the machined bearing. The range of crystallinities for the direct molded bearing was 63 – 72%, while that for the machined bearing was 57 – 74%.

From the top surface of the direct molded bearing, the crystallinity increased from 67% at the surface up to 71% just below the surface, showing a slight increase in crystallinity at depths up to about 600  $\mu\text{m}$ . Then the crystallinity decreased and remained almost constant at

**Table 11. Results from FTIR Spectroscopy and DSC determine the amount of interface.**

Specimen Type	Location	% Crystallinity from FTIR	% Crystallinity from DSC	% Interface (FTIR – DSC)
Machined, Unsterile (018A)	Top Surface	73.1 %	55.4 %	17.7 %
	Bulk	68.0 %	56.6 %	11.4 %
	Bottom Surface	73.4 %	57.9 %	15.5 %
	Mean ± Std. Dev.	71.53 ± 2.98 %	56.63 ± 1.25 %	14.87 ± 3.20 %
Direct Molded, Unsterile (016A)	Top Surface	67.2 %	42.9 %	24.3 %
	Bulk	66.2 %	49.1 %	17.1 %
	Bottom Surface	68.4 %	51.0 %	17.4 %
	Mean ± Std. Dev.	67.27 ± 1.10 %	47.67 ± 4.24 %	19.60 ± 4.07 %
Direct Molded, Sterile (020A)	Top Surface	67.2 %	57.3 %	9.9 %
	Bulk	63.8 %	60.1 %	3.7 %
	Bottom Surface	71.5 %	59.3 %	12.2 %
	Mean ± Std. Dev.	67.50 ± 3.86 %	58.90 ± 1.44 %	8.60 ± 4.40 %

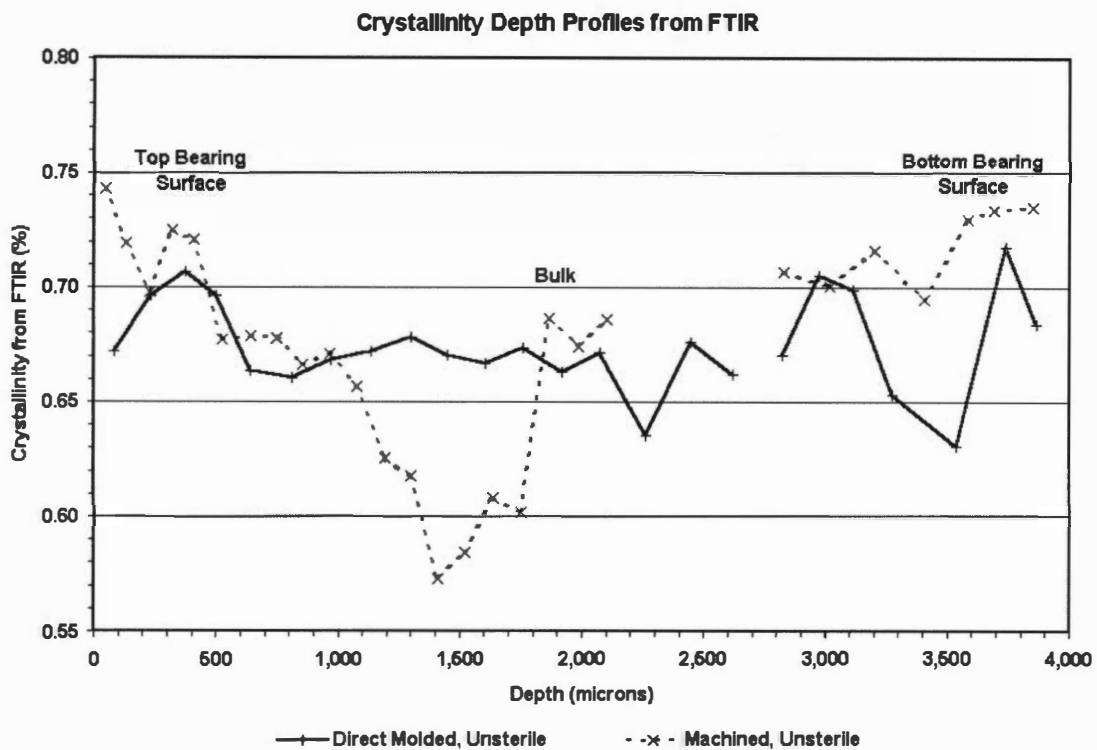


**Figure 24. Crystallinity vs. depth results from FTIR spectroscopy for direct molded vs. machined tibial bearings (unsterile).**

63 – 68% down to depths of over 2,500  $\mu\text{m}$ . From the bottom surface (which is machined) of the direct molded bearing, the crystallinity varied irregularly between 63% and 72% down to depths of about 1,000  $\mu\text{m}$ .

From the top surface of the machined bearing, the crystallinity decreased from 74% at the surface down to 57% about 1,500  $\mu\text{m}$  below the surface. Then the crystallinity increased up to 67 – 68% in the bulk. There is not sufficient data to determine whether the crystallinity remained relatively constant or varied throughout the central region of the bearing's thickness. From the bottom surface of the machined bearing, the crystallinity decreased from 73% at the surface to as low as 69% at depths up to 1,000  $\mu\text{m}$ . Comparing the two types of tibial bearings, the machined bearing had higher crystallinities than the direct molded bearing at both the top and bottom surfaces. However, the machined bearing also had greater variability in crystallinity as a function of depth, particularly from the top surface.

In contrast, the direct molded bearing had a fairly uniform level of crystallinity versus depth, particularly at depths of 600 – 2,500  $\mu\text{m}$  from the top surface. This uniformity of crystallinity indicates that the thermal cycles used to produce the direct molded bearing were more homogeneous and better controlled than those used to produce the machined bearing. This uniformity in crystallinity may contribute to better control over micromechanical properties and performance issues related to the long-term release of wear debris.

## **7.6 DIFFERENTIAL SCANNING CALORIMETRY**

Differential scanning calorimetry experiments were performed on specimens from the top bearing surface, the bottom bearing surface, and the bulk of the following tibial bearings: machined, unsterilized (018A); direct molded, unsterilized (016A); and direct molded, sterilized (020A). It was not possible to analyze the machined, sterilized specimens (019A) due to the breakdown of the calorimeter. Specimens were removed from the load-bearing region of each implant, 1.5-2.0 cm from the specimens for confocal and nanoindentation analysis, and adjacent to the specimens for small angle X-ray scattering. The calorimetry measurements

were made on a subset of the specimens analyzed with FTIR spectroscopy, following the FTIR measurements. These specimens included the top bearing surface, the last specimen (i.e. bulk) in the series from the top surface, and the bottom bearing surface.

Quantitative results from differential scanning calorimetry are summarized in Table 12. These results include heat of fusion, which was used to calculate crystallinity, and the peak melting temperature, which was used to calculate interfacial free energy using SAXS lamellar thickness from Table 8 (p. 141). For comparison, values of interface thickness are listed from SAXS.

Crystallinities from DSC as a function of specimen position are plotted as a bar chart in Figure 25. This chart shows that the direct molded, unsterile tibial bearing had the lowest crystallinities, the machined, unsterile bearing had intermediate values, and the direct molded, sterile bearing had the highest values (which were just slightly higher than those from the machined, unsterile bearing). Sterilization with gamma irradiation was shown to increase the crystallinity of the direct molded tibial bearing. The absolute values of crystallinity from DSC were much lower than those measured by SAXS, WAXD, and FTIR. The trends observed from DSC in ranking of crystallinity values for different types of tibial bearings were similar to those from SAXS and FTIR, but were different from the WAXD results.

Peak melting temperatures from DSC as a function of specimen position are plotted as a bar chart in Figure 26. This chart shows that the machined, unsterile tibial bearing specimens had higher peak melting temperatures (and therefore thicker lamellae) than the direct molded, unsterile tibial bearing specimens. This was consistent with results from SAXS. Sterilization of the direct molded tibial bearing had significantly raised the peak melting temperatures by about 3.2°C, due to crystallization of the interface zone that increased the lamellar thickness and decreased the interfacial energy.

Lamellar thicknesses calculated from the Gibbs-Thomson equation (using the peak melting temperatures) are compared to those measured from SAXS in Figure 27. Calculated values from the Gibbs-Thomson equation are plotted as lines in Figure 27, and the SAXS

**Table 12. Results from Differential Scanning Calorimetry.**

Specimen Type	Location	Heat of Fusion (J/g)	% Crystallinity*	Melting Temperature (C)			Interfacial Free Energy** (erg/cm <sup>2</sup> )	SAXS Interface Thickness (nm)
				Begin	Peak	End		
Machined, Unsterile (018A)	Top Surface	160.1	55.4 %	71.7	137.6	142.3	134	13.5
	Bulk	163.7	56.6 %	74.3	138.0	143.1	130	9.0
	Bottom Surface	167.2	57.9 %	74.5	138.4	143.2	120	12.2
	Mean ± Std. Dev.	163.67 ± 3.55	56.63 ± 1.25 %		138.00 ± 0.40		128.0 ± 7.21	11.57 ± 2.32
Direct Molded, Unsterile (016A)	Top Surface	124.0	42.9 %	109.1	134.1	138.0	167	16.4
	Bulk	141.9	49.1 %	90.2	135.4	141.0	146	11.5
	Bottom Surface	147.3	51.0 %	89.3	136.0	141.6	141	11.8
	Mean ± Std. Dev.	137.73 ± 12.20	47.67 ± 4.24 %		135.17 ± 0.97		151.3 ± 13.8	13.23 ± 2.75
Direct Molded, Sterile (020A)	Top Surface	165.6	57.3 %	78.3	137.6	141.9	113	6.3
	Bulk	173.7	60.1 %	78.2	138.2	141.6	98	2.2
	Bottom Surface	171.5	59.3 %	78.2	139.4	143.1	86	7.9
	Mean ± Std. Dev.	170.27 ± 4.19	58.90 ± 1.44 %		138.40 ± 0.92		99.0 ± 13.5	5.47 ± 2.94

\* Crystallinity was calculated based on a heat of fusion value of 289 J/g for fully crystalline polyethylene.<sup>236</sup>

\*\* Interfacial free energies were calculated from the Gibbs-Thomson equation using the following parameters:  $T_m^0 = 417.65$  K, heat of fusion of  $2.89 \times 10^9$  erg/cm<sup>3</sup>, and lamellar thicknesses from small angle X-ray scattering (refer to Table 8).



### Crystallinity from DSC

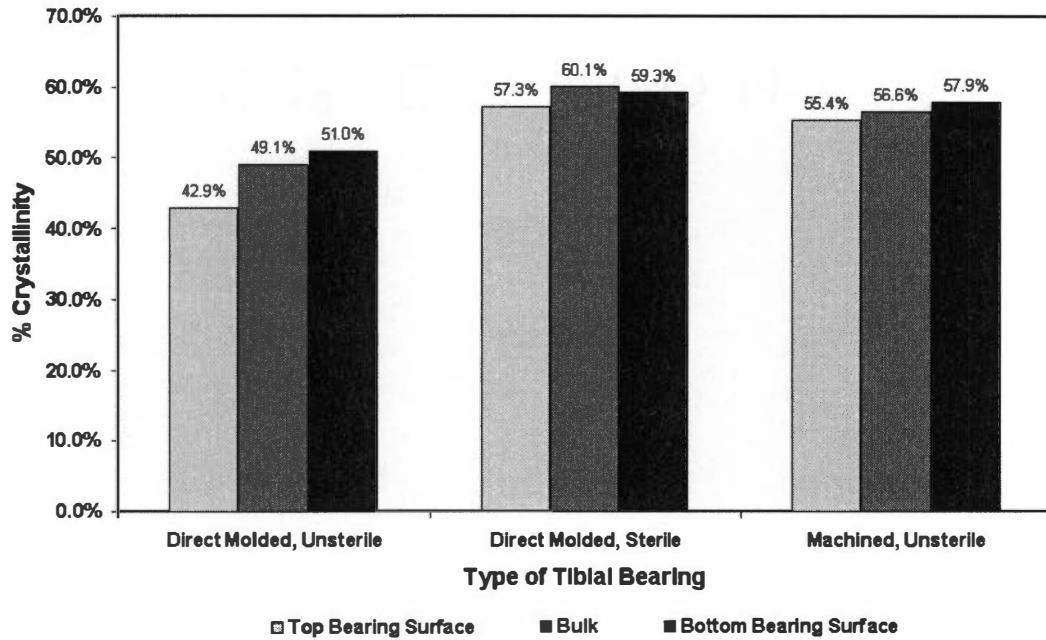


Figure 25. Bar chart of crystallinities from DSC analyses of UHMWPE tibial bearings comparing the top surface, the bulk, and the bottom surface.

### Melting Temperature from DSC

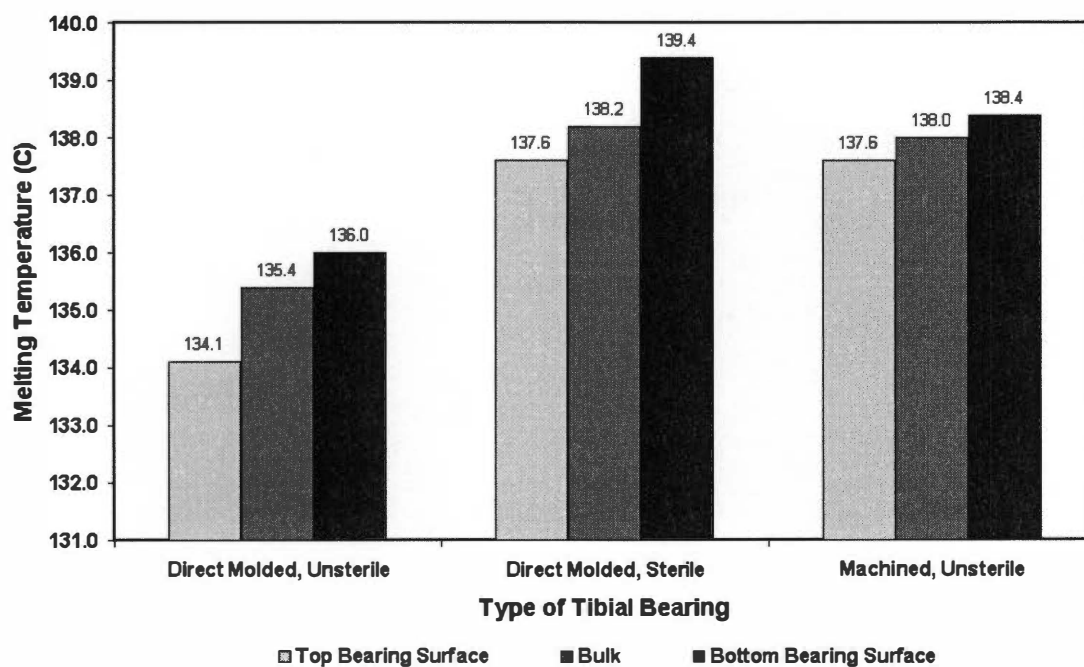
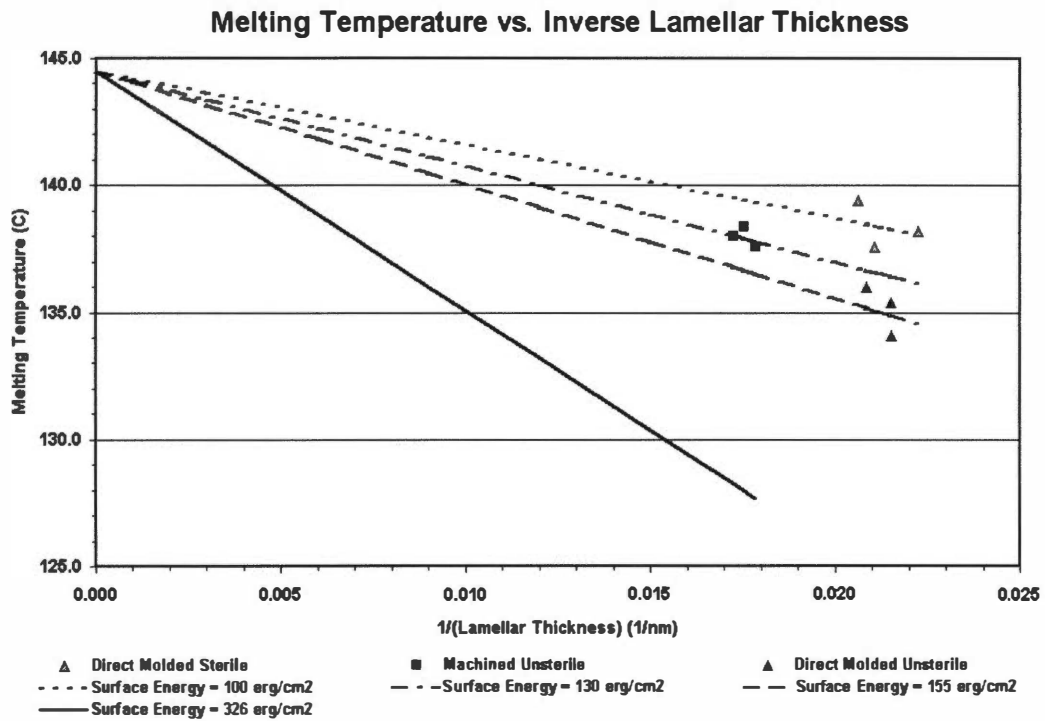


Figure 26. Bar chart of peak melting temperatures from UHMWPE tibial bearings comparing the top surface, the bulk, and the bottom surface.



**Figure 27. Peak melting temperature (from DSC) vs. inverse of lamellar thickness (from SAXS) for UHMWPE specimens from tibial bearings.**

measurements are plotted as points. The overall trends from the SAXS measurements were repeated in the calculated lamellar thicknesses, when the surface energies were adjusted to fit the measured data points (see Table 12). Differences between the top surface, the bulk, and the bottom surface (particularly for the direct molded bearings) were expanded in the calculated lamellar thicknesses. This was not unexpected, as the DSC specimens were much thinner than the SAXS specimens and therefore more sensitive to any variations in lamellar thickness with depth from the surface. The peak melting temperature from DSC can be measured directly at a very fine resolution (0.1°C), which is more sensitive than the indirect determination of lamellar thickness from SAXS (which is determined from the 1-dimensional correlation function as a difference between the long period and the amorphous thickness).

The Gibbs-Thomson equation uses the equilibrium melting temperature (for an infinite molecular weight, crystallized polymer chain), the heat of fusion (for a completely crystalline polymer molecule), and the interfacial free energy to calculate the lamellar thickness from the measured melting temperature. However, the interfacial free energy ( $\sigma_e$ ) is not a constant, but can vary depending on the molecular weight and on the structure of the interfacial zone between the crystalline lamellae and the amorphous phase. Values of  $\sigma_e$  as high as 326 erg/cm<sup>2</sup> have been reported for polyethylene with molecular weights above 10<sup>5</sup> g/mole, which had a significant interfacial zone. Values as low as 76 erg/cm<sup>2</sup> have been reported for low molecular weight polyethylene in the extended chain conformation.<sup>236</sup> Values of  $\sigma_e$  are expected to vary depending on the ratio of the lamellar thickness to the extended chain length, and on the relative thickness and structure of the interfacial zone.

The data plotted in Figure 27 show that the values of  $\sigma_e$  were different between the machined unsterile specimens ( $\sigma_e \sim 130$  erg/cm<sup>2</sup>), the direct molded unsterile specimens ( $\sigma_e \sim 155$  erg/cm<sup>2</sup>), and the direct molded sterile specimens ( $\sigma_e \sim 100$  erg/cm<sup>2</sup>). Lamellar thicknesses measured by SAXS were used to calculate the  $\sigma_e$  value for each data point, as listed in Table 12. The corresponding values of interface thickness from SAXS (Section 7.3) are also listed. Values of interfacial free energy were significantly lower than the value of

326 erg/cm<sup>2</sup> previously reported for molecular weights above 10<sup>5</sup>, but fell within a reasonable range for polyethylene. The lower values of  $\sigma_a$  resulted from lower interfacial zone thicknesses in these UHMWPE bearings, which were consolidated and crystallized under high pressures to produce high crystallinities.

Interfacial free energy is plotted versus interface thickness in Figure 28. The data points for all the specimens followed a linear relationship. The fitted line intercepted the Y-axis at 78 erg/cm<sup>2</sup>, very close to the value previously reported for polyethylene in the extended chain conformation, as mentioned previously. Note that data from both the unsterilized and the sterilized specimens were fitted to the same line. One of the significant effects of sterilization was to decrease the thickness of the interface zone, thus lowering the interfacial free energy.

The DSC data curves (from the first melting cycle) for each UHMWPE specimen are shown in Figure 29: (A) for the direct molded, unsterile tibial bearing, (B) for the direct molded, sterile, tibial bearing, and (C) for the machined, unsterile tibial bearing. Each heat flow curve was normalized for specimen mass, and then the linear baseline (fit to the low temperature data on first heating of each solid polymer specimen) was subtracted so that all the curves could be aligned for comparison. This allowed direct comparison of the temperatures where onset of melting occurred.

Difference functions were calculated from the datasets shown in Figure 29 by subtracting the data for the bulk specimen from the data for the specimens at the top and bottom surfaces, for each type of tibial bearing. These difference functions are shown in Figure 30, parts A, B and C. The peak melting temperature for each specimen was labeled on these plots. When the difference function lay above the zero line, the surface specimen released more heat than the bulk specimen, and vice versa. When the difference function lay on the zero line, the surface specimen had the same normalized heat flow during melting as the bulk specimen. The height of each peak, and the area enclosed by it (in the positive or negative direction), indicates the significance of the difference between the melting

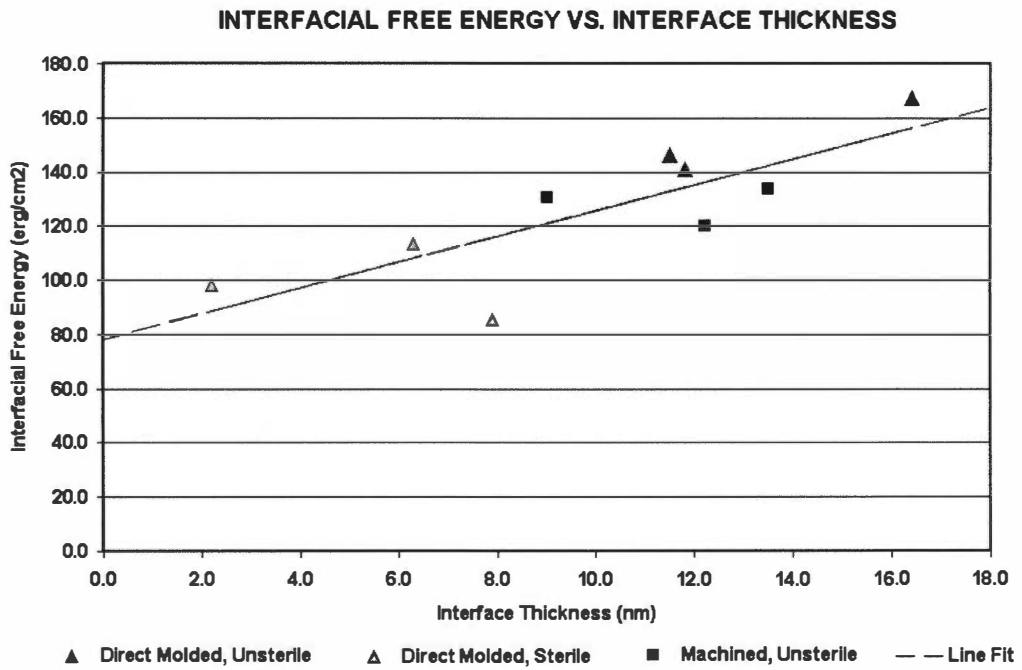
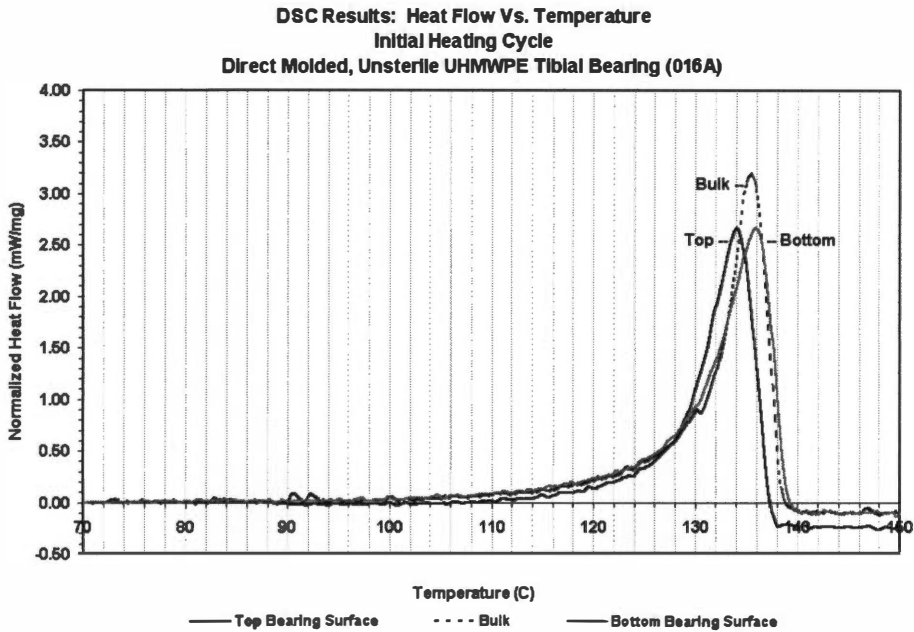
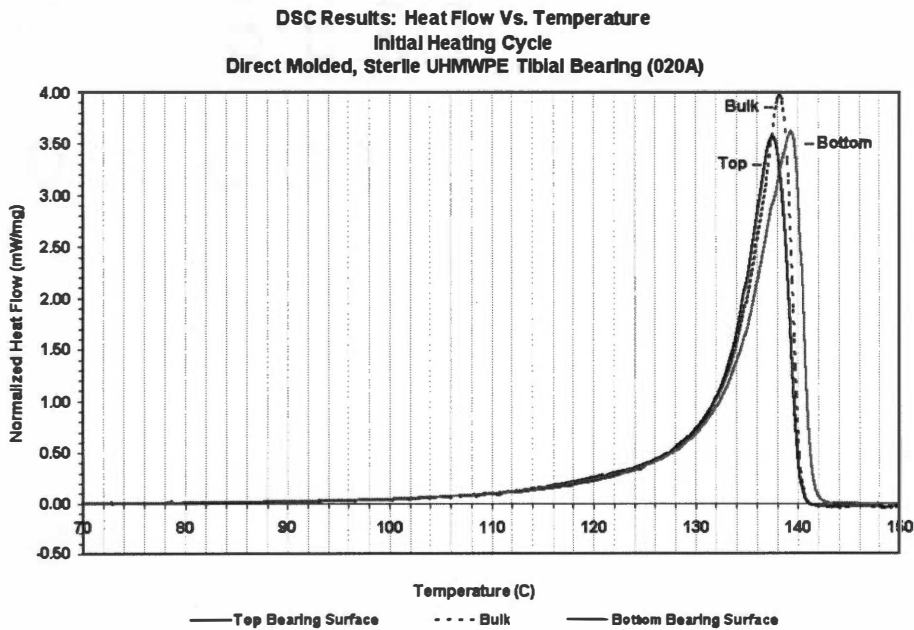


Figure 28. Interfacial free energy versus interface thickness.



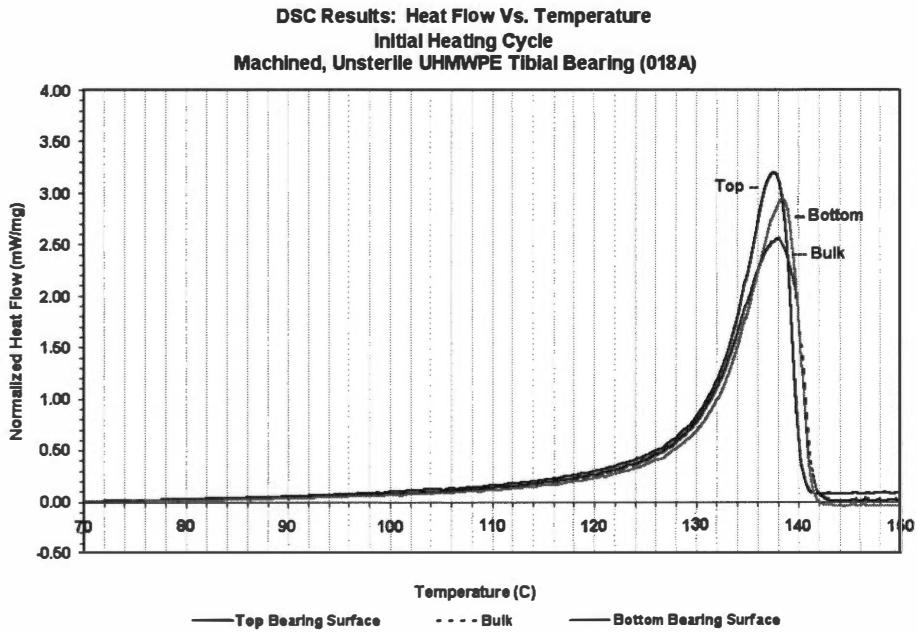
A.



B.

**Figure 29. Melting cycles from DSC for top, bulk, & bottom specimens.**

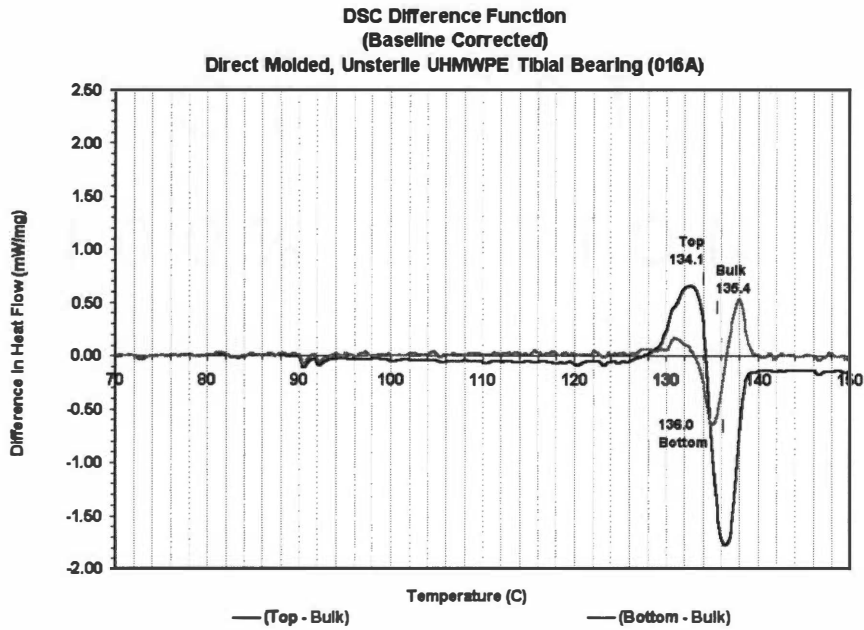
For direct molded UHMWPE tibial bearings that are (A) unsterile and (B) sterile (continued on next page).



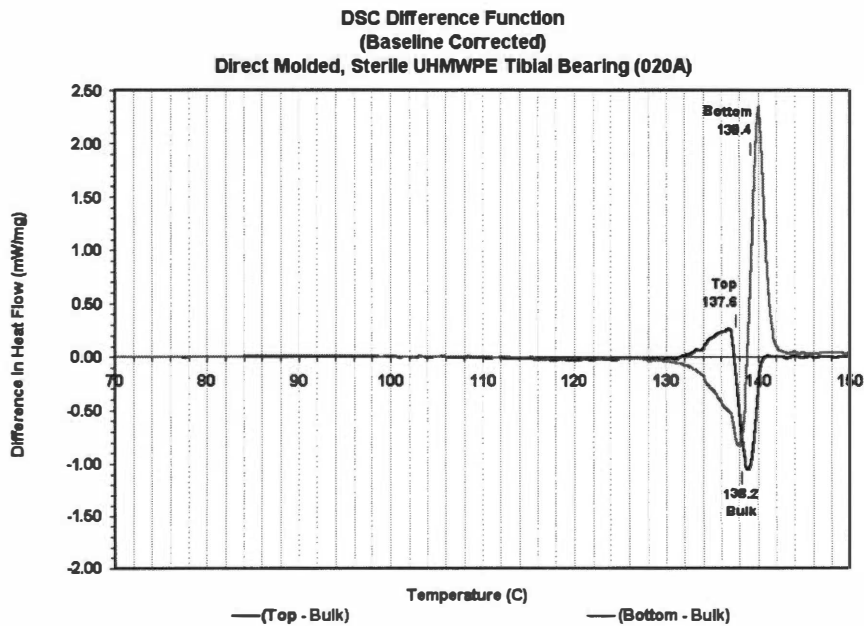
C.

Figure 29 (continued). Melting cycles from DSC for machined UHMWPE tibial bearings that are (C) unsterile.





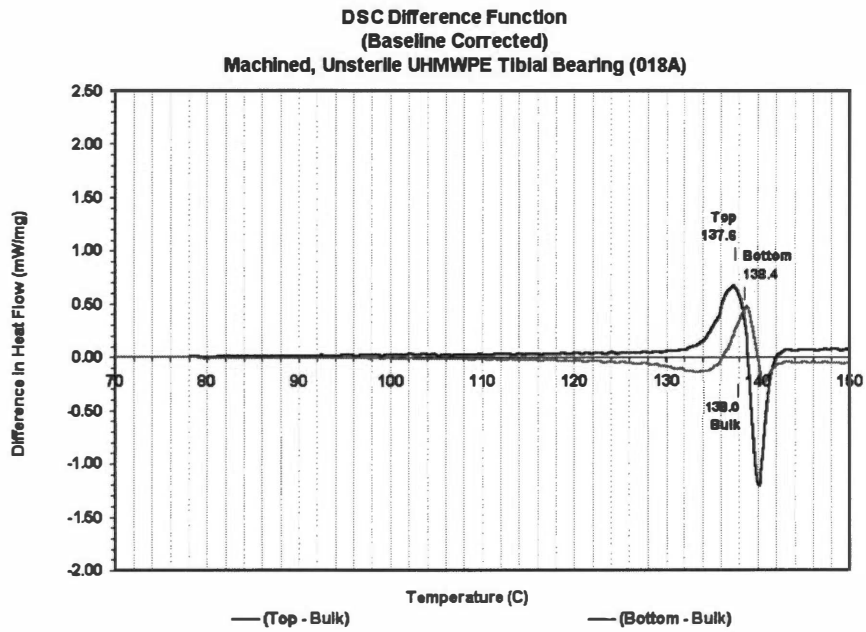
A.



B.

**Figure 30. Difference functions from DSC analysis for top & bottom specimens.**

For direct molded UHMWPE tibial bearings that are (A) unsterile and (B) sterile (continued on next page).



C.

**Figure 30 (continued). Difference functions from DSC analysis for machined UHMWPE tibial bearings that are (C) unsterile.**

behaviors of the surface and the bulk specimens.<sup>237</sup> This difference can be related to differences in lamellar thickness distribution between the surface and the bulk specimens.

Figure 29 (parts A and B) shows differences in the peak melting temperature ( $T_m$ ) as a function of specimen position for the direct molded bearings (unsterile and sterile). The top bearing surface had a lower  $T_m$  than the bulk (by 0.6 – 1.3°C), which had a lower  $T_m$  than the bottom bearing surface (by 0.6 – 1.2°C). This trend was observed in both the unsterile and the sterile tibial bearings manufactured by direct molding. The sterile bearing had  $T_m$  values that were about 3.2°C higher than values for the unsterile bearing, due to thicker lamellae. Part C shows that this same trend in  $T_m$  values versus specimen position was observed for the machined, unsterile bearing, but the differences between the peak melting temperatures were smaller (0.4°C).

Differences in onset and end melting temperatures were also observed in Figure 29, and these ranges were listed in Table 12. For the direct molded, unsterile specimens in part A, the specimen from the top surface had a narrower melting range (109.1 – 138.0°C) than the specimen from the bulk (90.2 – 141.0°C) and the specimen from the bottom surface (89.3°C – 141.6°C). Figure 30A shows that the top surface had different heat flows from the bulk at all temperatures above 90°C, whereas the bottom surface had heat flows different from the bulk only at 126 – 140°C. From 90 – 127°C, the bulk released more heat due to the melting of thin lamellae in the bulk that were not present in the top surface. Above 127°C, the difference function was determined from the melting peaks of the top surface and the bulk specimens. From 90 – 126°C, the bottom surface was identical to the bulk, and the differences in heat flow between the melting peaks were not very large at higher temperatures. These results can be related to the thermal history during direct molding and manufacturing of the tibial bearing. The top surface crystallized at a lower temperature and should have crystallized faster than the bulk, since it was in direct contact with the mold surface during the crystallization and cooling cycles. In contrast, the bottom surface of this bearing was machined after molding, so the original molded surface was removed on this side. Thus, the bottom bearing surface had

thermal properties that resembled those of the bulk. The slightly higher peak melting temperature on the bottom surface (relative to the bulk) could be due to limited annealing that resulted from frictional heat during machining.

For the direct molded, sterile specimens in Figure 29B, the melting temperature ranges were quite similar for specimens from the top surface, the bulk, and the bottom surface. All three specimens began melting around 78.2°C (which is much lower than specimens from the direct molded, unsterile specimen), but specimens from the top surface and the bulk ended melting around 141.8°C whereas the specimen from the bottom surface ended around 143.1°C. The difference functions in Figure 30B show that the top had similar heat flows to the bulk except in the range 131 – 141°C, and the bottom was different from the bulk at temperatures above 129°C. These differences resulted from the melting peaks for each specimen, as the melting peaks in Figure 29B diverged from each other around 130°C. The peak for the top surface was shifted slightly to the left of the peak for the bulk, but much less than that for the direct molded, unsterile tibial bearing. The peak for the bottom surface was shifted significantly to the right of the peak for the bulk, much more than that for the direct molded, unsterile tibial bearing.

The melting ranges for the sterilized specimens were quite different from what might be predicted, based on the ranges for the direct molded, unsterile specimens. Sterilization increased the peak melting temperatures by about 3.2°C, but the melting ranges did not follow this pattern. Melting began at much lower temperatures (by about 10 – 30°C) following sterilization, and this temperature was consistent between all three specimens. Melting ended at higher temperatures (by 1.5 – 3.9°C) for specimens from the top and bottom surfaces, but the increase was only 0.6°C for the specimen from the bulk.

Sterilization by gamma irradiation is known to produce both crosslinking and chain scission in polyethylene. Chain scission within the amorphous phase and/or the interface zone could lead to formation of new crystalline lamellae, which would be thinner than those formed during crystallization from the melt. These thinner lamellae would cause melting to begin at

lower temperatures in the sterilized specimens, and would explain why the temperature to begin melting was consistent between sterilized specimens from the top surface, the bulk, and the bottom surface. Results from this study have indicated that chain scission within the interface zone led to crystallization and increase of the thickness of adjacent lamellae. Since the end of melting temperature increased after sterilization for specimens from the top and bottom surfaces, but not for the bulk specimen, the effects of irradiation may be variable with depth from the bearing surfaces. Thus, more crystallization of the interface zone may have occurred near the top and bottom surfaces than in the bulk.

For the machined, unsterile specimens in Figure 29C, the specimen from the top surface had a slightly wider melting temperature range (71.7 – 142.3°C) than the specimens from the bulk (74.3 – 143.1°C) and from the bottom surface (74.5 – 143.2°C). The difference functions in Figure 30C show that the heat flow from the top surface was different from the bulk at temperatures above 95°C, and the bottom surface was different from the bulk at temperatures above 108°C. The melting peaks for all three specimens began around 128°C. The main body of the melting peak of the top surface was about the same width as that for the bottom surface, but was shifted to slightly lower temperatures. The width of the peak for the bulk was wider and spread from the tails of the top surface peak (at lower temperatures) to the tails of the bottom surface peak (at higher temperatures). The narrowing of the peaks for the machined surfaces, as compared to the bulk, may result from annealing due to frictional heat generated during machining.

Results from FTIR spectroscopy had previously shown that the crystallinity versus depth within this bearing was variable, suggesting a non-uniform thermal history. This may explain why the melting curves for the top and bottom surfaces were offset from each other, although similar in shape. All three curves had a long tail that extended down to low melting temperatures (much lower than for the direct molded, unsterile tibial bearing), in contrast to their peak melting temperatures that were higher than for the molded bearing. The crystallization temperature of the ArCom® UHMWPE was higher than that of the direct molded

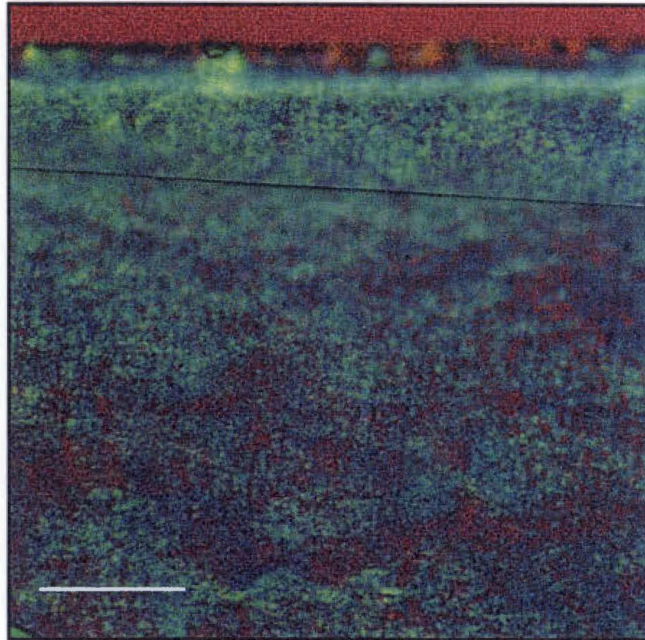
bearings, based on the higher peak melting temperature. The wide melting temperature range of the machined specimens indicates that the ArCom® UHMWPE was cooled slowly after consolidation and crystallization, which is consistent with it being processed as a large-diameter (9 cm) rod. Such a large block of polymer would cool much slower than a direct molded tibial bearing (about 1 cm thick). The lowest melting temperatures were below those for the direct molded, sterilized bearing, suggesting the possibility that chain scission might have resulted from the processing conditions (pressure and temperature) used in isostatic compression molding of ArCom®.

## **7.7 POLARIZED LIGHT MICROSCOPY**

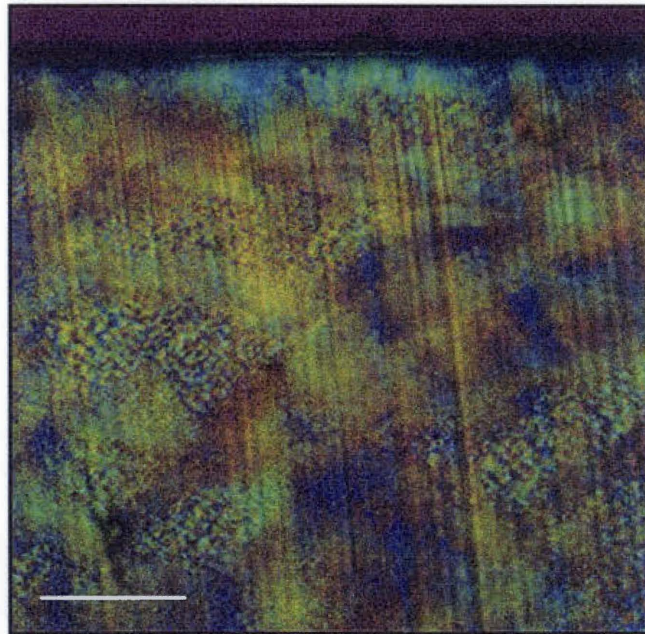
Results from polarized light microscopy are shown in Figure 31, Figure 32, and Figure 33 for unsterilized tibial bearings. Thin sections were cryomicrotomed from each type of tibial bearing, transverse to the bearing surface. In the photomicrographs, the original top surface of each implant bearing was shown at the top of the image.

Differences were observed between the two specimens. The machined bearing had a distinct layer (shown in Figure 31 as translucent at the top, with a bright band underneath) at the top surface, which resulted from plastic deformation and heating (and associated annealing) during machining. This layer was 25 – 40  $\mu\text{m}$  thick, and would be expected to wear off with 2 – 10 months (based on typical wear rates). Such a layer was not observed in the direct molded bearing, which had a uniform appearance from the bulk to the top surface.

The large-scale, bulk morphologies were also different between the two specimens. The machined specimen had a finer morphology (Figure 33A shows structures below 10  $\mu\text{m}$ ) that was uniform throughout the bulk, but with isolated regions of amorphous material (Figure 31A) that could be associated with boundaries between the original resin particles. The direct molded specimen had regions of coarse morphological features (Figure 33B shows structures 10 – 20  $\mu\text{m}$  in size) that were isolated between regions that appeared either oriented in a different direction or amorphous (Figure 31B).

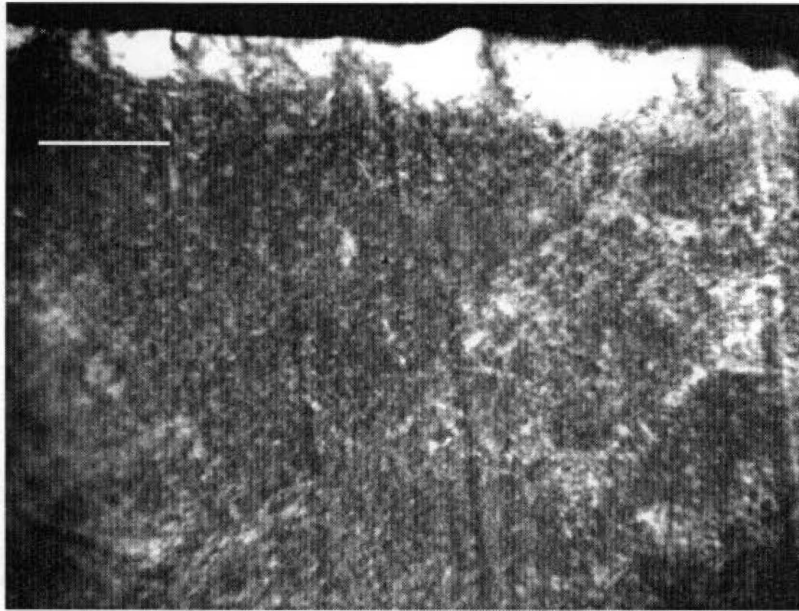


A. Machined Tibial Bearing (200X, scale bar = 100  $\mu\text{m}$ )

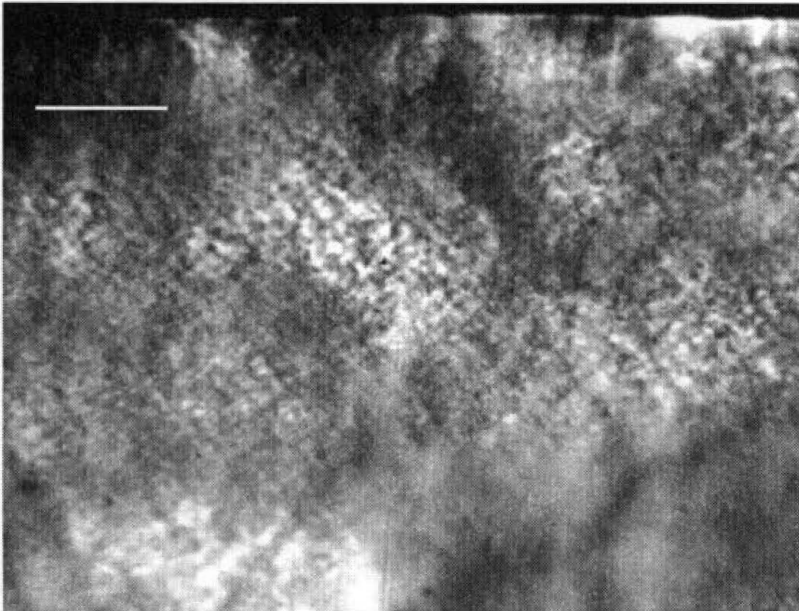


B. Direct Molded Tibial Bearing (200X, scale bar = 100  $\mu\text{m}$ )

**Figure 31. Polarized light microscopy with a quarter wave plate (200X, color). Differences in morphology are shown between (A) the machined bearing and (B) the direct molded bearing, both at the surface (top) and within the bulk.**



A. Machined Tibial Bearing (400X, scale bar = 50  $\mu\text{m}$ )

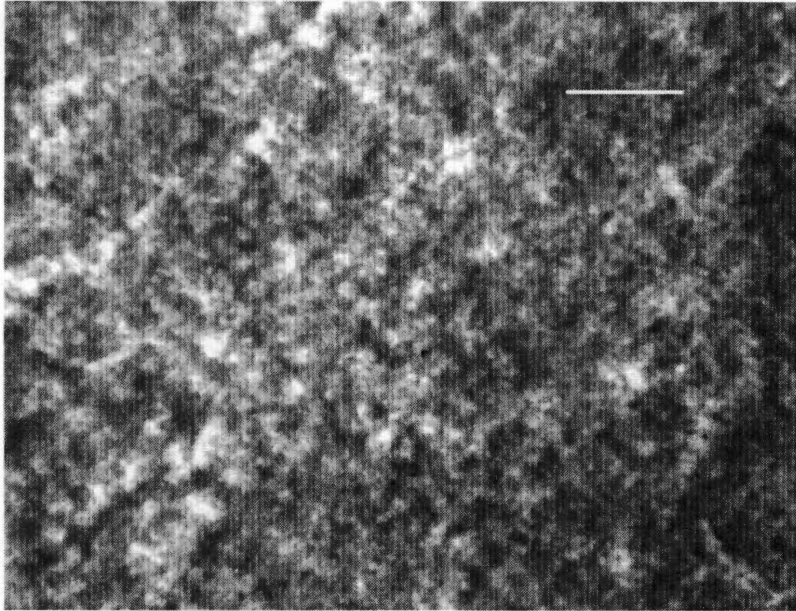


B. Direct Molded Tibial Bearing (400X, scale bar = 50  $\mu\text{m}$ )

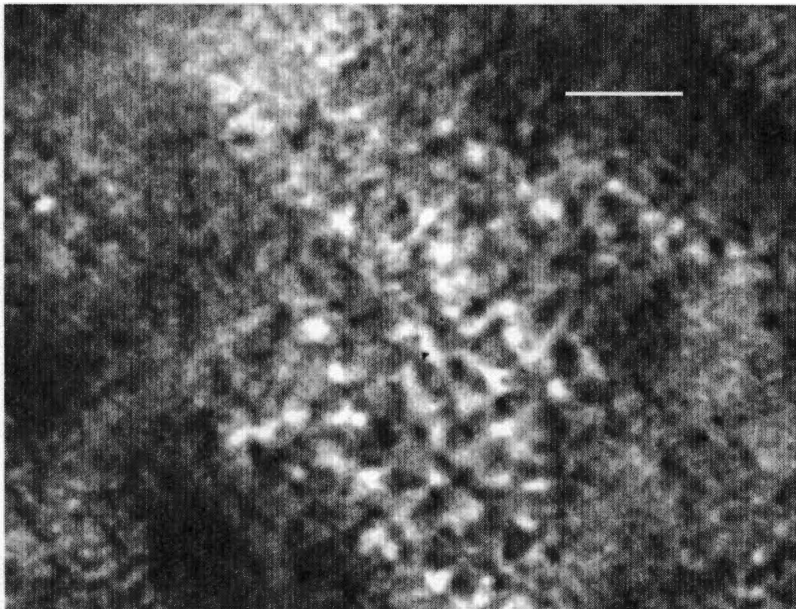
**Figure 32. Polarized light microscopy with crossed linear polarizers (400X, B&W).**

Differences in morphology are shown between (A) the machined bearing and (B) the direct molded bearing, both at the surface (top) and within the bulk.





A. Machined Tibial Bearing (1000X, scale bar = 25  $\mu\text{m}$ )



B. Direct Molded Tibial Bearing (1000X, scale bar = 25  $\mu\text{m}$ )

**Figure 33. Polarized light microscopy with crossed linear polarizers (1000X, B&W). Differences in morphology are shown between (A) the machined bearing and (B) the direct molded bearing, within the bulk.**

## 8. DISCUSSION

This research has proven that there were differences in surface texture and surface micromechanical behavior as well as in bulk and surface morphology of UHMWPE tibial bearings fabricated by machining versus direct molding. Many of these differences were present in the unsterilized tibial bearings, but additional changes in properties occurred after sterilization by gamma irradiation and shelf aging in air. Morphology was shown to be different in the bulk as well as the surfaces of the unsterilized specimens, and to undergo significant changes following irradiation and shelf aging in air for two years. These differences and changes in morphology affected micromechanical behavior and properties.

### 8.1 MORPHOLOGY OF UNSTERILE UHMWPE

Consolidation of the UHMWPE resin (Himont 1900H) powder by either isostatic compression molding (to form the ArCom® rod stock that was later machined) or by direct molding (to form bearings) produced different morphologies between these two products (prior to sterilization). These different processing methods used different thermal and pressure cycles, which produced different lamellar thicknesses and crystallinities in the unsterile UHMWPE bearings.

The machined bearing (from ArCom®) had higher values of long period and lamellar thickness than the direct molded bearing, based on SAXS analysis using the 2-phase model of crystallinity (Table 8, p. 141, and Figure 22A, p. 140). Long periods were 68 – 84 nm for the machined bearing versus 64 – 71 nm for the direct molded bearing. Lamellar thicknesses were 48 – 64 nm for the machined bearing versus 43 – 50 nm for the direct molded bearing. The peak melting temperatures from DSC (Table 12, p. 152) were also higher for the machined bearing (137 – 138°C) than for the direct molded bearing (134 – 136°C), confirming a difference in lamellar thickness. Because the amorphous thickness (based on the 2-phase model) was similar for both bearing types (20 – 22 nm), the crystallinity (from SAXS) was only slightly higher for the machined bearing (70 – 76%) than for the direct molded bearing (67 –

71%). Results from the bearing surfaces were similar to that from the bulk, so all three were averaged together for each bearing type.

When results from FTIR and DSC analyses were used to apply the 3-phase model of crystallinity to the SAXS data (Figure 22B, p. 140, and Table 9, p. 142), the average lamellar thicknesses decreased and a sizeable interface thickness was found. Lamellar thicknesses were distinctly higher in the machined bearing (49 – 54 nm) than in the direct molded bearing (39 – 42 nm). The difference in crystallinity also became more distinct between the machined bearing (65 – 68%) and the direct molded bearing (57 – 62%).

Results from FTIR and DSC (Table 11, p. 148) confirmed that crystallinity was higher in the machined bearing, but WAXD results (Table 10, p. 146) showed a small difference in the opposite direction. Crystallinity depth profile results from FTIR (Figure 24, p. 149) showed variations in crystallinity for both bearing types. The machined bearing had a decrease in crystallinity from the top surface into the bulk, which reached a minimum at 1,400  $\mu\text{m}$  deep and then increased to a moderate value at 2,000  $\mu\text{m}$  deep. The overall range of crystallinity was from 74% at the surface down to 57%. In contrast, the direct molded bearing had a more uniform crystallinity with depth, with a range from 64% to 71%. Variations in crystallinity versus depth affected the results from WAXD, as specimens for WAXD were approximately 1 mm thick. This depth profile particularly affected the crystallinity measurements on the machined specimens, causing them to be slightly (but not consistently) lower than the measurements on the direct molded specimens. Variations in crystallinity could have resulted from either thermal effects due to machining (i.e. melting or annealing near the surface) or incomplete fusion of the resin particles during isostatic compression molding (with variations in crystallinity between different resin particles). Examination of the polymer morphology in the machined bearing by polarized light microscopy showed that the most distinct effects of machining were localized to a depth of about 40  $\mu\text{m}$  from the surface. DSC results showed that melting peaks from specimens at the top and bottom machined surfaces were slightly narrower than the peak from the bulk specimen, but this only indicated an annealing effect at depths of a couple hundred

microns. Thus, incomplete fusion of the resin particles during consolidation (isostatic compression molding) was likely causing the variation in crystallinity with depth. Previous polymer research had shown that incomplete fusion of UHMWPE resin particles resulted in boundaries remaining distinct even after sintering of the particles (rather than boundaries disappearing after complete fusion and crystallization).<sup>238</sup>

Figure 34 compared the different crystallinity measurements from DSC, FTIR, WAXD, and SAXS. The difference in crystallinity between machined and direct molded bearings (both unsterile) was small (3 – 9%), but was more distinct when the interface was excluded from the crystallinity determination (as from DSC and 3-phase SAXS results). The 2-phase SAXS crystallinities were consistently higher than the WAXD crystallinities, although the same specimens were analyzed, indicating that segregated amorphous phase occurred outside the lamellar stacks. The difference between the SAXS (2-phase) and WAXD crystallinities was larger in the machined bearing than in the direct molded bearing. This segregation was confirmed by polarized light microscopy for the unsterile bearings, particularly for the machined bearings.

On a smaller structural scale, the presence of a thick interface zone (9 - 16 nm) between the lamellae and the amorphous phase was shown by the combined 3-phase analysis of the SAXS, FTIR and DSC results (Figure 22B, p. 140, Table 9, p. 142, and Figure 23, p. 144) for unsterile specimens. However, the 1-dimensional correlation functions from SAXS (Figure 21, p. 139) had not shown the typical shape representative of a thin interface zone. The thickness of the interface (in the unsterile specimens) was almost as large as that of the amorphous phase (13-17 nm), so that the model assumed for a thin interface zone (a few angstroms thick) was not well suited for interpretation of these correlation functions.

The Gibbs-Thomson equation was used to calculate the interfacial free energies (Table 12, p. 152) based on the peak melting temperatures from DSC and the lamellar thicknesses (based on the 2-phase model) from SAXS. The interface thicknesses ( $L_i$ ) were equal to or higher and the interfacial free energies ( $\sigma_e$ ) were consistently higher in the direct

### Comparison of Crystallinity by Different Techniques

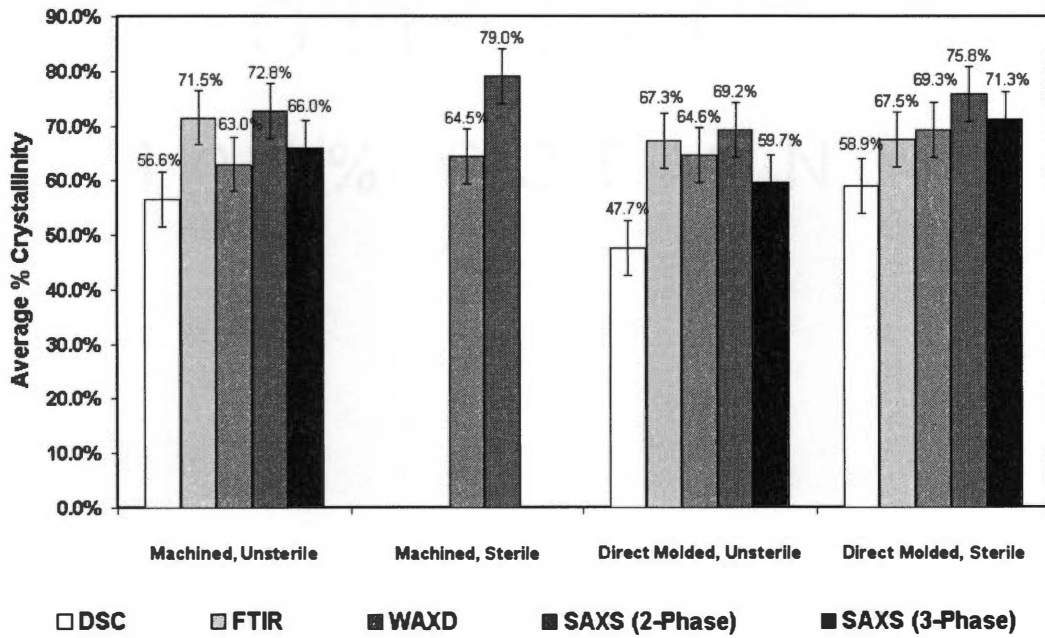


Figure 34. Comparison of crystallinity measurements by DSC, FTIR, WAXD, and SAXS.

molded specimens ( $L_i = 11.5 - 16.4$  nm,  $\sigma_e = 141 - 167$  erg/cm<sup>2</sup>) than in the machined specimens ( $L_i = 9 - 13.5$  nm,  $\sigma_e = 120 - 134$  erg/cm<sup>2</sup>). A plot of peak melting temperature versus inverse lamellar thickness (Figure 27, p. 155) confirmed that the data points did not fall along the same line, indicating differences in interfacial free energy.

A plot of interfacial free energy versus interface thickness (Figure 28, p. 158) showed a linear relationship, confirming that interfacial free energy could not be treated as a constant but instead varied with interface thickness. The intercept of the line was 78 erg/cm<sup>2</sup>, very close to the value of 76 erg/cm<sup>2</sup> previously reported for extended chain polyethylene (with a minimum interface thickness) of a low molecular weight.<sup>236</sup> This previous study had demonstrated that interfacial free energy varied depending on molecular weight, the ratio of the lamellar thickness to the extended chain length, and on the relative thickness and structure of the interfacial zone, with a minimum value for extended chain lamellae. Values as high as 326 erg/cm<sup>2</sup> were reported for polyethylene with molecular weights above 10<sup>5</sup> g/mole, but crystallization conditions were different from those used to fabricate the tibial bearings studied in this dissertation. Lamellar thicknesses had been determined by either electron microscopy or low-angle X-ray diffraction, and melting temperatures had been determined by either dilatometry or low-angle X-ray diffraction (based on the temperature where the diffraction peak disappeared).<sup>239,240</sup>

The micron-scale morphologies of the two bearing types (unsterile) were compared near their surfaces using polarized light microscopy (Figure 31, p. 167, Figure 32, p. 168, and Figure 33, p. 169). The morphology of the direct molded bearing was consistent between the bulk and the top bearing surface, showing no distinct change in structure near the surface. The machined bearing had a modified layer at the surface, 25 – 40  $\mu$ m thick, with a different morphology from the bulk due to plastic deformation and thermal effects. Figure 31A (p. 167) showed that this layer consisted of two different zones, each approximately half of the total thickness. The outer zone appeared to be non-uniformly crystalline or oriented, while the inner zone appeared to be either highly crystalline or highly oriented. The outer zone would be

highly oriented from plastic deformation during machining, unless it had melted and crystallized (perhaps quenched) from frictional heating.<sup>241</sup> The inner zone would have melted due to heat transfer from the surface, but would have cooled and crystallized much slower due to low thermal conductivity. Thus, the inner zone would have a higher crystallinity than the outer zone.

The modified layer on the machined bearing was so thin that it had a limited effect on FTIR and DSC analyses (specimen thickness 160 – 310  $\mu\text{m}$ ) comparing the surfaces to the bulk, and had little or no effect on WAXD and SAXS analyses (specimen thickness  $\sim 1$  mm). The FTIR depth profile (Figure 24, p. 149) showed an increase in crystallinity at the surface, but this trend extended through many specimens to a total depth of 1,400  $\mu\text{m}$  from the top surface. Thus, the variation in crystallinity resulted from more than just this thin, modified layer at the surface. Specimens from the top and bottom surfaces had higher FTIR crystallinities than the one from the bulk (Table 11, p. 148), but this trend extended beyond the range of the modified layer. Surface specimens analyzed with DSC had very similar crystallinities to the bulk specimen (Table 12, p. 152), and their peak melting temperatures did not vary significantly with specimen position. The widths of the melting peaks were slightly narrower for the top and bottom surfaces relative to the bulk (Figure 29C, p. 159), indicating that machining had an effect similar to annealing at the surfaces.

The significance of the modified layer was that polymer molecules in that region had been stretched and oriented in the machining direction, possibly leading to increased crystallization. Thus, these molecules would be less flexible and more stiff, and would fracture at a lower additional strain. The crystallinity may have increased, thus reducing the elasticity by reducing the amorphous phase fraction. This would contribute to increased plastic deformation upon loading. The articulations at the bearing surfaces would contribute to increased orientation and strain of these molecules until fracture occurred. Thus machining could reduce the number of articulating cycles leading to the release of wear debris particles, by pre-orienting the polymer molecules at the surface. This might not affect the long-term

wear performance, as this modified layer would be removed within 2 – 10 months (based on typical clinical wear rates).

Polarized light microscopy showed that the micron-scale, bulk morphologies were also different between the two specimens. The machined specimen had a finer crystalline morphology (Figure 33A, p. 169, showed structures below 10  $\mu\text{m}$ ) that was uniform in scale throughout the bulk. It contained isolated regions of amorphous material (shown in red in Figure 31A, p. 167) that could be associated with boundaries between the original resin particles (Table 5, p. 101), due to their size and spacing. The direct molded specimen had regions of coarse crystalline features (Figure 33B showed structures 10 – 20  $\mu\text{m}$  in size) that were separated by regions that appeared oriented in a different direction (Figure 31B). The scale of these different regions was below 150  $\mu\text{m}$ , slightly smaller than resin particles. Regions of segregated amorphous material were not as distinct as in the machined bearing, if they were present. These observations confirmed that the direct molding process was more effective in melting, fusing, and consolidating the UHMWPE resin than the isostatic compression molding process. Previous research has shown that melting of nascent UHMWPE powder is kinetically controlled,<sup>242</sup> and can proceed slowly depending on the temperature.

Differences in the thermal histories of the machined versus direct molded bearings from fabrication, prior to sterilization, were determined from DSC data. Figure 35 compared the initial melting cycles from bulk specimens of each bearing type. The machined bearing (ArCom®) was crystallized at a high temperature (peak melting temperature = 138°C), but crystallization occurred over a wide temperature range. The fine crystalline morphology (described above) indicated that the UHMWPE was melted, then held at the crystallization temperature for a short time before beginning the cooling cycle. The cooling rate was slow, because of the large thickness of the fabricated rod. Thus, significant crystallization occurred during the cooling cycle, producing a broad melting peak from DSC that extended from an



**DSC Results: Heat Flow Vs. Temperature  
Initial Heating Cycle  
Bulk Specimens from UHMWPE Tibial Bearings**

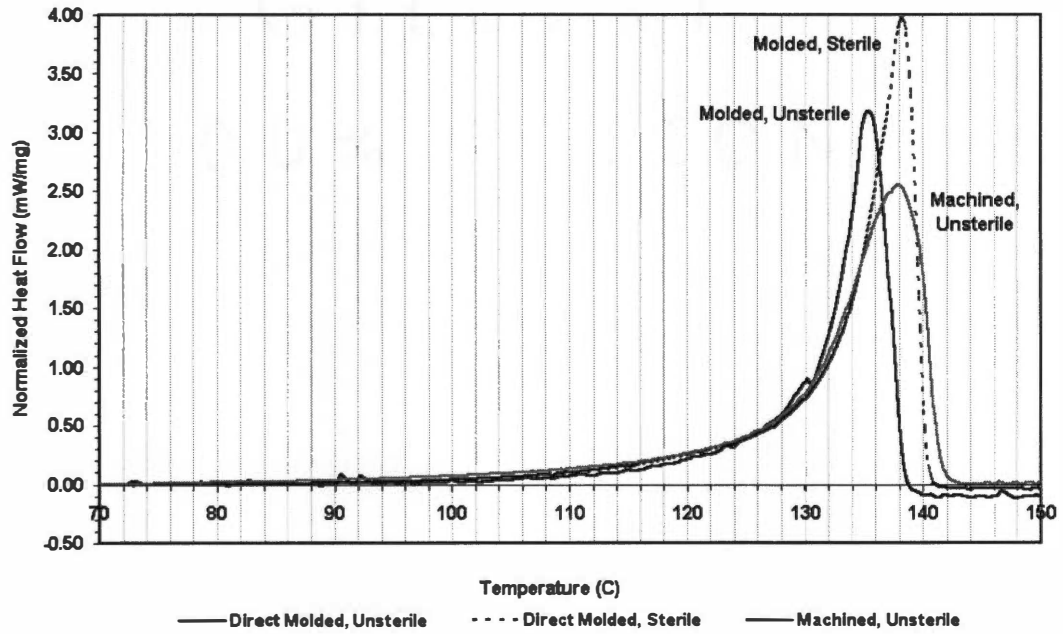


**Figure 35. Comparison of melting cycles from DSC for types of tibial bearings.**

onset temperature of 74°C to an end temperature of 143°C. The slow cooling also broadened the range of lamellar thicknesses produced, as shown by the long period data in Table 8 (p. 141) and the low height and large width of the first maximum in the one-dimensional correlation function (Figure 21, p. 139). Crystallization at lower temperatures during the cooling cycle produced finer crystalline morphologies, due to the increased nucleation rate and the decreased growth rate.

The direct molded bearing was crystallized at a lower temperature (peak melting temperature = 135°C), and crystallization occurred over a narrow temperature range. The coarse crystalline morphology indicated that the polymer was held at a relatively high crystallization temperature for an extended time, allowing large lamellar stacks (or domains) to grow. Thus, most of the crystallization occurred within a narrow temperature range, and less crystallization occurred on cooling. In addition, the comparably thin cross-section (~1 cm thickness) of the tibial bearing allowed a faster cooling rate than for a large rod. Thus, the melting peak was narrower, extending from an onset temperature of 90°C to an end temperature of 141°C. Likewise, the range of lamellar thicknesses was narrower, as shown by the long period data in Table 8 (p. 141) and the well-defined first maximum in the one-dimensional correlation function (Figure 21, p. 139). Crystallization at higher temperatures produced larger crystalline domains, due to the decreased nucleation rate and the increased growth rate.

Although polarized light microscopy did not show a modification of the top surface in the direct molded bearing, DSC results indicated differences in crystalline morphology between the top surface (as molded), the bulk, and the bottom surface (machined). The top surface had a lower crystallinity than the bulk or the bottom surface (which had similar values) based on DSC results (Table 11, p. 148), although this difference was not present in FTIR crystallinities (which included the interface). The top surface also had a lower peak melting temperature and a narrower melting range than either the bulk or the bottom surface (Table 12, p. 152, and Figure 29, p. 159). These differences translated into a higher interface

thickness and a higher interfacial free energy at the surface. This increase in the interface resulted from the thermal history during direct molding and manufacturing of the tibial bearing. The top surface crystallized at a lower temperature and faster than the bulk, since it was in direct contact with the mold surface during the crystallization and cooling cycles. Most of its crystallization would have occurred while the mold was held at the crystallization temperature, rather than on cooling. In contrast, the bottom surface was machined after molding so the original molded surface was removed on that side. Thus, the bottom bearing surface had thermal properties that were more like those of the bulk. The bulk finished much of its crystallization while the mold was held at the crystallization temperature, but additional crystallization occurred during the cooling cycle. The bottom surface had slightly higher values of crystallinity and peak melting temperature than the bulk (Table 12, p. 152), and had heat flows different from the bulk at 126 – 140°C (Figure 30A, p. 161). These differences indicated that machining of the bottom surface induced limited annealing from frictional heating. This annealing was observed in the machined bottom surface of the direct molded bearing, but was not as distinct in the surfaces of the machined bearing (except for a slight narrowing of the melting peaks), because of the difference in lamellar thicknesses. The lamellae were thinner in the direct molded bearing, allowing annealing to occur at a lower temperature.

Interface thickness and associated interfacial free energy were related to crystallization conditions, particularly temperature and time. Larger interface thicknesses resulted from crystallization at high temperatures, where most of the crystallization occurred within a narrow temperature range (as for the top surface of the direct molded bearing). When increased amounts of crystallization occurred during the cooling cycle, the interface thickness decreased (as for the bulk of the direct molded bearing and the machined bearing).

## **8.2 MORPHOLOGY OF IRRADIATED & AGED UHMWPE**

Gamma irradiation and shelf aging in air caused changes in the morphology of UHMWPE. These changes resulted from chain scission and crystallization that occurred

primarily in the interface and to a lesser extent in the amorphous phase. Previous work by others had shown that gamma irradiation increased the crystallinity of UHMWPE resin powder (Hercules 1900) within a range of low doses (below 5 Mrad).<sup>243</sup> The researchers interpreted this result as due to chain scission exceeding crosslinking where the strain energy in the polymer chains was high, particularly at entanglements. Chain scission was predicted to occur primarily in the amorphous phase and on lamellar surfaces (i.e. in the interface zone). Results of the present research support this interpretation, as a small increase in crystallinity resulted from a large decrease in the interface, a small decrease in the amorphous phase, and a small increase in the crystalline phase, with a net decrease in the long period.

Changes in morphology of the direct molded tibial bearing were determined by applying the 3-phase model of crystallinity to combined data from SAXS, WAXD, FTIR, and DSC (Figure 22B, p. 140, and Table 9, p. 142). The largest change was the decrease in the thickness of the interface (by about 60%) that resulted from chain scission. A smaller decrease in the thickness of the amorphous phase (by 10-15%) also occurred. The chain fragments then partially crystallized, contributing to an increase in the lamellar thickness (by about 10%). Thus, the long period decreased after sterilization. Similar effects were predicted and estimated for the machined tibial bearing, although FTIR and DSC data were not obtained from those specimens. (Note: The breakdown of the differential scanning calorimeter made it impossible to run the sterile, machined bearing specimens. Thus FTIR could not be used to characterize the interface, so FTIR analyses were not run.) The machined bearings were fabricated from the same UHMWPE resin as the direct molded bearings, and had significant thicknesses of interface zone and amorphous phase in the unsterile condition, so similar effects of irradiation and shelf aging were predicted. The increased lamellar thickness in the machined bearings could slow the migration of free radicals from the interior of the lamellae to the interface zone, but would not affect radicals formed in the interface or the amorphous phase.

Changes due to irradiation were not as distinct when the 2-phase model of crystallinity (without considering the interface) was used to interpret the SAXS and WAXD data (Figure 22A, p. 140, and Table 8, p. 141) for both direct molded and machined bearings. Based on this model, the amorphous thickness decreased but the lamellar thickness did not change, resulting in an overall decrease in the long period. Because the interface was divided between the amorphous and crystalline phases in this model, the increase in percent crystallinity after irradiation was smaller in magnitude than in the 3-phase model.

Sterilization and shelf aging caused a small increase in crystallinity in both machined and direct molded bearings, based on results from SAXS and WAXD, and in the direct molded bearings based on DSC results. However, FTIR results did not show a significant increase in crystallinity in the direct molded bearing. Crystallinity determinations from DSC excluded the interface from the crystalline phase, determinations from FTIR included the interface in the crystalline phase, and determinations from SAXS (based on the 2-phase model) included half the interface thickness in the crystalline phase but excluded any segregated amorphous phase outside the lamellar stacks. Thus, the crystallinity values from SAXS (2-phase model) should be intermediate between those from DSC and from FTIR, unless amorphous phase is segregated outside the lamellar stacks. The measured crystallinities from FTIR were consistently equal to or less than those from SAXS (2-phase model) for all specimens, confirming that segregated amorphous phase was present in both types of tibial bearings. This compensated for the small increase in crystallinity within the lamellar stacks, so that the change was not distinguishable by FTIR.

The increases in crystallinity and lamellar thickness resulted in increases in peak melting temperatures, and the decrease in interface thickness resulted in a decrease in interfacial energy (Table 12, p. 152, and Figure 26, p. 154) for the direct molded bearing. Thus, peak melting temperatures correlated well with the changes in crystalline structure determined from other measurements. The calculated interfacial free energies for the sterile,

direct molded, specimens followed the linear relationship versus interface thickness (Figure 28, p. 158) previously shown for the unsterile specimens of both bearing types.

The presence of thin lamellae, crystallized following chain scission, was confirmed by a significant decrease in the onset melting temperature (Table 12, p. 152) for sterile, direct molded, bearing specimens, when the peak melting temperature increased. The onset melting temperature decreased from 89 – 109°C (for unsterile specimens) to a constant value of 78°C (for sterile specimens) after irradiation and shelf aging. Chain scission within the amorphous phase and/or the interface zone led to formation of new crystalline lamellae that were thinner than those formed during crystallization from the melt. These thinner lamellae melted at lower onset temperatures in the sterile specimens (relative to onset temperatures in the unsterile specimens). The onset melting temperature was consistent between sterilized specimens from the top surface, the bulk, and the bottom surface.

Results from this study have shown that chain scission within the interface zone led to crystallization and increase of the thickness of adjacent lamellae. The end of melting temperature (Table 12, p. 152) increased from 138 – 142°C (unsterile) to 142 – 143°C after sterilization for direct molded specimens from the top and bottom surfaces. However, this temperature remained constant at 141 – 142°C for the bulk specimen. The peak melting temperatures from the top and bottom surfaces increased by 3.4 – 3.5°C after sterilization, while that from the bulk only increased by 2.8°C. The effects of irradiation varied with depth from the bearing surfaces. Thus, more crystallization of the interface zone occurred near the top and bottom surfaces than in the bulk. This can be explained by heterogeneous oxidation occurring due to diffusion of oxygen from the surfaces into the bulk, as described in Section 3.5.3.1.

### **8.3 SURFACE TEXTURE**

Surface texture differences resulted from the different fabrication methods – machining versus direct molding of UHMWPE tibial bearings. As expected, the machined

surfaces had a rougher, more irregular texture or topography than the direct molded surfaces. Confocal light microscopy demonstrated this at relatively low magnifications (100 – 200X), and provided quantitative data for calculation of the roughness average ( $R_a$ ), the RMS roughness ( $R_q$ ), and the skewness ( $R_{sk}$ ).

The machined surface was rough and irregular, as shown in Depth Maps from confocal microscopy in Figure 11B (p. 114) and Figure 13B (p. 117). Machining left an oriented topography on the surface along the machining direction, with fine machining lines (from defects in the cutting tool) oriented parallel to the X-direction (horizontal) of these micrographs. The interaction between the chatter of the machine tool and the large-scale structure of UHMWPE (due to the sintering of resin powder particles) created other features on the surface, oriented generally normal to the machining direction (i.e. along the Y-direction). These features had irregular, scalloped boundaries, with the scallops extending over large lateral distances, and they were spaced 150-350  $\mu\text{m}$  apart (along the X-direction) with a relatively smooth region between the boundaries. The scalloped edges indicated localized plastic deformation of the polymer as it was cut (or torn) by the cutting tool, and likely resulted from incomplete fusion and segregation of amorphous material at the boundaries of resin particles. The lateral spacing of the scallops was comparable to the size of resin powder particles (Table 5, p. 101).

The direct molded surface was very smooth, as shown in Depth Maps from confocal microscopy in Figure 12B (p. 116) and Figure 14B (p. 118). The banded appearances of these images resulted from regions of constant height – the surface was smoother than the Z-increment of the topographic measurements. This type of banded appearance appears as an artifact in any digital image where adjacent regions have constant intensity (gray-scale) values that vary by small increments. The slight curvature of these bands was representative of the true 3-dimensional topography of the bearing surface. Very fine scratches and surface defects were visible in the Maximum Intensity images. Some of these were also visible in the corresponding Depth Maps, but others were too shallow to be resolved in the Z-direction. No

surface features revealed any structures or boundaries related to the original resin powder, indicating that a high-quality molding process was successful in consolidating the resin particles at the surface.

All three surface texture parameters were found to be significantly different between the machined versus the direct molded tibial bearings (Table 6, p. 119), quantifying the visual observations described above. The direct molded bearings had significantly lower measurements of  $R_a$  and  $R_q$  ( $0.5 - 0.9 \mu\text{m}$ ) at 200X than the machined bearings ( $1.2 - 2.8 \mu\text{m}$ ). At 100X the  $R_a$  and  $R_q$  values were larger (by factors of 2 – 3X) than those measured at 200X, for both bearing types, because the surface area measured was four times as large so that more features were quantified. (However, the Z-increment was  $4.0 \mu\text{m}$  at 100X, versus  $1.5 \mu\text{m}$  at 200X, so the precision of the measurement was lower as magnification decreased.) For the machined bearings at 200X, the  $R_a$  and  $R_q$  values were different along the two axes (anterior-posterior, Y, and medial-lateral, X) of measurement, showing that orientation effects in the surface roughness resulted from machining. For the direct molded bearings at 200X, the  $R_a$  measurements were similar along these two axes, but the  $R_q$  measurements were different, showing that there was a lesser orientation effect in the molded surface roughness. The direct molded bearings had values of  $R_{sk}$  near zero ( $-0.30$  to  $+0.22$ ) at 200X, while the machined bearings had negative  $R_{sk}$  values ( $-0.63$  to  $+0.01$ ).

Surface roughness was represented by  $R_a$  and  $R_q$  and confirmed that the direct molded bearings had a smoother texture than the machined bearings. Roughness values fell within a reasonable range comparable to the size of larger wear debris particles. However, the  $R_a$  and  $R_q$  values did not directly measure the height of surface features – they were averaged values calculated from residuals. The average peak-to-valley height of surface features would be about a factor of four larger than the  $R_a$  or  $R_q$  values. Thus the average peak-to-valley height would be  $2.0 - 3.6 \mu\text{m}$  for direct molded bearings and  $4.8 - 11.2 \mu\text{m}$  for machined bearings. Measurements on individual surface features would sometimes be significantly larger than these values. The topography of the direct molded bearings could be smoother



than the measured values, as the roughness was near the lower limit for measurement by confocal microscopy. Surface features measured on the machined bearing were within the measurement capabilities of this technique.

Skewness is an indication of the shape of the surface profile, rather than a measurement of height variation or roughness. Skewness values were more negative for the machined bearings than for the direct molded bearings, which had values near zero. These  $R_{sk}$  values also changed in magnitude at different magnifications, with higher (more positive) values measured at 100X than at 200X for both types of bearings. It was important to match a representative surface area with a suitable vertical resolution (Z-increment) for the measurement. The theoretical skewness for a perfectly flat surface is zero, and  $R_q$  from the direct molded surfaces appeared very close to this ideal. When the Z-increment is larger than the scale of surface roughness, so that  $R_a$  decreases to one-fourth of the Z-increment, then the skewness value decreases toward zero. This must be considered in interpreting results from the direct molded bearings. Values of  $R_{sk}$  near zero indicated surfaces that were either flat or symmetric about the midline of the surface profile, which would be very good for load bearing. Negative values of  $R_{sk}$  indicated surfaces with rounded humps pointing upward and narrow valleys pointed downward, which would be better for load bearing than surfaces with positive values of  $R_{sk}$ , indicating surfaces with narrow peaks pointing upward and rounded valleys pointed downward that would be poor for load bearing. Thus the surface profile shapes from direct molded bearings were better for load bearing than those from machined bearings.

Wear debris particles fall within the range of 0.2 – 300  $\mu\text{m}$ , with a mean size of 0.5 – 0.6  $\mu\text{m}$  (from Section 2.2.1), which includes the ranges measured for surface roughness of machined and direct molded UHMWPE bearings. Thus, the release of debris by abrasive wear could be closely related to the surface texture and roughness of the UHMWPE bearings. The orientation of the surface profiles on the bearings relative to the reciprocating motion of the joint may also have an effect. The roughness of the metal bearing surfaces is typically 0.05  $\mu\text{m}^{102}$ , so that the corresponding average peak-to-valley height would be 0.20  $\mu\text{m}$  (at the

lower limit of size for wear debris particles). Grinding between the metal and polymer bearings would further reduce the size of the larger wear debris particles released in-vivo, leading to the mean wear debris size of 0.5 – 0.6  $\mu\text{m}$ .

## **8.4 MICROMECHANICS**

Polymer morphology and surface texture of the UHMWPE tibial bearings significantly affected micromechanical behavior and properties, as measured by nanoindentation on the top bearing surfaces. Surface texture, particularly roughness, affected the repeatability of nanoindentation results from both unsterile and sterile bearings. The direct molded specimens, with very low surface roughness, had very repeatable results from multiple indents. The machined specimens, with higher surface roughness, had significant differences in results between multiple indents. As the indentation depth increased (to several microns in depth), the effect of surface roughness decreased and measurements of hardness and modulus were related to polymer morphology.

The effect of surface texture on micromechanical behavior was examined from load – displacement results (obtained under load control) from multiple indents on each bearing type. When the entire load range (up to 625 mN) was examined (Figure 15, p. 123), significant differences between direct molded and machined bearings were observed in both the unsterile and sterile conditions. Indents on direct molded bearings gave very repeatable load – displacement curves, with the maximum displacements varying by only 0.5 – 1.0  $\mu\text{m}$ . Indents on machined bearings gave variable load – displacement curves, with the maximum displacements varying by 1.5 – 2.5  $\mu\text{m}$ . These variations in displacement with position on the bearing surface (at constant load) could contribute to release of wear debris due to non-uniform localized stresses and resulting strains in the polyethylene.

The four bearing types also showed differences in values of maximum displacement. Ranking them in order from largest to smallest overall displacement gave:

- Direct molded, unsterilized (specimen 016A)
- Direct molded, sterilized (specimen 020A)
- Machined, unsterilized (specimen 018A)
- Machined, sterilized (specimen 019A).

These differences in maximum displacement related to mechanical property differences, as shown by values of hardness and elastic modulus, resulting from differences in morphology. The two fabrication methods (direct molding vs. isostatic compression molding followed by machining) produced different morphologies, with different mechanical properties, in the unsterilized bearings. Sterilization by gamma irradiation then modified the polymer morphologies, increasing the values of hardness and elastic modulus for each bearing type. Sterilization significantly decreased the interface thickness, decreased the amorphous thickness, and increased the lamellar thickness. The ranking of bearings based on their maximum displacements was consistent with their ranking based on lamellar thicknesses (see Figure 22, p. 140), with displacement inversely related to lamellar thickness.

Micromechanical behavior was evaluated at very low loads to evaluate displacements comparable to the size of small wear debris particles (0.2 to 3.0  $\mu\text{m}$ ). Recall that the mean size of wear debris is 0.5 – 0.6  $\mu\text{m}$  (see Section 2.2.1). Load – displacement behavior at loads from 0 to 10 mN was shown in Figure 16 (p. 126). Even at these low loads, the differences in reproducibility of displacement response between direct molded and machined implants were obvious. At displacements below 0.5  $\mu\text{m}$  the machined bearings showed variations in their displacement responses for multiple indents, whereas the direct molded bearings had very consistent, repeatable displacement responses. This observation was made for both unsterilized and sterilized tibial bearings. Thus, surface texture affected the repeatability of displacements even at very low loads.

At low loads up to 10 mN, differences in the absolute magnitudes of displacement were not distinct between the four types of tibial bearings. The direct molded bearings had a narrower range of displacements at each load than the machined bearings did, but values for

the direct molded bearings fell within the range for the machined bearings. Sterilization had a small effect on the displacements for the direct molded bearings (decreasing the displacements), but did not affect the machined bearings. Thus within this range of low loads, the major difference between machined and direct molded bearings was the consistency or repeatability of the displacement response with position on the bearing surface. At the same load level, an indent on a machined bearing could produce a displacement that was either smaller, equal to, or larger than that on a direct molded bearing. Thus, wear on the machined surface would be non-uniform due to this variation in mechanical behavior, while that on the direct molded surface would be quite uniform. Over millions of loading cycles with associated abrasion, this non-uniformity of displacement on the machined surface could contribute to accelerated wear and release of debris.

Hardness and elastic modulus were calculated to examine micromechanical property variations with depth from the bearing surfaces. The variability in displacements from the machined bearings affected the values for hardness and elastic modulus. Thus, these mechanical property depth profiles varied significantly between multiple indents on the machined bearings, and were quite repeatable between multiple indents on the direct molded bearings. All bearing types had some variation in mechanical properties within a surface layer, due to a combination of surface texture and morphology effects, before properties reached a relatively constant value in the bulk, due to morphology. This surface layer extended 2 – 4  $\mu\text{m}$  in direct molded tibial bearings and 5 – 10  $\mu\text{m}$  in machined tibial bearings. The maximum contact depths that could be reached were 20 – 23  $\mu\text{m}$  for UHMWPE, producing indents with lateral dimensions of 150 – 173  $\mu\text{m}$ . Indents were spaced over 450  $\mu\text{m}$  apart. Nanoindentation results can be significantly affected by surface roughness within the area of the indent. These surface layer thicknesses matched the average peak-to-valley heights calculated from surface roughness measurements by confocal microscopy, as described in Section 8.3. In the machined bearings, the thickness of this surface layer corresponded with the outer zone of the modified layer observed from polarized light microscopy (see Figure 31,

p. 167), but in the direct molded bearings no surface layer was visible. The contributions of surface roughness and morphology cannot easily be separated within the contact depth range of these surface layers.

Figure 17 (p. 129) showed calculated results for hardness vs. contact depth throughout each loading cycle. For each type of tibial bearing, all the indents reached a constant hardness value within the bulk material below the surface. However, this bulk hardness value varied between multiple indents on each specimen, and this variation was sizeable on the machined tibial bearings (range was 15-18% of the mean for both unsterilized and sterilized). This variation in bulk hardness for machined bearings could relate to differences in crystallinity, as FTIR results showed variations with depth in the machined bearing but a more uniform depth profile in the direct molded bearing. However, the FTIR depth profile was measured over thousands of microns in depth, rather than tens of microns, so the results cannot be correlated directly to nanoindentation results. In comparing hardness values between different bearing types (see Table 7, p. 134), the differences did not relate directly to crystallinity values (compared in Figure 34, p. 173).

The bulk hardness variation in machined bearings more likely resulted from segregation of amorphous phase outside the lamellar stacks or domains and between the sintered resin particles. Segregated amorphous phase was observed by polarized light microscopy (Figure 31, p. 167) in the unsterile, machined bearing – at a scale comparable to the size of resin particles, and would give a significantly lower hardness if an indent were centered on an amorphous region. The contact area of an indent (see Figure 7, p. 82) was much larger than that observed for segregated amorphous material, so that micromechanical properties would result from a combination of amorphous material and lamellar stacks. Thus, hardness would vary with position on the machined bearing surface, depending on the micron-scale morphology beneath each indent.

Variation of bulk hardness with position on the direct molded surface was of a small magnitude, indicating that large regions of segregated amorphous phase were not present.

This suggested that the direct molding process was successful in fully melting and crystallizing the UHMWPE, removing the boundaries between the original resin particles.

Surface variations in hardness were observed. Variations of hardness in the surface layer were different between direct molded and machined tibial bearings. For indents on direct molded bearings (both unsterilized and sterilized), the surface hardness usually increased from the bulk toward the shallowest contact depths. Variations in hardness values (within the surface layer) were relatively small between multiple indents on the direct molded tibial bearings. Some indents had a localized peak in hardness at contact depths of 2 – 3  $\mu\text{m}$ , but this did not always result. For indents on machined bearings (both unsterilized and sterilized), the variation in hardness near the surface was not consistent between multiple indents. Sometimes the hardness increased from the bulk toward the surface, and sometimes it decreased. Hardness values near the surface were even more variable than the bulk hardness values, for machined tibial bearings. For both bearing types, sterilization slightly decreased the variability of hardness at depths with this surface layer, but this effect was minor. Surface roughness and morphology both affected surface hardness, and it was not possible to separate these effects in interpreting the results.

Figure 18 (p. 131) showed calculated results for elastic modulus vs. contact depth throughout each loading cycle. Results were similar in form to the results from hardness, although the modulus curves were noisier than the hardness curves. Modulus curves from indents on the direct molded bearings were more consistent and repeatable than from indents on the machined bearings. Modulus variations in the surface layer followed the same trends as for hardness: in direct molded bearings, the modulus usually increased as the contact depth decreased; in machined bearings, the modulus was highly variable – sometimes it increased and sometimes it decreased as the contact depth decreased. Indents on all bearing types reached a constant modulus level below the surface layer, in the bulk material.

Bulk hardness and elastic modulus values from nanoindentation were summarized in Table 7 (p. 134). Bulk properties were averaged for each indent, over all contact depths above

10.0  $\mu\text{m}$ . Then bulk properties for each bearing type were analyzed statistically, using the t test, as shown in this table. Results showed that there were statistically significant differences in micromechanical properties between direct molded and machined bearings, in both the unsterilized and sterilized conditions. Direct molded bearings consistently had lower hardness and elastic modulus values than machined bearings. Sterilization by gamma irradiation, followed by shelf aging in air for 2 years, increased hardness and elastic modulus values for both bearing types, but this effect was greater for machined bearings than for direct molded bearings. Other recent research has also shown that mechanical properties of UHMWPE were affected by irradiation and aging in air, increasing the elastic modulus.<sup>244</sup>

Variability in micromechanical properties was also examined using the standard deviations for hardness and elastic modulus. Sterilization did not affect this variability within each bearing type. Comparison of standard deviations using the F Test showed that the variability of both hardness and elastic modulus was statistically different between direct molded and machined bearings.

The ranking of bearing types by either bulk hardness or bulk elastic modulus (from minimum to maximum) was:

- Direct molded, unsterile (specimen 016A),  
Hardness = 47.2 MPa, Modulus = 1.44 GPa
- Direct molded, sterile (specimen 020A),  
Hardness = 50.6 MPa, Modulus = 1.61 GPa
- Machined, unsterile (specimen 018A),  
Hardness = 55.1 MPa, Modulus = 1.71 GPa
- Machined, sterile (specimen 019A),  
Hardness = 64.5 MPa, Modulus = 2.08 GPa.

The average values of hardness and elastic modulus were significantly different between these four types of tibial bearings, based on statistical analyses (calculating confidence intervals on means using the t test at 95% significance). Mechanical properties were 17 – 19% higher in

machined than in direct molded bearings, unsterilized, and this difference increased to 27 – 29% after sterilization. Mechanical properties were increased by 7 – 12% due to sterilization of direct molded bearings, and were increased by 17 – 22% due to sterilization of machined bearings. Sterilization had a larger effect on machined bearings than on direct molded bearings.

These differences in mechanical properties must have resulted from differences in morphology. Crystallinity differences between the bearing types were found, but Figure 34 (p. 173) showed that these differences were much smaller in magnitude and did not follow this same ranking for all four bearing types. However, Figure 22B (p. 140) and Figure 23 (p. 144) showed that differences in lamellar thickness (based on the 3-phase model) followed this ranking exactly, even considering all 12 specimens that were analyzed by SAXS (i.e. top, bulk, and bottom). Mechanical properties at the micro-scale must have been primarily related to the lamellar thickness of the crystalline phase in the polyethylene. This was consistent with previous research showing that microhardness resulted from the combined hardnesses of the crystalline and amorphous phases, and that the hardness of the crystalline phase increased with lamellar thickness.<sup>245,246</sup> The amorphous hardness would be extremely low relative to the crystalline hardness, so that the combined microhardness would depend primarily on the lamellar thickness.

Another factor that could increase the hardness of the machined bearing was the modified surface layer, since this was the depth range probed by nanoindentation. This layer was distinctly visible in polarized light, indicating that it contained either oriented amorphous or crystalline material. Either orientation or increased crystallinity would increase the stiffness, and thus the hardness, of the polymer molecules in the surface. This factor may contribute to the higher hardness of the machined bearing surfaces. However, the modified surface layer was so thin that variations in crystallinity were not measurable by FTIR or DSC (which used thin specimens). Quantitative measurements of orientation were not within the scope of this research project.



## 9. CONCLUSIONS

This experimental work has led to the following conclusions:

- Average crystallinity (as defined by the lamellar thickness without the interface) was slightly higher (6 – 9%) in the machined than in the direct molded bearing, in the unsterile condition, based on results from DSC and from SAXS (3-phase model). The crystallinity of the sterile, direct molded bearing was slightly higher (2 – 5%) than in the unsterile, machined bearing.
- Crystallinity varied with depth (up to 2,500  $\mu\text{m}$ ) in the unsterile, machined bearing, but was uniform in the unsterile, direct molded bearing, based on FTIR analyses. This variability was related to segregation of amorphous phase (seen in polarized light) in the machined bearing, which was not observed as distinctly in the direct molded bearing.
- Fusion and sintering of the initial resin particles were incomplete in the machined bearing, but were more complete in the direct molded bearing. This was observed from polarized light microscopy and correlated with results from nanoindentation.
- Machining of the top tibial bearing surface produced a modified surface layer that was 25 – 40  $\mu\text{m}$  thick (birefringent in polarized light microscopy). Within this layer, the polymer molecules were either oriented or highly crystalline, relative to the adjacent region. Mechanical deformation from machining would have caused orientation of the amorphous phase, and could have generated enough heat to melt the original crystalline lamellae.<sup>241</sup> The layer was too thin to detect differences in crystallinity by DSC.
- Changes were not observed in the large-scale, near-surface morphology of a direct molded tibial bearing, by polarized light microscopy.
- The melting temperature ranges were significantly different between machined bearings and direct molded bearings in the unsterile condition, indicating differences in

processing conditions or thermal history. Thermal history would control the nanometer-scale morphology (lamellar, interface, and amorphous thicknesses) and the micron-scale morphology of the polyethylene. The following inferences were reached for the unsterilized bearing types:

- The isostatic compression molding process used a higher crystallization temperature but a shorter crystallization time than the direct molding process.
- Rods fabricated by isostatic compression molding cooled at a slower rate than bearings fabricated by direct molding, due to low thermal conductivity and the relative thickness of the molded product.
- These differences in crystallization conditions created a finer morphology ( $<10\ \mu\text{m}$ ) in the machined bearings and a coarser morphology ( $10 - 20\ \mu\text{m}$ ) in the direct molded bearings.
- The average lamellar thickness was higher for the machined UHMWPE than for the direct molded UHMWPE, in both the surfaces and in the bulk (i.e. center of the implant). This was observed for both unsterile and sterile implant bearings. This difference in lamellar thickness correlated directly with differences in hardness and elastic modulus measured by nanoindentation.
- The variation in lamellar thickness was wider for the machined UHMWPE than for the direct molded UHMWPE, as more crystallization occurred during slow cooling of the isostatically molded bar.
- The surface of the direct molded bearing had thinner lamellae, smaller variation in lamellar thickness, and lower crystallinity than the bulk, due to faster heat transfer to the mold surface during cooling.
- Machining heated the UHMWPE surface, similar to annealing, and increased the thickness of thin lamellae. This effect was more distinct in the direct molded bearings, due to the lower average lamellar thickness, than in the

machined bearings. It was observed as a narrowing or sharpening of the primary melting peaks from DSC.

- The thickness of the interface zone (between the lamellae and the amorphous phase) was slightly less than the amorphous phase thickness in unsterile UHMWPE, for both machined and direct molded bearings. Thus the interface was present as a separate third phase, rather than as a thin boundary layer.
- Interfacial free energy was found to vary linearly with interface thickness, with an intercept of  $78 \text{ erg/cm}^2$  when the interface was eliminated. Thus, both the lamellar thickness and the interface thickness affected the peak melting temperature. Interfacial free energy could not be treated as a constant, even though the starting molecular weight of UHMWPE was the same for all bearing types.
- Interface thickness and associated interfacial free energy were related to crystallization conditions, particularly temperature and time. Larger interface thicknesses resulted from crystallization at high temperatures, where most of the crystallization occurred within a narrow temperature range (as for the top surface of the direct molded bearing). The interface thickness decreased when increased amounts of crystallization occurred during the cooling cycle (as for the bulk of the direct molded bearing and the machined bearing).
- Sterilization by gamma irradiation in air, followed by shelf aging for 2 years, caused significant changes in the morphology of the direct molded UHMWPE due to chain scission and crystallization at low temperature. These changes occurred in both the surfaces and in the bulk. (Similar changes were predicted to occur in the machined UHMWPE, but analyses were not completed on those specimens due to equipment failure.) The following inferences were reached:

- The lamellar thickness (based on the 3-phase model) increased by 4 nm, or approximately 10%. This change in lamellar thickness correlated directly with changes in hardness and elastic modulus measured by nanoindentation.
- The interface thickness (based on the 3-phase model) decreased by 8 nm, or approximately 60%. This was the largest relative change of any of the morphological parameters. The interfacial free energy decreased with the interface thickness, consistent with the linear relationship observed for unsterile bearings.
- The amorphous thickness (based on the 3-phase model) decreased by 1 nm, or approximately 7%.
- The total long period decreased from 67 nm to 62 nm, by approximately 7%.
- A small fraction of thin lamellae formed, which had not been present in the unsterile, direct molded bearing.
- Crystallinity and lamellar thickness increased following gamma irradiation and shelf aging, primarily resulting from a 60% decrease in the interface zone thickness between the crystalline and amorphous phases. This is believed to result from chain scission and crystallization. Relatively little contribution resulted from a 7% decrease in the amorphous phase thickness.
- The effects of irradiation and shelf aging varied with depth from the bearing surfaces, due to heterogeneous oxidation reactions. This variation affected chain scissions in the interface that led to increased lamellar thickness. It did not affect the formation of thin lamellae from crystallization of short fragments after chain scission. Oxidation reactions accelerated chain scission in the surfaces of the bearing relative to that in the bulk. Chain scission was accelerated at entanglements within the interface, where strain energy was high in the polymer chains.
- Wear debris particles (typically 0.5 – 0.6  $\mu\text{m}$  in size, see Section 2.2.1) would contain stacks of only 6 – 8 lamellae in machined bearings or of 7 – 10 lamellae in direct

molded bearings. These stack dimensions were calculated from the measured long periods and literature values of wear debris size. Thus, the size of wear debris particles is reasonable for a domain structure that could be present from stacks of lamellae in the UHMWPE.

- The surface texture (over lateral distances of 200 – 1000  $\mu\text{m}$ ) of machined tibial bearings was significantly different from that of direct molded tibial bearings. Machined bearings had higher roughness (based on  $R_a$  and  $R_q$ ) and less symmetric surface topography (based on  $R_{sk}$ ) than direct molded bearings. Orientation effects in topography were present in both types of bearings, but were of a larger magnitude in machined bearings (due to distinct machining lines).
- In the machined bearings, boundaries between the resin particles affected the surface topography that resulted from machining. This resulted in ridges on the surface with peak-to-valley heights of 5 – 11  $\mu\text{m}$ , on average.
- Surface topography of the direct molded bearings was extremely smooth, approaching an ideal flat surface. Vertical steps on the surface had average peak-to-valley heights of 2 – 4  $\mu\text{m}$  or less.
- The peak-to-valley heights of surface features on both machined and direct molded bearings were within the size range typical of wear debris particles (0.2 – 300  $\mu\text{m}$ ). Although peak-to-valley heights were larger than the average size of wear debris (0.5 – 0.6  $\mu\text{m}$ ), grinding of debris particles (formed by abrasive wear) could reduce their size to this range.
- Both surface texture and morphology affected nanoindentation measurements at the outer surface of all bearing types. The peak-to-valley height (representing surface texture) correlated well with the contact depth to which nanoindentation results were variable and inconsistent. Indents had to reach contact depths beyond the peak-to-valley height to obtain results that were related to morphology alone.

- The direct molded bearing surface was much more uniform, in terms of micro-scale mechanical properties, than the machined bearing surface. Micromechanical interactions, based on load-displacement measurements using nanoindentation, were different between these two types of bearing surfaces (both unsterile and sterile). Micro-contacts on the direct molded surfaces were uniform and gave very similar displacements for the same load. Micro-contacts on the machined surfaces were quite variable with position and gave a wide range of displacements for the same load. This resulted from differences in quality of fusion (of the original resin particles) between the bearing types, because large areas of segregated amorphous phase were present in the machined bearings. These trends in load-displacement behavior were also translated into variations in the hardness and elastic modulus values.
- The machined bearing surfaces were stiffer than the direct molded bearing surfaces, particularly at higher loads and higher displacements. Displacements into the machined bearing were lower than those into the direct molded bearing, under identical loading conditions at high loads (~600 mN). At low loads (0 - 10 mN), the displacements (up to 3  $\mu\text{m}$ ) were similar between both types of bearing surfaces but varied across a wider range in the machined bearings.
- The modified surface layer resulting from machining contributed to the variability in micromechanical behavior (load-displacement, hardness, and modulus) at the surface of the implant bearings, but did not consistently increase or decrease properties near the surface. Instead, the properties were observed to vary inconsistently relative to the properties of the underlying bulk material. It was believed that the variability resulted from combined effects due to surface roughness and variations of polymer morphology within this surface layer. The layer was too thin to affect the long-term wear performance (beyond 2 – 10 months) of the implant bearings, but it could accelerate the initial release of wear debris due to pre-orientation and hardening of polymer molecules near the surface.

- The machined bearing surfaces had higher mean values of hardness and elastic modulus than the direct molded bearing surfaces, in the unsterile condition, based on statistical comparison of the properties measured in the bulk (10 – 23  $\mu\text{m}$  below the top surface).
- Sterilization by gamma irradiation, followed by shelf aging in air for 2 years, modified the micromechanical properties of the top surfaces of both machined and direct molded tibial bearings. The stiffness of the surfaces increased, as reflected by a consistent decrease in the displacement under load. The bulk hardness and the bulk elastic modulus also consistently increased for each bearing type. Sterilization did not significantly affect the variability in micromechanical behavior for each bearing type. Mechanical properties increased proportionally more for the machined bearings than for the direct molded bearings after sterilization and shelf aging.
- Rankings of bearing types based on hardness or modulus were inverted relative to rankings based on maximum displacement, and were the same as rankings based on lamellar thickness. The dependence of micromechanical properties on morphology was primarily related to lamellar thickness. Thus, the changes in micromechanical behavior following sterilization were primarily due to increases in lamellar thickness from chain scission within the interface zone.

## 10. PROPOSALS FOR FUTURE RESEARCH

The effects of machining on the morphology and micromechanical properties of UHMWPE need to be studied in more detail. The modified surface layer should be examined to determine whether it contains oriented molecules in the amorphous phase or a higher level of crystallinity than the bulk. Polarized FTIR using a microscope attachment would provide this information. Electron microscopy of etched specimens would provide details of the exact morphological structure in this surface layer and how it compares to the bulk. The variation of micromechanical properties with depth from the surface needs to be examined at greater depths than could be achieved by indenting into the top bearing surface with a nanoindenter. Transverse cross-sections could be prepared by cryo-microtomy, then nanoindents could be made at different depths from the original bearing surface. This would increase understanding of how machining affects the surface micromechanical properties, how this varies with depth, and how properties vary with position within the bulk. Thin sections from cryo-microtoming could also be examined with light and electron microscopy techniques to correlate morphology with micromechanical behavior.

The morphological structures developed from processing conditions should be evaluated, and used to optimize mechanical properties. Of particular interest would be the elimination of segregated amorphous phase, the improvement of fusion between resin particles, the homogeneity of structures formed on scales of both hundreds of microns and between 1 and 100 microns, the size of domains formed by stacks of lamellae surrounded by interface zones and amorphous phases, and the thickness of amorphous zones adjacent to lamellae. Thus microscopy techniques would be used to characterize the UHMWPE structures, from the smallest structures examined by transmission or scanning electron microscopy to the largest structures examined by light microscopy (particularly polarized light). Microscopy results at the smallest scales need to be correlated to measurements of long period, lamellar thickness, interface thickness, amorphous thickness, and crystallinity from



SAXS, WAXD, FTIR, and DSC. Mechanical properties of interest include not only hardness and elastic modulus but also creep, viscoelasticity, and fatigue. Nanoindentation or instrumented microindentation would allow investigation of these mechanical properties at the micro-scale, comparable to dimensions at which wear debris particles are released.

The effects of gamma irradiation and aging on polymer morphology and micromechanical behavior need to be better understood. Studies are needed to separate the effects of irradiation from those of heterogeneous oxidation (which follows irradiation). Many studies are currently underway at other institutions to evaluate the effects of irradiation and oxidation, but few of these studies characterize morphology in any detailed, quantitative way. Changes occurring in the interface zone need to be understood in more detail. Techniques such as SAXS, FTIR, and DSC must be combined and run in carefully designed experiments to obtain conclusive results regarding changes in lamellar, interface, and amorphous thicknesses. Results need to be confirmed by electron microscopy. Surface changes due to heterogeneous oxidation can be difficult to measure by bulk mechanical tests that are typically conducted. Again, nanoindentation or instrumented microindentation would provide mechanical property data on a scale more appropriate to the chemical and structural changes that need to be evaluated.

Irradiation is known to produce free radicals in polyethylene, and exposure to oxygen or air increases the proliferation of these radicals. These radicals are long-lived in UHMWPE, and resulting reactions have been associated with degradation of mechanical properties. Thus, alternate sterilization methods need to be considered and evaluated in detail to see if they also degrade the polyethylene in some manner. Sterilization by other methods, such as ethylene oxide (EtO) gas exposure or plasma exposure, has been used on polyethylene. However, chemical and/or mechanical changes in the material have not been studied.

## REFERENCES

- 
- <sup>1</sup> A. Praemer, S. Furner, and D. P. Rice, *Musculoskeletal Conditions in the United States*, American Academy of Orthopaedic Surgeons, Park Ridge, Illinois, 1992.
  - <sup>2</sup> *National Hospital Discharge Survey, 1985-1988*, Data Tapes, National Center for Health Statistics.
  - <sup>3</sup> *Medicare Procedure File (BMAD-1), 1985-1989*, Data Tapes, Health Care Financing Administration.
  - <sup>4</sup> A. J. Moss, S. Hamburger, R. M. Moore, et al., "Use of Selected Medical Device Implants in the United States, 1988," *Advance Data from Vital and Health Statistics*, No. 191, National Center for Health Statistics, Hyattsville, Maryland, 1991.
  - <sup>5</sup> P. F. Doorn, P. A. Campbell, and H. C. Amstutz, "Metal Versus Polyethylene Wear Particles in Total Hip Replacements: A Review," *Clinical Orthopaedics and Related Research*, **329S**, pp. S206-S216 (1996).
  - <sup>6</sup> H. C. Amstutz, P. Campbell, N. Kossovsky, and I. C. Clarke, "Mechanism and Clinical Significance of Wear Debris-Induced Osteolysis," *Clinical Orthopaedics and Related Research*, **276 (3)**, pp. 7-18 (1992).
  - <sup>7</sup> H. G. Willert and M. Semlitsch, "Reactions of the Articular Capsule to Wear Products of Artificial Joint Prostheses," *Journal of Biomedical Materials Research*, **11**, pp. 157-164 (1977).
  - <sup>8</sup> K. Hirakawa, T. W. Bauer, B. N. Stulberg, A. H. Wilde, and M. Secic, "Characterization and Comparison of Wear Debris from Failed Total Hip Implants of Different Types," *Journal of Bone and Joint Surgery*, **78A (8)**, pp. 1235-1243 (1996).
  - <sup>9</sup> P. Campbell, S. Ma, B. Yeom, H. McKellop, T. P. Schmalzried, and H. C. Amstutz, "Isolation of Predominantly Submicron-Sized UHMWPE Wear Particles from Periprosthetic Tissues," *Journal of Biomedical Materials Research*, **29**, pp. 127-131 (1995).
  - <sup>10</sup> W. J. Maloney, R. L. Smith, T. P. Schmalzried, J. Chiba, D. Huene, and H. Rubash, "Isolation and Characterization of Wear Particles Generated in Patients Who Have Had Failure of a Hip Arthroplasty Without Cement," *Journal of Bone and Joint Surgery*, **77A (9)**, pp. 1301-1310 (1995).
  - <sup>11</sup> A. S. Shanbhag, J. J. Jacobs, T. T. Glant, J. L. Gilbert, J. Black and J. O. Galante, "Composition and Morphology of Wear Debris in Failed Uncemented Total Hip Replacement," *Journal of Bone and Joint Surgery*, **76B (1)**, pp. 60-67 (1994).
  - <sup>12</sup> O. L. Huk, M. Bansal, F. Betts, C. M. Rimnac, J. R. Lieberman, M. H. Huo, and E. A. Salvati, "Polyethylene and Metal Debris Generated by Non-Articulating Surfaces of Modular Acetabular Components," *Journal of Bone and Joint Surgery*, **76B (4)**, pp. 568-574 (1994).
  - <sup>13</sup> K. J. Margevicius, T. W. Bauer, J. T. McMahon, S. A. Brown, and K. Merritt, "Isolation and Characterization of Debris in Membranes Around Total Joint Prostheses," *Journal of Bone and Joint Surgery*, **76A (11)**, pp. 1664-1675 (1994).
  - <sup>14</sup> C. M. Rimnac, P. D. Wilson, Jr., M. D. Fuchs, and T. M. Wright, "Acetabular Cup Wear in Total Hip Arthroplasty," *Orthopedic Clinics of North America*, **19 (3)**, pp. 631-636 (1988).
  - <sup>15</sup> P. S. Walker, "Friction and Wear of Artificial Joints," *Human Joints and Their Artificial Replacements*, Charles C. Thomas Publisher, Springfield, Illinois, 1977, pp. 368-422.

- 
- <sup>16</sup> J. Charnley and D. K. Halley, "Rate of Wear in Total Hip Replacement," *Clinical Orthopaedics and Related Research*, **112**, pp. 170-179 (1975).
- <sup>17</sup> G. H. Isaac, D. Dowson, and B. M. Wroblewski, "An Investigation into the Origins of Time-Dependent Variation in Penetration Rates with Charnley Acetabular Cups--Wear, Creep or Degradation?" *Journal of Engineering in Medicine, Proceedings of the Institution of Mechanical Engineers Part H*, **210 (H3)**, pp. 209-216 (1996).
- <sup>18</sup> A. B. Bankston, E. M. Keating, C. Ranawat, P. M. Faris, and M. A. Ritter, "Comparison of Polyethylene Wear in Machined Versus Molded Polyethylene," *Clinical Orthopaedics and Related Research*, **317**, pp. 37-43 (1995).
- <sup>19</sup> K. R. Lee, S. P. James, J. R. McLaughlin, G. P. Beauregard, and E. D. Cox, "Direct Compression Molded Versus Ram Extruded Bar Stock Polyethylene: A Wear Rate Analysis of Surgically Retrieved Cementless Acetabular Components at 8 Years," in *Scientific Program of the American Academy of Orthopaedic Surgeons 1997 Annual Meeting Online*, Paper No. 481 (1997).
- <sup>20</sup> J. R. Hernandez, E. M. Keating, P. M. Faris, J. B. Meding, and M. A. Ritter, "Polyethylene Wear in Uncemented Acetabular Components," *Journal of Bone and Joint Surgery*, **76B (2)**, pp. 263-266 (1994).
- <sup>21</sup> S. P. James, K. R. Lee, G. P. Beauregard, E. Rentfrow, and J. R. McLaughlin, "Comparison of the *In Vivo* Wear Rates of 43 Surgically Retrieved Direct Compression Molded and Ram Extruded Ultra High Molecular Weight Polyethylene Acetabular Components," in *Transactions of the Fifth World Biomaterials Congress*, 1996, Vol. 2, p. 513.
- <sup>22</sup> M. A. Ritter, R. Worland, J. Saliski, J. V. Helphenstine, K. L. Edmondson, E. M. Keating, P. M. Faris, and J. B. Meding, "Flat-on-Flat, Nonconstrained, Compression Molded Polyethylene Total Knee Replacement," *Clinical Orthopaedics and Related Research*, **321**, pp. 79-85 (1995).
- <sup>23</sup> E. L. Feng, D. S. Stulberg, and R. S. Wixon, "Progressive Subluxation and Polyethylene Wear in Total Knee Replacements with Flat Articular Surfaces," *Clinical Orthopaedics and Related Research*, **299**, pp. 60-71 (1993).
- <sup>24</sup> L. Mintz, A. K. Tsao, C. R. McCrae, S. D. Stulberg, and T. Wright, "The Arthroscopic Evaluation and Characteristics of Severe Polyethylene Wear in Total Knee Arthroplasty," *Clinical Orthopaedics and Related Research*, **273**, pp. 215-222 (1991).
- <sup>25</sup> T. M. Wright, C. M. Rimnac, S. D. Stulberg, L. Mintz, A. K. Tsao, R. W. Klein, and C. McCrae, "Wear of Polyethylene in Total Joint Replacements," *Clinical Orthopaedics and Related Research*, **276**, pp. 126-134 (1992).
- <sup>26</sup> J. P. Collier, M. B. Mayor, J. L. McNamara, V. A. Surprenant, and R. E. Jensen, "Analysis of the Failure of 122 Polyethylene Inserts from Uncemented Tibial Knee Components," *Clinical Orthopaedics and Related Research*, **273**, pp. 232-242 (1991).
- <sup>27</sup> D. J. Kilgus, J. R. Moreland, G. A. M. Finerman, T. T. Funahashi, and J. S. Tipton, "Catastrophic Wear of Tibial Polyethylene Inserts," *Clinical Orthopaedics and Related Research*, **273**, pp. 223-231 (1991).
- <sup>28</sup> R. C. Miller, "UHMW Polyethylene," *Modern Plastics Encyclopedia Issue*, **66 (11)**, pp. 76-78 (1989).
- <sup>29</sup> T. Stevens, "UHMWPE: When the Going Gets Tough," *Materials Engineering*, pp. 23-24 (Jan., 1992).

- 
- <sup>30</sup> "Orthopedic Device Industry Loses UHMWPE Supplier," Online Article, *Orthopedics Today*, 1996.
- <sup>31</sup> Biomet, Inc., "Resin and Consolidation Issues with UHMWPE," Technical Brief, Biomet, Warsaw, Indiana.
- <sup>32</sup> S. Li and A. H. Burstein, "Current Concepts Review: Ultra-High Molecular Weight Polyethylene," *Journal of Bone and Joint Surgery*, **76A (7)**, pp. 1080-1090 (1994).
- <sup>33</sup> M. Field, J. F. Kahles, and W. P. Koster, "Surface Finish and Surface Integrity," *Machining, Vol. 16, Metals Handbook, 9th Ed.*, ASM International, Metals Park, Ohio, 1989, pp. 19-36.
- <sup>34</sup> H. Czichos, *Tribology: A Systems Approach to the Science and Technology of Friction, Lubrication, and Wear*, Elsevier Scientific Publishing Company, New York, 1978.
- <sup>35</sup> A. B. Bankston, M. A. Ritter, E. M. Keating, and P. M. Faris, "Measurement of Polyethylene Thickness in Total Hip Arthroplasty," *Journal of Arthroplasty*, **9 (5)**, pp. 533-538 (1994).
- <sup>36</sup> J. Livermore, D. Ilstrup, and B. Morrey, "Effect of Femoral Head Size on Wear of the Polyethylene Acetabular Component," *Journal of Bone and Joint Surgery [Am.]*, **72-A**, pp. 518-28 (1990).
- <sup>37</sup> D. R. Pedersen, J. J. Callaghan, J. P. Olejniczak, and R. C. Johnston, "Polyethylene Wear Rates for Five Different *In-Vivo* Acetabular Components Used Over a Five to Twenty-Two Year Period," in *Transactions of the 41st Annual Meeting of the Orthopaedic Research Society*, 1995, p. 115-20.
- <sup>38</sup> A. B. Bankston, H. Cates, M. A. Ritter, E. M. Keating, and P. M. Faris, "Polyethylene Wear in Total Hip Arthroplasty," *Clinical Orthopaedics and Related Research*, **317**, pp. 7-13 (1995).
- <sup>39</sup> J. J. Callaghan, D. R. Pedersen, J. P. Olejniczak, D. D. Goetz, and R. C. Johnston, "Radiographic Measurement of Wear in 5 Cohorts of Patients Observed for 5 to 22 Years," *Clinical Orthopaedics and Related Research*, **317**, pp. 14-18 (1995).
- <sup>40</sup> H. E. Cates, P. M. Faris, E. M. Keating, and M. A. Ritter, "Polyethylene Wear in Cemented Metal-Backed Acetabular Cups," *Journal of Bone and Joint Surgery [Br.]*, **75-B (2)**, pp. 249-253 (1993).
- <sup>41</sup> R. S. Nashed, D. A. Becker, and R. B. Gustilo, "Are Cementless Acetabular Components the Cause of Excess Wear and Osteolysis in Total Hip Arthroplasty?" *Clinical Orthopaedics and Related Research*, **317**, pp. 19-28 (1995).
- <sup>42</sup> A. B. Bankston, P. M. Faris, E. M. Keating, and M. A. Ritter, "Polyethylene Wear in Total Hip Arthroplasty in Patient-Matched Groups," *Journal of Arthroplasty*, **8 (3)**, pp. 315-322 (1993).
- <sup>43</sup> K. Brummitt, C. S. Hardaker, P. J. J. McCullagh, K. J. Drabu, and R. A. Smith, "Effect of Counterface Material on the Characteristics of Retrieved Uncemented Cobalt-Chromium and Titanium Alloy Total Hip Replacements," *Journal of Engineering in Medicine, Proceedings of the Institution of Mechanical Engineers Part H*, **210 (H3)**, pp. 191-195 (1996).
- <sup>44</sup> A. B. Joshi, L. Markovic, P. C. Noble, and J. C. Murphy, "Long Term Wear of the Acetabular Cup: Analysis of Risk Factors," in *Transactions of the 41st Annual Meeting of the Orthopaedic Research Society*, 1995, p. 243-40.

- 
- <sup>45</sup> M. M. Landy and P. S. Walker, "Wear of Ultra-High-Molecular-Weight Polyethylene Components of 90 Retrieved Knee Prostheses," *The Journal of Arthroplasty, Supplement*, pp. S73-85 (October, 1988).
- <sup>46</sup> R. M. Hall, A. Unsworth, P. Siney, and B. M. Wroblewski, "Wear in Retrieved Charnley Acetabular Sockets," *Journal of Engineering in Medicine, Proceedings of the Institution of Mechanical Engineers Part H*, **210**, pp. 197-207 (1996).
- <sup>47</sup> L. P. Zichner and H.-G. Willert, "Comparison of Alumina-Polyethylene and Metal-Polyethylene in Clinical Trials," *Clinical Orthopaedics and Related Research*, **282**, pp. 86-94 (1992).
- <sup>48</sup> N. L. Parks, G. A. Engh, K. A. Dwyer, and L. D. T. Topoleski, "Micromotion of Modular Tibial Components in Total Knee Arthroplasty," in *Transactions of the 40th Annual Meeting of the Orthopaedic Research Society*, 1994, p. 802.
- <sup>49</sup> P. C. Chen, E. H. Mead, J. G. Pinto, and C. W. Colwell, Jr., "Polyethylene Wear Debris in Modular Acetabular Prostheses," *Clinical Orthopaedics and Related Research*, **317**, pp. 44-56 (1995).
- <sup>50</sup> T. C. Doehring, S. Saigal, A. S. Shanbhag, and H. E. Rubash, "Micromotion of Acetabular Liners: Measurements Comparing the Effectiveness of Locking Mechanisms," in *Transactions of the 42nd Annual Meeting of the Orthopaedic Research Society*, 1996, p. 427.
- <sup>51</sup> M. A. Sosa, R. C. Wasielewski, and A. S. Litsky, "Micromotion Between the Tibial Tray and the Polyethylene Insert," in *Transactions of the Fifth World Biomaterials Congress*, 1996, p. 508.
- <sup>52</sup> K. J. Drabu, R. J. Michaud, P. J. J. McCullagh, K. Brummitt, and R. A. Smith, "Assessment of Titanium Alloy on Polyethylene Bearing Surfaces in Retrieved Uncemented Total Hip Replacements," *Journal of Engineering in Medicine, Proceedings of the Institution of Mechanical Engineers Part H*, **208 (H2)**, pp. 91-95 (1994).
- <sup>53</sup> O. L. Huk, M. Bansal, F. Betts, J. R. Lieberman, M. H. Huo, and E. A. Salvati, "Generation of Polyethylene and Metal Debris From Cementless Modular Acetabular Components in Total Hip Arthroplasty," in *Transactions of the 39th Annual Meeting of the Orthopaedic Research Society*, 1993, p. 506.
- <sup>54</sup> E. A. Salvati, J. R. Lieberman, O. L. Huk, and B. G. Evans, "Complications of Femoral and Acetabular Modularity," *Clinical Orthopaedics and Related Research*, **319**, pp. 85-93 (1995).
- <sup>55</sup> N. L. Parks, R. C. Wasielewski, I. R. Williams, J. P. Collier, and G. A. Engh, "Tibial Insert Metal Backing Articulation as an Important Source of Polyethylene Wear Debris," in *Scientific Program of the American Academy of Orthopaedic Surgeons 1997 Annual Meeting Online*, Paper No. 157 (1997).
- <sup>56</sup> R. C. Wasielewski, J. J. Jacobs, A. S. Shanbhag, and H. E. Rubash, "Acetabular Insert-Metal Backing Articulation as an Important Source of Polyethylene Wear Debris," in *Scientific Program of the American Academy of Orthopaedic Surgeons 1997 Annual Meeting Online*, Paper No. 541 (1997).
- <sup>57</sup> S. M. Gabriel, D. A. Dennis, M. J. Honey, and R. D. Scott, "Polyethylene Wear on the Distal Tibial Insert Surface in Total Knee Arthroplasty," in *Transactions of the Fifth World Biomaterials Congress*, 1996, p. 783.

- 
- <sup>58</sup> J. E. Lemons, P. R. Beck, J. R. Tamarapalli, and J. M. Cuckler, "Effects on Polyethylene of Metal Backing of Modular TKA Tibial Components," in *Transactions of the 23rd Annual Meeting of the Society for Biomaterials*, 1997, p. 95.
- <sup>59</sup> J. P. Collier, M. B. Mayor, J. L. McNamara, V. A. Surprenant, and R. E. Jensen, "Analysis of the Failure of 122 Polyethylene Inserts From Uncemented Tibial Knee Components," *Clinical Orthopaedics and Related Research*, **273**, pp. 232-242 (1991).
- <sup>60</sup> N. L. Parks, R. C. Wasielewski, I. R. Williams, J. P. Collier, and G. A. Engh, "Tibial Insert Metal Backing Articulation as an Important Source of Polyethylene Wear Debris," in *Scientific Program of the American Academy of Orthopaedic Surgeons 1997 Annual Meeting Online*, Paper No. 157 (1997).
- <sup>61</sup> J. P. Collier, M. B. Mayor, R. E. Jensen, V. A. Surprenant, H. P. Surprenant, J. L. McNamara, and L. Belec, "Mechanisms of Failure of Modular Prostheses," *Clinical Orthopaedics and Related Research*, **285**, pp. 129-139 (1992).
- <sup>62</sup> P. C. Chen, E. H. Mead, J. G. Pinto, and C. W. Colwell, Jr., "Polyethylene Wear Debris in Modular Acetabular Prostheses," *Clinical Orthopaedics and Related Research*, **317**, pp. 44-56 (1995).
- <sup>63</sup> J. P. Paul, "The Biomechanics of the Hip-Joint and its Clinical Relevance," *Proceedings of the Royal Society of Medicine*, **59** (10), pp. 943-948 (1966).
- <sup>64</sup> R. C. Johnston and G. L. Smidt, "Measurement of Hip-Joint Motion During Walking," *Journal of Bone and Joint Surgery*, **51-A** (6), pp. 1083-1094 (1969).
- <sup>65</sup> R. C. Johnston, R. A. Brand, and R. D. Crowninshield, "Reconstruction of the Hip," *Journal of Bone and Joint Surgery*, **61-A** (5), pp. 639-652 (1979).
- <sup>66</sup> G. K. Rose, "Clinical Gait Assessment: A Personal View," *Journal of Medical Engineering & Technology*, **7** (6), pp. 273-279 (1983).
- <sup>67</sup> M. P. Kadaba, H. K. Ramakrishnan, and M. E. Wootten, "Measurement of Lower Extremity Kinematics During Level Walking," *Journal of Orthopaedic Research*, **8**, pp. 383-392 (1990).
- <sup>68</sup> D. Bourbonnais, P. Duval, D. Gravel, C. Steele, J. Gauthier, J. Filiatrault, M. Goyette, and B. Arseneault, "A Static Dynamometer Measuring Multidirectional Torques Exerted Simultaneously at the Hip and Knee," *Biomechanics*, **26** (3), pp. 277-283 (1993).
- <sup>69</sup> G. Bergmann, F. Graichen, A. Rohlmann, and H. Linke, "Hip Joint Forces During Load Carrying," *Clinical Orthopaedics and Related Research*, **335**, pp. 190-201 (1997).
- <sup>70</sup> F. J. Shelley, D. D. Anderson, M. J. Kolar, M. C. Miller, and H. E. Rubash, "Physical Modelling of Hip Joint Forces in Stair Climbing," *Journal of Engineering in Medicine, Proceedings of the Institution of Mechanical Engineers Part H*, **210** (H1), pp. 65-68 (1996).
- <sup>71</sup> D. T. Davy, G. M. Kotzar, R. H. Brown, K. G. Heiple, V. M. Goldberg, K. G. Heiple, Jr., J. Berilla, and A. H. Burstein, "Telemetric Force Measurements Across the Hip After Total Arthroplasty," *Journal of Bone and Joint Surgery*, **70-A** (1), pp. 45-50 (1988).
- <sup>72</sup> W. A. Hodge, K. L. Carlson, R. S. Fijan, R. G. Burgess, P. O. Riley, W. H. Harris, and R. W. Mann, "Contact Pressures from an Instrumented Hip Endoprosthesis," *Journal of Bone and Joint Surgery*, **71-A** (9), pp. 1378-1386 (1989).
- <sup>73</sup> G. M. Kotzar, D. T. Davy, V. M. Goldberg, K. G. Heiple, J. Berilla, K. G. Heiple, Jr., R. H. Brown, and A. H. Burstein, "Telemeterized In Vivo Hip Joint Force Data: A Report on

- 
- Two Patients After Total Hip Surgery," *Journal of Orthopaedic Research*, **9** (5), pp. 621-633 (1991).
- <sup>74</sup> G. Bergmann, F. Graichen, and A. Rohlmann, "Hip Joint Loading During Walking and Running, Measured in Two Patients," *Journal of Biomechanics*, **26** (8), pp. 969-990 (1993).
- <sup>75</sup> D. L. Bartel, T. M. Wright, and D. Edwards, "The Effect of Metal Backing on Stresses in Polyethylene Acetabular Components," in *The Hip: Proceedings of the 11th Open Scientific Meeting of the Hip Society*, pp. 229-239, C. V. Mosby, St. Louis, Missouri, 1983.
- <sup>76</sup> T. A. Maxian, T. D. Brown, D. R. Pedersen, and J. J. Callaghan, "Variability of Polyethylene Contact Stress Due to Current Industrial Tolerances for Femoral Head Sizes," in *Transactions of the 41st Annual Meeting of the Orthopaedic Research Society*, 1995, p. 760.
- <sup>77</sup> D. L. Bartel, V. L. Bicknell, and T. M. Wright, "The Effect of Conformity, Thickness, and Material on Stresses in Ultra-High Molecular Weight Components for Total Joint Replacement," *Journal of Bone and Joint Surgery*, **68-A** (7), pp. 1041-1051 (1986).
- <sup>78</sup> Z. M. Jin, D. Dowson, and J. Fisher, "A Parametric Analysis of the Contact Stress in Ultra-High Molecular Weight Polyethylene Acetabular Cups," *Med. Eng. Phys.*, **16**, pp. 398-405 (1994).
- <sup>79</sup> S. M. Kurtz, A. A. Edidin, and D. L. Bartel, "The Effects of Thickness, Backside Polishing, and Cup Angle on Contact Stresses in a Metal-Backed Acetabular Component," in *Transactions of the 42nd Annual Meeting of the Orthopaedic Research Society*, 1996, p. 460.
- <sup>80</sup> K. L. Gunsallus and D. L. Bartel, "Stresses and Surface Damage in PCA and Total Condylar Polyethylene Components," in *Transactions of the 38th Annual Meeting of the Orthopaedic Research Society*, 1992, p. 329.
- <sup>81</sup> Z. M. Jin, T. Stewart, D. D. Auger, D. Dowson, and J. Fisher, "Contact Pressure Prediction in Total Knee Joint Replacements, Part 2: Application to the Design of Total Knee Joint Replacements," *Journal of Engineering in Medicine, Proceedings of the Institution of Mechanical Engineers Part H*, **209** (H1), pp. 9-15 (1995).
- <sup>82</sup> D. L. Bartel, J. J. Rawlinson, A. H. Burstein, C. S. Ranawat, and W. F. Flynn, Jr., "Stresses in Polyethylene Components of Contemporary Total Knee Replacements," *Clinical Orthopaedics and Related Research*, **317**, pp. 76-82 (1995).
- <sup>83</sup> R. E. Bristol, D. C. Fitzpatrick, J. J. Callaghan, and T. D. Brown, "Local Non-Uniformities of UHMWPE Contact Stresses in TKA Designs," in *Transactions of the 40th Annual Meeting of the Orthopaedic Research Society*, 1994, p. 176-30.
- <sup>84</sup> J. A. Szivek, L. Cutignola, and R. G. Volz, "Tibio-Femoral Contact Stress Distribution Evaluation of Artificial Total Knees," in *Transactions of the 39th Annual Meeting of the Orthopaedic Research Society*, 1993, p. 424.
- <sup>85</sup> P. J. Rullkoetter, D. D. Anderson, and B. M. Hillberry, "The Effects of Rotation and Sliding on the Stress State in UHMWPE Tibial Inserts," in *Transactions of the 40th Annual Meeting of the Orthopaedic Research Society*, 1994, p. 801.
- <sup>86</sup> D. L. Hahn, D. A. McQueen, and C. D. Pence, "Volumetric Considerations for Stress in Irradiated UHMWPE for Total Joint Replacement," in *Transactions of the 41st Annual Meeting of the Orthopaedic Research Society*, 1995, p. 761.



- 
- <sup>87</sup> J. Fisher, J. L. Hailey, K. L. Chan, D. Shaw, and M. Stone, "The Effect of Ageing Following Irradiation on the Wear of UHMWPE," in *Transactions of the 41st Annual Meeting of the Orthopaedic Research Society*, 1995, p. 120-20.
- <sup>88</sup> G. W. Blunn and C. J. Bell, "The Effect of Oxidation on the Wear of Untreated and Stabilised UHMWPE," in *Transactions of the 42nd Annual Meeting of the Orthopaedic Research Society*, 1996, p. 482.
- <sup>89</sup> J. M. Bapst, R. H. Valentine, and R. Vasquez, "Wear Simulation Testing of Direct Compression Molded UHMWPE Irradiated in Oxygenless Packaging," in *Transactions of the 23rd Annual Meeting of the Society for Biomaterials*, 1997, p. 72.
- <sup>90</sup> D. W. Schroeder and K. M. Pozorski, "Hip Simulator Testing of Isostatically Molded UHMWPE: Effect of EtO and Gamma Irradiation," in *Transactions of the 42nd Annual Meeting of the Orthopaedic Research Society*, 1996, p. 478.
- <sup>91</sup> R. Sommerich, T. Flynn, M. B. Schmidt, and E. Zalenski, "The Effects of Sterilization on Contact Area and Wear Rate of UHMWPE," in *Transactions of the 42nd Annual Meeting of the Orthopaedic Research Society*, 1996, p. 486.
- <sup>92</sup> H. McKellop, F. W. Shen, T. Ota, B. Lu, H. Wiser, and E. Yu, "Wear of UHMWPE Acetabular Cups After Gamma Sterilization in Nitrogen, Thermal Stabilization and Artificial Aging," in *Transactions of the 23rd Annual Meeting of the Society for Biomaterials*, 1997, p. 45.
- <sup>93</sup> A. Wang, V. K. Polineni, C. Stark, and J. H. Dumbleton, "Effect of Femoral Head Surface Roughening on the Wear of Unirradiated and Gamma Irradiated UHMWPE Acetabular Cups," in *Transactions of the 42nd Annual Meeting of the Orthopaedic Research Society*, 1996, p. 473.
- <sup>94</sup> L. Lin and A. S. Argon, "Review: Structure and Plastic Deformation of Polyethylene," *Journal of Materials Science*, **29**, pp. 294-323 (1994).
- <sup>95</sup> G. Kanig, "Neue Elektronenmikroskopische Untersuchungen Uber Die Morphologie Von Polyathylenen," *Progress in Colloid and Polymer Science*, **57**, pp. 176-191 (1975).
- <sup>96</sup> L. C. Sawyer and D. T. Grubb, *Polymer Microscopy*, Chapman and Hall, New York, 1987.
- <sup>97</sup> B. L. Carvalho and E. L. Thomas, "Near Surface Morphology of UHMWPE Tibial Inserts," in *Transactions of the Fifth World Biomaterials Congress*, 1996, Vol. 1, p. 983.
- <sup>98</sup> "Standard Specification for Ultra-High-Molecular-Weight Polyethylene Powder and Fabricated Form for Surgical Implants," Standard F648-98, *Annual Book of ASTM Standards*, Vol. 13.01, American Society for Testing and Materials, 2000, pp. 158-163.
- <sup>99</sup> M. Deng and S. W. Shalaby, "Thermo-Oxidative Degradation of Ultrahigh Molecular Weight Polyethylene," in *Transactions of the 23rd Annual Meeting of the Society for Biomaterials*, 1997, p. 219.
- <sup>100</sup> J. T. Black, "Mechanics of Chip Formation," *Machining*, Vol. 16, *Metals Handbook*, 9th Ed., ASM International, Metals Park, Ohio, 1989, pp. 7-12.
- <sup>101</sup> S. Bhambri and S. Lin, "High Resolution Electron Microscopic Evaluation of Polyethylene," in *Transactions of the Fifth World Biomaterials Congress*, 1996, Vol. 2, p. 510.
- <sup>102</sup> "Standard Specification for Total Hip Joint Prosthesis and Hip Endoprosthesis Bearing Surfaces Made of Metallic, Ceramic, and Polymeric Materials," Standard F2033\_00a, *Annual Book of ASTM Standards*, Vol. 13.01, American Society for Testing and Materials, 2001.

- 
- <sup>103</sup> "Implants for Surgery-Part 2: Partial and Total Hip Joint Prostheses-Bearing Surfaces Made of Metallic and Plastic Materials," ISO 7206-2, International Organization for Standardization, American National Standards Institute, New York, New York.
- <sup>104</sup> "Surface Texture (Surface Roughness, Waviness, and Lay)," ANSI/ASME B46.1-1995, American National Standards Institute, New York, New York.
- <sup>105</sup> R. M. Rose, A. Crugnola, M. Ries, W. R. Cimino, I. Paul, and E. L. Radin, "On the Origins of High *In Vivo* Wear Rates in Polyethylene Components of Total Joint Prostheses," *Clinical Orthopaedics and Related Research*, **145**, pp. 277 (1979).
- <sup>106</sup> R. M. Rose and E. L. Radin, "A Prognosis for Ultra High Molecular Weight Polyethylene," *Biomaterials*, *BIOMAT* **89**, **11**, pp. 63-67 (1990).
- <sup>107</sup> J. P. Collier, M. B. Mayor, R. E. Jensen, V. A. Surprenant, H. P. Surprenant, J. L. McNamara, and L. Belec, "Mechanisms of Failure of Modular Prostheses," *Clinical Orthopaedics and Related Research*, **285**, pp. 129-139 (1992).
- <sup>108</sup> R. E. Jensen, J. P. Collier, M. B. Mayor, and V. A. Surprenant, "The Role of Polyethylene Uniformity and Patient Characteristics in the Wear of Tibial Knee Components," in *Transactions of the Implant Retrieval Symposium of the Society for Biomaterials*, 1992, p. 17.
- <sup>109</sup> M. B. Mayor, M. Wrona, J. P. Collier, and R. E. Jensen, "The Role of Polyethylene Quality in the Failure of Tibial Knee Components," in *Transactions of the 29th Annual Meeting of the Orthopaedic Research Society*, 1993, p. 292.
- <sup>110</sup> M. Wrona, M. B. Mayor, J. P. Collier, and R. E. Jensen, "The Correlation Between Fusion Defects and Damage in Tibial Polyethylene Bearings," *Clinical Orthopaedics and Related Research*, **299**, pp. 92-103 (1994).
- <sup>111</sup> L. C. Sutula, J. P. Collier, K. A. Saum, B. H. Currier, J. H. Currier, W. M. Sanford, M. B. Mayor, R. E. Wooding, D. K. Sperling, I. R. Williams, D. J. Kasprzak, and V. A. Surprenant, "Impact of Gamma Sterilization on Clinical Performance of Polyethylene in the Hip," *Clinical Orthopaedics and Related Research*, **319**, pp. 28-40 (1995).
- <sup>112</sup> S. Li, J. D. Chang, E. G. Barrena, B. D. Furman, T. M. Wright, and E. Salvati, "Nonconsolidated Polyethylene Particles and Oxidation in Charnley Acetabular Cups," *Clinical Orthopaedics and Related Research*, **319**, pp. 54-63 (1995).
- <sup>113</sup> R. King, D. Devanathan, R. Gsell, S. Lin, and W. Rohr, "Process Induced Defects in Ultra-High Molecular-Weight Polyethylene (UHMWPE)," in *Transactions of the 41st Annual Meeting of the Orthopaedic Research Society*, 1995, p. 759.
- <sup>114</sup> M. B. Schmidt and J. V. Hamilton, "The Effects of Calcium Stearate on the Properties of UHMWPE," in *Transactions of the 42nd Annual Meeting of the Orthopaedic Research Society*, 1996, p. 22-4.
- <sup>115</sup> C. R. Bragdon, M. Jasty, J. Elder, J. Lowenstein, and W. H. Harris, "Types of Fusion Defects in UHMW Polyethylene and Their Role in Wear *In Vivo*," in *Transactions of the 42nd Annual Meeting of the Orthopaedic Research Society*, 1996, p. 489.
- <sup>116</sup> M. G. Tanner, D. Hoernschemeyer, and L. A. Whiteside, "Polyethylene Quality Variations in Currently Available Bar Stock," in *Scientific Program of the American Academy of Orthopaedic Surgeons 1997 Annual Meeting Online*, Paper No. 477 (1997).

- 
- <sup>117</sup> B. D. Furman, M. A. Ritter, and S. Li, "Effect of Polyethylene Type on Oxidation in Total Joint Replacement," in *Scientific Program of the American Academy of Orthopaedic Surgeons 1997 Annual Meeting Online*, Paper No. 479 (1997).
- <sup>118</sup> O. K. Muratoglu, M. Jasty, and W. H. Harris, "High Resolution Synchrotron Infra-Red Microscopy of the Structure of Fusion Defects in UHMWPE," in *Transactions of the 23rd Annual Meeting of the Society for Biomaterials*, 1997, p. 229.
- <sup>119</sup> R. E. Jensen, J. P. Collier, M. B. Mayor, and V. A. Surprenant, "The Role of Polyethylene Uniformity and Patient Characteristics in the Wear of Tibial Knee Components," in *Transactions of the 38th Annual Meeting of the Orthopaedic Research Society*, 1992, p. 328.
- <sup>120</sup> S. P. James, K. R. Lee, G. P. Beauregard, E. Rentfrow, and J. R. McLaughlin, "Comparison of the *In Vivo* Wear Rates of 43 Surgically Retrieved Direct Compression Molded and Ram Extruded Ultra High Molecular Weight Polyethylene Acetabular Components," in *Transactions of the Fifth World Biomaterials Congress*, 1996, Vol. 2, p. 513.
- <sup>121</sup> K. R. Lee, S. P. James, J. R. McLaughlin, G. P. Beauregard, and E. D. Cox, "Direct Compression Molded Versus Ram Extruded Bar Stock Polyethylene: A Wear Rate Analysis of Surgically Retrieved Cementless Acetabular Components at 8 Years," in *Scientific Program of the American Academy of Orthopaedic Surgeons 1997 Annual Meeting Online*, Paper No. 481 (1997).
- <sup>122</sup> J. B. Park, *Biomaterials Science and Engineering*, Plenum Press, New York, New York, 1984.
- <sup>123</sup> V. D. McGinniss, "Cross-Linking With Radiation," *Encyclopedia of Polymer Science and Engineering*, Vol. 4, John Wiley and Sons Inc., 1986, pp. 418-449.
- <sup>124</sup> D. F. Sangster, "Early Events in High-Energy Irradiation of Polymers," in *The Effects of Radiation on High-Technology Polymers*, E. Reichmanis and J. H. O'Donnell, Eds., ACS Symposium Series No. 381, ACS, Washington, D.C., 1989, pp. 14-26.
- <sup>125</sup> H. J. Nusbaum and R. M. Rose, "The Effects of Radiation Sterilization on the Properties of Ultrahigh Molecular Weight Polyethylene," *Journal of Biomedical Materials Research*, **13**, pp. 557-576 (1979).
- <sup>126</sup> H. H. Trieu and R. D. Paxson, "The Oxidized Surface Layer in Shelf-Aged UHMWPE Tibial Inserts," in *Transactions of the 41st Annual Meeting of the Orthopaedic Research Society*, 1995, p. 758.
- <sup>127</sup> B. Masri, L. C. Duus, E. A. Salvati, B. D. Brause, F. J. Zoda, and S. Li, "Optimal Dosage of Gamma Irradiation for the Sterilization of UHMWPE Used in Total Joint Replacements," in *Transactions of the 42nd Annual Meeting of the Orthopaedic Research Society*, 1996, p. 19-4.
- <sup>128</sup> J. V. Hamilton and T. Flynn, "The Role of Packaging in Sterilization of UHMWPE," in *Transactions of the Fifth World Biomaterials Congress*, 1996, Vol. 2, p. 807.
- <sup>129</sup> R. M. Streicher, "Improving UHMWPE by Ionizing Irradiation Crosslinking During Sterilization," in *Transactions of the 17th Annual Meeting of the Society for Biomaterials*, 1991, p. 181.
- <sup>130</sup> M. D. Ries, K. Weaver, and N. Beals, "Safety and Efficacy of Ethylene Oxide Sterilized Polyethylene in Total Knee Arthroplasty," *Clinical Orthopaedics and Related Research*, **331**, pp. 159-163 (1996).

- 
- <sup>131</sup> "Ethylene Oxide, Ethylene Chlorohydrin, and Ethylene Glycol: Proposed Maximum Residue Limits and Maximum Levels of Exposure," United States Food and Drug Administration, *Federal Register*, **43**, pp. 27473-27483 (1983).
- <sup>132</sup> "Notification Requirements: Reportable Quantity Adjustments," United States Environmental Protection Agency, *Federal Register*, **48**, pp. 23552-23584 (1983).
- <sup>133</sup> "Ethylene Oxide Sterilizers in Health Care Facilities, Engineering Controls and Work Practices," United States National Institute for Occupation Safety and Health, *Current Intelligence Bulletin*, **523**, p. 1-12 (1989).
- <sup>134</sup> "Biologic Evaluation of Medical Devices, Part 7: Ethylene Oxide Sterilization Residuals," ISO 10993-7 (R/2-94), International Organization for Standardization, American National Standards Institute, New York, New York, 1994.
- <sup>135</sup> R. Clough, "Radiation-Resistant Polymers," in *Encyclopedia of Polymer Science and Engineering*, Vol. 13, Wiley-Interscience, New York, 1988, pp. 667-708.
- <sup>136</sup> J. H. O'Donnell, "Radiation Chemistry of Polymers," in *Effects of Radiation on High-Technology Polymers*, E. Reichmanis and J. H. O'Donnell, Eds., ACS Symposium Series No. 381, ACS, Washington, D.C., 1989, pp. 1-13.
- <sup>137</sup> W. Schnabel, *Polymer Degradation: Principles & Practical Applications*, Hanser International, New York, 1981.
- <sup>138</sup> W. L. Hawkins, *Polymer Degradation and Stabilization*, Springer-Verlag, New York, 1984.
- <sup>139</sup> B.-A. Sultan, "Crosslinking (of Polyolefins)," in *Polymeric Materials Encyclopedia*, Vol. 2, J. C. Salamone, Ed., CRC Press, Inc., New York, 1996, pp. 1552-1565.
- <sup>140</sup> B. D. Furman, D. Kasprzak, and S. Li, "Differences in Oxidation Between Shelf Life Aged and Retrieved UHMWPE Components," in *Trans. of the 42nd Ann. Mtg. of the Orthop. Res. Soc.*, 1996, p. 484.
- <sup>141</sup> W. M. Sanford and K. A. Saum, "Accelerated Oxidative Aging Testing of UHMWPE," in *Trans. of the 41st Ann. Mtg. of the Orthop. Res. Soc.*, 1995, pp. 119-20.
- <sup>142</sup> K. R. St. John, M. J. Takeuchi, and R. A. Poggie, "Effects of Radiation Dose and Packaging Condition on the Oxidation of UHMWPE," in *Trans. of the 23rd Ann. Mtg. of the Soc. for Biomat.*, 1997, p. 46.
- <sup>143</sup> M. A. Flynn, K. W. Greer, et al., "Correlation Between Oxidation, Crystallinity, and Density of Shelf-Aged UHMWPE Implants," in *Trans. of the 5th World Biomat. Cong.*, 1996, Vol. 2, p. 187.
- <sup>144</sup> C. M. Rimnac, R. W. Klein, et al., "Post-Irradiation Aging UHMWPE," *The J. of Bone and Joint Surgery*, **76-A (7)**, pp. 1052-1056 (1994).
- <sup>145</sup> J. C. Higgins and D. R. Roesener, "Evaluation of Free Radical Reduction Treatments for UHMWPE," in *Transactions of the 42nd Annual Meeting of the Orthopaedic Research Society*, 1996, p. 485.
- <sup>146</sup> K. H. Lee, C. C. Chu, R. A. Gsell, and S. Lin, "Electron Spin Resonance Study of Free Radical Properties of Ultra-High Molecular Weight Polyethylene Upon  $\gamma$ -Irradiation," in *Transactions of the Fifth World Biomaterials Congress*, 1996, Vol. 1, p. 296.
- <sup>147</sup> M. S. Jahan, D. E. Thomas, H. H. Trieu, W. O. Haggard, R. L. Conta, and J. E. Parr, "Investigation of Free Radicals in Shelf-Aged Polyethylene Tibial Components," in *Transactions of the Fifth World Biomaterials Congress*, 1996, Vol. 1, p. 298.

- 
- <sup>148</sup> H. H. Trieu, W. O. Haggard, R. L. Conta, J. E. Parr, D. E. Thomas, and M. S. Jahan, "Investigation of Free Radicals in UHMWPE Materials Following Irradiation and Aging," *Symposium on Characterization and Properties of Ultra-High Molecular Weight Polyethylene*, American Society for Testing and Materials, 1996, p. 12.
- <sup>149</sup> H. H. Trieu, W. O. Haggard, J. E. Parr, D. E. Thomas, and M. S. Jahan, "A Study of Long-Lived Free Radicals in Irradiated UHMWPE Materials," in *Transactions of the 23rd Annual Meeting of the Society for Biomaterials*, 1997, p. 47.
- <sup>150</sup> J. V. Hamilton, R. Walton, and P. Lahti, "The Effects of Sterilization Atmosphere and Depth on Free Radicals in UHMWPE," in *Transactions of the 23rd Annual Meeting of the Society for Biomaterials*, 1997, p. 48.
- <sup>151</sup> M. S. Jahan and D. E. Thomas, "Detection of Thermoluminescence in Irradiated and Aged UHMWPE," in *Transactions of the 23rd Annual Meeting of the Society for Biomaterials*, 1997, p. 214.
- <sup>152</sup> R. S. Pascaud, W. T. Evans, P. J. J. McCullagh, D. FitzPatrick, and K. Brummitt, "Results of a Two-Year Differential Scanning Calorimetry (DSC) Programme on UHMW-PE," in *Transactions of the Fifth World Biomaterials Congress, 1996, Vol. 2*, p. 193.
- <sup>153</sup> R. S. Pascaud, W. T. Evans, P. J. J. McCullagh, and D. FitzPatrick, "Effects of Batch to Batch Variations and Test Methodology on Degree of Crystallinity and Melting Temperature of UHMW-PE as Measured by Differential Scanning Calorimetry," *Journal of Biomedical Materials Research*, **32**, pp. 619-626 (1996).
- <sup>154</sup> K. A. Saum, "Oxidation Vs. Depth and Time for Polyethylene Gamma Sterilized in Air," in *Transactions of the 40th Annual Meeting of the Orthopaedic Research Society*, 1994, pp. 174-30.
- <sup>155</sup> F. A. Menschik, D. E. Weiland, G. H. Menschik, and C. M. Rimnac, "FTIR Analysis of Oxidation in Retrieved and Shelf-Aged UHMWPE Tibial Inserts," in *Transactions of the 42nd Annual Meeting of the Orthopaedic Research Society*, 1996, p. 491.
- <sup>156</sup> B. D. Furman, D. Kasprzak, and S. Li, "Differences in Oxidation Between Shelf Life Aged and Retrieved Ultra High Molecular Weight Polyethylene Components," in *Transactions of the 42nd Annual Meeting of the Orthopaedic Research Society*, 1996, p. 484.
- <sup>157</sup> D. C. Sun, A. Halleck, G. Schmidig, A. Wang, C. Stark, and J. H. Dumbleton, "FTIR Oxidation Analysis of UHMWPE Implants: Possible Contamination From Synovial Fluid and Serum," *Symposium on Characterization and Properties of Ultra-High Molecular Weight Polyethylene*, American Society for Testing and Materials, 1996, p. 5.
- <sup>158</sup> W. M. Sanford and K. A. Saum, "Accelerated Oxidative Aging Testing of UHMWPE," in *Transactions of the 41st Annual Meeting of the Orthopaedic Research Society*, 1995, p. 119-20.
- <sup>159</sup> K. R. St. John, M. J. Takeuchi, and R. A. Poggie, "Effects of Radiation Dose and Packaging Condition on the Oxidation of UHMWPE," in *Transactions of the 23rd Annual Meeting of the Society for Biomaterials*, 1997, p. 46.
- <sup>160</sup> M. A. Flynn, K. W. Greer, J. V. Hamilton, and D. J. Treacy, "Correlation Between Oxidation, Crystallinity and Density of Shelf-Aged UHMWPE Implants," in *Transactions of the Fifth World Biomaterials Congress, 1996, Vol. 2*, p. 187.
- <sup>161</sup> C. M. Rimnac, R. W. Klein, F. Betts, and T. M. Wright, "Post-Irradiation Aging of Ultra-High Molecular Weight Polyethylene," *The Journal of Bone and Joint Surgery*, **76-A (7)**, pp. 1052-1056 (1994).

- 
- <sup>162</sup> M. P. Bostrom, A. P. Bennett, C. M. Rimnac, and T. M. Wright, "The Natural History of Ultra High Molecular Weight Polyethylene," *Clinical Orthopaedics and Related Research*, **309**, pp. 20-28 (1994).
- <sup>163</sup> B. D. Furman, G. L. Furman, and S. Li, "Effect of Resin Type on the Oxidation of UHMWPE," in *Transactions of the Fifth World Biomaterials Congress*, 1996, Vol. 2, p. 188.
- <sup>164</sup> S. M. Kurtz, C. M. Rimnac, and D. L. Bartel, "Degradation Rate of Ultra-High Molecular Weight Polyethylene," *Journal of Orthopaedic Research*, **15** (1), pp. 57-61 (1997).
- <sup>165</sup> S. M. Kurtz, C. M. Rimnac, and D. L. Bartel, "The Degradation Rate of UHMWPE Components," in *Transactions of the 42nd Annual Meeting of the Orthopaedic Research Society*, 1996, p. 492.
- <sup>166</sup> H. McKellop, B. Yeom, D. C. Sun, and W. M. Sanford, "Accelerated Ageing of Irradiated UHMW Polyethylene for Wear Evaluations," in *Transactions of the 42nd Annual Meeting of the Orthopaedic Research Society*, 1996, p. 483.
- <sup>167</sup> R. King, G. Taylor, D. Devanathan, S. Lin, and W. Rohr, "Gamma Radiation Effect on Crosslinking of Ultra-High Molecular-Weight Polyethylene," in *Transactions of the 23rd Annual Meeting of the Society for Biomaterials*, 1997, p. 217.
- <sup>168</sup> H. McKellop, F. Shen, T. Ota, B. Lu, H. Wisner, and E. Yu, "The Effect of Sterilization Method, Calcium Stearate and Molecular Weight on Wear of UHMWPE Acetabular Cups," in *Transactions of the 23rd Annual Meeting of the Society for Biomaterials*, 1997, p. 43.
- <sup>169</sup> R. A. Gsell, K. Lee, C. Chu, and S. Lin, "Minimizing Oxidative Degradation on Gamma Sterilization," in *Transactions of the Fifth World Biomaterials Congress*, 1996, Vol. 2, p. 191.
- <sup>170</sup> R. A. Gsell, K. H. Lee, C. C. Chu, and S. Lin, "Surface Oxidation Index and its Depth Profile of Ultra-High Molecular Weight Polyethylene Upon  $\gamma$ -Irradiation Sterilization," in *Transactions of the Fifth World Biomaterials Congress*, 1996, Vol. 2, p. 806.
- <sup>171</sup> D. C. Sun, A. Wang, C. Stark, and J. H. Dumbleton, "Development of Stabilized UHMWPE Implants with Improved Oxidation Resistance via Crosslinking," a Scientific Exhibition presented at the 63rd Annual Meeting of the American Academy of Orthopaedic Surgeons, 1996.
- <sup>172</sup> D. C. Sun, G. Schmidig, C. Stark, and J. H. Dumbleton, "A Simple Accelerated Aging Method for Simulations of Long-Term Oxidative Effects in UHMWPE Implants," in *Transactions of the 42nd Annual Meeting of the Orthopaedic Research Society*, 1996, p. 493.
- <sup>173</sup> D. C. Sun, G. Schmidig, C. Stark, and J. H. Dumbleton, "A Simple Accelerated Aging Method for Long Term Post-Radiation Effects in UHMWPE Implants," in *Transactions of the Fifth World Biomaterials Congress*, 1996, Vol. 2, p. 523.
- <sup>174</sup> G. Taylor, R. Gsell, R. King, D. Devanathan, and S. Lin, "Stability of N<sub>2</sub> Packaged Gamma Irradiated UHMWPE," in *Transactions of the 23rd Annual Meeting of the Society for Biomaterials*, 1997, p. 421.
- <sup>175</sup> D. Swarts, R. Gsell, R. King, D. Devanathan, S. Wallace, S. Lin, and W. Rohr, "Aging of Calcium Stearate-Free Polyethylene," in *Transactions of the Fifth World Biomaterials Congress*, 1996, Vol. 2, p. 196.
- <sup>176</sup> R. A. Poggie, M. T. Takeuchi, and R. Averill, "Effects of Resin Type, Consolidation Method, and Sterilization on UHMWPE," in *Transactions of the 23rd Annual Meeting of the Society for Biomaterials*, 1997, p. 216.

- 
- <sup>177</sup> T. Johnson, D. Devanathan, D. Swarts, R. King, S. Lin, R. Gsell, and W. Rohr, "Process Dependent Characteristics of Polyethylene," in *Transactions of the Fifth World Biomaterials Congress*, 1996, Vol. 2, p. 514.
- <sup>178</sup> D. C. Sun, S. S. Yau, C. Stark, and J. H. Dumbleton, "The Location of the Oxidation Maximum in Relation to the Post-Radiation History of UHMWPE Implants," in *Transactions of the Fifth World Biomaterials Congress*, 1996, Vol. 1, p. 297.
- <sup>179</sup> K. B. Farber and J. P. Collier, "Oil Red O Staining: Determining Oxidation of Ultra High Molecular Weight Polyethylene," in *Transactions of the Fifth World Biomaterials Congress*, 1996, Vol. 1, p. 294.
- <sup>180</sup> C. J. Bell, M. Abeysondera, P. S. Walker, and G. W. Blunn, "Wear and Oxidation of Ultra High Molecular Weight Polyethylene," in *Transactions of the Fifth World Biomaterials Congress*, 1996, Vol. 1, p. 655.
- <sup>181</sup> J. Scheirs, O. Delatycki, S. W. Bigger, and N. C. Billingham, "Staining Techniques for Detecting Localized Oxidation in High-Density Polyethylene Powders and Films," *Polymer International*, 26 (3), pp. 187-193 (1991).
- <sup>182</sup> K. A. Dwyer and J. T. Bryant, "The Role of Incomplete Fusion of UHMWPE Powder: Mechanical and Chemical Degradation of Total Joint Arthroplasties," in *Transactions of the Fifth World Biomaterials Congress*, 1996, Vol. 1, p. 986.
- <sup>183</sup> L. C. Sutula, K. A. Saum, J. P. Collier, and B. H. Currier, "Time Dependent Oxidation and Damage in Retrieved and Never Implanted UHMWPE Components," in *Transactions of the 41st Annual Meeting of the Orthopaedic Research Society*, 1995, p. 118-20.
- <sup>184</sup> H. A. Bartholf, I. R. Williams, L. C. Sutula, D. R. Lund, and T. W. Baldwin, "Subsurface Oxidation of Retrieved and Never Implanted Polyethylene Tibial Trays," *Scientific Program of the American Academy of Orthopaedic Surgeons 1997 Annual Meeting Online*, Paper No. 153 (1997).
- <sup>185</sup> S. Cristante, B. R. Harris, M. E. Carroll, H. H. Trieu, W. O. Haggard, and J. E. Parr, "The Role of Sterilization in Fatigue Wear of UHMWPE Tibial Components," in *Transactions of the Fifth World Biomaterials Congress*, 1996, Vol. 1, p. 295.
- <sup>186</sup> O. Muratoglu, A. Liu, M. Jasty, C. R. Bragdon, J. R. Elder, and W. H. Harris, "Oxidative Degradation and Embrittlement of Ultrahigh Molecular Weight Polyethylene: Analysis of 107 Components," in *Transactions of the Fifth World Biomaterials Congress*, 1996, Vol. 2, p. 808.
- <sup>187</sup> A. Bellare, M. Spector, and R. E. Cohen, "Alterations in Microstructure of UHMWPE Due to Post-Irradiation Aging," in *Transactions of the Fifth World Biomaterials Congress*, 1996, Vol. 2, p. 183.
- <sup>188</sup> A. Bellare, M. Spector, and R. E. Cohen, "Mechanisms of Morphological Alteration Accompanying Post-Irradiation Aging in Ultra-High Molecular Weight Polyethylene," *Symposium on Characterization and Properties of Ultra-High Molecular Weight Polyethylene*, American Society for Testing and Materials, 1996, p. 6.
- <sup>189</sup> S. Bhambri, R. King, D. Devanathan, L. Gilbertson, S. Lin and W. Rohr, "Effect of Aging on the Morphology and Ultrastructure of Polyethylene Gamma-Irradiated in Nitrogen," in *Transactions of the 23rd Annual Meeting of the Society for Biomaterials*, 1997, p. 213.
- <sup>190</sup> "Standard Test Methods for Determination of Gel Content and Swell Ratio of Crosslinked Ethylene Plastics," Standard D2765-95, *Annual Book of ASTM Standards*, Vol. 8.02, American Society for Testing and Materials, 2000, pp. 112-118.

- 
- <sup>191</sup> D. C. Sun, G. Schmidig, S. S. Yau, M. Huffmann, C. Stark, and J. H. Dumbleton, "Assessment of Gel Content and Crosslinking Density in UHMWPE," in *Transactions of the 23rd Annual Meeting of the Society for Biomaterials*, 1997, p. 431.
- <sup>192</sup> A. Wang, D. C. Sun, C. Stark, and J. H. Dumbleton, "Effects of Sterilization Methods on the Wear of Ultra-High Molecular Weight Polyethylene Acetabular Cups," in *Transactions of the Fifth World Biomaterials Congress*, 1996, Vol. 2, p. 198.
- <sup>193</sup> P. Eyerer, M. Kurth, H. A. McKellup, and T. Mittlmeier, "Characterization of UHMWPE Hip Cups Run on Joint Simulators," *Journal of Biomedical Materials Research*, **21**, pp. 275-291 (1987).
- <sup>194</sup> F. F. Brossa, R. Chiesa, A. Cigada, A. Galli, L. Paracchini, and M. C. Tanzi, "Degradation of UHMWPE Due to Compression Molding and  $\gamma$ -Sterilization," in *Transactions of the Fifth World Biomaterials Congress*, 1996, Vol. 2, p. 197.
- <sup>195</sup> D. C. Sun, A. Wang, C. Stark, and J. H. Dumbleton, "The Concept of Stabilization in UHMWPE," in *Transactions of the Fifth World Biomaterials Congress*, 1996, Vol. 2, p. 195.
- <sup>196</sup> D. C. Sun and C. F. Stark, "Non-Oxidizing Polymeric Medical Implant," U.S. Patent 5,414,049, 1995.
- <sup>197</sup> D. C. Sun, A. Wang, C. F. Stark, and J. H. Dumbleton, "Effect of Radiation-Induced Crosslinking on Creep and Wear Performance of Ultra-High Molecular Weight Polyethylene," *Scientific Program of the American Academy of Orthopaedic Surgeons 1996 Annual Meeting Online*, Paper No. 393 (1996).
- <sup>198</sup> J. V. Hamilton, M. B. Schmidt, and K. W. Greer, "Improved Wear of UHMWPE Using a Vacuum Sterilization Process," in *Transactions of the 42nd Annual Meeting of the Orthopaedic Research Society*, 1996, pp. 20-4.
- <sup>199</sup> K. Ramani, N. C. Parasnis, and D. Devanathan, "Use of Design of Experiments to Reveal Process-Property Effects in Compression Molding of Ultra High Molecular Weight Polyethylene," in *Transactions of the Fifth World Biomaterials Congress*, 1996, Vol. 2, p. 521.
- <sup>200</sup> "Data Requirements for Ultrahigh Molecular Weight Polyethylene (UHMWPE) Used in Bearing Surfaces for Orthopedic Devices," Final Draft, U.S. Food and Drug Administration, September 7, 1997, in a personal communication from M. Ken McDermott (October 10, 1997).
- <sup>201</sup> "Standard Test Method for Tensile Properties of Plastics," Standard D638-99, *Annual Book of ASTM Standards*, Vol. 08.01, American Society for Testing and Materials, 2000, pp. 46-58.
- <sup>202</sup> M. Ries, R. Rose, J. Greer, K. Weaver, W. Sauer, and N. Beals, "Sterilization Induced Effects on UHMWPE Performance Properties," in *Transactions of the 41st Annual Meeting of the Orthopaedic Research Society*, 1995, p. 757.
- <sup>203</sup> M. D. Ries, K. Weaver, R. M. Rose, J. Gunther, W. Sauer, and N. Beals, "Fatigue Strength of Polyethylene After Sterilization by Gamma Irradiation or Ethylene Oxide," *Clinical Orthopaedics and Related Research*, **333**, p. 87-95 (1996).
- <sup>204</sup> S. E. White, R. D. Paxson, M. G. Tanner, and L. A. Whiteside, "Effects of Sterilization on Wear in Total Knee Arthroplasty," *Clinical Orthopaedics and Related Research*, **331**, pp. 164-171 (1996).



- 
- <sup>205</sup> S. M. Kurtz, C. M. Rimnac, T. J. Santner, and D. L. Bartel, "Exponential Model for the Tensile True Stress-Strain Behavior of As-Irradiated and Oxidatively Degraded Ultra High Molecular Weight Polyethylene," *Journal of Orthopaedic Research*, **14** (5), pp. 755-761 (1996).
- <sup>206</sup> J. E. Windau and T. J. Mackin, "The Effects of Processing and Sterilization on Ultra High Molecular Weight Polyethylene," in *Transactions of the Fifth World Biomaterials Congress*, Vol. 2, 1996, p. 199.
- <sup>207</sup> S. J. Megremis and S. F. Hulbert, "The Effects of the Manufacturing Process and Sterilization Technique on the Tensile Properties of Ultra-High-Molecular-Weight Polyethylene," in *Transactions of the Fifth World Biomaterials Congress*, Vol. 2, 1996, p. 512.
- <sup>208</sup> S. J. Megremis and S. F. Hulbert, "Fatigue Crack Propagation Rates of Isostatic Pressed and Ram Extruded Ultra-High-Molecular-Weight Polyethylene," in *Transactions of the Fifth World Biomaterials Congress*, Vol. 2, 1996, p. 517.
- <sup>209</sup> J. P. Collier, L. C. Sutula, B. H. Currier, J. H. Currier, R. E. Wooding, I. R. Williams, K. B. Farber, and M. B. Mayor, "Overview of Polyethylene as a Bearing Material," *Clinical Orthopaedics and Related Research*, **333**, pp. 76-86 (1996).
- <sup>210</sup> M. A. Schmidt and R. D. Compton, "Confocal Microscopy," in *Friction, Lubrication, and Wear Technology*, ASM Handbook, Vol. 18, ASM International, 1992, pp. 357-361.
- <sup>211</sup> M. Petran, M. Hadravsky, M. D. Egger, and R. Galambos, "Tandem-Scanning Reflected-Light Microscope," *Journal of the Optical Society of America*, **58** (5), pp. 661-664 (1968).
- <sup>212</sup> T. Wilson, *Confocal Microscopy*, Academic Press, New York, 1990, pp. 1-64.
- <sup>213</sup> J. F. Song and T. V. Vorburger, "Surface Texture," in *Friction, Lubrication, and Wear Technology*, ASM Handbook, Vol. 18, ASM International, 1992, pp. 334-345.
- <sup>214</sup> J. L. Hay and G. M. Pharr, "Instrumented Indentation Testing," in *Mechanical Testing and Evaluation*, ASM Handbook, Vol. 8, ASM International.
- <sup>215</sup> G. M. Pharr, "Measurement of Mechanical Properties by Ultra-Low Load Indentation," *Materials Science and Engineering*, **A253**, pp. 151-159 (1998).
- <sup>216</sup> B. N. Lucas, C. T. Rosenmayer, and W. C. Oliver, "Mechanical Characterization of Sub-Micron Polytetrafluoroethylene (PTFE) Thin Films," in *Thin Films: Stresses and Mechanical Properties VII*, Materials Research Society, Fall Meeting 1997.
- <sup>217</sup> B. N. Lucas, "Measuring the Viscoelastic Properties of Polymers Using Frequency Specific Depth-Sensing Indentation," *Plastics Analysis Division Review*, Vol. XXVI (1), Society of Plastics Engineers, 1998.
- <sup>218</sup> L. Mandelkern, "The Structure of Crystalline Polymers," *Accounts of Chemical Research*, **23** (11), pp. 380-386 (1990).
- <sup>219</sup> L. Mandelkern, "Thermodynamic and Morphological Properties of Crystalline Polymers," *The Journal of Physical Chemistry*, **75** (26), pp. 3909-3920 (1971).
- <sup>220</sup> N. Stribeck, R. G. Alamo, L. Mandelkern, and H. G. Zachmann, "Study of the Phase Structure of Linear Polyethylene by Means of Small-Angle X-ray Scattering and Raman Spectroscopy," *Macromolecules*, **28**, pp. 5029-5036 (1995).
- <sup>221</sup> L. Mandelkern, "Characterization of Crystalline Polymers by Raman Spectroscopy and Differential Scanning Calorimetry," in *Polymer Characterization: Physical Property*,

- 
- Spectroscopic, and Chromatographic Methods*, Advances in Chemistry Series, Vol. 227, American Chemical Society, Washington, D.C., pp. 377-395, 1990.
- <sup>222</sup> R. W. Hendricks, "The ORNL 10-Meter Small-Angle X-ray Scattering Camera," *Journal of Applied Crystallography*, **11**, pp. 11-15 (1978).
- <sup>223</sup> J. S. Higgins and R. S. Stein, "Recent Developments in Polymer Applications of Small-Angle Neutron, X-ray and Light Scattering," *Journal of Applied Crystallography*, **11**, pp. 346-375 (1978).
- <sup>224</sup> C. G. Vonk, "The Determination of the Lamellar Thickness in Semi-Crystalline Polymers by Small-Angle Scattering," *Makromol. Chem., Macromol. Symp.*, **15**, pp. 215-222 (1988).
- <sup>225</sup> G. R. Strobl and M. Schneider, "Direct Evaluation of the Electron Density Correlation Function of Partially Crystalline Polymers," *Journal of Polymer Science: Polymer Physics Edition*, **18**, pp. 1343-1359 (1980).
- <sup>226</sup> B. D. Cullity, *Elements of X-Ray Diffraction*, 2nd Edition, Addison-Wesley Publishing Company, Inc., 1978.
- <sup>227</sup> J. L. Matthews, H. S. Peiser, and R. B. Richards, "The X-Ray Measurement of the Amorphous Content of Polythene Samples," *Acta. Cryst.*, **2**, p. 85 (1949).
- <sup>228</sup> S. Kavesh and J. M. Schultz, "Meaning and Measurement of Crystallinity in Polymers: A Review," *Polymer Engineering and Science*, **9** (6), pp. 452-460 (1969).
- <sup>229</sup> S. M. Stevens, "The Use of FTIR-Microspectrometry for the Measurement of Crystallinity in Polyethylene Welds and Helical Content in Polypropylene Welds," *Analytical Applications of Spectroscopy II*, A. M. C. Davies and C. S. Creaser, Eds., Royal Society of Chemistry, Cambridge, Cambridgeshire, UK, 1991.
- <sup>230</sup> G. Kämpf, *Characterization of Plastics by Physical Methods*, Hanser Publishers, New York, 1986.
- <sup>231</sup> J. P. Runt, "Crystallinity Determination," *Encyclopedia of Polymer Science and Engineering*, Vol. 4, John Wiley & Sons, Inc., pp. 482-519, 1986.
- <sup>232</sup> Private communication from R. A. Phillips, Montell USA, Inc., Research & Development Center, Elkton, Maryland.
- <sup>233</sup> G. D. Wignall, J. S. Lin, and S. Spooner, "Reduction of Parasitic Scattering in Small-Angle X-Ray-Scattering by a 3-Pinhole Collimating System," *Journal of Applied Crystallography*, **23** (4), pp. 241-245 (1990).
- <sup>234</sup> R. W. Hendricks, "ORNL 10-Meter Small-Angle X-Ray Scattering Camera," *Journal of Applied Crystallography*, **11**, pp. 15-30 (1978).
- <sup>235</sup> T. P. Russell, J. S. Lin, S. Spooner and G. D. Wignall, "Intercalibration of Small-Angle X-Ray and Neutron-Scattering Data," *Journal of Applied Crystallography*, **21** (6), pp. 629-638 (1988).
- <sup>236</sup> L. Mandelkern, "Morphology of Semicrystalline Polymers," Chapter 13, *Characterization of Materials in Research, Ceramics and Polymers*, J. J. Burke and V. Weiss, Eds., Syracuse University Press, pp. 369-415, 1975.
- <sup>237</sup> P. J. Phillips, *Fingerprinting the Thermal History of Polymeric Materials*, EPRI TR-101205, Research Project 2614-32 Final Report, Electric Power Research Institute, Palo Alto, CA, 1992.

- 
- <sup>238</sup> S. Rastogi, L. Kurelec, and P. J. Lemstra, "Chain Mobility in Polymer Systems: On the Borderline between Solid and Melt. 2. Crystal Size Influence in Phase Transition and Sintering of Ultrahigh Molecular Weight Polyethylene via the Mobile Hexagonal Phase," *Macromolecules*, **31**, pp. 5022-5031 (1998).
- <sup>239</sup> L. Mandelkern, J. M. Price, M. Gopalan, and J. G. Fatou, "Sizes and Interfacial Free Energies of Crystallites Formed from Fractional Linear Polyethylene," *Journal of Polymer Science, Part A-2*, **4**, pp. 385-400 (1966).
- <sup>240</sup> J. M. Schultz, W. H. Robinson, and G. M. Pound, "Temperature-Dependent X-Ray Small-Angle Scattering from Melt-Crystallized Polyethylene," *Journal of Polymer Science, Part A-2*, **5**, pp. 511-33 (1967).
- <sup>241</sup> P. J. Phillips and R. J. Philpot, "Direct Evidence for Melting During Drawing of Polyethylene," *Polymer Communications*, **27**, pp. 307-309 (1986).
- <sup>242</sup> R. A. Phillips, "Morphology and Melting Behavior of Nascent Ultra-High Molecular Weight Polyethylene," *Journal of Polymer Science: Part B, Polymer Physics*, **36**, pp. 495-517 (1998).
- <sup>243</sup> I. Kamel and L. Finegold, "A Model for Radiation-Induced Changes in Ultrahigh-Molecular-Weight Polyethylene," *Journal of Polymer Science: Polymer Physics Edition*, **23**, pp. 2407-2409 (1985).
- <sup>244</sup> M. Deng and S. W. Shalaby, "Long-term  $\gamma$  Irradiation Effects on Ultrahigh Molecular Weight Polyethylene," *Journal of Biomedical Materials Research*, **54** (3), pp. 428 – 435 (2001).
- <sup>245</sup> F. J. Baltá-Calleja, J. Martínez-Salazar, and D. R. Rueda, "Hardness," in *Encyclopedia of Polymer Science and Engineering*, 2nd Edition, Vol. 7, John Wiley & Sons, Inc., pp. 614-626, 1987.
- <sup>246</sup> D. R. Rueda, J. Martínez-Salazar, and F. J. Baltá-Calleja, "Annealing Effects in Lamellar Linear Polyethylene as Revealed by Microhardness," *Journal of Materials Science*, **20**, pp. 834-838 (1985).

## VITA

Monica A. Schmidt was born in Moberly, Missouri, on August 14, 1960. She graduated from Moberly High School in May, 1978. She entered the University of Missouri-Rolla the following August, and graduated in May, 1982, Summa Cum Laude, with a Bachelor of Science degree in Ceramic Engineering. During college she held summer jobs at the Mound Facility in Miamisburg, Ohio, and the Y-12 Plant in Oak Ridge, Tennessee.

In 1983, she returned to Oak Ridge to work at the Oak Ridge Gaseous Diffusion Plant (K-25). She worked as the Refurbishment Engineer on the AVLIS Program from 1983 until 1986, and then transferred to the Metals and Ceramics Division at the Oak Ridge National Laboratory as a Research Associate. She developed expertise in microscopy, digital imaging, and materials characterization techniques, and met her future doctoral advisor, Dr. David C. Joy, who introduced her to confocal microscopy. She accepted a position as a Project Manager in the Decontamination and Decommissioning Program at the K-25 Site in 1991.

The next year she began graduate studies in the Materials Science and Engineering Department, and continued working part-time at K-25. She pursued her goal of applying her materials characterization expertise to materials used in orthopaedic surgery. In 1994, she attended the NATO Advanced Study Institute on Materials Science and Implant Orthopaedic Surgery II in Chania, Crete (Greece), to train with biomaterials experts from around the world. In 1996, she became a full-time student to complete her research on UHMWPE implant bearings. Later she took two semesters to gain experience as a Graduate Teaching Assistant in Materials Science and Engineering and in Biomedical Engineering. The doctoral degree in Metallurgical Engineering was received on August 10, 2001.

She has been married for over 20 years to a Chemical Engineer, and has two children. She teaches Sunday School, and volunteers with Girl Scouts of Tanasi Council, where she develops science and microscopy programs for girls.